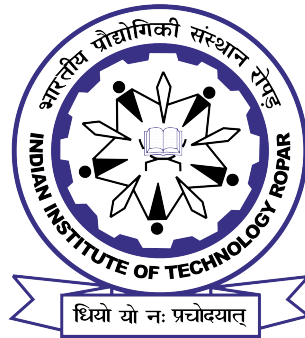# Generation and Characterization of Spatially Controlled Structured Light with Exotic Propagation Properties

By

Vasu Dev

Submitted

in fulfillment of the requirements for the degree

of

Doctor of Philosophy

Department of Physics

Indian Institute of Technology Ropar

June 2023

This thesis is dedicated to

My Parents

and

My Supervisor

Certificate

It is certified that the work contained in this thesis entitled "**Generation and Characterization of Spatially Controlled Structured Light with Exotic Propagation Properties**" by **Mr. Vasu Dev**, a student in the Department of Physics, to Indian Institute of Technology Ropar, for the award of degree of **Doctor of Philosophy** has been carried out under my supervision and this work has not been submitted elsewhere for a degree.
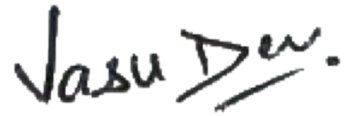
Dr. Vishwa Pal

Assistant Professor

Department of Physics

Indian Institute of Technology Ropar

Date: 17 October 2023

Declaration

I hereby declare that the work presented in the thesis entitled "**Generation and Characterization of Spatially Controlled Structured Light with Exotic Propagation Properties**" submitted for the degree of **Doctor of Philosophy** in Physics by me to the Indian Institute of Technology Ropar has been carried out under the supervision of **Dr. Vishwa Pal**. This work is original and has not been submitted in part or full by me elsewhere for a degree.

Vasu Dev

Vasu Dev

PhD Research Scholar

Department of Physics

Indian Institute of Technology Ropar

Date: 17 October 2023

Acknowledgements

The PhD journey is one of the most happening and learning parts of my life taught me so many things which have been greatly influenced by many people whom I have come across. It is a pleasure to thank everyone who supported directly or indirectly during this wonderful journey. I am trying my best to mention them, but my apologies to those who remain to be mentioned.

First and foremost, I would like to express my deepest gratitude towards the most influential and important person in this journey, my esteemed PhD supervisor Dr. Vishwa Pal for his unwavering support and guidance throughout my doctoral journey. His expertise, encouragement, and dedication have been instrumental in the successful completion of my research work. I am truly grateful for his exceptional mentorship and invaluable insights, which have shaped my understanding of the subject matter and enhanced my research skills. His profound knowledge and enthusiasm for the field have inspired me to pursue excellence and push the boundaries of knowledge. I express my gratitude towards him for his invaluable assistance in enhancing the aesthetic appeal of my manuscripts, presentations, and thesis, rendering them more visually appealing and polished. I feel privileged to be nourished under his guidance. I extend my heartfelt appreciation to him, as without his indispensable support, this journey would not be possible.

I would also like to thank my Doctoral Committee (DC) members at IIT Ropar, Dr. Kailash C. Jena, Dr. Mukesh Kumar, Dr. Anil Shukla, and chairperson Dr. Shubhrangshu Dasgupta for their careful evaluation of my progress during my PhD. I would also like to acknowledge our collaborator, Dr. Andra Naresh K. Reddy, who provided valuable inputs in computational and experimental studies and enhanced my knowledge with fruitful discussions. I am thankful to our collaborators Prof. Svetlana N. Khonina and Prof. Andrey V. Ustinov for an interesting collaborative research work.

I am thankful to the Indian Institute of Technology Ropar for financial support. I also thank the Department of Physics for the infrastructure, and other faculty members for their support. I gratefully acknowledge Mr. Anshu Vaid, Sr. Assistant, Department of Physics, for his genuine assistance that helped me a lot in the smoother process of administrative paperwork.

Above all, I owe my heartfelt gratitude to my parents; their unwavering trust and guidance have profoundly influenced my development, molding me into the individual I have become today. I wholeheartedly express my gratitude towards them. Their constant support and enthusiasm have helped me to face several challenges throughout my PhD journey. I am also thankful to my brother Shashikant Pandey and Jagdeep Sharma

Vasu Dev
Indian Institute of Technology Ropar, India-140001
June 2023

Abstract

Light possesses various spatial and temporal degrees of freedom, such as amplitude, phase, polarization, time, and frequency. Controlling these aspects for generating light with complex field distributions possessing exotic propagation properties, has renewed its interest in numerous applications both in fundamental science as well in applied fields. Due to this there has been growing interest in synthesizing such complex light field distributions, also called as structured light. Typically, the output from a laser consists of a Gaussian distribution, which exhibits physical limitations for various applications. However, with continuous advancements, it has become possible to control the distribution of light in different degrees of freedom. In this thesis, our aim has been to develop simple, cost-effective, and efficient outer-cavity and intra-cavity methods for generation and characterization of novel spatially structured light with customised intensity and phase distributions as well as possessing exotic propagation properties. In addition to these, our emphasis has also been to improve the quality, resolution, resilience against perturbations, and spectral range of spatially controlled structured light.

Chapter 1 is an introduction to the thesis, where we begin with the role of structured light in the modern world by mentioning its applications in fundamental and applied fields where conventional Gaussian beams pose physical limitations. We have discussed various types of spatially structured light along with their propagation properties, obtained by tailoring light in its various spatial degrees of freedom. Further, we have discussed the generation of spatially structured light based on various outer-cavity and intra-cavity methods. We have also described the analytical and numerical methods for modeling the laser cavities as well as the propagation and quantification of spatially structured light. We have also provided a brief overview of spatial light modulators including the mechanism for modulating light in the amplitude and phase degrees of freedom.

Chapter 2 emphasizes the tailoring of amplitude degree of freedom of light to generate uniform-intensity distribution with customized spatial shapes, such as square, annular, hollow-square, rectangular, and plus-sign, based on an outer-cavity method. Such structured light beams are non-trivial, as these are not the regular modes of conventional laser systems. We have generated such beams from diffractive optical elements (DOEs) whose phase distributions are obtained from an iterative algorithm that involves Fresnel propagation and spatial Fourier filtering. Particularly, an input Gaussian beam from a laser illuminates the DOE, and after propagating a certain distance (working distance) transforms into a desired structured light output. In our method, the spatial Fourier filtering enables to obtain a relatively simple design of DOE (smooth phase distribution),

and produces a high-quality uniform-intensity output beam. The simple smooth phase distribution offers the possibility of easy manufacturing of DOEs. We have simulated different DOEs, and demonstrated the generation of uniform-intensity beams with different spatial shapes. We have characterized the quality of shaped output beams by the root mean square error, and show that the shaped output beams are generated with high-quality. Further, we have performed a detailed robustness analysis of our method, where the quality of shaped output beam is investigated against the various imperfections in an input beam, such as misalignment with respect to DOE, effect of asymmetry, speckle noise, presence of higher-order transverse modes, and mismatch of beam sizes. We have found that for imperfections $< 10\%$, the quality of shaped output beams remains reasonably good. We have also shown that the quality of shaped output beams can be further improved by additional external spatial Fourier filtering. We have also demonstrated the generation of shaped output beam over a broad spectral range using a single DOE.

In **Chapter 3**, we present the tailoring of amplitude and phase degrees of freedom of light based on an outer-cavity method for generating aberration laser beams (ALBs) containing multiple bright lobes in a transverse plane and possessing unique propagation properties, such as controlled autofocusing and self-healing in both free space as well as in turbulent media. The ALBs are generated using a DOE whose phase distribution consists of radial (r^q) and periodic angular dependence ($\sin(m\phi)$). Owing to the radial phase term, the ALBs possess autofocusing properties, and the periodic angular dependence generates diffraction pattern with $m^{\text{th}}-$order symmetry. We have given a detailed mathematical formulation for describing the propagation of ALBs in turbulent media by solving Huygen-Fresnel integral using stationary phase method. Further, the numerical and experimental investigations for the generation and propagation of ALBs are also carried out. We have observed that the turbulence deteriorates the spatial structure of ALBs and causes the beam wandering. The effect of turbulence on the propagation of ALBs is quantified by calculating an overlap integral with respect to ALB in free space. The ALBs possess good autofocusing properties both in free space as well as in turbulent media, where on-axis peak intensity becomes maximum with tight focusing. The autofocusing properties of ALBs remain invariant irrespective of turbulence strength. The autofocusing distance, both in free space and turbulent media, can be controlled from any small to large values by controlling the ALB parameters. Further, we have also investigated the spectral dependence of autofocusing of ALBs in turbulent medium, and found that the autofocusing distance does not depend on the turbulence, however, it decreases with an increase in wavelength.

Furthermore, we have performed a detailed investigation of self-healing of ALBs both

in free space as well as in turbulent media. We have found that, both in free space and turbulent media, the truncated ALB self-heals by redistributing the intensity within the beam, and it can self-heal reasonably well even for a large amount of truncation $\sim 60\%$. The maximum self-healing always occurs at autofocusing distance, which remains invariant irrespective of amount of truncation and strength of turbulence.

In **Chapter 4**, we have presented the generation of asymmetric aberration laser beams (aALBs) with controlled intensity distribution based on an outer-cavity method employing a DOE with phase asymmetry. The asymmetry in the phase distribution is introduced by shifting the coordinates in a complex plane, which provides additional control over the spatial intensity distribution of the beam. We have derived the mathematical formulations for general aALBs as well as the special cases of it. We have explored the mechanism of asymmetric control of intensity in aALBs, and found that the asymmetry parameters control the position of indeterminate phase point of the trigonometric phase term in aALBs, which creates a controlled asymmetric intensity distribution in the near-field plane, and upon propagation further provides a controlled transfer of intensity within the aALBs. In ALBs the intensity is symmetrically distributed in all lobes, and we have shown that by introducing asymmetry most of the intensity can be transferred to any one of the single lobe, and generates a high-energy density. In general, for aALB with number of lobes m, the spatial location of high-energy density lobe can be controlled with a precise variation in the asymmetry parameter (β), and we have determined empirical relations between β and m. We show that, for specific values of β, the intensity in high-energy density lobe can be increased by several times as compared to other lobes. Further, we have investigated the propagation of aALBs, and have found that similar to ALBs, the aALBs also possess good autofocusing properties, which are not affected by the asymmetry. The autofocusing distance of aALBs can be varied from small to large values by changing the parameters of aALB. The aALBs provide a more general framework for controlling intensity distribution, as for the specific values of asymmetry parameters the aALB behaves as an ALB.

In **Chapter 5**, we present the generation of high-energy densities by suppression of higher-order sidelobes in the far-field of phase-locked lasers in different array geometries. We have generated an array of lasers in various one-dimensional (1D) and two-dimensional (2D) array geometries in a degenerate cavity and phase-locked them in the in-phase [out-of-phase] configuration using far-field coupling with Gaussian apodizer [binary circular aperture]. Owing to non-uniform amplitude the geometry of laser array, the far-field of phase-locked lasers consists of higher-order sidelobes. These sidelobes contain a significant amount of energy, which limits the use of an output beam for high-power applications.

Our method relies on modifying the combined field (near-field and far-field) distribution of phase-locked lasers to obtain uniform amplitude and uniform phase distributions in the near-field plane, which enables the generation of high-energy density lobe (zeroth-order) in the far-filed intensity distribution. The method is applied to various 1D and 2D array geometries, such as square, triangular, Kagome, random, and 1D ring. We have shown that for the long-range in-phase locked laser arrays, the diffraction efficiency of zeroth-order lobe can be improved by several factors ($\sim 3-4$). The improved diffraction efficiencies are found to be in a range of $90\%-95\%$ (for 2D arrays) and $\sim 75\%$ (for 1D ring array). Further, the effects of range of phase locking, system size, as well as topological defects are examined on the diffraction efficiency of zeroth-order lobe in the far-field of phase-locked laser arrays.

We have also investigated our method for the out-of-phase locked lasers in a square array, where the zeroth-order has no intensity. With our method, we have obtained a high-energy-density zeroth-order lobe with a diffraction efficiency of 81%. Our results on producing high-energy density beams with suppressed higher-order sidelobes can be exploited for various applications in different areas.

In **Chapter 6**, we present a novel and efficient intra-cavity method for the generation of high-power discrete optical vortices with precisely controlled topological charges (l) by phase locking one-dimensional (1D) ring array of lasers in a degenerate cavity that involves spatial Fourier filtering. Owing to the special geometry of a degenerate cavity, it enables an efficient formation of a 1D ring array of lasers, where each laser consists of a nearly fundamental Gaussian distribution, and independent from each other. Initially, the lasers consist of random phase distribution, and are equally probable. To force 1D ring array of lasers in desired phase-locked steady state of optical vortex configuration, we employ a spatial Fourier filter (amplitude mask) at the Fourier plane inside the degenerate cavity, whose transmission function is engineered by the Fourier transform of a desired discrete optical vortex. The spatial Fourier filtering mechanism helps to eliminate the undesired phase distributions by introducing additional losses to them, thereby, enables the lasers to find a correct phase distribution in the form of a desired discrete optical vortex. With the specifically engineered spatial Fourier filters, we have demonstrated generation of discrete optical vortices with different system sizes and precisely controlled topological charges.

Further, we have performed a detailed investigation of propagation, such as divergence and self-healing, of discrete optical vortices, and compared them with the conventional continuous optical vortices (Laguerre-Gaussian/Bessel-Gauss beams). Unlike conventional continuous optical vortices, we have found that for a given system size (number of lasers) and fixed distance between the neighbouring lasers, the size of a discrete optical

vortex and its divergence does not depend on l. Further, we have performed a detailed investigation of self-healing by partially truncating a discrete optical vortex in the waist plane ($z = 0$) and propagated plane ($z > 0$). The results show that partially truncated discrete optical vortices can self-heal quite well. The self-healing distance is found to be dependent on the amount of truncation, particularly, it increases with an increase in the amount of truncation. We have found a good agreement between the experimental and numerical results.

In **Chapter 7**, we present a novel and efficient method for accurate determination of magnitude and sign of topological charge of an unknown discrete optical vortex, which is formed by an array of lasers in a 1D ring geometry. It relies on measuring the interference pattern of a discrete optical vortex, which is obtained by interfering a single selected laser with itself and with all the other lasers in a 1D ring array, using a Mach-Zhender interferometer. The interference pattern is quantified by analyzing the fringe visibility at each laser in a 1D ring array. The discrete laser arrays with $l = 0$ and $l \neq 0$ have different phase distributions, thus producing interference patterns with shifted interference fringes. The averaging of these phase shifted interference patterns gives rise to a variation in the fringe visibility as a function of laser number in a discrete optical vortex, thus enables the identification of topological charge. The magnitude of topological charge of a discrete optical vortex is found to be proportional to the number of dips observed in the fringe visibility curve.

Further, for an accurate determination of sign of an unknown discrete optical vortex, we have averaged the interference pattern of an unknown discrete optical vortex ($l \neq 0$) with the interference pattern of a discrete optical vortex with known topological charge $l = +1$. The number of dips in the fringe visibility curve decreases by one for positive values of l, and increases by one for negative values of l. We have also investigated the robustness of our method against the presence of phase disorder that may occur due to aberrations in a system. It is found that the phase disorder does not affect an accurate determination of topological charge. We have demonstrated our method for discrete optical vortices with topological charges from small to large values, and accurately determined their magnitude and sign. We have provided theoretical descriptions along with the numerical and experimental results, and found an excellent agreement between them, indicating that our method is highly efficient.

The interest in the field of spatially controlled structured light is growing because of its potential applications in many branches of modern technology. It has shown potential where commonly used Gaussian beams have encountered physical limitations. The results presented in this thesis will contribute in developing novel structured light sources as well

as characterization tools, with widespread potential applications. Our experimental and theoretical findings will open new possibilities in the field of fundamental research, health, defense, industries, optical communications, optical computing, etc.

List of abbreviations

aALB - Asymmetric Aberration Laser Beam

ALB - Aberration Laser Beam

aLG - Asymmetric Laguerre Gaussian

ASM - Angular Spectrum Method

BM - Back Mirror

BG - Bessel Gauss

CAB - Circular Airy Beam

DDCL - Digital Degenerate Cavity

DMD - Digital Micromirror Device

DOE - Diffractive Optical Element]

FF Mask - Far Field Mask

HG - Hermite Gaussian

LG - Laguerre Gaussian

LC - Liquid Crystal

MIP - Maximum Intensity Point

NF Mask - Near Field Mask

OC - Output Coupler

OV - Optical Vortex

RMSE - Root Mean Square Error

SLM - Spatial Light Modulator

SPP - Spiral Phase Plate

List of symbols

η - Diffraction efficiency

V - Fringe Visibility

M^2 - Beam Quality Factor

$\mathcal{F}$ - Fourier Transform

$\mathcal{F}^{-1}$ - Inverse Fourier Transform

$C(z)$ - Overlap Integral

λ - Wavelength

k - Wavenumber

m - Number of lobes in ALB

q - Radial power of ALB/aALB

σ_0 - Beam waist

σ_G - Size of Gaussian apodizer

(w, β) - Asymmetry parameters for aALB

E_0 - Maximum amplitude of beam

C_n^2 - Structure constant

Contents

Chapter 1

Introduction

1.1 Structured light

Light is characterized primarily by its spatial and temporal degrees of freedom. The spatial degrees of freedom of light are defined by amplitude/intensity, phase, and polarisation, whereas, the temporal degrees of freedom include time and frequency/wavelength. Structured light refers to the tailoring of light in all its degrees of freedom-weather controlling spatial degrees of freedom to form custom intensity and phase distributions with desired polarization [1, 2]; or, in time and frequency, to tailor time pulses with controlled pulse duration, repetition rate, and spectral content [3, 4]. Our main focus in this thesis is to unravel the potential of light in its spatial degrees of freedom, specifically in the amplitude and phase degrees of freedom. Typically, the output from a laser source consists of a Gaussian distribution, which encounters physical limitations in several applications. However, with the advancement in optical technologies, it has become possible to control light in the spatial degrees of freedom, which allows to produce controlled intensity [5] and phase distributions [6]. The spatially controlled structured light has attracted considerable interest due to numerous applications both in fundamental and applied fields [7]. A few examples of potential applications include the optical communications with increased data capacity [8], optical trapping and manipulation [9], super-resolution microscopy [10],

precision material processing [11], optical meteorology [12], lithography, quantum information processing [13], and atomtronic devices [14], etc. The spatially structured light such as optical vortex has been exploited to generate optical spanners to rotate particles at ultrafast speeds, trapping the particles in multiple planes, and sorting blood cells [15, 16]. The optical vortices have also been used to increase the data carrying capacity in optical communications [6], as well as to explore the magnetic materials [17]. A daisy-petal-like intensity distribution has been used to probe planer and non-planner surface displacements at picometer scale resolution [18, 19], which has paved the way for assessing the effects of low radiation pressures and altering the interaction of light with the interface of liquids and solids, which has significant implications for optofluidics [20], microfluidics, and gravitational wave detection [21]. A novel approach for controlling the interactions of chiral compounds with structured light has been proposed [22], which offers potential applications in drug development [23]. The well-known Rayleigh limit is shown to be overcome by structured illumination, and thus allowed to achieve super-resolution in the imaging techniques [14]. For example, the compressive three-dimensional super-resolution microscopy with speckle-saturated fluorescence excitation has been demonstrated [24].

Furthermore, manipulating spatial degrees of freedom of light allows for the acquisition of highly desirable propagation features, such as autofocusing [25], self-healing [26], diffraction-free nature (extended depth-of-focus) [27], and resilience against perturbations [28]. The controlled autofocusing allows the beam to precisely focus its energy at a desired distance, resulting in high-energy density that is useful for high-power applications [25]. In some cases, autofocusing results into parabolic trajectory of light, which is crucial for selective illumination of the sample in material processing [25]. The self-healing aspect is especially important when the beam travels through various apertures and complex media (for example, turbulence and biological tissues), as it prevents the loss of information carried by the beam [29]. The diffraction-free beams are critical for applications that require a large depth-of-focus, such as optical coherence tomography (OCT) [30], microscopy [14], and micro-machining [31]. The light beams robust to perturbations are important in precision-based applications, where the propagation of light

beam in a system can avoid the imperfections introduced from misalignment of components, aberrations, and disorder in the media. For example, in underwater oceanic communication, investigation of complex biological tissues, precision material processing and atmospheric sensing and meteorology [28].

In general, renewed interest of structuring light with various degrees of freedom has increased in a wide range of applications. Therefore, there is an increasing interest in synthesizing such beams with high-quality, high-resolution, precisely controlled intensity and phase distributions, good self-healing abilities, controlled autofocusing, resilience against perturbations, and broad spectral range. To realize such spatially controlled structured light fields, continuous efforts are being made towards the development of simple, cost-effective and efficient methods as well as characterization tools in order to improve these properties for their potential applications in various fields.

In this thesis, we theoretically, numerically, and experimentally investigate simple, cost-effective and efficient intra-cavity and outer-cavity methods, for generating and characterizing the novel structured light with precisely controlled intensity and phase distributions, as well as possessing exotic propagation properties, such as controlled autofocusing, self-healing, and strong resilience against perturbations. In addition to these, our emphasis has also been to improve the quality, resolution, and spectral range of spatially controlled structured light.

We have tailored the amplitude degree of freedom of light to generate high-quality laser beams with controlled spatial shapes and intensity distribution. For example, we have generated high-quality uniform-intensity beams with customized spatial shapes (circular, square, annular, hollow-square, and plus-sign), which are not the regular modes of a conventional laser system [32,33]. Such beams are useful in several applications as mentioned earlier, as well as in quantum emulation [34], ultra-cold experiments, optical lattice atomic clocks [35], and efficient high harmonic generation [36], etc. In various applications simultaneous illumination of multiple regions is also required. To address this issue, we have tailored the amplitude and phase to generate aberration laser beams (ALBs) containing multiple bright lobe structure, where the localization of intensity among the

lobes can be controlled precisely in a symmetric and asymmetric manner [37–39]. This control enables to generate high-energy densities in a transverse plane at any desired location [38,40]. Further, to attain ultra-high energy density, the power from several lasers can also be coherently combined (phase-locking of lasers) that can be tightly focused to a desired narrow region. However, in this approach a significant amount of intensity lies in higher-order sidelobes (higher diffraction orders in the far-field intensity distribution), which causes a reduced diffraction efficiency of high-energy density zeroth-order lobe. To resolve this issues, we have presented an approach to suppress these higher-order sidelobes and transfer their intensity to the zeroth-order lobe, which enables the generation of high-energy density with good diffraction efficiency [41,42].

Further, every customized intensity distribution exhibits distinct propagation behavior for different phase distributions; hence, controlled phase modulation is essential to provide adequate propagation control. We have tailored the phase distribution of light to enable special propagation properties, such as controlled autofocusing, self-healing, and resilience against perturbations both in free space as well as in complex media (random disorder media). Particularly, we have shown that the spatially controlled structured light autofocuses its intensity upon propagation, and generates high-energy density. The autofocusing distance can be precisely controlled from small to large values. As opposed to conventional light beams, the specific structured light also possesses self-healing abilities for a large amount of truncation, and the self-healing distance is found to be independent of the amount of truncation. Further, the structured light also shows good resilience against perturbations both in free space as well as in turbulent media of weak to strong turbulent strengths [41].

Furthermore, controlled tailoring of the phase distribution enables to generate structured light with helical wavefront, known as optical vortex. Helical wavefront results in additional orbital angular momentum, which is different from an intrinsic spin angular momentum of light. The number of intertwined helical phases per wavelength is known as its topological charge. Despite the remarkable progress on optical vortex, there still remains a vital issue that restricts the practical implementation and application of the

optical vortex in the future, namely the limitation of power scaling capacity. Generally, conventional optical vortices are formed from a single laser, whose output power is limited due to various physical constraints, such as damage threshold of laser gain medium, gain saturation, and non-linear effects. Furthermore, strong pumping in a laser may excite higher-order transverse modes, which results in an output beam with low quality. To address these issues, we have generated optical vortices by phase-locking lasers in a one-dimensional (1D) ring array, where phase circulates from one laser to another in a clockwise or anti-clockwise direction [43–45]. Owing to the step like behaviour of intensity and phase, these are known as discrete optical vortices. It is well-known that discrete systems behave differently than continuous systems, so we have performed a detailed investigation on the propagation, such as divergence and self-healing, of discrete optical vortices, and compared them with the conventional continuous optical vortices. These investigations have opened the door for new applications, where conventional continuous optical vortices pose limitations [43, 44]. The applications of optical vortices are usually associated with their orbital angular momentum (topological charge), therefore over the past several years various methods have been proposed with a particular emphasis on simple, cost-effective and efficient approach for accurately determining the topological charge. However, these characterization methods have been employed mostly for conventional continuous vortices, also many of these suffer from various limitations, and may not be suitable for discrete optical vortices [46]. We have presented a novel and efficient characterization method for accurately determining the magnitude and sign of topological charge (from small to large values) of unknown discrete optical vortices lasers [46].

Although, beam shaping started long ago when Archimedes structured light by using a set of mirrors to set fire to Roman ships, still the field suffers from various limitations, such as the generation of high-quality and high-resolution structured light with precisely controlled spatial degrees of freedom, robustness against imperfections such as presence of noise, sensitive to misalignment, aberrations, self-healing in random media with a small self-healing distance, generation of high-energy densities with good diffraction efficiency, simple and cost-effective design of experimental setup. The goal of this thesis is to develop

simple, cost-effective, and efficient intra-cavity and outer-cavity methods for generating and characterizing novel structured light with controlled intensity and phase distributions as well as possessing exotic propagation properties, such as controlled autofocusing, self-healing, and strong resilience against perturbations both in free space as well as in complex media. Further, our emphasis has also been to improve the quality, resolution, and spectral range of spatially controlled structured light. The overall goal of this thesis is to contribute new knowledge in the field of structured light, as well as to develop novel and efficient structured light sources and characterization tools, with widespread potential applications in fundamental research as well as in applied fields [1, 2].

The chapter is organized as follows. Section 1.2 presents a detailed discussion on various types of spatially structured light. In Sec. 1.3, various outer-cavity and intra-cavity methods for the generation of spatially controlled structured light are discussed. Section 1.4 presents the analytical and numerical methods for modeling the laser cavities as well as propagation and quantification of spatially structured light. In Sec. 1.5, we have provided a brief overview of spatial light modulators, including the mechanism for modulating light in the amplitude and phase degrees of freedom. Finally, Sec. 1.6 presents an outline of the thesis.

1.2 Types of spatially structured light

Over time, numerous spatially structured light beams have been proposed theoretically and generated experimentally, each possessing unique intensity and phase distributions as well as exotic propagation properties [2]. Light can be spatially tailored by modifying one or more of its spatial degrees of freedom, such as amplitude/intensity, phase, and polarization. The amplitude tailoring results in the generation of light with controlled spatial shapes and intensity distribution [47]. Whereas, the propagation properties of light can be controlled by tailoring the phase and amplitude degrees of freedom. The main examples of such beams are the modes of paraxial Helmholtz equation in Cartesian, cylindrical and elliptical coordinates, which include Hermite-Gaussian (HG) beams [48],

Laguerre-Gaussian (LG) beams [6], and Icne-Gaussian (IG) beams [49]. However, other categories include the beams with exotic propagation properties, for example, diffraction-free beams such as Airy beams [50], Bessel beams [51], Weber beams, and Mathieu beams [52]; and autofocusing beams such as circular Airy beam (CAB) and its higher-order radial derivatives (CADBs), aberration laser beams (ALBs), circular Airy vortex beams (CAVB), radial carpet beam, and Pearcey beams [53–57]. Further, controlling these degrees of freedom has also enabled the generation of other special types of structured light, such as optical bottle beams [58], discrete optical vortex [59], optical pin beams [55], etc. Below we have provided a detailed description of various types of spatially structured light, obtained by symmetric and asymmetric tailoring of amplitude and phase degrees of freedom of light.

1.2.1   Amplitude tailoring

Tailoring an amplitude degree of freedom of light enables to obtain controlled intensity distribution with customized spatial shapes. It is essentially required in various applications involving light-matter interactions, where precise control of intensity distribution improves the efficiency of interaction. For example, in material processing, the shape of heat affected region strongly depends on the intensity distribution of a laser beam. Thus, precise control of intensity distribution improves the quality and efficiency of material processing [60]. It also improves plastic welding, cladding, selective laser melting, hardening, brazing, and annealing [5], tweezing for manipulating microparticles and biological cells with high accuracy [61].

The output of most of lasers is represented by a Gaussian distribution, which poses physical limitations for various applications. The intensity in peripheral regions of Gaussian distribution is lower, and hence wasted in applications, for example in laser surgery and material processing. Further, the intensity in long tail of Gaussian distribution can also affect the neighboring undesired regions. For such purposes, uniform-intensity beams (also called flat-top beams) can be potentially advantageous [5].

Ideally, uniform-intensity beams are represented by a disc or square function, with an abrupt transition of intensity (from maximum to zero) on the edges. Therefore, due to diffraction, their intensity distributions are strongly distorted after propagating a short distance, resulting in a shorter depth-of-focus. To extend the depth-of-focus, required for many applications, the uniform-intensity beams can be approximated with round corners with a continuous transition at the edges (nearly flat-top beam). Such uniform-intensity beams can be described by a super-Gaussian function [62]. These uniform-intensity beams have also been proposed as flattened Gaussian function [63], finite sum of fundamental Gaussian beams [64], sum of LG beams [65], Fermi-Dirac distribution [66], and super-Lorentzian function [64, 67]. A few examples of uniform-intensity beams with different spatial shapes are shown in Fig 1.1.

Figures 1.1(a1)-1.1(f1) represent the mathematical functions, and Figs. 1.1(a2)-1.1(f2) show the corresponding beams with uniform-intensity distribution and different spatial shapes, such as circular, square, annular, hollow square, rectangle, and plus-sign. E_0 denotes maximum amplitude, (x, y) represents the Cartesian coordinates, and n, n_1 & n_2 denote the uniformity indices. In Figs. 1.1(a1)-(b1), σ_0 denotes the beam waist of circular and square shaped uniform-intensity beams. In Fig. 1.1(c1) r_0 is the width of annular region, and σ_0 is the inner radius of annular uniform-intensity beam. In Fig. 1.1(d1) σ_{01} and σ_{02} represent the waist of inner and outer sides of hollow-square shaped uniform-intensity beam. For the case of rectangular shaped uniform-intensity beam, σ_{01} and σ_{02} represent beam waists in horizontal and vertical directions (Fig. 1.1(e1)). Similarly, for plus shaped beam, σ_{01} and σ_{02} denote the beam waist along the longest and shortest sides (Fig. 1.1(f1)). The increase in the values of n, n_1 and n_2 makes more sharp variation of intensity at the edges, and upon propagation such beams experience more distortions in their intensity distribution and exhibit a short depth-of-focus [47]. The depth-of-focus has been shown to extend by generating these uniform-intensity beams with uniform-phase distribution [47]. Furthermore, the propagation of uniform-intensity beams has been extensively investigated, and shown exceptional stability in a turbulent environment [68]. With these excellent properties, such uniform-intensity beams are highly useful in different
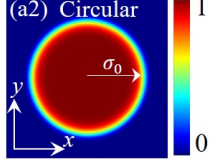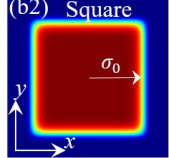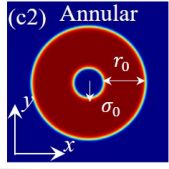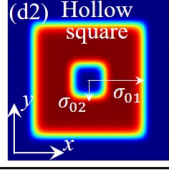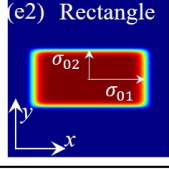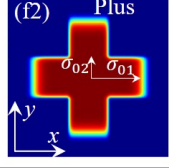
Mathematical function	Structured light
(a1) $$E(x,y) = E_0 \, \exp\left(-\frac{\left(\sqrt{x^2+y^2}\right)^n}{\sigma_0^n}\right)$$ $E_0 = 1$, $n = 14$, $\sigma_0 = 2$ mm	(a2) Circular
(b1) $$E(x,y) = E_0 \exp\left(-\frac{x^n+y^n}{\sigma_0^n}\right)$$ $E_0 = 1$, $n = 14$, $\sigma_0 = 2$ mm	(b2) Square
(c1) $$E(x,y) = E_0 \exp\left(-\frac{\left(\sqrt{x^2+y^2}-r_0\right)^n}{\sigma_0^n}\right)$$ $E_0 = 1$, $n = 14$, $r_0 = 1.25$ mm, $\sigma_0 = 0.75$ mm	(c2) Annular
(d1) $$E(x,y) = E_0 \, \exp\left(-\frac{x^{n_1}+y^{n_1}}{\sigma_{01}^{n_1}}\right) - E_0 \exp\left(-\frac{x^{n_2}+y^{n_2}}{\sigma_{02}^{n_2}}\right)$$ $E_0 = 1$, $n_1 = 14$, $n_2 = 4$, $\sigma_{01} = 2$ mm, $\sigma_{02} = 0.6$ mm	(d2) Hollow square
(e1) $$E(x,y) = E_0 \, \exp\left(-\frac{x^n}{\sigma_{01}^n} - \frac{y^n}{\sigma_{02}^n}\right)$$ $E_0 = 1$, $n = 14$, $\sigma_{01} = 2$ mm, $\sigma_{02} = 1$ mm	(e2) Rectangle
(f1) $$E(x,y) = E_0 \exp\left(-\frac{x^n}{\sigma_{01}^n} - \frac{y^n}{\sigma_{02}^n}\right) + E_0 \, \exp\left(-\frac{x^n}{\sigma_{02}^n} - \frac{y^n}{\sigma_{01}^n}\right) - E_0 \, \exp\left(-\frac{x^n+y^n}{\sigma_{02}^n}\right)$$ $E_0 = 1$, $n = 14$, $\sigma_{01} = 2$ mm, $\sigma_{02} = 0.7$ mm	(f2) Plus

Figure 1.1: (a1)-(f1) Mathematical expressions, and (a2)-(f2) intensity distributions for circular, square, annular, hollow-square, rectangle, and plus shaped uniform-intensity beams.

areas, as discussed previously [69].

1.2.2   Symmetric amplitude-phase tailoring

Tailoring of amplitude along with phase provides additional control over the propagation properties of structured light. However, based on the symmetry of intensity distribution with respect to origin (on-axis center), the tailoring can be classified into two types: (a) symmetric amplitude-phase tailoring, and (b) asymmetric amplitude-phase tailoring. Below, we have discussed various types of structured light obtained by tailoring simultaneously the amplitude and phase of light, which provides spatially symmetric intensity and phase distributions.

1.2.2.1   Laguerre-Gaussian (LG) beams

Laguerre-Gaussian (LG) beams are characterized by a helical phase distribution, which results into a doughnut-shape intensity distribution with zero intensity at the center [70] Owing to the phase distribution function $\exp(il\phi)$, the Poynting vector in these beams is skewed with respect to the axis of propagation at an angle $\delta = |l|/kr$, and gives rise to orbital angular momentum of $l\hbar$ per photon, where l is the number of intertwined helical phase distributions in the beam (also called topological charge), $k = 2\pi/\lambda$ is the wave number (λ is wavelength of light), and r is a radial distance [71]. These beams are also referred to as optical vortices (OVs). The Laguerre-Gaussian (LG) beams are the solution of paraxial Helmholtz equation in cylindrical coordinates [6, 28].

Figure 1.2 shows the field (intensity and phase) distributions of LG beams with various orders (l, p), where p is a redial index of Laguerre polynomial. As evident, the region of zero intensity increases with an increase in the topological charge l. The radial index p controls the number of rings in LG beams. Furthermore, these beams exhibit special propagation properties, such as l dependent beam divergence, self-healing, robustness against perturbations, and conservation of orbital angular momentum [72]. The LG beams have potential applications in various areas, as discussed earlier [14].
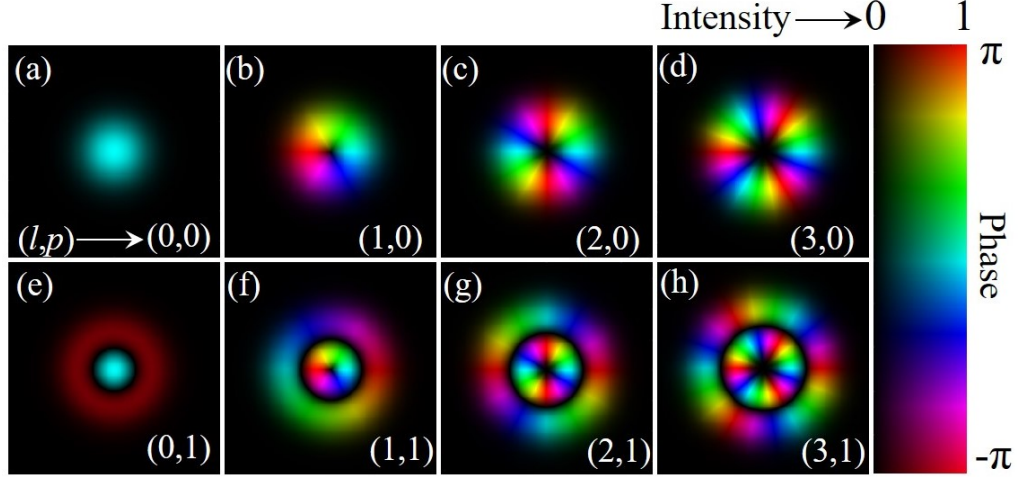
Figure 1.2: Field (intensity and phase) distribution of LG beams with different indices (l, p). l is the topological charge, and p is a radial index. Note, brightness represents the intensity and color represents the phase.

1.2.2.2 Discrete optical vortex beams

The intensity distribution of discrete optical vortex consists of a finite number of lasers (or beamlets/waveguides) in a 1D ring array, where phase circulates from one laser to another in a clockwise or anti-clockwise direction. The discrete optical vortices are particularly interesting for high-power applications, where conventional continuous optical vortices pose limitations due to physical constraints, as mentioned in Sec. 1.1. However, in a discrete optical vortex several lasers are combined coherently to achieve a high-power output with reasonably good beam quality [59, 73, 74]. The electric field of a discrete optical vortex can be written as [59]

$$E(x, y; z = 0) = E_0 \sum_{j=1}^{N} e^{-\frac{(x-\alpha_j)^2 + (y-\beta_j)^2}{2\sigma_0^2}} e^{i\phi_j}, \tag{1.1}$$

where $(\alpha_j, \beta_j) = a(\cos\theta_j, \sin\theta_j)$, $a = d/\sqrt{1 - \cos(2\pi/N)}$, $\theta_j = \pi(2j-1)/N$, and $\phi_j = \pi l(2j-1)/N$. N denotes the number of lasers in a discrete optical vortex (system size), a denotes radial distance of each laser from centre of discrete optical vortex. d denotes the distance between two nearest neighbour lasers. Each laser (j) has the same amplitude E_0, same beam waist σ_0, and different initial phase ϕ_j. The topological charge l of a discrete

optical vortex can be defined as [74]:

$$l = \frac{1}{2\pi} \sum_{j=1}^{N} \arg(E_j^* E_{j+1}), \tag{1.2}$$

with the argument taking the values $\arg(\Theta) \, \epsilon [-\pi, \pi]$, and E_j represents the complex field of site j on a ring. Further, a continuous system can support a continuum of stable solutions, however, a discrete system can only have a finite number $|l| \leq N/2$ [75].
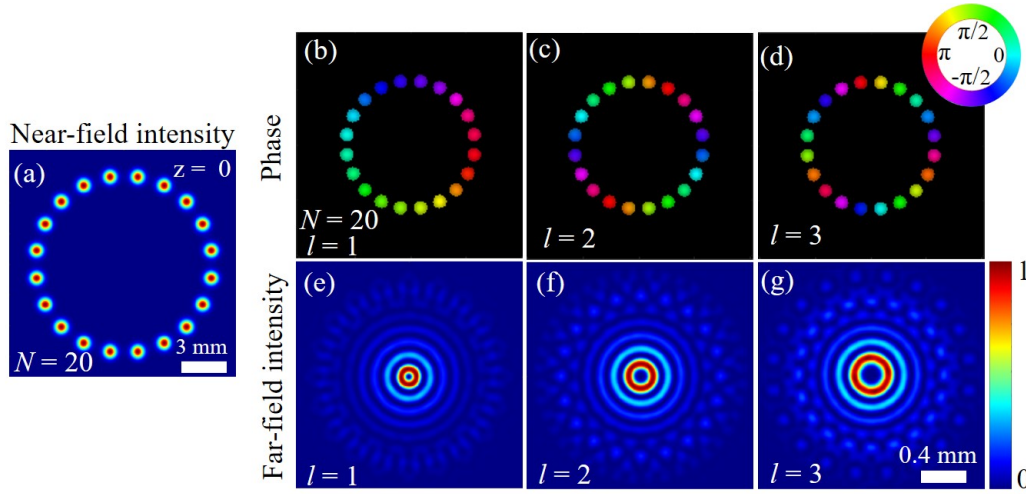
Figure 1.3: (a) Near-field intensity distribution of discrete optical vortex for a system size of $N = 20$ lasers for all values of l with condition $l \leq N/2$. (b)-(d) Near-field phase distribution of discrete optical vortex with topological charge $l = 1$, $l = 2$, and $l = 3$ respectively. (e)-(g) Far-field intensity distributions of discrete optical vortices with $l = 1$, 2, and 3, respectively.

Figure 1.3(a) shows the near-field intensity distribution of a discrete optical vortex with system size $N = 20$. Figures 1.3(b)-1.3(d) show the phase distributions of discrete optical vortices with $N = 20$ and topological charge $l = 1$, 2 and 3, respectively. Note, the near-field intensity distribution of discrete optical vortex corresponding to Figs. 1.3(b)-1.3(d) remains the same as given in Fig. 1.3(a). Figures 1.3(e)-1.3(f) show the far-field intensity distribution of discrete optical vortices with $l = 1$, 2, 3, respectively. As evident, in contrast to continuous optical vortices, the near-field intensity distribution of discrete optical vortices remains the same for all topological charges. However, the intensity distribution in a far-field plane is different.

It is well-known that discrete systems behave differently than the continuous system. In continuous optical vortices, the size and divergence strongly depend on l, which limits the transfer of vortices with higher l values over a long distance due to problems in detection (detector has finite active area) [72]. Therefore, discrete optical vortices can be a solution to such limitations. Further, discrete systems also provide the most general framework for investigating networks of nonlinear coupled oscillators [75].

1.2.2.3   Bessel beams

Bessel beams possess a unique intensity distribution with multiple concentric rings and a helical phase distribution. The intensity gradually diminishes in the rings along the radial direction. This distinctive combination of intensity and phase distribution grants Bessel beams their unique propagation characteristics, such as the ability to self-heal and exhibit diffraction-free properties. Bessel beam is an exact solution of the Helmholtz equation whose intensity distribution is governed by the Bessel function with a vortex phase $\exp(il\phi)$, where l is the topological charge [76].

Owing to the dependence on $J_l^2(k_r r)$, where J_l is l^{th} order Bessel function and k_r is a radial wave vector, Bessel beam possesses infinite width with zero divergence leads to an ideal plane wave like behaviour. A bessel beam can be considered as a set of plane waves propagating on a cone, therefore, possesses an additional property of self-healing. Thus, if the beam is subjected to an obstruction, the constituting waves move past the obstruction by casting a shadow on the beam and eventually reconstruct the spatial structure of the beam. The minimum distance required to reconstruct the beam is known as self-healing distance and is given as $z_{min} \approx ak/2k_z$, where a is width of obstruction and k_z is a wave vector in axial direction. Figures 1.4(a),1.4(c) and 1.4(e) show the intensity distributions, whereas Figs. 1.4(b), 1.4(d) and 1.4(f) show the corresponding phase distributions, for $l = 0$, 1 and 2 respectively. As evident, an increase in the topological charge results in different intensity and phase distributions.

Owing to the infinite beam width, an ideal Bessel beam is impossible to construct, however, a hybrid Bessel-Gauss beam is a reasonably good approximation, where the

$l = 0$ $l = 1$ $l = 2$
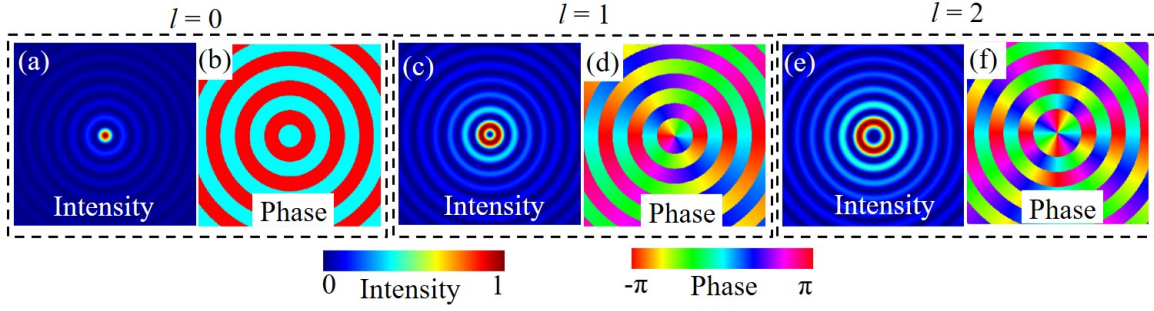
Figure 1.4: Intensity and phase distributions of Bessel beams for topological charges (a)-(b) $l = 0$, (c)-(d) $l = 1$, and (e)-(f) $l = 2$ respectively.

external rings are restricted by the Gaussian function, and instead of plane waves, Bessel-Gauss beams are composed of superposition of Gaussian beams, whose axes are uniformly distributed on a cone [77]. Such beams have applications in diverse fields due to diffraction-free and self-healing characteristics.

1.2.2.4 Airy beams

The intensity distribution of Airy beams can be described as having a central lobe surrounded by oscillating side lobes and possess diffraction-free behavior as well as self-healing capabilities [78]. Further, the self-bending or self-acceleration in free space differentiates Airy beams from Bessel beams [79]. The diffraction-free nature can be attributed to the infinite energy of Airy beam. However, in actual practice, such beams are truncated by an aperture, which results in diffraction during the propagation. If the size of an aperture exceeds the spatial features of ideal diffraction-free beam, the diffraction process can be slowed down considerably during the propagation.

The intensity and phase distributions of 1D and 2D Airy beams at propagation distance $z = 0$ are shown in Figs. 1.5(a)-1.5(b) and Figs. 1.5(c)-1.5(d), respectively. As evident, these beams possess unique intensity and phase distributions, therefore, show different propagation properties. Figure 1.5(e) shows the propagation of 1D Airy beam, indicating the behaviour of self-acceleration. The Airy beam also possesses resilience against the perturbations (turbulence), and shows self-healing properties against various types of obstructions. Such beams with these exotic features can be exploited for various
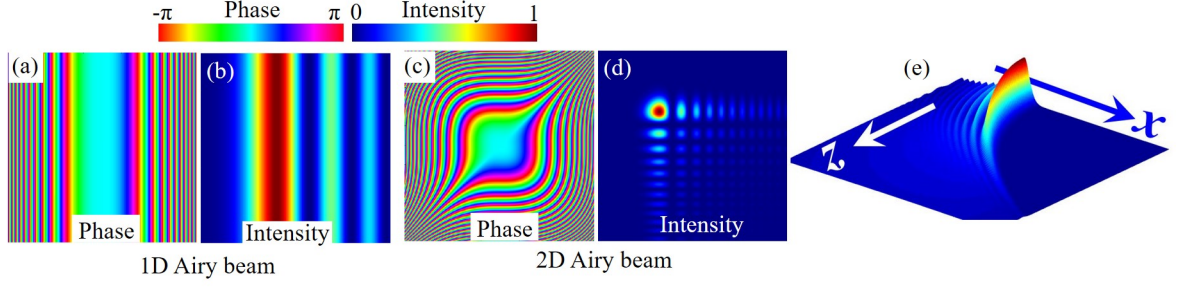
Figure 1.5: (a)-(b) Intensity and phase distributions of 1D Airy beam. (c)-(d) Intensity and phase distributions of 2D Airy beam. (e) Intensity distribution of Airy beam in longitudinal (propagation) plane, indicating self-acceleration.

applications involving light-matter interactions.

1.2.2.5   Aberration laser beams (ALBs)

Aberration laser beams (ALBs) possess multiple bright lobes in the near-field plane with $m^{th}-$order symmetry, and several distinct propagation properties such as autofocusing, self-healing, and resilience against the perturbations in complex media. Generally, aberrations are recognized as distortions in the phase distribution and cause undesired effects like blurring, widening, and distortion in an optical field [80]. Several attempts have been made to reduce the impact of aberrations [81, 82]. However, aberrations have also been deliberately exploited to create optical systems with specific characteristics [83, 84]. For example, a certain type of aberration in an optical system can produce a focal plane with a more strongly focused region [85]. ALBs are realized by combining angular dependence of Zernike polynomials with a r^q type approximation of chirped Airy function and can be expressed as:

$$E(r, \theta) = A(r) \exp\left(-i\alpha r^q + i\sin\left(m\theta\right)\right), \quad r \leq R. \tag{1.3}$$

Where $A(r) = \exp(-r^2/2\sigma_0^2)$ denotes a Gaussian with beam waist σ_0, m is an integer that controls the symmetry (lobe structure), R is the radius of a circular aperture, q is radial power, α is a scaling parameter having unit mm^{-q} and controls the steepness of the phase distribution of ALB. In free space, for such ALB the autofocusing distance is

given as [86]:

$$z_{\max} \approx \frac{2\pi}{q\alpha\lambda(2\sigma_0/3)^{q-2}},$$ (1.4)

where λ is the wavelength. As seen from Eq. (1.4), the auto-focusing distance can be controlled from small to large values by controlled variation of beam parameters. Note, for $q = 2$, r^q is equivalent to a classical lens, results in abrupt autofocusing properties, and autofocusing distance becomes independent of beam waist of an input Gaussian beam.
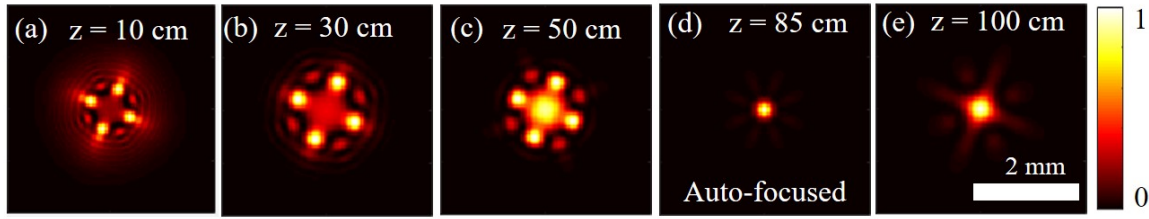
Figure 1.6: Intensity distributions of ALB at various propagation distances (a) $z = 10$ cm, (b) $z = 30$ cm, (c) $z = 50$ cm, (d) $z = 85$ cm, and (e) $z = 100$ cm. Simulation parameter: parameters: $\alpha = 3.5$ mm^{-2}, $q = 2$, $m = 4$, $\sigma_0 = 1.35$ mm, $\lambda = 1064$ nm.

Figures 1.6(a)-1.6(e) show the intensity distributions of ALB at different propagation distances $z = 10$ cm, 30 cm, 50 cm, 85 cm, and 100 cm, respectively. As evident, ALB possesses spatially controlled intensity distribution and shows autofocusing behaviour at $z = 85$ cm. At the autofocusing distance, the intensity becomes tightly focused and creates a high-energy density. With these unique features, such beams can be exploited for various applications in different areas [87–90].

1.2.3 Asymmetric amplitude-phase tailoring

In symmetric amplitude-phase tailoring, the generated structured light consists of symmetric intensity distribution. However, to gain an additional control on the intensity distribution, the asymmetry can be exploited in the phase of structured light. The phase asymmetry can be introduced by shifting coordinates in a complex plane [91]. Several types of asymmetric beams have been realized experimentally and also exploited for various applications. For example, asymmetric Gaussian optical vortex, asymmetric Bessel modes, asymmetric Bessel-Gauss (aBG) beams, asymmetric Laguerre-Gaussian

(aLG) beams, nonparaxial asymmetric Bessel beams, and paraxial asymmetric Bessel-Gaussian [91–95]. As asymmetry allows better control on the intensity distribution, so it has been used to form various kinds of specialized optical traps for controlling and manipulating microparticles. Further, it has also been used to steer the intensity at desired spatial locations to form high-energy density, which is useful for high-power applications. A few examples of asymmetrically structured light are discussed below.

1.2.3.1 Asymmetric Laguerre-Gaussian (aLG) beams:

Asymmetric Laguerre-Gaussian (aLG) beams are asymmetric counterpart of LG beams, where asymmetry is introduced for additional intensity control in a transverse plane [91]. An aLG beam consists of intensity distribution in a crescent shape, which differs significantly from LG beam. The intensity distribution of aLG beam at different propagation distances are shown in Figs. 1.7(a)-1.7(d). During the propagation, the intensity redistributes from the central ring to peripheral areas asymmetrically (Figs. 1.7(b)-1.7(d)) [91]. As evident, in aLG beams, the asymmetry results in rotation of crescent shape intensity
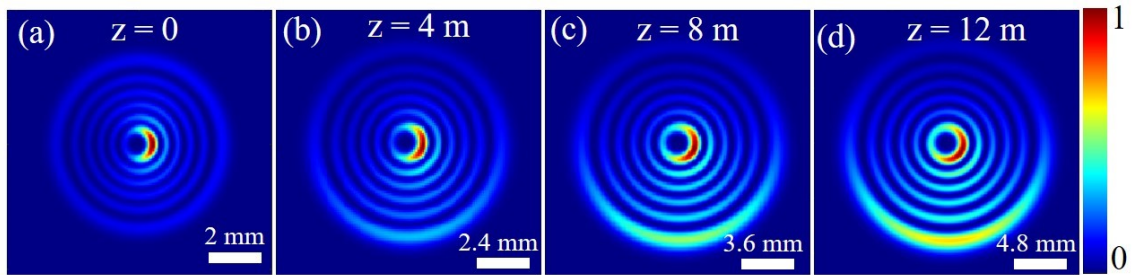
Figure 1.7: The intensity distribution of aLG beam at various propagation distances (a) $z = 0$, (b) $z = 4$ m, (c) $z = 8$ m, (d) $z = 12$ m.

and additional orbital angular momentum (OAM). The additional OAM can be exploited to control the motion of living cells without any thermal damage. Such beams can also be utilized to create a set of entangled photons with wide orbital angular momentum through the process of spontaneous parametric down-conversion [16, 96].

1.2.3.2   Asymmetric Bessel-Gauss beams (aBG):

An aBG beam is expressed as the superposition of BG beams that contain Bessel function with complex argument and possess a crescent shape intensity distribution [95]. Furthermore, asymmetry in Bessel beam also affects the propagation properties as the aBG beam rotates non-uniformly about the optical axis, causing the vortex centers to rotate $\pi/4$ within the Rayleigh range and another $\pi/4$ throughout the remaining distance, which makes them different from aLG beams [95] Unlike Bessel-Gauss (BG) beams, the asymmetric Bessel-Gauss beams possess more flexible controlled intensity distribution [95].

The asymmetric Bessel-Gauss beams are shown in Fig. 1.8. Figures 1.8(a),1.8(c) and
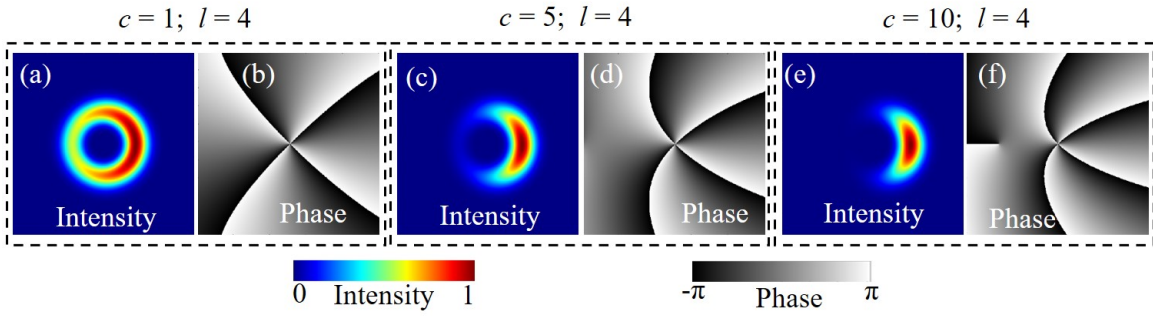
Figure 1.8: The phase and intensity distributions of asymmetric Bessel-Gauss beam with topological charge $l = 4$ and asymmetry parameter (a)-(b) $c = 1$, (c)-(d) $c = 5$, and (e)-(f) $c = 10$. [95]

1.8(e) show the intensity distributions, whereas, Figs. 1.8(b),1.8(d) and 1.8(f) show the phase distributions of aBG with $l = 4$ and asymmetry parameter $c = 1$, 5 and 10, respectively. As evident, the position of optical nulls in the intensity distribution varies with the parameter c, causing variation in the orbital angular momentum (OAM) carried by the beam. Similar to aLG beams, asymmetry in aBG also results in additional fractional OAM, which increases almost linearly with an increase in asymmetry c [95]. These additional features increase the applicability of aBG beams for various applications.

1.2.3.3 Asymmetric aberration laser beams (aALBs):

The asymmetric aberration laser beams are obtained by introducing phase asymmetry to the ALBs. As opposed to ALBs, the aALBs have better flexibility in controlling the intensity distribution, and intensity distributes asymmetrically in the multiple bright lobes. In an ideal ALB containing equal intensity bright lobes, by introducing asymmetry most of the intensity can be shifted to any of the single bright lobe, and creates a high-energy density [38]. Similar to ALBs, aALBs possess good autofocusing properties, which remain invariant irrespective of asymmetry.

The asymmetry in an ALB is introduced by complex coordinate shifting in the phase term of Eq. (1.3) [38, 91], we have

$$\xi = \exp(-i\alpha s^q + i\sin(m\theta)), \tag{1.5}$$

where, $s^2 = (x - x_o)^2 + (y - y_o)^2$, $x_o = a + ib$ and $y_o = c + id$. Solving Eq. (1.5) for $q = 2$ yields

$$\xi = \exp(-i\alpha \ (x^2 + y^2 - (b^2 + d^2)) + i\sin(m\theta)), \tag{1.6}$$

where $\theta = \tan^{-1}\left(\frac{y-b}{x-(-d)}\right)$. The asymmetry parameters a and c mimic the misalignment, hence taken as 0. The asymmetry parameters b and d can be expressed in terms of polar coordinates (w, β), which only shifts the origin of trigonometric phase without changing the functional form of chirped phase [38].

The controlled intensity distributions of aALBs for two different sets of asymmetry parameters are shown in Fig. 1.9. Figures 1.9(a1)-1.9(e1) and Figs. 1.9(f1)-1.9(j1) show the intensity distribution of aALB at different propagation distances for asymmetry $\beta = \pi$ and $3\pi/2$, respectively. As evident, in both cases the intensity evolves asymmetrically and differently, however, the autofocusing is obtained at the same distance. This indicates that asymmetry does not influence the autofocusing properties of aALB. Further, with the help of asymmetry, the longitudinal intensity can also be controlled, as shown in Fig. 1.9. The aALBs with these novel features can be exploited for various applications in different
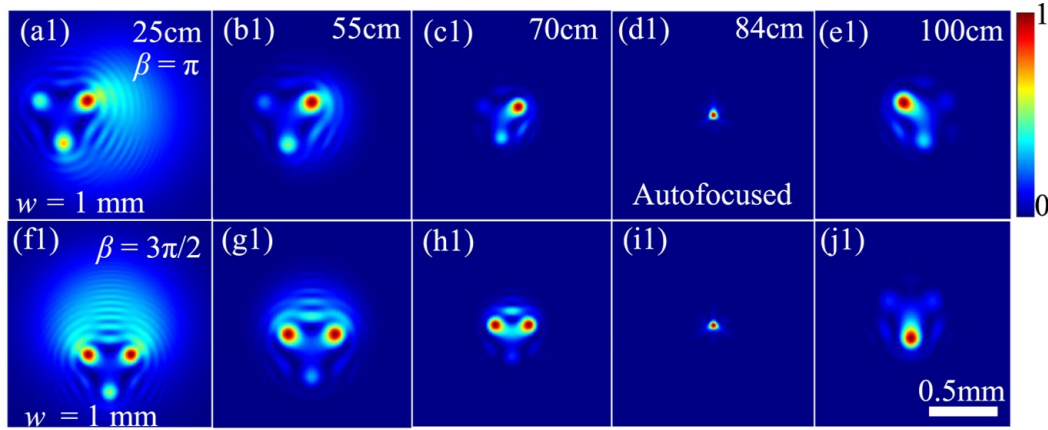
Figure 1.9: For asymmetry parameters $\beta = \pi$ (top row) and $\beta = 3\pi/2$ (bottom row), the intensity distribution of aALB at various propagation distances (a1, f1) $z = 25$ cm, (b1, g1) $z = 55$ cm, (c1, h1) $z = 70$ cm, (d1, j1) $z = 84$ cm, and (e1, j1) $z = 100$ cm. We have taken the value of $w = 1$. Simulation parameters: $\alpha = 5.9$ mm^{-2}, $\sigma_0 = 1.45$ mm, $m = 3$, $q = 2$ and $\lambda = 632$ nm.

areas. An extensive study on aALBs is given in Chapter 4, where the mechanism behind the intensity transfer as well as the propagation properties are discussed.

In addition to these examples, various other forms of spatially structured light are also discovered, which are mentioned above in Sec. 1.2. It is clearly visible that controlling amplitude and phase degrees of freedom has enabled to generate various kinds of spatially structured light, possessing distinct intensity and phase distributions as well as unique propagation properties. With these distinct properties, the spatially structured light can be potentially applied in various fields, for finding new solutions to old problems.

1.3 Methods for generating structured light

As mentioned above, structured light fields are increasingly finding applications in various areas, therefore, there has been growing interest in generating such beams possessing distinct properties. Special efforts are being made towards the development of methods that include various aspects, namely, arbitrary control of intensity and phase distributions, high-power damage threshold, less sensitive to imperfections, simple and cost-effective design, high efficiency, and wide spectral range. Over the past several years, various

methods have been proposed, which are broadly classified into two main categories: (a) outer-cavity methods and (b) intra-cavity methods. The outer-cavity methods involve the modification of an input Gaussian beam external to the laser source by means of transforming device/element, such as spatial light modulators (SLMs), digital micromirror devices (DMDs), diffractive optical elements (DOEs), mask and mask-like mirrors, refractive elements like spiral phase plates, q-plates, etc. On the other hand, in intra-cavity methods, the modifications are applied directly at the laser source, which includes placing of transforming device/element inside the laser cavity, and due to that structured light is generated directly at the source [97–100]. Methods based on both categories have their own advantages and disadvantages, for example, outer-cavity methods may be simple and efficient, whereas intra-cavity methods can be suitable for high-power, high-purity, and high-resolution structured light [101, 102].

1.3.1 Outer-cavity methods

In an outer-cavity method, the light is tailored external to the laser, by using external devices/elements, such as lenses, mirrors, different shape apertures, diffractive elements, SLMs, DMDs, etc. [1, 2, 103, 104], as shown in Fig. 1.10. Figure 1.10 shows that an input
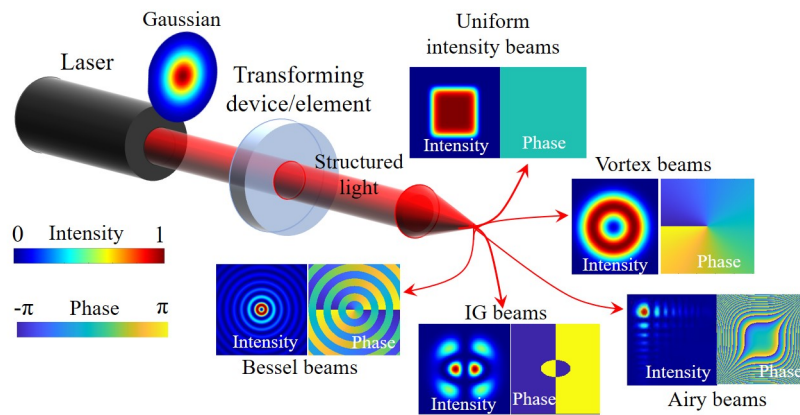
Figure 1.10: Illustration of an outer-cavity beam shaping method.

Gaussian beam from laser incidents on a transforming device/element, and after propagation to a certain distance it transforms into a desired structured light. Note, for obtaining

different types of structured light, the required transforming devices/elements will be different. We have discussed below a few commonly used transforming devices/elements for outer-cavity methods.

Apertures and Masks: The apertures and masks are straight forward mechanical elements that modify an input laser beam by selectively blocking or allowing certain portions of it. These elements have the ability to tailor the amplitude degree of freedom of light, to produce light beams with customized spatial shapes. Further, the size of the shaped output beam can be controlled by the size of the aperture [105]. Here, the shaping is not lossless, and conversion efficiency strongly depends upon the size of an aperture [5, 106].

Reflective and refractive elements: The lossless beam shaping can be achieved by simultaneous tailoring of amplitude and phase degrees of freedom. The transforming elements, such as reflective mirrors, lenses, anisotropic crystals, and various other phase elements can be employed to modify the intensity and phase distribution of laser beam. In reflective mirrors the phase shift is introduced by changing the orientation of the mirror [107], for example, conical mirrors can be used to generate optical vortices without chromatic aberrations [108]. Further, refractive elements can shape the light in the form of uniform-intensity, doughnut, or other desired intensity distributions [66, 103, 104]. In refractive elements, the phase shift is introduced by varying surface curvature and thickness of element [109]. For example, spiral phase plate (SPP) is a phase element with uniform refractive index, with increasing thickness in the circular direction. SPPs are potential phase elements to generate optical vortices with topological charge [110]. A controllable transformation of HG modes to LG modes can be obtained by a pair of astigmatic lenses by introducing a Gouy phase shift [111]. The Axicons can be exploited for the interference of plane waves which in turn can be used to generate Bessel beam [51]. Further, birefringent liquid crystal-based q-plates can be used to generate optical vortex with topological charge from a laser beam having a well-defined spin angular momentum [112].

Grating/Diffractive optics: Gratings, diffractive lenses, and far-field diffractive diffusers are examples of beam shaping diffractive optical elements. The computer generated

holograms can be used to generate optical vortices from an input Gaussian beam [113]. For the generation of uniform-intensity laser beams, the diffractive optical elements can be designed by various methods, such as holographic conversion [114], geometric transformation and ray tracing [115,116], hybrid methods [117], Gerchberg–Saxton algorithm [118], modified Gerchberg–Saxton algorithm [119], Yang–Gu algorithm [120], genetic algorithm [121], and simulated annealing algorithm [122].

Spatial Light Modulators (SLMs) and digital micromirror devices (DMDs): Spatial light modulators and digital micromirror devices are electronically controlled devices and can modulate the phase or amplitude of an incident laser beam. By applying specific phase or amplitude patterns on the SLM or DMD, the incident laser beam can be tailored into various forms of structured light, including customized intensity and phase distributions [123]. In this thesis, we have investigated tailoring of light by using SLM, hence, a detailed description of SLM is presented in Sec. 1.5.

Other methods such as adaptive optics based systems use wavefront sensing and correction techniques to compensate for aberrations and distortions in a laser beam. By actively controlling deformable mirrors or other optical elements, adaptive optics can shape the beam as per desire. Several of these methods pose different kinds of limitations, and accordingly, these methods are evolved over the past several years, and still, the field is actively growing in finding more suitable methods (simple, cost-effective, and efficient) for realizing structured light with improved properties, such as high-quality, high-resolution, flexible intensity control, flexible phase control, good self-healing, controlled autofocusing, large depth-of-focus, strong resilience against the perturbations, broad spectral range, etc.

1.3.2   Intra-cavity methods

Although, outer-cavity methods have a number of advantages, still they suffer from various limitations. For instance, the quality and resolution of shaped laser beams may be compromised by aberrations caused by optical components. A relatively small damage threshold of transforming elements limits the use of outer-cavity methods for high-power

applications. Also, the residual reflection and absorption from various optical components cause significant power loss in the outer-cavity methods. To overcome such limitations, intra-cavity methods can be used, where, the degrees of freedom of light are tailored inside the laser cavity by utilizing a variety of optical devices, including mirrors, lenses, and spatial light modulator. The laser cavities possess inherent filtering properties that enable them to remove undesired modes, thereby enhancing the purity and power of the desired modes. For example, outer-cavity generation of OAM modes by azimuthal phase change, often results in the numerous radial modes, with a low power desired zeroth-order radial mode [2,124]. However, by employing the same approach in an intra-cavity method, all undesired higher-order modes can be suppressed, thereby enables the generation of a high-purity desired mode [2,124]. A general illustration of an intra-cavity beam shaping method is given in Fig. 1.11. Figure 1.11 shows a laser cavity with two mirrors, a
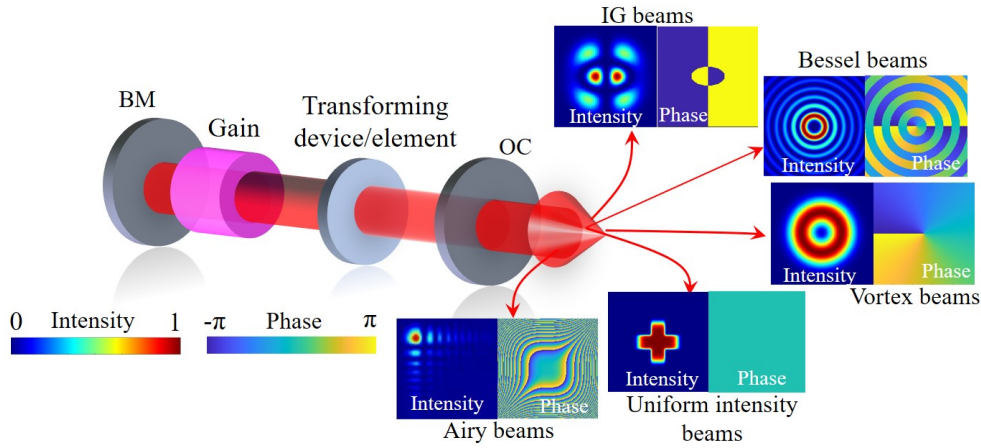
Figure 1.11: Illustration of an intra-cavity beam shaping method. BM: back mirror; OC: output coupler.

back mirror (BM) with high reflectivity ($R \approx 100\%$), a partially reflecting output coupler (OC) ($R < 100\%$), and a gain medium for light amplification. Depending upon the pump strength and cavity parameters, such as curvature of mirrors and length of the cavity, the laser will lase in a light field distribution with minimum loss in the cavity. However, to attain a controlled distribution of the output beam, the cavity is modified either by placing any transforming device/element inside the cavity or changing the cavity param-

eters (for example, structured cavity mirrors and structured illumination of gain medium by structured pump). Such manipulations introduce additional losses to the undesired modes (light field distributions) of the cavity, and eventually, a desired structured light beam will be obtained as a steady-state minimum loss solution of the laser at the output.

Intra-cavity beam shaping entails inserting a transforming device/element within the laser cavity to select a single desired mode among all the available modes. Most of the mode selection methods introduce an extra loss to undesirable modes, forcing the laser to lase in a desired mode. For example, the Laguerre-Gaussian modes, are selected by inserting wires and regulating the intra-cavity aperture size [125]. Depending upon the transforming device/element, the intra-cavity beam shaping can be divided into three types:

(a) Absorptive, reflective, and transmissive

(b) Digital cavity laser

(c) Degenerate cavity laser

1.3.2.1 Absorptive, reflective and transmissive

A particular mode in a laser cavity can be selected by inserting additional absorption masks or wires, phased mirrors, and transmissive optics such as diffractive optical elements, binary phase elements, spiral phase plates, etc. For example, a Gaussian mode is selected by placing a circular aperture inside the laser cavity. Apart from the fundamental Gaussian mode, the higher-order LG and HG modes can be selected by inserting wires and controlling the aperture size of the laser cavity [125].

In connection to reflective elements, a graded phase mirror (GPM) with non-spherical curvature can be used to generate uniform-intensity beams. The back mirror in the cavity is replaced by a GPM, which results in an additional phase shift of $\Delta\phi$ (phase constraint). Hence, the desired shaped beam can be generated at the output coupler by controlling the phase profile of GPM [126]. Similarly, a precise phase control can be obtained with diffractive mirrors having a phase distribution with many 2π discontinuities [127, 128].

As discussed, the attenuation of light by absorbing elements such as wires can produce heat and reduce the system's overall efficiency. Therefore, non-absorbing phase elements (transmissive elements) can be used, where loss is introduced by diffraction and interference of the laser beam. For example, a wire grid is replaced by a phase element where a phase shift of π is introduced along the narrow lines instead of wires, keeping the phase same in other regions [129]. Such phase elements having a phase shift of either 0 or π, are known as binary phase elements (BPEs).

Further, as discussed earlier, a spiral phase plate (SPP) (transmissive element) introduces a phase shift of $\exp(il\phi)$ (l is an integer) and can be used to generate orbital angular momentum modes (optical vortices) outside the laser cavity. However, SPPs are designed such that, their thickness increases in azimuthal direction to produce optical vortices corresponding to a particular wavelength. Therefore, depending upon the finite bandwidth of an incident light, the purity of modes is strongly affected. To resolve this issue, SPPs are placed inside the laser cavity [130, 131]. In this intra-cavity method, SPPs are nearly lossless for the desired modes and introduce high losses to all other undesired modes. Therefore, it leads to the generation of a desired optical vortex with high efficiency. Recently, a similar approach has been employed to generate uniform-intensity beams either by inserting phase elements or by curvature of cavity mirrors [132]. The intra-cavity laser beam shaping with these absorptive, reflective, and transmissive elements is shown in Figs. 1.12(a)-1.12(c), respectively.
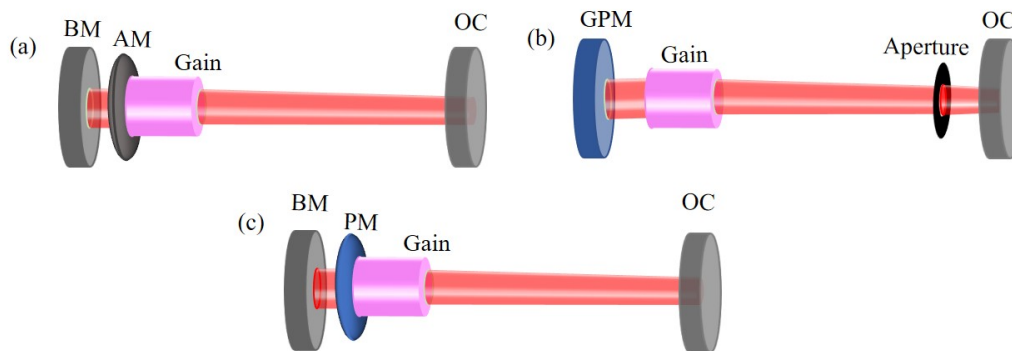
Figure 1.12: Schematics for intra-cavity laser beam shaping consisting of (a) amplitude mask (AM) (absorptive), (b) graded phase mirror (GPM) (reflective), and (c) phase mask (PM) (transmissive).

1.3.2.2 Digital cavity laser

In the previous Sec. 1.3.2.1, we have discussed the generation of a particular light field distribution by modifying amplitude and phase of light inside the laser cavity. The generation of a specific field distributions requires inserting of specific optical elements inside the cavity, and the cavity needs to be aligned properly every time. Further, the generation of a complex light field distribution requires an optical device/element (amplitude/phase mask) with complex features, which involves manufacturing difficulties. These aspects pose limitations for generating arbitrary light field distributions.

To overcome these limitations, SLM based approach is proposed, where the back mirror of a laser cavity is replaced with a reflective type phase-only SLM [102,133]. With this modification, it is known as a digital cavity laser because the SLM can be controlled electronically, and modulation of light can be achieved by implementing amplitude and phase masks digitally on the SLM. The power and quality of generated structured light depends on the SLM, thus SLM should have high-damage threshold, high reflectivity, high resolution, high conversion efficiency, and small cross-talk between the pixels. The schematic of a digital cavity laser as well as illustrative results are shown in Fig. 1.13. It consists of a Brewster window to control polarization and solid-state Nd:YAG (neodymium-doped yttrium aluminium garnet) gain medium pumped by an external laser diode (LD). The desired structured light is obtained at the output coupler (OC).

With an ability to easily control amplitude and phase on the SLM, a digital laser can be used to generate arbitrary light field distributions. For generating a desired light field distribution, the required phase hologram for SLM can be simulated by a suitable approach described in Sec. 1.5. Figure 1.13(b) shows the generated structured light (top row) and corresponding SLM holograms (bottom row). Particularly, $HG_{3,0}$ mode is generated with a hologram having loss lines containing checkerboard pattern, which causes amplitude modulation. Other beams such as Airy and uniform-intensity are generated by phase-only modulation. The $LG_{1,0}$ is generated by modulating both amplitude and phase. As compared to the previously mentioned approaches, a digital cavity laser has advantages,
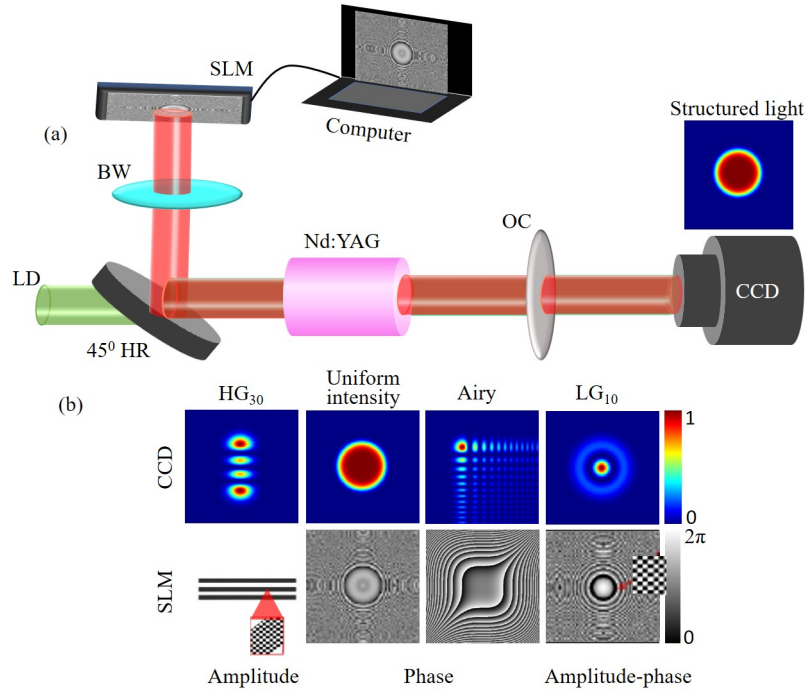
Figure 1.13: (a) Schematic of a digital cavity laser. SLM: spatial light modulator; BW: Brewster window; HR: high reflectivity mirror at an angle of 45°; LD: external laser diode source; OC: output coupler. [102]

such as it is a dynamic method, and different types of structured light can be generated on demand, without re-alignment/modification/optimization of the cavity.

1.3.2.3   Degenerate cavity laser

In the previous Sec. 1.3.2.2, we have discussed a dynamic method involving intra-cavity SLM to digitally select and control desired structured light in a conventional laser cavity. Unfortunately, in such a conventional laser cavity the number of lasing modes is limited, and due to that the resolution of generated structured light at the output of laser is inherently poor and mostly limited to the standard predetermined modes of the cavity. Further, the local independent control of intensity and phase distributions of laser modes by each pixel of SLM is strongly affected by the diffractive coupling between the pixels due to round-trip propagation of light.

Further, in a digital cavity laser, a desired mode is selected from a single laser source. However, single laser sources are limited, particularly, for high-power applications be-

cause of various physical constraints, such as damage threshold of the gain medium, gain saturation, optical facet damage, and non-linear effects. Further, strong pump may lead to excitation of higher-order transverse modes, which may deteriorate the output beam quality ($M^2 >> 1$). The presence of higher-order modes results in an increase in the diffraction and a decrease in the focusing abilities of a laser beam. Furthermore, higher-order modes distort the beam profile, reduce power density in the far field, as well as reduce the spatial coherence of an output laser beam. To overcome such limitations, phase-locking of several lasers can be employed to generate structured light with high output power. The structured light with high-quality, high-resolution, and high-power can be generated using a degenerate cavity laser [134].
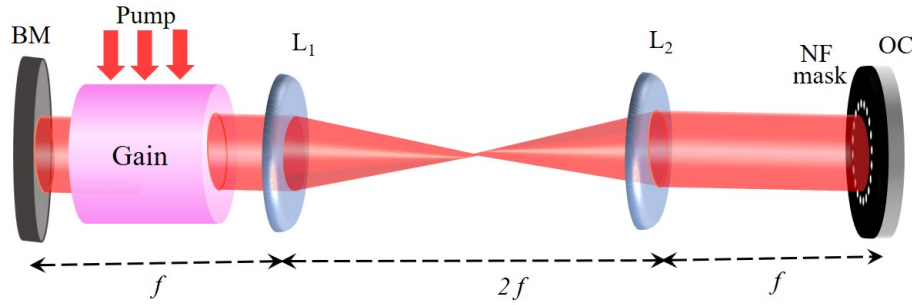
Figure 1.14: Schematic of a degenerate cavity laser for generating an array of lasers. BM: back mirror; OC: output coupler; L_1, L_2: plano-convex lenses of focal length f; NF mask: near-field mask.

A degenerate cavity laser consists of two mirrors, a high-reflectivity back mirror (BM) and a partially reflecting output coupler (OC), a gain medium (Nd:YAG), and two plano-convex lenses L_1 and L_2 arranged in $4f$ telescopic configuration (Fig. 1.14). The $4f$ arrangement ensures perfect imaging inside the cavity, as a ray from each point on the back mirror will map onto itself after a complete round-trip. Hence, the transverse field at each point on the back mirror will act as a mode of the laser cavity. All the modes are having same path length, same quality factor, and are equally probable. Therefore, all the modes are degenerate in losses, and hence it is known as degenerate cavity laser. In a degenerate cavity laser, the number of lasing transverse modes is proportional to cross-section area of the gain medium. A typical degenerate cavity supports $> 10^5$ transverse

modes [135]. The number of transverse modes can be controlled precisely by inserting additional various intracavity elements, such as near-field and far-field amplitude masks, phase plates, lenses, etc [136, 137].

The array of independent lasers in various network geometries can be generated using a degenerate cavity. A binary amplitude mask with circular holes (diameter $\sim 200~\mu$m and center-to-center separation $\sim 300~\mu$m) (NF mask in Fig. 1.14) in an array geometry is placed close to OC, and because of perfect imaging, each hole behaves as an independent laser with a nearly Gaussian distribution (TEM$_{00}$ mode profile). The lasers can be phase-locked by coupling them using various mechanisms, such as near-field coupling with Talbot diffraction (OC is displaced from NF mask by a distance of αz_T, as shown in Fig. 1.15) and the far-field coupling with Fourier aperture (FF mask in Fig. 1.15) [136, 138]. In the near-field coupling with Talbot diffraction, the sign of coupling can be changed by varying the distance αz_T. Due to the dissipative nature of coupling as well as mode competition over the same gain, the mode with minimum loss is obtained as the steady-state phase-locked solution.
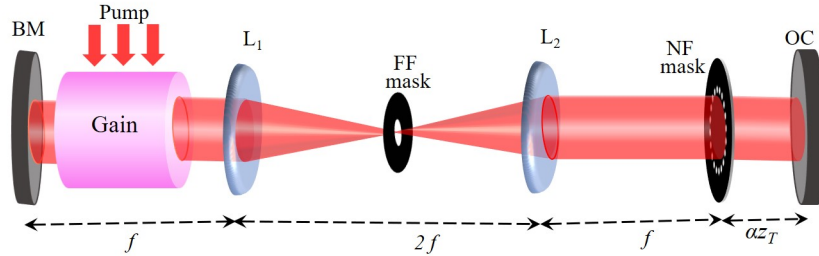
Figure 1.15: Schematic of a degenerate cavity laser. BM: back mirror; OC: output coupler; L_1, L_2: plano-convex lenses; NF mask: near-field mask; αz_T denotes Talbot length, and by changing factor α Talbot length can be varied. [136].

Further, to overcome the issues related with digital cavity laser, a more efficient digital degenerate cavity laser (DDCL) has been demonstrated [101]. It has several advantages, such as it supports a very large number of independent spatial lasing modes, and has access of both near-field and far-field planes. These properties enable for independent manipulations and control of several degrees of freedom of the lasing beam. Therefore, in DDCL, by simultaneously controlling the intensity, phase, and coherence of the laser,

a variety of unique, high-quality, and high-resolution arbitrarily shaped structured light have been generated [101].

The degenerate cavity laser can also be used in rapid phase retrieval problems [139], to simulate classical XY spin array [140], investigation of complex network dynamics [141], and, to solve computationally hard problems [142].

1.4 Numerical and analytical methods

1.4.1 Modeling of laser cavity

To analyze the output of a laser cavity, we can perform an eigenvalue analysis. The eigenvalue equation can be given as

$$KU_n = \gamma_n U_n, \tag{1.7}$$

where U_n represents the field of the eigenvectors/modes, corresponding to eigenvalues γ_n. The power loss per round-trip for each mode can be calculated as $1 - |\gamma_n|^2$. K denotes the free space propagation kernel, computed by the Kirchhoff-Fresnel integral [143].

The eigenvectors for a specific cavity can be calculated by solving Eq. (1.7) numerically or analytically. The Fox-Li iterative algorithm is commonly used to simulate the laser cavities [144]. It considers an initial vector ($U = V_0$) with an arbitrary field distribution, and for the round-trip propagation, the kernel K is applied repeatedly to obtain a sequence of vectors $V_{m+1} = KV_m$. Note, one round-trip corresponds to one iteration in the algorithm. If the initial vector V_0 is written as a linear superposition of eigenvectors of the cavity as $V_0 = \sum_n a_n U_n$, then the sequence of vectors can be expressed as $V_m = \sum_n a_n \gamma_n^m U_n$. If the eigenvalues follow the relation $\gamma_1 \geq \gamma_2 \geq \gamma_3... \geq \gamma_N$, then eigenvectors corresponding to higher m will suffer more losses, hence, U_1 will be a dominant mode. Therefore, $V_m \approx a_1 \gamma_1^m U_1$, and after several iterations, the fundamental mode with minimum loss is obtained. Furthermore, the approach can be employed to a multimode cavity that supports various modes with the same losses (known as degenerate cavity).

For such a cavity, the eigenvalues will be approximately equal ($\gamma_1 \approx \gamma_2 \approx \gamma_3...$).

Another approach for simulating the laser cavity is based on the Gerchberg-Saxton (GS) iterative algorithm [145]. Although, GS algorithm is widely used for the phase retrieval between the two planes with known intensity distributions, and are related by mathematical operation, namely, Fresnel propagation or Fourier transform. However, based on the intensity or phase constraints at two different planes, it can compute the field distribution at any plane in a laser cavity. For example, in a degenerate cavity shown in Fig. 1.16, for a particular desired intensity distribution at the output coupler and a phase constraint at the back mirror, the field distribution at any plane inside the laser cavity can be calculated.
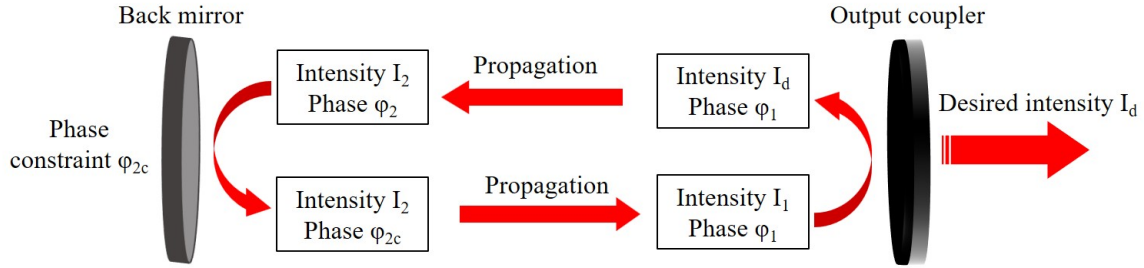
Figure 1.16: Schematic of a laser cavity with Gerchberg-Saxton algorithm to generate desired intensity I_d having a phase constraint ϕ_{2c} at back mirror.

Figure 1.16 shows the GS algorithm and basic schematic of a laser cavity. The algorithm starts with an initial random phase and desired intensity I_d at the output coupler. Now, this field is propagated to the back mirror and becomes $\sqrt{I_2}\exp(i\phi_2)$. At the back mirror, the phase of this field is modified due to a phase constraint $\phi_2 c$, and produces field $\sqrt{I_2}\exp(i\phi_2 c)$. Now, a back propagation of this modified field to the output coupler results in a field $\sqrt{I_1}\exp(i\phi_1)$, where the intensity constraint I_d is imposed. This procedure is repeated until I_1 converges to I_d [145].

Apart from these methods, several other methods are also reported to realize the laser cavities. For example, Prony's method can be employed to calculate the losses and phase shifts over a wide range of parameters of a laser cavity with circular mirrors. It provides an effective algorithm to solve eigenvalue equation to obtain all the significant lowest order modes in a laser cavity. In Prony's method the orthogonality of modes is

employed to construct a set of equations containing eigenvalues of the laser cavity, and upon solving these equations eigenvalues and eigenvectors can be obtained [146]. In the matrix diagonalization method, Eq. (1.7) is solved by diagonalization of a propagation matrix. For example, for a laser cavity with two mirrors, the round-trip matrix can be written as $M_{(round-trip)} = M_{(free\ space)} M_{(mirror1)} M_{(free\ space)} M_{(mirror2)}$. The diagonalization of matrix $M_{(round-trip)}$, results in eigenvectors/modes U with eigenvalues γ, and thereby the round-trip losses.

1.4.2   Propagation of light in free space and complex media

In several applications, the propagation of structured light is required either in free space or in complex media. In this thesis, our aim has also been to investigate the propagation of structured light, for example, to analyze properties such as autofocusing, self-healing, and resilience to perturbations. To calculate the intensity distribution as a function of propagation distance, the wave equation can be solved to obtain Huygen-Fresnel integral. The wave equation can be written as [76, 147]:

$$\nabla^2 u = \frac{1}{c^2} \frac{\partial^2 u}{\partial t^2},$$

(1.8)

where u denotes the electric field of light, ∇^2 is Laplacian operator in the Cartesian coordinates (x,y,z), c denotes the speed of light in free space, and t represents the time. Now, for a wave with sinusoidal variation, the above equation leads to a time independent Helmholtz equation.

$$[\nabla^2 + k^2]E(x, y, z) = 0.$$

(1.9)

Further $E(x, y, z) = U(x, y, z) \exp(ikz)$, therefore Eq. (1.8) can be written as

$$\frac{\partial^2 u}{\partial x^2} + \frac{\partial^2 u}{\partial y^2} + \frac{\partial^2 u}{\partial z^2} - 2ik\frac{\partial u}{\partial z} = 0.$$

(1.10)

The slow variation of $u(x, y, z)$ with respect to z is known as paraxial approximation. Mathematically it can be expressed as

$$\left| \frac{\partial^2 u}{\partial z^2} \right| \ll \left| 2k \frac{\partial u}{\partial z} \right|. \tag{1.11}$$

Therefore, on omitting second order partial derivative term in Eq. (1.10), the resulting equation can be written as

$$[\nabla_t^2 + k^2]u(s, z) = 0, \tag{1.12}$$

where s refers to transverse coordinates and ∇_t^2 represents Laplacian operator in these coordinates. The general solution to an exact wave equation is a uniform spherical wave diverging from a point source r_0.

$$E(r, r_0) = \frac{\exp(-ik\rho(r, r_0))}{\rho(r, r_0)}, \tag{1.13}$$

where $E(r, r_0)$ is mean field at point r due to a source at point r_0 and $\rho(r, r_0)$ represents the distance between them. Therefore,

$$\rho(r, r_0) = \sqrt{(x - x_0)^2 + (y - y_0)^2 + (z - z_0)^2}. \tag{1.14}$$

According to Fresnel approximation in diffraction theory, in the expansion of $\rho(r, r_0)$ the terms higher than quadratic order can be dropped. Therefore, Eq. (1.13) can be written as

$$E(x, y, z) \approx \frac{1}{z - z_0} \exp\left(-ik(z - z_0) - ik \frac{(x - x_0)^2 + (y - y_0)^2}{2(z - z_0)} \right), \tag{1.15}$$

Now, according to Huygen's principle, for an incident field distribution $E(x_0, y_0, z_0)$ over any closed surface S_0, each point on that surface can act as a source of uniform spherical wave or Huygens' wavelet. The resultant field at any other point (x, y, z) beyond (or inside) S_0 can be obtained by adding the fields of all Huygens' wavelets originating from

S_0. Mathematically, this can be expressed as

$$E(x, y, z) = \frac{i}{\lambda} \iint_{S_0} E(x_0, y_0, z_0) \frac{\exp(-ik\rho(r, r_0))}{\rho(r, r_0)} \cos\theta dS_0, \tag{1.16}$$

where $\cos\theta$ is obliquity factor. After substituting Eq. (1.15) in Eq. (1.16), we get

$$E(x, y, z) \approx \frac{ie^{-ik(z-z_0)}}{(z-z_0)\lambda} \iint E_0(x_0, y_0, z_0) \exp\left[-ik\frac{(x-x_0)^2 + (y-y_0)^2}{2(z-z_0)}\right] dx_0 dy_0. \tag{1.17}$$

Further, for $z_0 = 0$, and in cylindrical coordinates the above integral is written as

$$\begin{aligned}
E(\rho, \phi, z) &= -\frac{ik_0}{2\pi z} \exp(ikz) \exp\left(\frac{ik}{2z}\rho^2\right) \iint E(r, \theta) \exp\left(\frac{ik}{2z}r^2\right) \\
&\times \exp\left(-\frac{ik}{z}\rho r \cos(\theta - \phi)\right) r dr \, d\theta, \tag{1.18}
\end{aligned}$$

where (r, θ) and (ρ, ϕ) represent coordinates of source and observation (output) planes, respectively, separated by a distance z. $k = 2\pi/\lambda$ represents the wavenumber of an optical field in free space.

Equation (1.18) can also be exploited to investigate the propagation of structured light fields in turbulent/random medium. For that, a complex phase function $\psi(\rho, r, z)$ is introduced in the integral describing a turbulent medium.

$$\begin{aligned}
E(\rho, \phi, z) &= -\frac{ik}{2\pi z} \exp(ikz) \exp\left(\frac{ik}{2z}\rho^2\right) \iint E(r, \theta) \exp\left(\frac{ik}{2z}r^2\right) \\
&\times \exp\left(-\frac{ik}{z}\rho r \cos(\theta - \phi)\right) \exp[\psi(\rho, r, z)] r dr \, d\theta, \tag{1.19}
\end{aligned}$$

Intensity after propagating distance z in a turbulent medium is given by

$$\langle I(\rho, \phi, z) \rangle = \langle E(\rho, \phi, z) E^*(\rho, \phi, z) \rangle \tag{1.20}$$

Where $\langle \, . \, \rangle$ denotes an ensemble averaging over different realizations of random phases

corresponding to a turbulent medium. Using Eq. (1.19) into Eq. (1.20), we get

$$
\begin{aligned}
\langle I(\rho, \phi, z) \rangle &= \left(\frac{k}{2\pi z} \right)^2 \iint \iint E(r, \theta) E^*(r', \theta') \exp\left(\frac{ik}{2z}(r^2 - r'^2) \right) \\
&\times \exp\left(-\frac{ik}{z} r\rho \cos(\phi - \theta) \right) exp\left(\frac{ik}{z} r'\rho \cos(\phi - \theta') \right) \\
&\times \langle \exp[\psi(\rho, r, z) + \psi^*(\rho, r', z)] \rangle rr' \, dr \, dr' \, d\theta \, d\theta'.
\end{aligned}
\tag{1.21}
$$

The last term in above integral describes the correlation of random fluctuations, which is given as

$$
\langle \exp[\psi(\rho, r, z) + \psi^*(\rho, r', z)] \rangle = \exp(-0.5 D_\psi) = \exp\left(-\frac{(r - r')^2}{l(z)^2} \right).
\tag{1.22}
$$

D_ψ denotes the phase structure function in Rytov's representation, and $l(z)$ is the coherence length of the spherical wave propagating in a turbulent medium and depends upon turbulence strength C_n^2 as $l(z) = (0.545 C_n^2 k^2 z)^{-3/5}$. After substituting Eq. (1.22) into Eq. 1.21, we get

$$
\begin{aligned}
\langle I(\rho, \phi, z) \rangle &= \left(\frac{k}{2\pi z} \right)^2 \iint \iint E(r, \theta) E^*(r', \theta') \exp\left(\frac{ik}{2z}(r^2 - r'^2) \right) \\
&\times \exp\left(-\frac{ik}{z} r\rho \cos(\phi - \theta) \right) exp\left(\frac{ik}{z} r'\rho \cos(\phi - \theta') \right) \\
&\times \exp\left(-\frac{(r - r')^2}{l(z)^2} \right) rr' \, dr \, dr' \, d\theta \, d\theta'.
\end{aligned}
\tag{1.23}
$$

Equation (1.23) represents an intensity distribution at a propagation distance z in a turbulent medium. The last term in Eq. (1.23) restricts the separability of radial and angular parts, making it difficult to solve it in its present form. The integral in Eq. (1.23) is difficult to solve analytically for complicated intensity and phase distributions. Therefore, it can either be solved by a stationary phase method or numerically by the Angular Spectrum Method (ASM) [148].

ASM is a mathematical approach for simulating the wave propagation. It is useful for analyzing wavefront propagation through optical systems including lenses, diffraction

gratings, and free space propagation. The ASM is based on the idea of breaking down a wavefront into a series of plane waves with varying propagation directions (angles). Each plane wave component of the wavefront contains information of spatial frequency content and propagation direction of the wavefront. By accounting for a number of plane wave components, the ASM successfully simulates wave propagation over long distances as well as in sophisticated optical systems.

A step-by-step procedure of the angular spectrum method is given as [148]:

1. **Fourier transform**: Using a Fourier transform operation, the electric field $E(r, \theta)$ with its complex phase is divided into its spatial frequency components. Now the spatial domain of the field is transformed into the frequency domain. The Fourier spectrum of the field is splitted into angular slices or planes, each of which corresponds to a certain propagation direction. The angular slices are perpendicular to the propagation axis.

2. **Propagation of angular slice**: Each angular slice is propagated individually using a propagator for a certain distance. This involves applying a phase shift that is in line with the angular slice's unique propagation direction and propagation distance.

3. **Inverse Fourier transform**: After propagating each angular slice, an inverse Fourier transform is applied to obtain the wavefront in the spatial domain.

The above steps can be summarized as [148]:

$$E(\rho, \phi; z) = \mathcal{F}^{-1}.H(f, z).\mathcal{F}(E(r, \theta)), \tag{1.24}$$

where, $\mathcal{F}$ and $\mathcal{F}^{-1}$ denote the Fourier and inverse Fourier transform operations. $H(f, z) = e^{ik_0 z} e^{-i\pi\lambda z(f_x^2 + f_y^2)}$ is a propagator for distance z. f_x and f_y are the spatial frequencies along horizontal and vertical directions. The ASM enables simulation of wave propagation through various optical systems, including free space propagation, diffraction, and phase elements. The ASM also provides a flexible and computationally efficient approach to understand the propagation of light in random or turbulent media.

1.4.3   Quantification parameters

To characterize the various properties of generated spatially structured light, different types of quantification approaches are required. Here, we have discussed various quantification parameters to measure the quality, purity, self-healing, autofocusing, and coherence of spatially controlled structured light.

1.4.3.1   Root mean square error (RMSE)

The quality of generated light can be quantified by the root mean square error (RMSE), and it can be defined as [149]

$$\text{RMSE}(z) = \sqrt{\frac{\sum_{i=1}^{N} \left(I_g(x, y; z) - I_t(x, y; z) \right)^2}{\sum_{i=1}^{N} I_t(x, y; z)}}, \tag{1.25}$$

where $I_g(x, y; z)$ and $I_t(x, y; z)$ represent the intensity distributions of generated and target structured light at a distance z. It measures the differences between generated and target intensity distributions, and accordingly, it quantifies the quality of generated structured light.

1.4.3.2   Overlap integral

An overlap integral measures similarities between the generated and target intensity distributions of structured light. It is defined as [150]

$$C(z) = \frac{\iint I_t(x, y; z) I_g(x, y; z) \, dx \, dy}{\sqrt{\iint I_t^2(x, y; z) \, dx \, dy \iint I_g^2(x, y; z) \, dx \, dy}}. \tag{1.26}$$

It is a normalized integral whose value varies between 0 to 1. The value "0" denotes the poor similarity, whereas value "1" denotes high similarity. It also determines the quality

of generated structured light. This parameter is highly used in quantifying the degree of self-healing of partially truncated structured light. Further, it is also used to quantify the distortions introduced by propagation of light through complex media.

1.4.3.3 Beam quality factor (M^2)

The beam quality factor is used to assess the quality of a laser beam. Particularly, M^2 is a dimensionless quantity that measures the divergence and focusing capabilities of a laser beam. The $M^2 = 1$ corresponds to a perfect Gaussian beam. A lower value of M^2 indicates a good beam quality and has less divergence as well as better focusing abilities [151]. It is defined as

$$\theta_d = M^2 \frac{\lambda}{\pi \sigma_0},\tag{1.27}$$

where θ_d is half-angle beam divergence, λ denotes the wavelength of light, and σ_0 is minimum beam waist. The M^2 provides a simple means for accurately calculating the most commonly required features of laser beams, namely, divergence angle, propagation characteristics, and the size of focused spot.

1.4.3.4 Modal decomposition

Owing to the completeness and orthogonality of HG and LG beams, any beam can be expressed as a linear superposition of higher orders LG and HG modes [152].

$$I(r) = \sum_{p,l} |c_{pl}|^2 |u_{pl}(r,\theta)|^2,\tag{1.28}$$

where $|c_{pl}|$ is the weight of each mode. The self-healing properties of structured light can be quantified by calculating the modal spectrum. For example, if $U(x,z)$ and $\bar{U}(x,z)$ are ideal and self-heald beam, then

$$\bar{U}(x,z) \approx \alpha\, U(x,z),\tag{1.29}$$

where α represents the power loss due to truncation. The modal spectrum can be written as

$$\bar{c}_{pl} \approx \alpha\, c_{pl}, \tag{1.30}$$

This suggests that for self-healing to occur the modal spectrum of the truncated beam should resemble the modal spectrum of an ideal beam. Since the modal spectrum is invariant under propagation, this decomposition can be performed at any convenient plane [152].

1.4.3.5 Diffraction efficiency (η)

Diffraction efficiency determines the fraction of light in any local region of transverse plane compared to the total amount of light. It is defined as

$$\eta = \frac{\text{Intensity in a selected region}}{\text{Total intensity of light}}. \tag{1.31}$$

It is a dimensionless quantity, and its modified versions can also be used to calculate the conversion efficiency η_c of beam shaping methods.

$$\eta_c = \frac{\text{Intensity in the shaped output beam}}{\text{Total intensity of incident light}}. \tag{1.32}$$

1.4.3.6 Fringe visibility (V)

It quantifies the coherence of two interfering sources by calculating the contrast between the maxima and minima of interference pattern. It is defined as [153]

$$V = \frac{I_{\max} - I_{\min}}{I_{\max} + I_{\min}}, \tag{1.33}$$

where $I_{\max}$ and $I_{\min}$ denote the intensity at the locations of interference maxima and minima.

1.5 Spatial light modulators: A tool for laser beam shaping

In this thesis, we have employed Spatial light modulators (SLMs) for generation and characterization of spatially controlled structured light. Therefore, in this section, we have discussed working principle of SLM for amplitude and phase modulation of light. SLMs are computer controlled devices and can act as transforming elements in laser beam shaping. Owing to the digital control, SLMs can modulate the light both inside as well as outside the laser cavity. SLMs allow the precise control and manipulation of light by modifying the amplitude, phase, or polarization of an incident light.

In most of the SLMs, nematic liquid crystals (LCs) are used to introduce phase shift in the incident laser beams. In the absence of an electric field (voltage), the LC molecules are randomly oriented. However, applying a voltage (V) can change the orientation of the LCs in a pixel by an amount (δ). Due to this, the refractive index corresponding to an extraordinary light ray will change according to the relation

$$\frac{1}{n_e^2(\delta)} = \left(\frac{\cos\delta}{n_e}\right)^2 + \left(\frac{\sin\delta}{n_o}\right)^2. \tag{1.34}$$

Where n_e and n_o are refractive indices corresponding to ordinary and extraordinary light rays. According to Jones matrix formulation, the matrix for a phase retarder can be written as:

$$M = \begin{pmatrix} \exp\left(i\theta_{\mathrm{e}}\right) & 0 \\ 0 & \exp\left(i\theta_{\mathrm{o}}\right) \end{pmatrix} = \exp\left(i\theta_{\mathrm{o}}\right) \begin{pmatrix} \exp\left(i\left(\theta_{\mathrm{e}} - \theta_{\mathrm{o}}\right)\right) & 0 \\ 0 & 1 \end{pmatrix}. \tag{1.35}$$

Here, $\theta_o = kdn_o$ and $\theta_e = kdn_e$ are phase offsets in the directions of n_o and n_e respectively. $k = 2\pi/\lambda$ is the wavenumber of an incident light and d denotes the thickness of liquid crystals. Therefore, the total phase shift is given by:

$$\Delta\Theta = k(n_e - n_o)d. \tag{1.36}$$

For an incident electric field in the form $E_{\text{in}} = E_e\hat{\mathbf{e}} + E_o\hat{\mathbf{o}}$, the output electric field can be written as:

$$E_{\text{out}} = ME_e = \begin{pmatrix} E_{\text{in}} \exp\left(i\left(\theta_{\text{e}} - \theta_{\text{o}}\right)\right) \\ E_{\text{o}} \end{pmatrix}. \tag{1.37}$$

Equation (1.37) shows that the component of electric field parallel to n_e, acquires a phase shift, whereas, the component parallel to n_o remains unchanged. Figure 1.17 shows the structure of LCoS-SLM (liquid crystal on silicon based SLM). Figure 1.17(a) shows the schematic of an SLM, where a transparent layer of electrode controls the LCs sandwiched between two transparent alignment layers. The SLM includes a silicon substrate at the bottom, with an active matrix circuit on top, directly connected to pixelated metal electrodes. These electrodes control the orientation of the LC molecules at each pixel. Finally, the top of the SLM is covered with a transparent glass substrate. Figure 1.17(b) shows a front view of HOLOEYE reflective type phase-only SLM, used for the investigation of beam shaping throughout this thesis. Our SLM has a resolution of 1920 × 1080 pixels, with a pixel size of 8 μm. The SLM is connected to a driver board with the flex cable, which is further connected to a computer. Thus, any phase distribution in grayscale, divided into 256 levels can be projected on SLM display, which can change the phase of an incident beam from 0 to 2π.
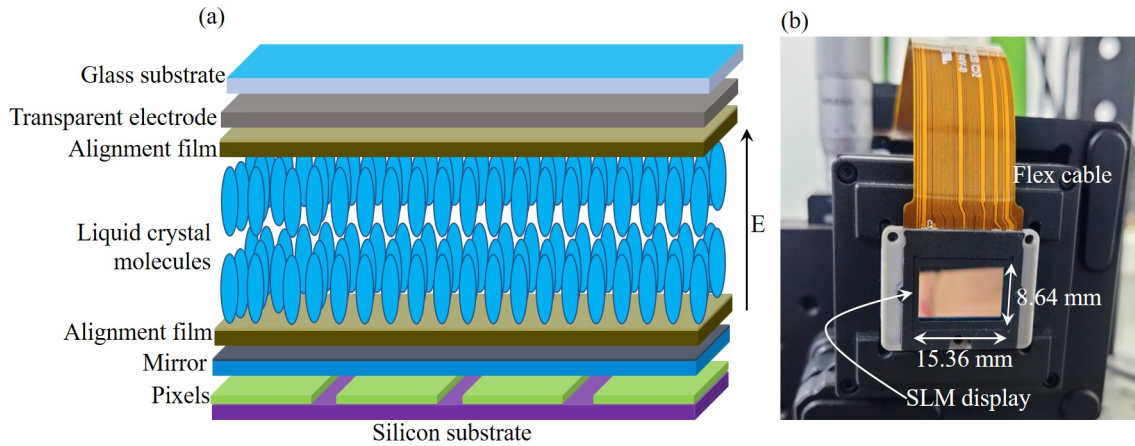
Figure 1.17: (a) Schematic of SLM structure. (b) Image of a commercial phase-only reflective type HOLOEYE SLM.

1.5.1   Computer generated holograms for SLMs

As discussed above, SLM is an electronically controlled device, where the phase shift from 0 to 2π can be given by the controlled rotation of LCs. The rotation of LCs is directly proportional to an applied voltage, however, for a precise rotation/orientation, the calibration of SLM is required. The calibration of SLM can be done either by the provided calibration data or by performing a double slit experiment with SLM. Once calibrated, a computer-generated hologram can be projected on the SLM display, allowing modification of phase or complex-amplitude (both amplitude and phase) of the light. The methods for preparing phase-only holograms for both types of modulations are discussed below.

1.5.1.1   Phase-only modulation

In phase-only modulation, the amplitude of an incident laser beam remains the same as that of modulated beam. This is similar to a case when any point in a complex plane lying on the circumference of a circle is shifted to another point on the circle keeping the radius (amplitude) same (shown in Fig. 1.18). Therefore, points inside the circle are not available for the transformation. Let us assume that $E_1 = E_{01}\exp(i\phi_1)$ is an incident field with amplitude E_{01} and phase ϕ_1, and $E_2 = E_{02}\exp(i\phi_2)$ is a desired field. Then, the
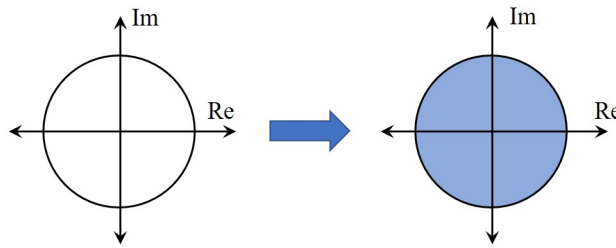
Figure 1.18: Representation of a complex plane for phase-only modulation.

transfer function can be written as

$$t = \frac{E_2}{E_1} = \frac{E_{02}\,\exp(i\phi_2)}{E_{01}\,\exp(i\phi_1)}.$$

(1.38)

For phase-only modulation, $E_{01} = E_{02}$, hence the transfer function is simplified as

$$t = \exp[i(\phi_2 - \phi_1)] \tag{1.39}$$

Corresponding to the above transfer function (Eq. (1.39)), the phase of a computer-generated hologram is given as $\mathrm{mod}(\phi_2 - \phi_1, 2\pi)$. Now, for any phase encoded on SLM, the conversion efficiency is not 100% even for an accurate polarisation state of an incident light. It is due the fact that a 2D grating is formed by a pixel array (pixelation), and because of it light diffracts in many directions. Also, imperfections in the calibration and residual reflection from electrodes result in unmodulated light. If these are not separated, then it may interfere with the modulated light, which in turn may degrade the output beam quality. To isolate the modulated light, a blazed grating is added to the hologram, which separates the modulated light in the first-order and the unmodulated light in zeroth-order. The angle of separation can be controlled by the spatial frequency of the grating. Therefore, the phase of hologram can be given as

$$t = \exp[i(2\pi N_x x + 2\pi N_y y + (\phi_2 - \phi_1))]. \tag{1.40}$$

Also, if an incident light is assumed to be a plane wave then $\phi_1 = 0$, and $\phi_2 = \phi$ represents the phase of a desired beam. In this scenario, the transfer function is written as

$$t = \exp[i(2\pi N_x x + 2\pi N_y y + \phi)]. \tag{1.41}$$

1.5.1.2   Complex amplitude modulation

Simultaneous modulation in both amplitude and phase of an incident beam is known as complex-amplitude modulation. Phase-only SLMs face challenges when it comes to complex-amplitude modulation, as they can only modulate the phase of an incident laser beam. Also, SLM is not a component with an active medium, hence it cannot increase the amplitude of an incident laser beam. Therefore, to change the amplitude of the beam,

light is steered away from the desired locations in the modulated first order. Hence, the phase hologram must contain information about both the amplitude and phase of a desired beam. To modulate the amplitude, a blazed grating with high spatial frequency is added to the field, and the diffracted beam is filtered out in higher orders. This can be understood
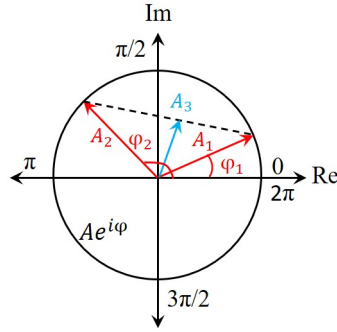
Figure 1.19: Representation of a complex plane for modulation of complex-amplitude.

from a generalized example of complex plane, where A_1 and A_2 represent vectors on unit circle with phase ϕ_1 and ϕ_2 .The resultant vector is represented by vector A_3, which is not on unit circle i.e., a non-unit amplitude with any desired phase (Fig. 1.19). A simple example is checkerboard pattern described by binary phase distribution, where ϕ_1 and ϕ_2 represent phase values of neighboring boxes with equal amplitude. In complex plane this can be assumed as two vectors with equal amplitude with different phase angles. Therefore the resultant amplitude can be controlled by the phase difference $(\phi_2 - \phi_1)$ [154]. In recent past, various methods for the generation of holograms have been proposed [155, 156].

The complex electric field of a desired beam can be expressed as

$$E(x,y) = E_0(x,y)\exp(i\phi(x,y)), \qquad (1.42)$$

where $E_0(x,y)$ is normalised field amplitude and $\phi(x,y)$ represents the phase of a desired beam. The aim is to encode the complex field $E(x,y)$ by means of a phase transmittance function (phase hologram) to incorporate amplitude variations as the phase variations, that is, a function $t(x,y)$ must be given by

$$t(x,y) = \exp\left[i\psi\left(E_0, \phi\right)\right], \qquad (1.43)$$

where $\psi(E_0, \phi)$ accounts both the amplitude and phase variations. To find the desired form of phase function $\psi(E_0, \phi)$, $t(x, y)$ can be expressed as the Fourier series in a domain of ψ as [155]

$$t(x, y) = \sum_{p=-\infty}^{\infty} c_p^{E_0} \exp(ip\phi), \tag{1.44}$$

where

$$c_p^{E_0} = \frac{1}{2\pi} \int_{-\pi}^{\pi} \exp[i\psi(E_0, \phi)] \exp(-ip\phi) d\phi. \tag{1.45}$$

The field $E(x, y)$ can be recovered from only the first-order term of Eq. (1.45), provided that the following identity is fulfilled

$$c_1^{E_0} = E_0 a, \tag{1.46}$$

where a is a positive constant. Further, the phase function $\psi(E_0, \phi)$ with odd symmetry can be expressed as

$$\psi(E_0, \phi) = f(E_0) \sin(\phi). \tag{1.47}$$

In this case, the phase transmittance function (Eq. 1.43) becomes $t(x, y) = \exp[i.f(E_0) \sin(\phi)]$. Expressing it in the Fourier series using Jacobi-Anger identity, we get

$$\exp[i.f(E_0) \sin(\phi)] = \sum_{q=-\infty}^{\infty} J_q[f(E_0)] \exp(iq\phi), \tag{1.48}$$

where J_q represents Bessel function of qth order. Using Eqs. (1.44), (1.46) and (1.48), we get

$$c_1^{E_0} = J_1[f(E_0)]. \tag{1.49}$$

Therefore, from Eqs. 1.46 and (1.49), we get

$$E_0 a = J_1[f(E_0)]. \tag{1.50}$$

The function $f(E_0)$ can be determined by numerical inversion of Eq. (1.50). The maximum

value of a for which Eq. (1.50) can be fulfilled is ~ 0.58, which corresponds to the maximum value of the first-order Bessel function $J_1(x)$, which occurs at $x \approx 1.84$. This restricts $f(E_0)$ in the interval [0, 1.84]. The modulated field consists of first and higher orders, thus to separate the first order, a blazed grating is added to the phase of hologram, as described previously.

1.6 Outline of thesis

The thesis is structured into eight chapters. In present chapter, we have given a brief review of the literature relevant to the thesis to provide state-of-the-art in the field of structured light by discussing various types of spatially structured light and methods to generate them. We emphasize the challenges in the field of structured light and elaborate on how we address those challenges. The summary of the contents of each chapter is provided below.

In **Chapter 2**, we have presented an outer-cavity method for tailoring the light in amplitude degree of freedom to generate high-quality uniform-intensity beams with customized shapes, using diffractive optical elements (DOEs) [32, 33]. The phase of DOEs is obtained by an iterative method (modified Gerchberg-Saxton algorithm) that involves spatial Fourier filtering. The obtained DOEs consist of simple design (smooth phase distribution), which makes them easier to fabricate. An input laser beam with Gaussian intensity distribution illuminates the DOE, and after propagating a certain distance (working distance) transforms into the desired uniform-intensity output beams with customized shapes such as square, annular, rectangular, hollow square, and plus spatial shapes. The quality of the output beams is quantified by calculating root mean square error (RMSE) with respect to the ideal beams. We have performed a detailed robustness analysis on the quality of shaped output beams against various types of imperfections in an input beam, such as misalignment with respect to DOE, presence of speckle noise, asymmetry, presence of higher order transverse modes, and mismatch of beam sizes. We have found that the shaped output beams with reasonably good quality are obtained over a broad

range of imperfections. However, in the case of speckle noise, the quality of shaped output beams can be further improved by an additional external spatial Fourier filter of suitable transmission function. Furthermore, to investigate spectral properties of method, we have designed a DOE for a particular wavelength and illuminated it with an input beam over a broad range of wavelengths. We have found that the quality of shaped output beams remains excellent over a broad spectral range. However, the working distance decreases with an increase in the wavelength.

In **Chapter 3**, we have presented tailoring of light in the amplitude and phase degrees of freedom for generating special type of structured light (called aberration laser beams (ALBs)) containing multiple bright lobes and possessing unique propagation features, such as autofocusing and self-healing in both free space as well as in turbulent media [37, 39]. The ALBs are generated, based on an outer-cavity method, using a DOE whose phase distribution consists of radial and periodic angular dependence. We have presented a detailed mathematical formulation for describing the propagation of ALBs in turbulent media by solving Huygen-Fresnel integral using stationary phase method. We have found that the presence of turbulence leads to distortions in the spatial intensity distribution of ALBs, as well as causes beam wandering. The effect of turbulence on the propagation of ALBs is quantified by calculating overlap integral with respect to ALB in free space. The ALBs possess good autofocusing properties both in free space as well as in turbulent media, where on-axis peak intensity becomes maximum with tight focusing. In particular, the autofocusing properties of ALBs remain invariant, irrespective of turbulence strength. The autofocusing distance can be controlled from any small to large values, by controlling the ALB parameters. Further, we have also investigated the spectral dependence of autofocusing of ALBs in turbulent medium and found that autofocusing distance does not depend on the turbulence, however, it decreases with an increase in wavelength.

Furthermore, we have performed a detailed investigation of self-healing of ALBs both in free space as well as in turbulent media of different turbulence strengths. We have found that, both in free space and turbulent media, the truncated ALB self-heals by re-distributing the intensity within the beam. The ALBs self-heal reasonably well even for a

large amount of truncation ($\sim 60\%$). The maximum self-healing always occurs at an autofocusing distance, which remains invariant irrespective of the amount of truncation and strength of turbulence. A good agreement between theory, simulations, and experimental results is obtained.

In **Chapter 4**, we have presented generation of asymmetric aberration laser beams (aALBs) with controlled intensity distribution, based on an outer-cavity method employing a DOE with phase asymmetry [38, 40]. We have introduced the phase asymmetry in DOE by shifting coordinates in a complex plane, which provides an additional control over spatial intensity distribution of beam. We have derived the mathematical formulations for general aALBs as well as the special cases of it. We have shown that in an ideal ALB containing equal intensity bright lobes, by introducing asymmetry most of the intensity can be transferred to any one of the single lobe, and generates a high-energy density. Further, we have explored the mechanism of asymmetric control of intensity in aALBs and found that the asymmetry parameters control the position of indeterminate phase point of the trigonometric phase term in aALB, which creates a controlled asymmetric intensity distribution in the near-field plane. As a result of propagation it provides a controlled transfer of intensity within aALB. In general, for a given parameter m of aALB, the precise spatial location of high-energy density lobe can be controlled by by the precise variation in the asymmetry parameter β, and we have determined empirical relations for them. We have found that for the specific values of β and m, the intensity in the high-energy density lobe can be enhanced by several times the intensity in other lobes. Further, we have investigated the propagation of aALBs, and found that similar to ALBs, the aALBs possess good autofocusing properties, which are not affected by the asymmetry. The autofocusing distance in aALBs can be varied from small to large values by changing the beam parameters. We have found a good agreement between the experimental results and numerical simulations.

In **Chapter 5**, we have presented the generation of high-energy densities by suppression of higher-order sidelobes in the far-field of phase-locked lasers [41, 42]. We have generated an array of lasers in various 1D and 2D array geometries in a degenerate cav-

ity and phase-locked them in the in-phase [out-of-phase] configuration with the far-field coupling using Gaussian apodizer [binary circular aperture]. Owing to the non-uniform amplitude and definite geometry, the far-field of phase-locked lasers consists of higher-order sidelobes. These sidelobes contain a significant amount of energy, which limits the use of an output beam for high-power applications. Our method relies on modifying the combined field (near-field and far-field) distribution of phase-locked lasers to obtain uniform amplitude and phase distributions in a near-field plane, which enables the formation of a high-power density lobe (zeroth-order) in the far-field. We have demonstrated our method for phase-locked lasers in various array geometries, such as square, triangular, Kagome, random, and 1D ring. The results are quantified by calculating the diffraction efficiency of the zeroth-order lobe. It is found that for long-range in-phase locked laser arrays, the diffraction efficiency of zeroth-order lobe can be improved by several factors ($\sim 3 - 4$). The improved diffraction efficiencies are found to be in a range of $90\% - 95\%$ (for 2D arrays) and $\sim 75\%$ (for 1D ring array). Further, we have analyzed robustness of our method against various factors, such as the range of phase-locking, system size, and presence of topological defects in a 1D ring array. We have also investigated our method for out-of-phase locked lasers in a square array, where the zeroth-order has no intensity. We have obtained a high-energy-density zeroth-order lobe with a high diffraction efficiency of 81%.

In **Chapter 6**, we have presented a novel and efficient intra-cavity method for the generation of high-power discrete optical vortices with precisely controlled topological charges (l) by phase-locking one-dimensional (1D) ring array of lasers in a degenerate cavity that involves spatial Fourier filtering [43–45]. Owing to the special geometry of a degenerate cavity, it enables an efficient formation of a 1D ring array of lasers, where each laser consists of a nearly fundamental Gaussian distribution, and independent from each other. Initially, the lasers consist of random phase distribution and are equally probable. To force them into a desired phase-locked state of optical vortex configuration, we employ a special Fourier filter (amplitude mask) at the Fourier plane inside the cavity. The spatial Fourier filtering mechanism helps to eliminate the undesired phase distributions

by introducing additional losses to them, thereby, enables the lasers to find a correct phase distribution in the form of a desired discrete optical vortex. We have performed a detailed investigation on the propagation, such as divergence and self-healing, of discrete optical vortices, and compared them with the conventional continuous optical vortices. We have found that for a given system size (number of lasers) and fixed distance between the neighbouring lasers, the size of a discrete optical vortex and its divergence does not depend on the topological charge, which is found to be different than the conventional continuous optical vortices (Laguerre-Gaussian/Bessel-Gaussian beams). Further, we have performed a detailed investigation of self-healing by partially truncating a discrete optical vortex in the waist plane ($z = 0$) and propagated plane ($z > 0$). To quantify the self-healing, we have calculated an overlap integral to analyze the similarities between the self-healed and ideal discrete optical vortices. The results show that partially truncated discrete optical vortex can self-heal reasonably well. Moreover, we have found that the self-healing distance increases with the value of topological charge of discrete optical vortex. The self-healing distance is also found to be dependent on the amount of blocking, particularly, it increases with an increase in the amount of blocking. We have obtained a good agreement between the analytical and numerical results.

In **Chapter 7**, we present a novel and efficient method for accurate determination of magnitude and sign of topological charge (l) of an unknown discrete optical vortex, which is formed by an array of lasers in a 1D ring geometry [46]. We have presented a simple analytical formulation of working principle of our method. It relies on measuring the interference pattern of a discrete optical vortex, which is obtained by interfering a single selected laser with itself and with all the other lasers in a 1D ring array, using a Mach-Zhender interferometer. The interference pattern is quantified by analyzing the fringe visibility at each laser in a 1D ring array. The discrete laser arrays with $l = 0$ and $l \neq 0$ have different phase distributions, thus produce interference patterns with shifted interference fringes. The averaging of these phase-shifted interference patterns gives rise to a variation in the fringe visibility as a function of laser number in the discrete optical vortex, thus enabling identification of l. The magnitude of l of a discrete optical vortex

is found to be proportional to the number of dips observed in the fringe visibility curve. Further, for an accurate determination of sign of an unknown discrete optical vortex ($l \neq 0$), we have averaged the interference pattern of it with the interference pattern of known $l = +1$. The number of dips in the fringe visibility curve increases by one for positive values of l and increases by one for negative values of l. We have also investigated the robustness of our method against the presence of phase disorder that may occur due to the presence of aberrations in a system. It is found that the phase disorder does not affect an accurate measurement of topological charge of an unknown discrete optical vortex. We have demonstrated our method for discrete optical vortices with topological charges from small to large values and accurately determined their magnitude and sign. We have provided a theoretical description along with numerical and experimental results, and found an excellent agreement between them, indicating that our method is accurate and highly efficient.

At the end, the conclusive chapter (**Chapter 8**) contains a summary of the results discussed in the aforementioned main chapters of the thesis. We also consider some future directions that might aid in gaining a deeper understanding of structured light and its propagation properties.

Chapter 2

Generation of structured light with uniform-intensity and customized spatial shapes

2.1 Introduction

In previous chapter, we have discussed the concept of spatially structured light with relevance to applications in diverse fields as well as its generation based on various intra-cavity and outer-cavity methods. This chapter emphasizes on simple, cost-effective, and efficient outer-cavity method for tailoring of amplitude degree of freedom of light to obtain uniform-intensity beams with customized spatial shapes. As discussed in Sec. 1.2.1, uniform-intensity beams are desired for numerous applications where conventional Gaussian beam poses physical limitations, for example, in material processing, micro structuring, laser thermal annealing, laser fusion, lithography, laser radars that use detector arrays, laser scanning, efficient power extraction in laser amplifiers, medical, optical data processing, interferometric gravity wave detectors, optical lattices, etc. [36, 47, 157–161].

Over the years several methods have been investigated to generate uniform-intensity beams, including transmissive optics (images of masks and mask-like mirrors) [97, 98], re-

fractive optics (lenses, aspheric elements and anisotropic crystals) [99,100,162], diffractive optics (with propagation to far field plane or near-field plane) [47,127,157,163–165], and spatial light modulators (SLMs) [123,158,166–168] [and refs. there in]. Further, another approach is also realized based on that the spatial coherence of an optical field in the source plane is closely related to the intensity distribution of its far-field [169,170].

For efficient light tailoring, a method is desired with low loss, high throughput, high damage threshold, robustness against errors, and simple and cost-effective design. As many investigations are based on SLMs, which pose limitations due to low damage threshold, and exhibits power loss due to higher diffraction orders and polarization elements [167,168]. It also involves challenges such as inherent wavefront error of SLM, digitization effect of SLM command resolution, as well as cross-talk between the pixels [171]. Whereas, methods based on diffractive optical element (DOE) rely only on few passive elements in a compact configuration, exhibits high power efficiency, high damage threshold, and low cost of production and replication [163,172], which are particularly important for high-power applications.

The DOE based method involves a rapid conversion from an input beam into a shaped output beam with high-quality after a certain propagation distance [47]. The quality of beam shaping also depends on the DOE design parameters, for example, input/output beam size, wavelength, and imperfections in an input beam. For example, when a DOE designed with specific parameters, is illuminated with an input beam that has either a different size or wavelength or is misaligned or consists of noise (speckles or higher order modes), the quality of the shaped output beam deteriorates as well as the energy losses also occurs [165,173,174]. Thus to achieve high-quality shaped output beams, we have investigated these aspects of robustness in detail.

In this chapter, we present a DOE based outer-cavity method for generation of uniform-intensity beams with customized spatial shapes. Quality of generated beams is quantified by the calculation of root mean square (RMSE) (Eq. (1.25)). Further, we have performed a detailed robustness analysis on the quality of generated shaped output beams against the various imperfections in an input beam. We have also performed spectral analysis of

method and show that the quality of shaped output beam remains excellent over a broad spectral range of input beam. In Section 2.2, we present a method to determine the phase distribution of DOE for generating uniform-intensity beams. In Section 2.3, the designs of DOEs for generating different spatial shape beams are presented. In Section 2.4, a detailed analysis on the quality of generation of spatially shaped beams is presented. Finally, in Section 2.5 we present concluding remarks. The results presented in this Chapter are given in Refs. [32, 33].

2.2   Basic procedure

The uniform-intensity beams with customized spatial shapes are generated with a simple yet efficient outer-cavity method by means of DOEs using the basic procedure illustrated in Fig. 2.1. An input Gaussian beam illuminates the DOE at $z = 0$, the phase distribution
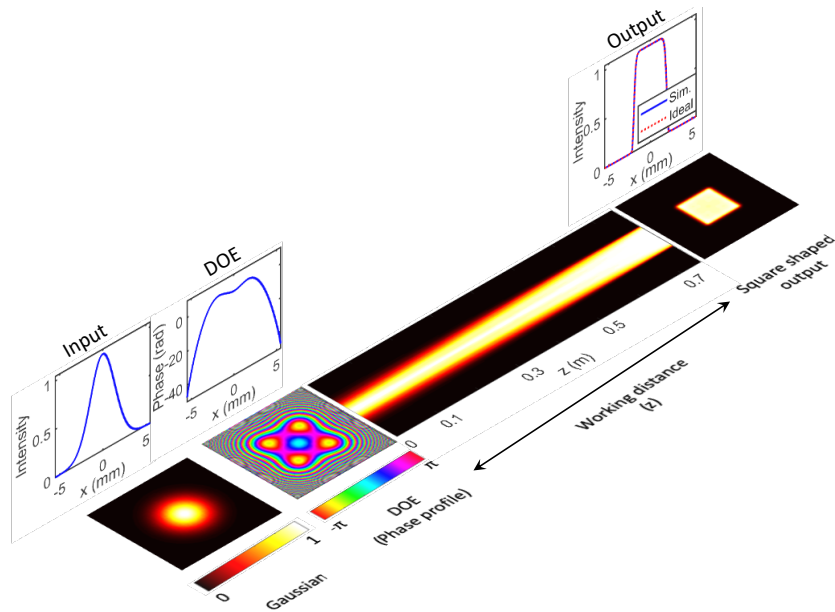
Figure 2.1: Basic arrangement for forming uniform-intensity spatial shaped beams based on a DOE. The schematic illustrates the conversion of an input Gaussian beam into a uniform-intensity square shaped output beam. The representative results are simulated with parameters: input/output beam waist = 2 mm, $n = 14$, $\lambda = 1.064$ μm, and working distance z = 75 cm. The intensity is normalized to the maximum value of 1 (same in other figures).

2 Generation of structured light with uniform-intensity and customized spatial shapes

of DOE is imposed on it, which then transforms into an output beam of desired spatial shape with uniform-intensity distribution after propagating a certain distance z (called working distance). Specifically, Fig. 2.1 shows the generation of a square-shaped beam with uniform-intensity distribution.

The DOEs are phase-only elements whose phase distributions can be determined by either analytical [114, 115], hybrid [117], or numerical methods [47, 165]. The analytical methods have been realized by the holographic conversion [114], ray-tracing and geometric transformation [115, 116], whereas, the hybrid methods involve analytical solution as a start step in the iterative process [117]. Beam shaping has also been obtained with a conformal approach based on 1D symmetrical solutions [175, 176]. This method relies on a Fourier transform relation between the input and output beam functions. Several numerical methods based on iterative algorithms are also proposed for designing DOEs. These include Gerchberg-Saxton (GS) algorithm [118] and its modified versions [149], the Yang-Gu algorithm [120], the simulated annealing algorithm [122], and the genetic algorithm [121]. Many of these algorithms suffer from various limitations, such as (i) presence of speckle noise or intensity fluctuations in shaped output beam, which leads to poor beam quality, (ii) irregular phase distribution of DOE, which leads to fabrication difficulties, and (iii) strong dependence on initial conditions of algorithm results in convergence difficulties. However, considerable efforts have been made to improve the quality of generated shaped output beam [47, 123, 165, 166]. Recently, new methods based on deep learning have also been proposed to overcome issues related to traditional time-consuming iterative methods for designing non-trivial optical elements [177, 178].

We determine the phase distribution of DOEs by using a modified Grechberg-Saxton algorithm, which is an iterative algorithm for determining the phase of a pair of field distributions that are related by the Fresnel propagation, and involves a spatial Fourier filtering mechanism to ensure a smooth and accurate phase distribution [47, 165]. In our method (Fig. 2.2), the incorporation of spatial Fourier filtering is inspired by an experimental approach, where a variable intracavity Fourier aperture helps to control the number of spatial modes [179]. By varying the size of Fourier aperture introduces losses
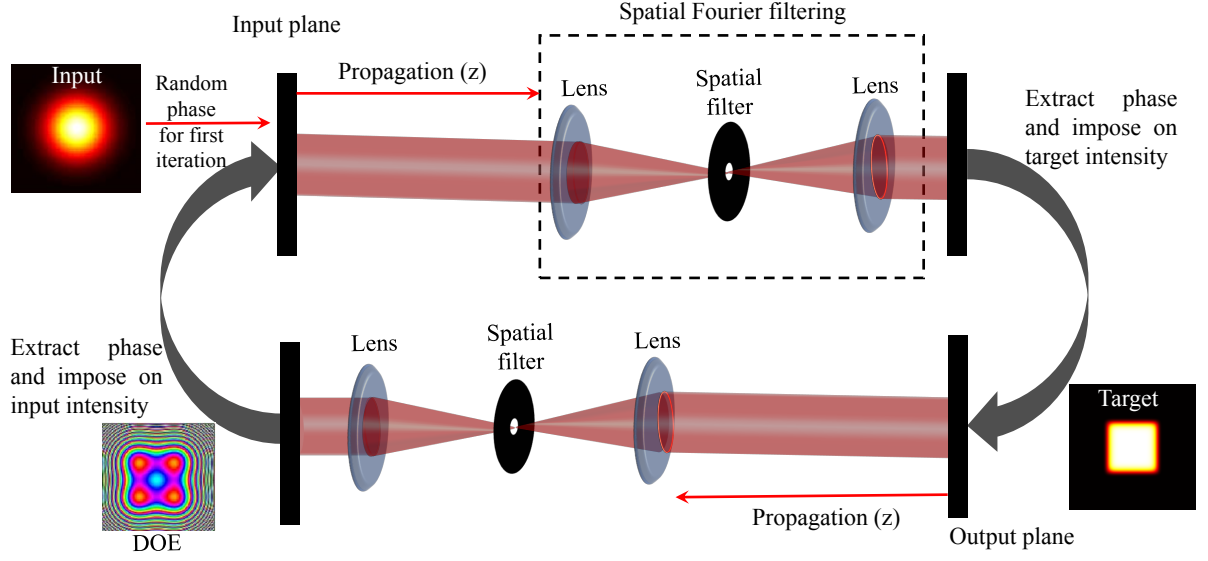
Figure 2.2: Modified GS algorithm for obtaining the phase distribution of DOEs, which are used for generating uniform-intensity beams with customized spatial shapes.

to some of the modes, and thus these modes stop lasing in the cavity. Similarly, in our approach, spatial Fourier filtering with variable aperture eliminates the undesired phase distributions and enables to find the correct phase distribution that can transform an input field distribution into a desired output field distribution. Particularly, only those phase distributions can pass through the spatial filter that satisfies the input and output field distributions. The process involved in our method is similar to that in phase retrieval [139]. Further, spatial Fourier filtering also ensures a smooth phase distribution of DOE, which makes it technically suitable for fabrication.

Particularly, in our method we start with a known Gaussian field distribution having an initial random phase distribution at the input $z = 0$, and then propagate it to the output plane at distance z by the Fourier transform and spatial Fourier filtering (shown in Fig. 2.2). The propagation of beams at a distance z in free space can be realized using either Fresnel propagation or based on Fourier transform taking into account the diverging wavefront [180, 181]. Since we have used spatial Fourier filtering, thus propagated beam based on the Fourier transform method. After that we obtain new amplitude and phase distributions. We replace this new amplitude distribution with the amplitude of the desired output field and keep the new phase distribution. The resultant field distribution

is propagated back to z=0 by Fourier transform and spatial Fourier filtering. We repeat this process iteratively such that a correct phase distribution is obtained at z=0, which can convert an input Gaussian beam into a desired output beam at the working distance z. As opposed to the Gerchberg-Saxton algorithm, where the conversion is highly sensitive to the initial choice of phase distributions, our method does not depend on the initial conditions [165].

2.3 Uniform-intensity beams with customized spatial shapes

We have generated different customized spatial shape beams with uniform-intensity distribution by means of different DOEs. The field distribution of a uniform-intensity square shaped beam can be given as

$$E_T(x,y) = E_0 \ \exp\left(-\frac{x^n + y^n}{\sigma_0^n}\right), \tag{2.1}$$

where σ is the beam waist, n is the order that describes the steepness of edges of $E_T(x,y)$, and E_0 is the maximum field amplitude. The results for generating a square shaped output beam are shown in Fig. 2.1. The results are obtained with the parameter values of input/output beam waist $\sigma_0 = 2$ mm, working distance $z = 75$ cm, order $n = 14$, and wavelength $\lambda = 1.064$ μm. As evident, the generated square shaped output beam shows good qualitative agreement with an ideal beam (Eq. (2.1)). We have quantified the quality of generated output beam by calculating RMSE (Eq. (1.25)). We have found the RMSE value of 0.0076 (0.76%) for the square shaped output beam, which indicates a high-quality generation.

The quality of the shaped output beam also depends on the working distance z for which DOE is designed. For the very small and large values of z, the phase distribution of DOE does not result a high-quality conversion [47]. Therefore, it is required to select an optimal working distance in a proper range that can maintain the generation of

shaped output beam with high-quality. The optimal working distance depends on several parameters, for example, wavelength, input beam size, and output beam size [47, 165]. By changing the input beam waist or output beam waist, it is also possible to change the optimal working distance.

Further, we have generated uniform-intensity beams with various customized spatial shapes such as annular, hollow square, rectangle, and plus. The results are shown in Fig. 2.3.
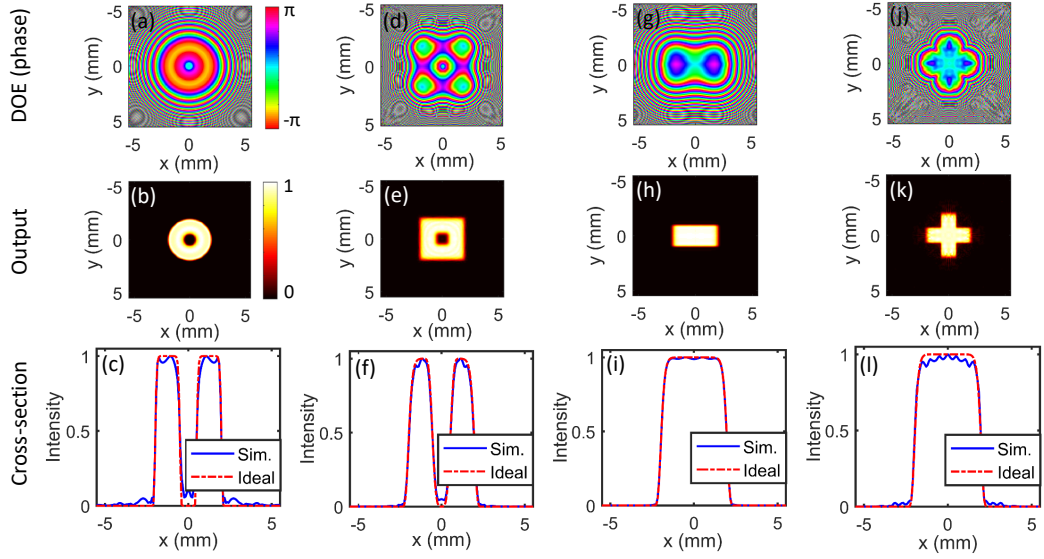
Figure 2.3: The phase distributions of DOEs for annular, hollow square, rectangle, and plus spatial shapes (top row). The corresponding intensity distributions of generated output beams with different spatial shapes (middle row). The corresponding intensity cross-sections of the generated output beams (blue curves) together with the intensity cross-sections of ideal beams (dot-dashed red curves) (bottom row).

The field distribution of a uniform-intensity annular shaped beam can be written as [11]

$$E_T(x,y) = E_0 \ \exp\left(-\frac{\left(\sqrt{x^2+y^2}-r_0\right)^n}{\sigma_0^n}\right),$$ (2.2)

where r_0 is width of annular region, E_0 is maximum amplitude, and σ_0 is the radius of inner ring. The results for the uniform-intensity annular shaped beam are shown in Figs. 2.3(a)-2.3(c). Figure 2.3(a) shows the phase distribution of DOE. The corresponding generated annular shaped output beam is shown in Fig. 2.3(b). Figure 2.3(c) shows the

intensity cross-sections of generated annular shaped beam and ideal beam (Eq. (2.2)), which shows a reasonably good qualitative agreement. The results are obtained with the parameter values of $n = 14$, $\sigma_0 = 0.75$ mm, $r_0 = 1.25$ mm, $z = 70$ cm, and $\lambda = 1.064$ μm. We have found the RMSE value of 7.95%, indicating a good quality of annular shaped output beam.

Next, we have formed a uniform-intensity hollow-square shaped beam, whose field distribution is given as

$$E_T(x, y) = E_0 \, \exp\left(-\frac{x^{n_1} + y^{n_1}}{\sigma_{01}^{n_1}}\right) - E_0 \, \exp\left(-\frac{x^{n_2} + y^{n_2}}{\sigma_{02}^{n_2}}\right). \tag{2.3}$$

The results for the hollow-square shaped beam are shown in Figs. 2.3(d)-2.3(f). The simulations are performed with the parameters $n_1 = 14$, $n_2 = 4$, $\sigma_{01} = 2$ mm, and $\sigma_{02} = 0.6$ mm, $z = 40$ cm, and $\lambda = 1.064$ μm. Figure 2.3(d) shows the phase distribution of DOE. The corresponding generated hollow-square shaped beam is shown in Fig. 2.3(e). Figure 2.3(f) shows the intensity cross-sections of generated hollow-square shaped beam and ideal beam (Eq. (2.3)), which shows a reasonably good qualitative agreement. The RMSE value is found to be 8.55%.

Further, we have generated a uniform-intensity rectangular shaped beam for which the field distribution is given as

$$E_T(x, y) = E_0 \, \exp\left(-\frac{x^n}{\sigma_{01}^n} - \frac{y^n}{\sigma_{02}^n}\right). \tag{2.4}$$

The simulated results with the parameters $n = 14$, $\sigma_{01} = 2$ mm, $\sigma_{02} = 1$ mm, and $z = 79$ cm, are shown in Figs. 2.3(g)-2.3(i). Figure 2.3(g) shows the phase distribution of DOE. The corresponding generated rectangular shaped beam is shown in Fig. 2.3(h). Figure 2.3(i) shows the intensity cross-sections of generated rectangular shaped beam and ideal beam (Eq. (2.4)), which shows a reasonably good qualitative agreement. The RMSE value is found to be 3.83%.

Finally, we have generated a uniform-intensity plus shaped beam for which the field

distribution is written as

$$E_T(x,y) = E_0 \exp\left(-\frac{x^n}{\sigma_{01}^n} - \frac{y^n}{\sigma_{02}^n}\right) + E_0 \exp\left(-\frac{x^n}{\sigma_{02}^n} - \frac{y^n}{\sigma_{01}^n}\right)$$
$$- E_0 \exp\left(-\frac{x^n + y^n}{\sigma_{02}^n}\right). \tag{2.5}$$

The simulated results with the parameters $n = 14$, $\sigma_{01} = 2$ mm, $\sigma_{02} = 0.7$ mm, and $z = 41$ cm, are shown in Figs. 2.3(j)-2.3(l). Figure 2.3(j) shows the phase distribution of DOE. The corresponding generated rectangular shaped beam is shown in Fig. 2.3(k). Figure 2.3(l) shows the intensity cross-sections of generated plus shaped beam and ideal beam (Eq. (2.5)), which shows a reasonably good qualitative agreement. The RMSE value is found to be 13.88%.

For generalization of our method, we have also examined the Fermi-Dirac, Flattened-Gaussian, and Super-Lorentzian beams [63, 182]. The results are shown in Fig. 2.4. As
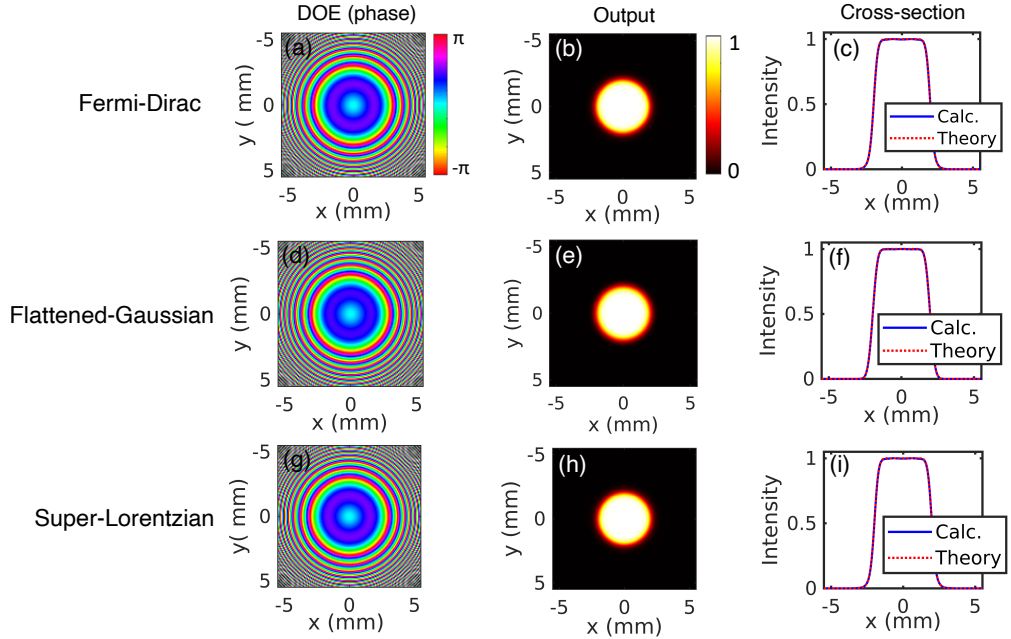
Figure 2.4: Simulated results for the Fermi-Dirac, Flattened-Gaussian, and Super-Lorentzian beams. First column: DOE phase distribution. Second column: Shaped output beam. Third column: Intensity cross-sections of calculated and theoretical output beams. The input/output beam waist $\sigma_0 = 2$ mm, flat-top index $n = 14$ and working distance z=75 cm.

evident, our method results in a very high-quality conversion from Gaussian input beam into Fermi-Dirac, Flattened-Gaussian, and Super-Lorentzian shaped output beams, for which RMSE is found to be $\sim 0.5\%$. Although, these beams have different mathematical expressions, but for the same parameters (degree of flatness and beam waist) all these beams behave in a similar fashion [182], and thus the results appear to be the same.

2.4 Robustness analysis

In generation of structured light by means of DOE, the process of finding the phase distribution of DOE involves the well defined parameters of input and output beams. For example, to convert an input Gaussian beam into a square shaped output beam, the design of DOE requires specific parameters, such as input and output beam size (waist), and wavelength. Now, when a DOE designed with specific parameters, is illuminated with an input beam which has either different waist, or wavelength, or includes misalignment, speckles, and higher order transverse modes, the quality of shaped output beam becomes deteriorated. So, we have performed a detailed analysis on the quality of shaped output beams when various types of imperfections are introduced in an input beam. Such analysis is important for the general applications of structured light in various fields. Note, the robustness analysis is performed with square shaped output beam. A similar analysis is also valid for other types of shaped output beams.

2.4.1 Effect of input beam size

Here, we have analyzed the quality of square shaped output beam against the imperfections introduced in the size of an input Gaussian beam. Specifically, we design a DOE for an input Gaussian beam of waist $\sigma_0 = 2$ mm and then illuminate it with an input Gaussian beam whose waist is varied from $\sigma_0' = 1$ mm to $\sigma_0' = 3$ mm. The quality of generated square shaped output beam is analyzed by calculating RMSE using Eq. (1.25). The results are shown in Fig. 2.5. Figure 2.5(a) shows the variation of RMSE with the deviation ($\Delta\sigma = \sigma_0' - \sigma_0$) of input Gaussian beam waist with respect to σ_0. As evident,
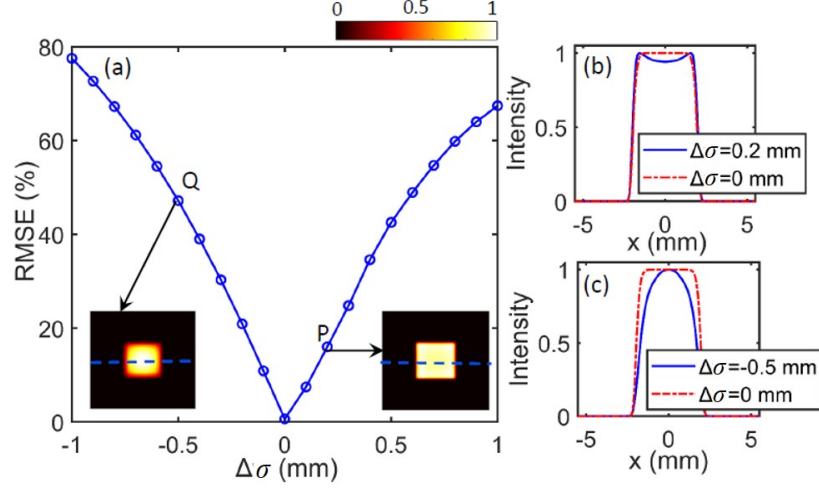
Figure 2.5: (a) The RMSE as a function of deviation in the input beam waist ($\Delta\sigma = \sigma_0' - \sigma_0$). (b) The intensity cross-sections of square shaped output beams (along dashed blue line in inset corresponding to point P) for $\Delta\sigma = 0.2$ mm (solid blue curve), and for $\Delta\sigma = 0$ mm (dot-dashed red curve). (c) The intensity cross-sections of square shaped output beams (along dashed blue line in inset corresponding to point Q) for $\Delta\sigma = -0.5$ mm (solid blue curve), and for $\Delta\sigma = 0$ mm (dot-dashed red curve). The working distance z= 75 cm, wavelength $\lambda = 1.064~\mu$m, and square shaped output beam waist = 2 mm.

the RMSE is zero for $\Delta\sigma = 0$, and increases with the increase of $|\Delta\sigma|$. The insets show the intensity distributions of generated square shaped output beams for the deviations $\Delta\sigma = 0.2$ mm and $\Delta\sigma = -0.5$ mm, corresponding to points P and Q, respectively. Figures 2.5(b) and 2.5(c) show the intensity cross-sections of the insets (along dashed blue line) corresponding to points P and Q (solid blue curve), together with intensity cross-section of square shaped output beam for $\Delta\sigma = 0$ (dot-dashed red curve). Specifically, for $\Delta\sigma = 0.2$ mm, the RMSE is found to be 16% (Fig. 2.5(b)), whereas, for $\Delta\sigma = -0.5$ mm the RMSE is increased to 47% (Fig. 2.5(c)). We have found that for the deviation $|\Delta\sigma| < 0.2$ mm, the quality of generated square shaped output beam remains reasonably good.

2.4.2 Effect of misalignment

In various applications of structured light generation, misalignment may occur, which can cause distortion in the shaped output beam. So, we have investigated the effect of

misalignment of input Gaussian beam with respect to DOE. The results are presented in Fig. 2.6. Figure 2.6(a) shows the RMSE of square shaped output beam as a function of decentering offset (Δx) (Gaussian is shifted horizontally with respect to the central position of DOE). As evident, the RMSE increases with an increase in $|\Delta x|$. The RMSE increases due to the non-uniformity in the intensity distribution of square shaped output beam. Specifically, when an input Gaussian beam is decentered towards the right ($x > 0$) with respect to the center ($x = 0$) of DOE, the corresponding intensity decreases on the left side ($x < 0$) of the square shaped beam (see insets in Fig. 2.6(a)). This is due to the fact that left side ($x < 0$) of the DOE is illuminated with less intensity than the right side ($x > 0$) of DOE.
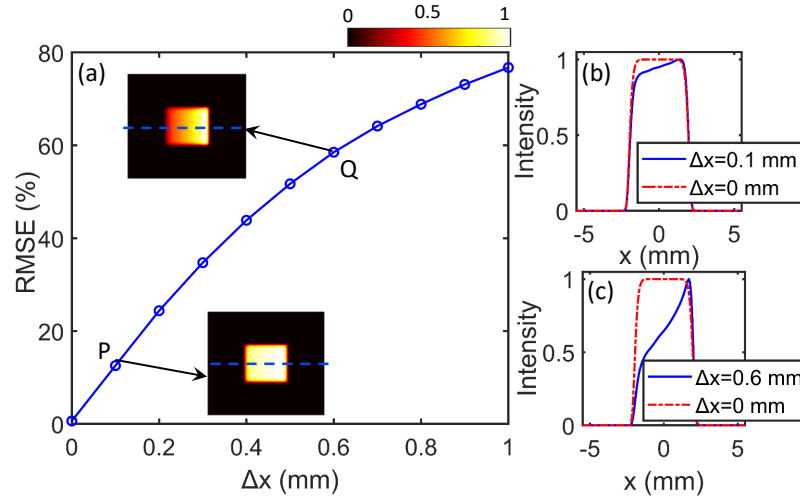
Figure 2.6: (a) The RMSE as a function of decentering offset (Δx). The insets show square shaped output beams corresponding to different offset values of $\Delta x = 0.1$ mm and $\Delta x = 0.6$ mm. (b) The intensity cross-sections of square shaped output beams (along dashed blue line in inset corresponding to point P) for $\Delta x = 0.1$ mm (solid blue curve), and for $\Delta x = 0$ (dot-dashed red curve). (c) The intensity cross-sections of square shaped output beams (along dashed blue line in inset corresponding to point Q) for $\Delta x = 0.6$ mm (solid blue curve), and for $\Delta x = 0$ (dot-dashed red curve). The working distance z=75 cm, wavelength $\lambda = 1.064$ μm, and input/output beam waist = 2 mm.

The insets show the intensity distributions of generated square shaped output beams for the decentring offsets $\Delta x = 0.1$ mm and $\Delta x = 0.6$ mm, corresponding to points P and Q, respectively. Figures 2.6(b) and 2.6(c) show the intensity cross-sections of the insets (along dashed blue line) corresponding to points P and Q (solid blue curve), together

with the intensity cross-section of square shaped output beam for $\Delta x = 0$ (dot-dashed red curve). Specifically, for $\Delta x = 0.1$ mm, the RMSE is found to be $\sim 10\%$ (Fig. 2.6(b)), whereas, for $\Delta x = 0.6$ mm the RMSE is increased to $\sim 60\%$ (Fig. 2.6(c)). We have found that for the offset $|\Delta x| < 0.1$ mm, the generated square shaped output beam consists of $> 90\%$ uniformity, and thus quality remains reasonably good.

2.4.3 Effect of asymmetry in the input beam

In many cases, the laser's output profile is not circularly symmetric. When such a non-circular (asymmetric) laser beam is used to illuminate DOE, the quality of shaped output beam can be significantly impacted. Thus, we have investigated the effect of asymmetry in an input Gaussian beam on the quality of shaped output beam. The asymmetry in an input beam is introduced by increasing the beam waist in the horizontal direction (σ_{0x}), whereas it remains the same in a vertical direction (σ_{0y}). The asymmetry is measured as $\Delta r = \sigma_{0x}/\sigma_{0y}$. The results are shown in Fig. 2.7.
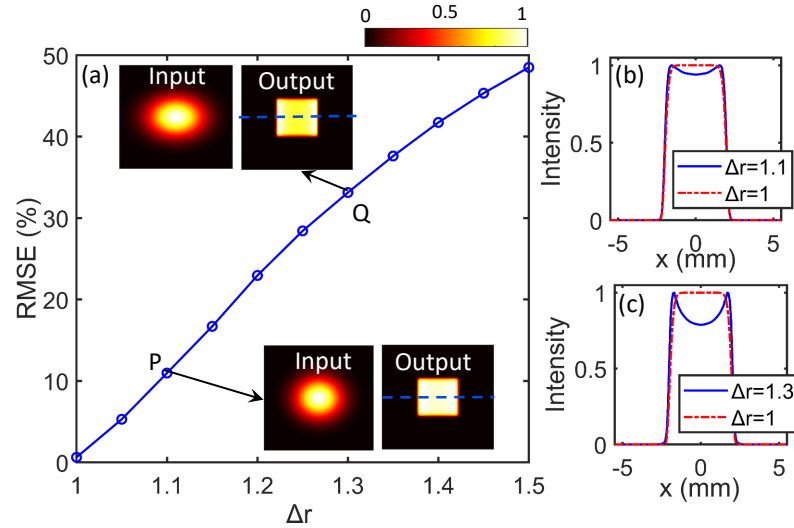
Figure 2.7: (a) The RMSE as a function of asymmetry Δr in an input Gaussian beam. (b) The intensity cross-sections of square shaped output beams (along dashed blue line in inset corresponding to point P) for $\Delta r = 1.1$ (solid blue curve), and for $\Delta r = 1$ (dot-dashed red curve). (c) The intensity cross-sections of square shaped output beams (along dashed blue line in inset corresponding to point Q) for $\Delta r = 1.3$ (solid blue curve), and for $\Delta r = 1$ (dot-dashed red curve). The working distance z = 75 cm, $\lambda = 1.064$ μm, and output beam waist = 2 mm.

Figure 2.7(a) shows the RMSE in the shaped output beam as a function of asymmetry Δr in an input Gaussian beam. As evident, RMSE increases with the increase of asymmetry Δr. The insets show the intensity distributions of input Gaussian beam and generated square shaped output beams for $\Delta r = 1.1$ and $\Delta r = 1.3$, corresponding to points P and Q, respectively. Figures 2.7(b) and 2.7(c) show the intensity cross-sections of square shaped output beams (along dashed blue line of insets) corresponding to points P and Q (solid blue curve), together with the intensity cross-section of square shaped output beam for $\Delta r = 1$ (dot-dashed red curve). Specifically, for $\Delta r = 1.1$, the RMSE is found to be $\sim 10\%$ (Fig. 2.7(b)), whereas, for $\Delta r = 1.3$, the RMSE is increased to $\sim 34\%$ (Fig. 2.7(c)). We have found that for asymmetry $\Delta r < 1.1$, the quality of generated square shaped output beam remains reasonably good.

Next, we have considered asymmetric input Gaussian beam (beam waist 3 mm along y-axis and 2 mm along x-axis) with different orientations in a transverse plane. The
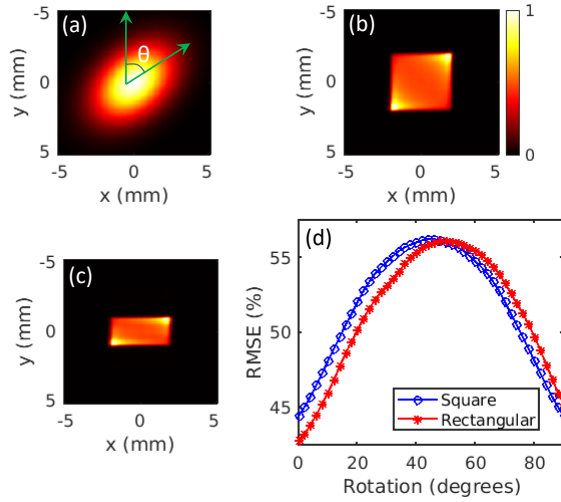
Figure 2.8: (a) Asymmetric input Gaussian beam rotated by an angle θ with respect to vertical y-axis. (b) The square shaped output beam when asymmetric input beam rotated with $\theta = 45^o$ illuminates DOE. (C) The rectangular shaped output beam when asymmetric input beam rotated with $\theta = 45^o$ illuminates DOE. (d) The RMSE of square (blue line with squares) and rectangular (red line with stars) shaped output beams as a function of rotation angle θ of asymmetric input Gaussian beam

asymmetric input Gaussian beam consists of 38% RMSE (with respect to an ideal symmetric Gaussian with a beam waist of 2 mm), which remains unchanged with rotation.

The results are shown in Fig. 2.8. Fig. 2.8(a) shows an asymmetric input Gaussian beam rotated with an angle of $\theta = 45^o$ with respect to y-axis. Figures 2.8(b) and 2.8(c) show the square and rectangular shaped output beams when an asymmetric input Gaussian beam (Fig. 2.8(a)) incidents on DOEs. As evidenced, the rotation of asymmetric input Gaussian beam leads to the reduction of uniformity in the intensity distributions of square and rectangular shaped output beams. A more generalized study for several rotation angles is presented in Fig. 2.8(d), which indicates that RMSE curves for both square and rectangular shaped beams are not the same.

2.4.4 Effect of speckle noise in an input beam

The speckle noise is one of the major factors to affect the quality of shaped output beam. Several efforts have been made to reduce the speckle noise in the shaped output beam generated by means of different approaches [149, 165, 183]. Here, we explore how the speckle noise (ζ) in an input Gaussian beam that illuminates the DOE (designed with specific parameters), affects the quality of shaped output beam. This is an important issue, as the input Gaussian beam from many laser sources consists of intensity fluctuations (speckles). ζ refers to the root mean square error in input laser beam with respect to ideal Gaussian beam, due to the presence of random intensity fluctuations. The simulated results are shown in Fig. 2.9.

Figure 2.9(a) shows the RMSE as a function of speckle noise (ζ) in an input Gaussian beam. As evident, the RMSE increases with the increase of ζ. The insets show the intensity distributions of input Gaussian beam and generated square shaped output beam for $\zeta = 18\%$ and $\zeta = 52\%$, corresponding to points P and Q, respectively. Figures 2.9(b) and 2.9(c) show the intensity cross-sections of square shaped output beams (along dashed blue line in insets) corresponding to points P and Q (solid blue curve), together with the intensity cross-section of square shaped output beam for $\zeta = 0\%$ (dot-dashed red curve). Specifically, for $\zeta = 18\%$, the RMSE is found to be $\sim 10\%$ (Fig. 2.9(b)), whereas, for $\zeta = 52\%$, the RMSE is increased to $\sim 34\%$ (Fig. 2.9(c)). We have found that for the

speckle noise $\zeta < 20\%$, the quality of generated square shaped output beam remains very good.
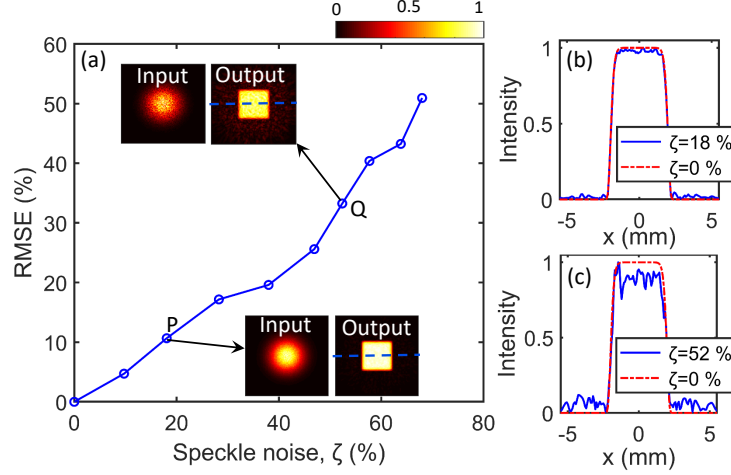
Figure 2.9: (a) The RMSE as a function of the speckle noise (ζ) present in the input Gaussian beam. (b) The intensity cross-sections of square shaped output beams (along dashed blue line in inset corresponding to point P) for $\zeta = 18\%$ (solid blue curve), and for $\zeta = 0\%$ (dot-dashed red curve). (c) The intensity cross-sections of square shaped output beams (along dashed blue line in inset corresponding to point Q) for $\zeta = 52\%$ (solid blue curve), and for $\zeta = 0\%$ (dot-dashed red curve). The working distance z=75 cm, $\lambda = 1.064$ μm, and input/output beam waist = 2 mm.

Furthermore, we have also demonstrated that the quality of shaped output beam can be further improved by using an additional external spatial filter. Above, we have shown that controlling speckle noise in an input Gaussian beam allows to reduce the speckles in the square shaped output beam. However, for a large amount of speckles in an input Gaussian beam (e.g., $\zeta > 20\%$), the square shaped output beam consists of significant amount of speckles, thus quality remains poor. So, we have found that for such cases the quality of square shaped output beam can be further improved by passing it through an additional external spatial filter. Spatial filtering has also been emphasized in other works, for example, in beam shaping [165], manipulating spatial coherence [179], and object reconstruction [139]. The schematic and representative results are shown in Fig. 2.10. Figure 2.10(a) shows a spatial filtering mechanism that involves two plano-convex lenses (focal length f) in a telescope configuration, and a spatial filter (pinhole) at the Fourier plane in between the two lenses. The first lens performs a Fourier transform of the

speckled beam (Fig. 2.10(b)) and converts it into a spatial frequency domain ($F_x = x/\lambda f$, $F_y = y/\lambda f$), where the speckle noise in the form of high-frequency components is filtered out by the pinhole, and then second lens performs an inverse Fourier transform to convert it again in the real domain (x, y), and accordingly improves the quality of the (Fig. 2.10(c)).
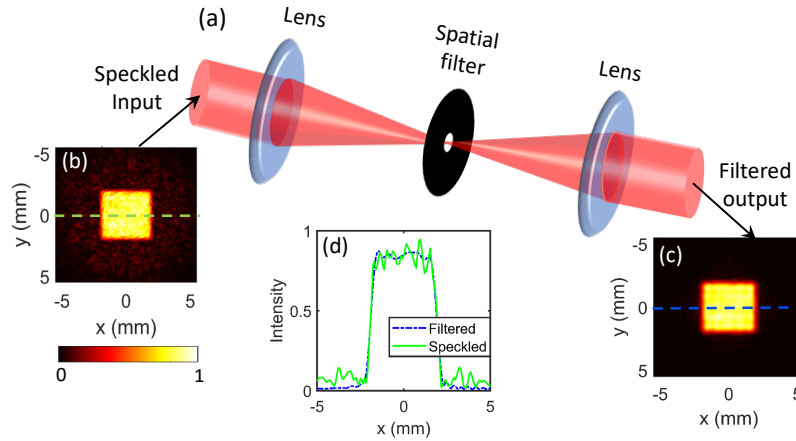
Figure 2.10: (a) Schematic and working principle of a spatial filter. (b) The intensity distribution of square shaped beam with speckled noise. (c) The intensity distribution of square shaped beam after spatial filtering. (d) The intensity cross-sections of square shaped beams (along dashed lines in (b) and (c)) before and after spatial filtering. Note, the filtered intensity plots are not normalized.

Figure 2.10(b) shows the intensity distribution of a square shaped output beam gener-ated by means of a DOE (as discussed above), and served as speckled input for the spatial filter. It consists of a significant amount of speckle noise, which has the RMSE value of 34.6%. Figure 2.10(c) shows the square shaped output beam after spatial filtering (filtered output), where the RMSE is reduced to 14.7%. The corresponding intensity cross-sections of the square shaped output beam before spatial filtering (green solid curve) and after spatial filtering (dot-dashed blue curve) are shown in Fig. 2.10(d). As evident, the quality of square shaped output beam has improved significantly by the spatial filtering.

We have also performed filtering of speckle noise by considering an example of a Fermi-Dirac beam, the results are shown in Fig. 2.11. We have passed the speckled Fermi-Dirac beam (Fig. 2.11(a)) with RMSE value of 42% through the circular (Fig. 2.11 (b)) and Airy (Fig. 2.11(c)) spatial filters. Airy filter, obtained by the Fourier transform of a
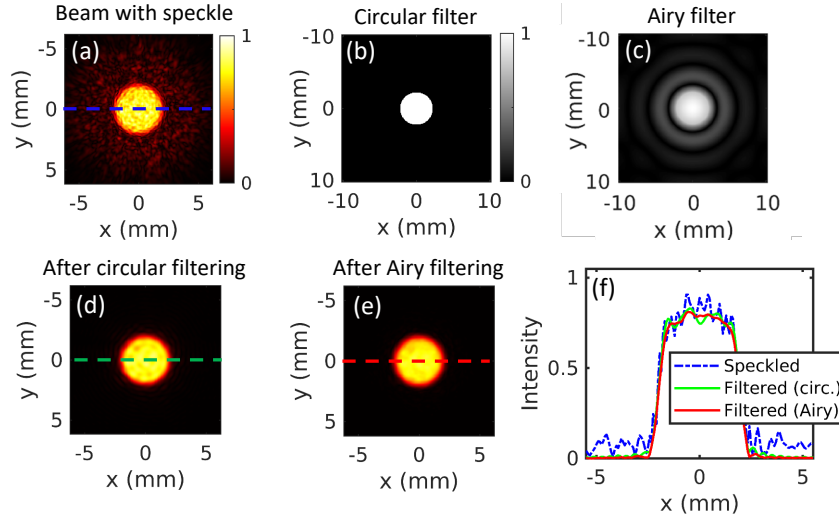
Figure 2.11: Filtering of speckle noise from a Fermi-Dirac beam. (a) The intensity distribution of a Fermi-Dirac beam with speckle noise. (b) Circular filter. (c) Airy filter (Fourier transform of Fermi-Dirac beam). (d) Intensity distribution of Fermi-Dirac beam after circular filtering (e) Intensity distribution of Fermi-Dirac beam after Airy filtering. (f) The intensity cross-sections of Fermi-Dirac beams (along dashed lines in (a), (d) and (e)) before and after spatial filtering.

Fermi-Dirac beam, has a central lobe waist 2.8 mm (calculated by $1/e^2$ method), and the circular filter has a radius 2.2 mm. After filtering we obtained Fermi-Dirac beams with RMSE of 19% (with Airy filter, Fig. 2.11(d)) and 22% (with circular filter, Fig. 2.11(e)). The corresponding intensity cross-sections of Fermi-Dirac beams before and after filtering are shown in Fig. 2.11(f). As evident, the quality of filtered beams has improved in both cases. However, the RMSE of filtered beams is not reduced to zero, indicating that speckle noise is not completely constrained by the filters.

2.4.5 Spectral effect

The quality and stability of formed patterns under illumination of DOEs with different wavelengths are important in various applications, particularly, based on the use of structured pulsed beams [90, 184]. It has been shown that DOE microrelief is optimal for monochromatic radiation. Particularly, spectral dispersion accompanying short laser pulses lead to a loss in the quality of the formed spatial distribution [185]. However, it was shown that phase DOEs match with laser radiation modes and are quite resistant

to chromatic dispersion [186]. Further, it has been shown that energy losses occur when specific DOEs are illuminated with different wavelengths, which causes the decrease in diffraction efficiency of generated shaped output beams [187].
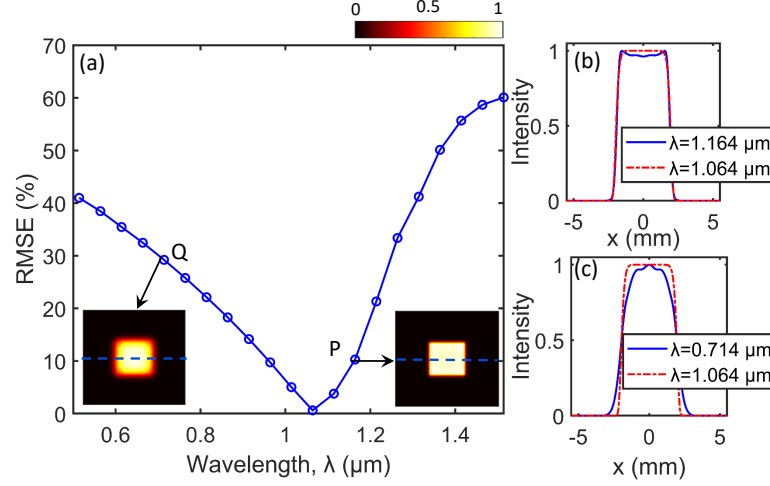
Figure 2.12: (a) The RMSE as a function of wavelength of an input Gaussian beam. (b) The intensity cross-sections of square shaped output beams (along dashed blue line in inset corresponding to point P) for $\lambda = 1.164\,\mu$m (solid blue curves), and for $\lambda = 1.064\,\mu$m (dot-dashed red curve). (c) The intensity cross-sections of square shaped output beams (along dashed blue line in inset corresponding to point Q) for $\lambda = 0.714\,\mu$m (solid blue curves), and for $\lambda = 1.064\,\mu$m (dot-dashed red curve).

As discussed above, the generation of structured light by means of DOEs involves well-defined parameters of input and output beams. Specifically, when a DOE designed for a specific wavelength, is illuminated with an input beam of different wavelengths, the quality of shaped output beam becomes deteriorated [165, 173, 174]. First, we design a DOE (for converting an input Gaussian into a square shaped output beam) for the specific parameters of input/output beam waist $\sigma_0 = 2$ mm, wavelength $\lambda = 1.064\ \mu$m, and working distance $z = 75$ cm. After that, we illuminate DOE with an input Gaussian beam whose wavelength is varied from $\lambda = 0.5\ \mu$m to $\lambda = 1.5\ \mu$m, and then analyzed the quality (RMSE) of generated square shaped output beam at a working distance z=75 cm. The results are shown in Fig. 2.12. Figure 2.12(a) shows the RMSE as a function of wavelength λ, which indicates that RMSE increases for wavelengths $\lambda \neq 1.064\ \mu$m (design wavelength). The insets show the intensity distributions of square shaped output beams

for $\lambda = 0.714$ μm and $\lambda = 1.164$ μm, corresponding to points P and Q, respectively. Figures 2.12(b) and 2.12(c) show the intensity cross-sections of square shaped output beam (along dashed blue lines of insets) corresponding to points P and Q, together with the intensity cross-section of square shaped output beam for $\lambda = 1.064$ μm (dot-dashed red curve). Specifically, for $\lambda = 1.164$ μm, the RMSE is found to be $\sim 10\%$ (Fig. 2.12(b)), whereas, for $\lambda = 0.714$ μm, the RMSE is increased to $\sim 30\%$ (Fig. 2.12(c)). We have found that for RMSE of $< 10\%$, the quality of generated square shaped output beam remains reasonably good.

The distortion in the shaped output beam by varying the wavelength of an input Gaussian beam can also be understood by the effect of diffraction. When an input Gaussian beam incidents on DOE at z= 0, after a propagation distance z the desired shaped output beam is created as a result of redistribution of light intensity. The diffraction occurs as a result of beam propagation, which depends on the wavelength of a beam. Due to diffraction, the beam diverges, resulting in distortions as it propagates. For a Gaussian beam, the beam divergence can be approximated as $\phi \approx \lambda/\pi\sigma$, σ is the beam waist. The beam with a small wavelength diverges less as compared to a large wavelength. Specifically, an increase in wavelength will cause more divergence of a beam, so the desired shaped output beam should be formed at smaller distances. Thus, when a specific DOE, designed for a particular wavelength and working distance z, is illuminated with other wavelengths then it leads to distortion in the desired shaped output beam at working distance z (as shown in Fig. 2.12).

Furthermore, for various applications in different spectral (wavelength) regimes, it is required to obtain the high-quality beam shaping over a broad range of wavelengths. In our earlier study, we obtained high-quality beam shaping over a broad spectral range by using different DOEs for the different wavelengths [165]. However, in few studies wavelength tunable beam shaping has been shown to obtain in a narrow range of wavelengths by means of only a single DOE [174]. It was shown that in a conformal approach for the same $\beta \propto 2\pi/\lambda f$, the beam shaping remains unchanged, as wavelength λ can be traded for focal length f of a Fourier transforming lens [175, 176]. To the best of our knowledge,

so far no studies have reported where only a single DOE can perform high-quality beam shaping over a broad range of wavelengths. Here, we demonstrate that a single DOE can generate a high-quality shaped output beam over a broad range of wavelengths.
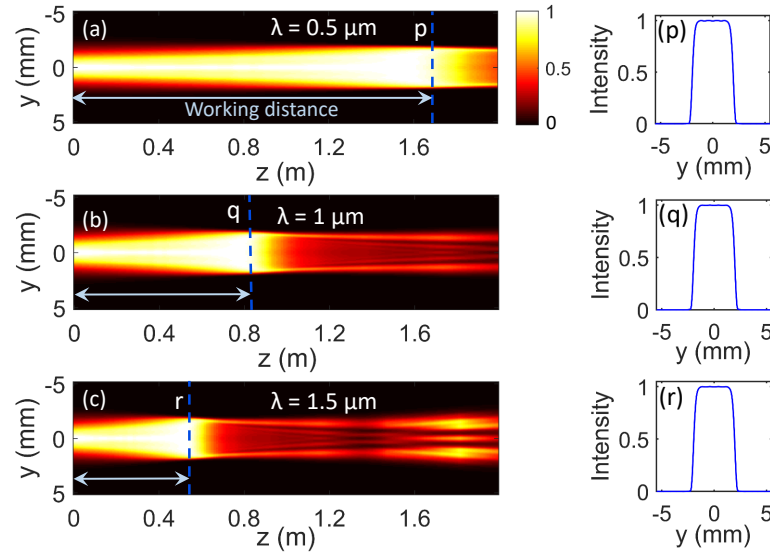
Figure 2.13: (a-c) The conversion of an input Gaussian beam into square shaped output beam for different wavelengths $\lambda = 0.5$ μm, $\lambda = 1.0$ μm, and $\lambda = 1.5$ μm. (p-r) Intensity cross-sections (along dashed blue line) corresponding to points p, q, and r.

Above, we have analyzed the quality of generated square shaped output beam at a fixed working distance z = 75 cm for a broad range of wavelengths. Further, we have illuminated a DOE (designed for specific parameters as described above) by an input Gaussian beam at z = 0, and after that investigated the propagation of resulting beam for distance z > 0. Due to wavelength dependence of diffraction of beam, the desired shaped output beam can occur at different working distances z, when the wavelength is varied. Specifically, an increase in wavelength will cause more divergence of beam, so the desired shaped output beam will be formed at smaller distances. The results for different wavelengths are shown in Fig. 2.13. As evident, for different wavelengths, the high-quality square shaped output beam occurs at different propagation distances z (indicated by dashed blue line). Specifically, for wavelength $\lambda = 0.5$ μm, the high-quality square shaped output beam is found at propagation distance z = 1.65 m (working distance) (Fig. 2.13(a)). For $\lambda = 1.0$ μm and $\lambda = 1.5$ μm, the working distances are 0.8 m and 0.5 m, respectively

(Figs. 2.13(b) and 2.13(c)). Specifically, the working distance decreases with an increase in wavelength. Figures. 2.13(p), 2.13(q), 2.13(r) show the intensity cross-sections (along dashed blue line) corresponding to points p, q, and r in Figs. 2.13(a), 2.13(b), and 2.13(c), respectively.

A more general study on the variation of working distance as a function of wavelength is shown in Fig. 2.14. As evident, the working distance decreases with an increase in wavelength. This analysis confirms that a single DOE can be used for high-quality generation of structured light over a broad range of wavelengths.
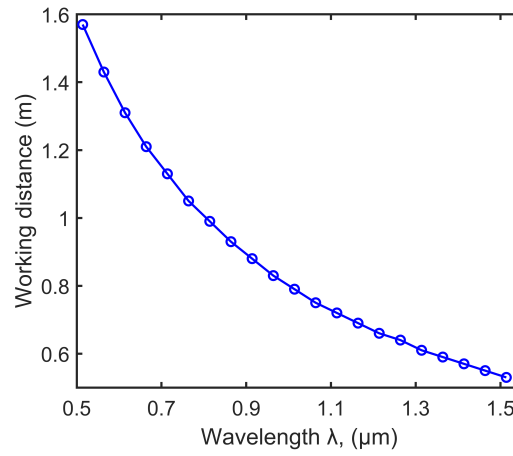
Figure 2.14: The variation of working distance as a function of wavelength. Input/output beam waist = 2 mm.

2.4.6 Effect of higher order modes

Generally, the output light from high-power lasers consists of higher-order transverse modes along with the fundamental mode (TEM_{00}). Thus, the intensity distribution of such laser beams strongly deviates from the Gaussian distribution of pure TEM_{00} mode. Since the diffraction properties of these laser beams strongly differ from a pure TEM_{00}, so it can influence the quality of shaped output beam. We have investigated how the presence of higher-order modes in an input Gaussian beam that illuminates the DOE (designed with specific parameters as given for Fig. 2.1), affects the quality of shaped output beam. The presence of high-order modes in an input beam can be determined by a beam quality

parameter ϵ (RMSE). We have generated such input beams by incoherent superposition of several Laguerre-Gauss modes ($u_{pl}(r,\theta)$) with different fractional amplitudes (weights) in each mode ($|c_{pl}|$) [147, 188].

$$I(r) = \sum_{p,l} |c_{pl}|^2 |u_{pl}(r,\theta)|^2, \qquad (2.6)$$

where r and θ denote the radius and azimuthal angle. The l and p represent the azimuthal mode index and radial index. The resultant multimode beam intensity given by Eq. (2.6) is normalized such that the total intensity $\sum_{p,l} |c_{pl}|^2 = 1$. The ϵ of a pure TEM$_{00}$ (Gaussian distribution) mode is zero. The intensity distributions of beams with different values of ϵ are shown in Fig. 2.15.
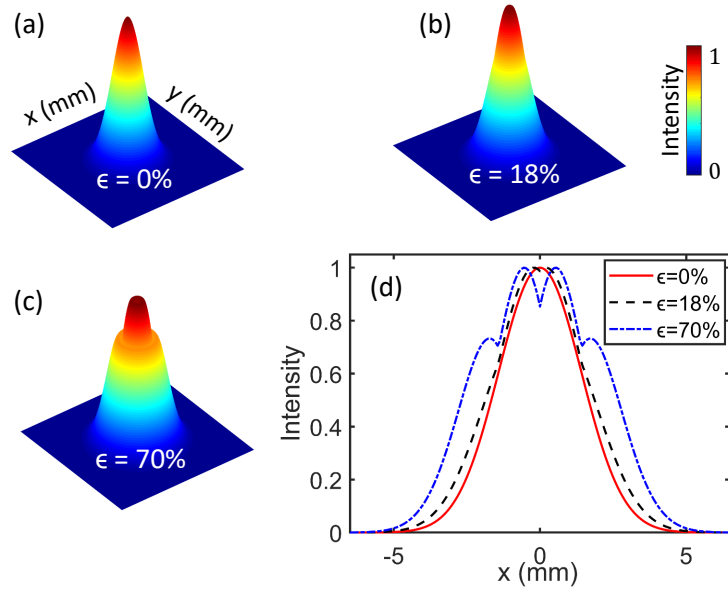
Figure 2.15: (a-c) The intensity distributions of beams with RMSE of input beam $\epsilon = 0\%$, 18% and 70%. (d) Corresponding intensity cross-sections for $\epsilon = 0\%$ (solid red curve), $\epsilon = 18\%$ (dashed black curve), and $\epsilon = 70\%$ (dot-dashed blue curve).

Figure 2.15(a) shows the intensity distribution of a fundamental mode LG$_{00}$ (TEM$_{00}$) with $\epsilon = 0\%$. Figure. 2.15(b) shows the intensity distribution of a beam with $\epsilon = 18\%$ that includes the superposition of 0.80 (u_{00})+0.10 (u_{01})+0.10 (u_{10}). Figure. 2.15(c) represents the intensity distribution of a beam with $\epsilon = 70\%$ that includes superposition of 0.30 (u_{00})+0.35 (u_{01})+0.35 (u_{10}). We use these beams as the input beams to illuminate the

DOE (designed with specific parameters as given for Fig. 2.1) to obtain the desired square shaped output beam. The quality of generated squared shaped beam is analyzed, and results are shown in Fig. 2.16.
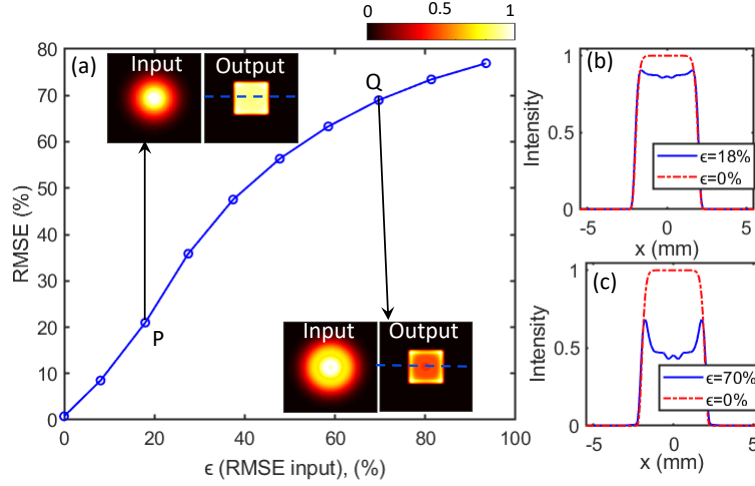
Figure 2.16: (a) The RMSE of output as a function of RMSE of input beam (ϵ). The insets show the intensity distributions of input and square shaped output beams corresponding to the points P and Q. (b) The intensity cross-sections of square shaped output beams (along dashed blue line in inset corresponding to point P) for $\epsilon = 18\%$ (solid blue curve) and $\epsilon = 0$ (dot-dashed red curve). (c) The intensity cross-sections of square shaped output beams (along dashed blue line in inset corresponding to point Q) for $\epsilon = 70\%$ (solid blue curve) and $\epsilon = 0$ (dot-dashed red curve). Note, the intensity cross-sections of shaped output beams are not normalized.

Figure 2.16(a) shows the RMSE as a function of input beam quality factor (ϵ). As evident, the RMSE increases with the increase of ϵ. The presence of higher-order LG modes broadens the input Gaussian beam, and thus we observe a caustic in the shaped output beam [175], which increases the RMSE. The insets show the intensity distributions of input beam and generated square shaped output beams for $\epsilon = 18\%$ and $\epsilon = 70\%$, corresponding to the points P and Q, respectively. Figures 2.16(b) and 2.16(c) show the intensity cross-sections of the square shaped output beams (along dashed blue line in insets) corresponding to points P and Q (solid blue curve), together with the intensity cross-section of square shaped output beam for $\epsilon = 0$ (dot-dashed red curve). Specifically, for $\epsilon = 18\%$, the RMSE is found to be $\sim 21\%$, whereas, for $\epsilon = 70\%$, the RMSE is increased to $\sim 69\%$. Here, the RMSE is mainly caused by the difference in the amplitudes as well

as non-uniformity in the output beams, as shown in Figs. 2.16(b) and 2.16(c).

We have considered another case in which higher order modes are taken as Hermite-Gaussian (HG) modes [147, 188], and performed the quality analysis of shaped output beam by increasing the percentage of higher order modes in the input beam. Specifically, we have generated input beam by an incoherent superposition of HG modes, namely HG_{00} (Gaussian), HG_{01}, and HG_{10} with different fractional amplitudes (weights) in each mode (as shown above for LG modes). The results are shown in Fig. 2.17, which evident that the RMSE of square shaped output beam increases with an increase of RMSE of the input beam (by increasing the weights of HG_{01} and HG_{10} modes).
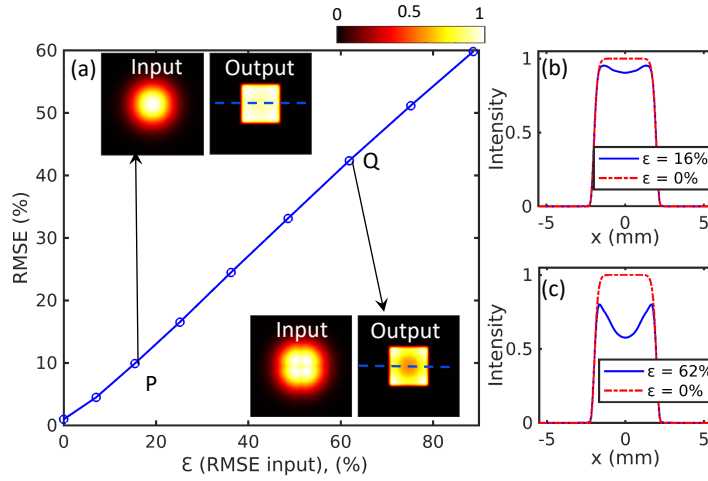
Figure 2.17: The RMSE of output as a function of RMSE of input beam, where input beam consists of superposition of HG modes. The insets show the intensity distributions of input and square shaped output beams corresponding to the points P and Q. (b) The intensity cross-sections of square shaped output beams (along dashed blue line in inset corresponding to point P) for $\epsilon = 16\%$ (solid blue curve) and $\epsilon = 0$ (dot-dashed red curve). (c) The intensity cross-sections of square shaped output beams (along dashed blue line in inset corresponding to Q) for $\epsilon = 62\%$ (solid blue curve) and $\epsilon = 0$ (dot-dashed red curve).

In Fig. 2.17, insets show the intensity distributions of input beam and generated square shaped output beams for $\epsilon = 16\%$ and $\epsilon = 62\%$, corresponding to points P and Q, respectively. The corresponding intensity cross-sections of square shaped output beams (for $\epsilon = 16\%$ and 62%) together with intensity cross-section of a square shaped output beam for $\epsilon = 0$ are shown in Figs. 2.17(b) and 2.17(c). Similar to the LG modes (Fig. 2.16),

the presence of higher-order HG modes also leads to an increase of RMSE in the square shaped output beam.

2.5   Conclusion

In this Chapter, we have investigated tailoring of light in the amplitude degree of freedom to generate uniform-intensity distribution with customized spatial shapes. Such structured light beams are non-trivial, as these are not the regular modes of a conventional laser system. We have generated these beams, based on an outer-cavity method, using diffractive optical elements (DOEs) whose phase distributions are obtained from a modified Gerchberg–Saxton algorithm that involves Fresnel propagation and spatial Fourier filtering. In particular, an input Gaussian beam from a laser illuminates the DOE, and after propagating a certain distance (working distance) transforms into a desired uniform-intensity output beam. The spatial Fourier filtering enables to obtain a relatively simple design of DOE (smooth phase distribution) and produces a high-quality uniform-intensity output beam. The simple smooth phase distribution offers the possibility of easy manufacturing of DOEs. We have simulated different DOEs and demonstrated the generation of uniform-intensity beams with several customized spatial shapes, such as square, annular, rectangular, hollow square, and plus-sign. We have characterized the quality of shaped output beams by calculating root mean square error (RMSE), and found that quality of shaped output beams is reasonably good. Further, the RMSE is found to be dependent on spatial shapes and increases with an increase in the complexity of shape. The quality of shaped output beam also depends on the working distance (z) for which DOE is designed, in particular, for very small and large values of z, the phase distribution of DOE does not result in a high-quality conversion. The optimal working distance depends on several parameters, such as wavelength, order of uniformity, input beam size, and output beam size.

Further, we have performed a detailed robustness analysis on the quality of generated shaped output beams against various imperfections in an input beam, for example,

misalignment with respect to DOE, effect of asymmetry, speckle noise, presence of higher-order modes, and mismatch of beam sizes. We have found that for imperfections $< 10\%$, the quality of shaped output beams remains reasonably good. In the case of speckle noise up to 18%, the quality of shaped output beam remains excellent. In this case, we have also shown that the quality of shaped output beam can be further improved using an additional external spatial Fourier filter of suitable transmission function. Further, we have shown that our method generates shaped output beam with excellent quality over a broad spectra range, however, the working distance z is found to be decreased with an increase in the wavelength. The results presented in this chapter are reported in Refs. [32, 33].

Chapter 3

Aberration laser beams with controlled autofocusing and self-healing

3.1   Introduction

In previous Chapter 2, we have discussed a simple and efficient outer-cavity method for tailoring an amplitude degree of freedom of light to generate uniform-intensity beams with customized spatial shapes. However, for various applications, light beams with more complex intensity distribution and exotic propagation properties are required. Such beams can be achieved by tailoring the light both in amplitude and phase degrees of freedom simultaneously. In this Chapter, we present an outer-cavity method for tailoring the amplitude and phase degrees of freedom of light to generate novel aberration laser beams (ALBs) containing multiple bright lobes in a transverse plane and possessing exotic propagation properties, such as controlled autofocusing and self-healing both in free space as well as in turbulent media.

Owing to unique intensity distribution and exotic propagation properties, ALBs have attracted considerable interest due to their widespread applications, such as in optical

81

communications, imaging and investigation of bio-medical materials and examination of small complex biological samples or tissues, ablation, trapping and guiding the micro-particles, material processing, etc. [25, 55, 56, 189, 190]. Generally, the term aberration refers to an error (distortions) in the phase distribution of light, which degrades the quality of imaging and focusing properties of a system [80]. Aberration can cause various symmetric and asymmetric adverse effects like blurring, widening, and distortion in light fields, and for the minimization of these effects, various methods have been proposed [191–193]. However, in certain cases, aberrations have been deliberately exploited for various purposes. For example, the presence of a certain type of aberrations in an optical system has been shown to increase the sharp focusing features of an imaging system [85, 194]. The aberrations have also been explored to generate diffraction free laser beams [195], identification of the order of singularity in optical vortices [196–198], and generation of zero intensity spot in a focal plane [199]. ALBs can be realized by combining angular dependence of Zernike polynomials with a r^q type approximation of chirped Airy function. Further, it has been shown that for $q > 1$, ALBs possess an abrupt autofocusing during propagation.

Further, in various applications, laser beams are required to propagate either in free space or in a random disorder media. The propagation of laser beam through a random media encounters various effects like scattering, intensity fluctuations, attenuation of beam, loss of coherence, and localization [200–202]. Although scattering is a primary phenomenon in random media, these scattering and intensity fluctuations can be controlled by introducing disorder-specific active components to the medium [203]. Atmospheric turbulence can be considered as a disordered media having random fluctuations in the refractive index and wind velocity due to uncertain variations in the temperature gradient of the medium [204]. Although, several works have been carried out to study the propagation of light through random media. However, the field is still growing to better understand the propagation of structured light in random media of different strengths [28, 205].

Recently non-diffracting optical beams, called pin-like optical beams, have been investigated, and shown that these beams exhibit autofocusing after a certain distance

and convert to Bessel beam that remains invariant upon further propagation [55, 189]. The invariant propagation characteristic was also shown in turbulent media for longer distances. Further, these invariant characteristics were also compared with abruptly autofocused beams [189]. The width of main lobe of these beams was shown to be inversely proportional to propagation distance, so a tight focusing of energy can be obtained over a long distance. Further, the linearly and circularly polarized circular Airy beams are shown to possess robust autofocusing properties against strong disturbance by large sized particles and are found to be a decent candidate for trapping and guiding the microparticles [56, 206]. In topological beams (LG and Bessel beams) atmospheric turbulence induces a cross-talk between the modes, making them inadequate for free space optical communication. However, it has been shown that autofocused beams can overcome such effects for free space optical communications [190]. Although, several works have reported various kinds of autofocused and non-diffracting beams, such as pin-like optical beams and abruptly focused beams [25,55,56,189,206]. However, with these autofocused beams, several aspects such as easy control on tuning the autofocusing position from small to large values, self-healing abilities in free space as well as in turbulent media, and spectral dependence of autofocusing, have not been explored in great detail.

In this Chapter, we present the investigations on the propagation (autofocusing) and self-healing properties of ALBs in free space and in turbulent media. In Section 3.2, we present detailed analytical modelling of the propagation of ALBs in turbulent media. In Section 3.3, the numerical and experimental results are presented for the propagation of ALBs in free space and in turbulent media under weak, moderate, and strong turbulence conditions. The quantification of autofocusing distance is performed by analyzing the overlap integral. In Section 3.4, we present the spectral dependence of autofocusing properties of ALB in a turbulent medium. In Sections 3.5 and 3.6, we present the self-healing properties of ALBs in free space as well as in turbulent media, respectively. Finally, in Section 3.7, we present the concluding remarks. The investigations presented in this Chapter are given in Refs. [37, 39].

3 Aberration laser beams with controlled autofocusing and self-healing

3.2   Theoretical description

The ALBs can be defined in multiple ways, however, the electric field of a specific type can be expressed as [86, 207]:

$$E(r,\theta) = A(r)\exp\left(-i\alpha r^q + i\sin\left(m\theta\right)\right), \quad r \leq R. \tag{3.1}$$

where $A(r) = \exp(-r^2/2\sigma_0^2)$ denotes a Gaussian with beam waist σ_0, m is an integer, which controls the lobe structure in ALB, R is the radius of a circular aperture, q is radial power, α is a scale parameter having unit mm^{-q}. In free space, for such ALB the autofocusing distance can be given as [86]:

$$z_{\text{max}} \approx \frac{2\pi}{q\alpha\lambda(2\sigma_0/3)^{q-2}}, \tag{3.2}$$

where λ is the wavelength. As seen from Eq. (3.2), the autofocusing distance can be controlled by several parameters, however, dependence on α is the simplest and most convenient to manage. α is a scale parameter that controls the steepness in aberrated wavefront (Eq. (3.1)). The high value of α results in greater steepness in the wavefront, and autofocuses the beam at shorter propagation distances. Note, the value of m (Eq. (3.1)) controls the number of lobes in the ALB and does not affect the autofocusing distance.

For various applications, a light field is required to propagate through a disordered media. For example, when a light field propagates through a typical atmosphere, it encounters various random temperature fluctuations in its optical path. These random temperature fluctuations result in random variation in the refractive index of the medium, which leads to the distortion in wavefront of the propagated light field. The Kolmogorov model for atmospheric turbulence gives an appropriate description for such random variation in the refractive index of the medium [28, 204, 208]. The propagation of ALB in a free space and in a turbulent medium can be described using extended Huygens-Fresnel integrals, as shown in Sec. 1.4.2 by Eqs. (1.18) and (1.21) [204, 209].

For the propagation of light field in a turbulent media, the expression of an average

intensity at the output plane can be given as (Eq. (1.21))

$$
\begin{aligned}
\langle I(\rho, \phi, z) \rangle &= \left(\frac{k}{2\pi z}\right)^2 \iint \iint E(r, \theta) E^*(r', \theta') \exp\left(\frac{ik}{2z}(r^2 - r'^2)\right) \\
&\quad exp\left(-\frac{ik}{z} r\rho \cos(\phi - \theta)\right) exp\left(\frac{ik}{z} r'\rho \cos(\phi - \theta')\right) \\
&\quad \times \langle \exp[\psi(\rho, r, z) + \psi^*(\rho, r', z)] \rangle r r' \, dr \, dr' \, d\theta \, d\theta'.
\end{aligned} \tag{3.3}
$$

Where $\psi(\rho, r, z)$ represents a random complex phase function describing the irregularities of turbulent medium. The last term in Eq. (3.3) describes the correlation of random fluctuations, and can be expressed as [205, 209].

$$
\begin{aligned}
\langle \exp[\psi(\rho, r, z) + \psi^*(\rho, r', z)] \rangle &= \exp(-0.5 D_\psi) \\
&= \exp\left(-\frac{(r - r')^2}{l(z)^2}\right).
\end{aligned} \tag{3.4}
$$

D_ψ represents the phase structure function in Rytov's representation, and $l(z)$ is the coherence length of the spherical wave propagating in a turbulent medium [205, 209]. In a turbulent medium $l(z) = (0.545 C_n^2 k^2 z)^{-3/5}$, where C_n^2 denotes the structure constant of medium. Generally, the analytical calculation of the intensity from Eq. (3.3) is very difficult. However, the calculation of intensity on the optical axis becomes relatively simple. Thus, substituting $\rho = 0$ (for on optical axis intensity) as well as light field from Eq. (3.1), Eq. (3.3) can be written as

$$
\begin{aligned}
\langle I(\rho = 0, z) \rangle &= \left(\frac{k}{2\pi z}\right)^2 \iint \iint \exp\left(-\frac{r^2 + r'^2}{2\sigma_0^2}\right) \exp\left(-\frac{(r - r')^2}{l(z)^2}\right) \\
&\quad \exp\left(-i\alpha r^q + i\sin(m\theta)\right) \exp\left(+i\alpha r'^q - i\sin(m\theta')\right) \\
&\quad \times \exp\left(\frac{ik}{2z}(r^2 - r'^2)\right) r r' \, dr \, dr' \, d\theta \, d\theta'.
\end{aligned} \tag{3.5}
$$

The expression in Eq. (3.5) is now factorized into angular and radial parts as

$$
\begin{aligned}
\langle I(\rho = 0, z)\rangle \;=\; & \left(\frac{k}{2\pi z}\right)^2 \int_0^{2\pi} \exp(i\sin(m\theta))\, d\theta \int_0^{2\pi} \exp(-i\sin(m\theta'))\, d\theta' \\
& \int_0^R \int_0^R \exp\left(-\frac{r^2 + r'2}{2\sigma_0^2}\right) \exp\left(-\frac{(r - r')^2}{l(z)^2}\right) \\
& \times \exp\left(\frac{ik}{2z}(r^2 - r'^2)\right) \exp[-i\alpha\,(r^q - r'^q)]\, rr'\, dr\, dr'.
\end{aligned}
\tag{3.6}
$$

Note that only the factor $\exp\left(-\frac{(r-r')^2}{l(z)^2}\right)$ prevents the separability of radial part in Eq. (3.6). Moreover, for $l(z) \to \infty$ (completely coherent case) this factor is equal to unity, and factorization occurs, as it should be in the coherent case. The integrals over the angles θ and θ' are the same and equal to $2\pi J_0(1)$ regardless of m. If the radius of the aperture R satisfies the inequality $R > 2\sigma_0$ then without the loss of accuracy, an upper limit can be replaced by $+\infty$. Nevertheless, the exact solution of above expression (Eq. (3.6)) is not easy to get. Therefore, we apply a stationary phase method for the analysis of expression in Eq. (3.6).

3.2.1   Simple application of the stationary phase method

In this case, we assume that all real factors are slowly varying. Thus, the radial part in Eq. (3.6) can be represented as follows:

$$
\begin{aligned}
T(z) \;=\; & \int_0^R \int_0^R \exp\left(-\frac{r^2 + r'2}{2\sigma_0^2}\right) \exp\left(-\frac{(r - r')^2}{l(z)^2}\right) \\
& \exp\left(\frac{ik}{2z}(r^2 - r'^2)\right) \exp[-i\alpha\,(r^q - r'^q)]\, rr'\, dr\, dr' \\
\approx\; & \int_0^\infty \int_0^\infty A(r, r'; \sigma_0, l)\, \exp(i\psi(r, r'; z))\, dr\, dr',
\end{aligned}
\tag{3.7}
$$

where

$$
A(r, r'; \sigma_0, l) = \exp\left(-\frac{r^2 + r'2}{2\sigma_0^2}\right) \exp\left(-\frac{(r - r')^2}{l(z)^2}\right) rr'.
\tag{3.8}
$$

$$
\psi(r, r'; z) = -\alpha r^q + \frac{k}{2z}r^2 + \alpha r'^q - \frac{k}{2z}r'^2.
\tag{3.9}
$$

The inseparable factor is in the amplitude (Eq. (3.8)), and the phase is factorized (Eq. (3.9))), therefore the mixed derivative of the phase is zero. Therefore, the integral in Eq. (3.7)) can be approximated in a simple form:

$$T(z) \approx \pi A(r_0, r_0'; \sigma_0, l) \left[\left| \frac{\partial^2 \psi(r_0; z)}{\partial r^2} \frac{\partial^2 \psi(r_0'; z)}{\partial r'^2} \right| \right]^{-1/2}, \tag{3.10}$$

where r_0 and r_0' are stationary points. To solve it, we need to find the stationary points as well as the second derivatives.

$$
\begin{aligned}
\frac{\partial \psi(r, r'; z)}{\partial r} &= -\alpha q r^{q-1} + \frac{k}{z} r = 0 \\
&\Rightarrow \quad r_0 = \left(\frac{k}{\alpha q z} \right)^{1/(q-2)}, \tag{3.11a} \\
\frac{\partial \psi(r, r'; z)}{\partial r'} &= \alpha q r'^{q-1} - \frac{k}{z} r' = 0 \\
&\Rightarrow \quad r_0' = \left(\frac{k}{\alpha q z} \right)^{1/(q-2)}. \tag{3.11b}
\end{aligned}
$$

$$
\begin{aligned}
\frac{\partial^2 \psi(r_0; z)}{\partial r^2} &= -\frac{k}{z}(q-2), \tag{3.12a} \\
\frac{\partial^2 \psi(r_0'; z)}{\partial r'^2} &= \frac{k}{z}(q-2). \tag{3.12b}
\end{aligned}
$$

Thus, the expression in Eq. (3.10) has the following explicit form:

$$T(z) \approx \frac{\pi z}{k|q-2|} \exp\left(-\frac{r_0^2}{\sigma_0^2} \right) r_0^2. \tag{3.13}$$

The main disadvantage of the obtained expression (Eq. (3.13)) is that there is no dependence on the coherence length $l(z)$ (turbulent media). The resulting expression for the intensity as a zero approximation can now be given as:

$$\langle I(0, z) \rangle = \frac{\pi}{|q-2|} J_0^2(1) \frac{k}{z} \left(\frac{k}{\alpha q z} \right)^{\frac{2}{q-2}} \times \exp\left(-\left(\frac{k}{\alpha q z} \right)^{\frac{2}{q-2}} \cdot \frac{1}{\sigma_0^2} \right). \tag{3.14}$$

As can be seen, Eq. (3.14) has a singularity at $q = 2$, which is explained from the physical point of view as follows: the used propagation operator corresponds to the expansion in parabolic waves, therefore the operator's kernel has a quadratic dependence on the radius. In this regard, a converging parabolic wavefront ($q = 2$ corresponds to a parabolic lens) is special in this situation and will be discussed in more detail below.

Above, we have not taken into account the presence of an entrance pupil of radius R. If we take it into account, then in certain areas there will be shadows, so the obtained expressions will work correctly in the following areas [86, 207]:

$$z \; < \; \frac{k}{\alpha q R^{(q-2)}}, \qquad (q < 2), \tag{3.15a}$$

$$z \; > \; \frac{k}{\alpha q R^{(q-2)}}, \qquad (q > 2). \tag{3.15b}$$

It can be seen that the boundary of the shadow is determined by one formula, but the location of the shadow area depends on the degree of q. Note, even a rough approximation (Eq. (3.14)) allows finding the position of intensity maximum, and thereby the autofocusing distance. Discarding the factors, that are independent of z, Eq. (3.14) can be written as:

$$\langle I(0, z) \rangle \approx z^{q/(2-q)} \exp\left(-\mu \, z^{2/(2-q)} \right), \tag{3.16}$$

where $\mu = \left(\frac{k \sigma_0^{2-q}}{\alpha q} \right)^{2/q-2}$. It can be shown that for any q, the on-axis intensity (Eq. (3.16)) tends to zero at $z \to 0$ and at $z \to \infty$. The intensity maximum is reached at $z_{\max} = \left(\frac{q}{2\mu} \right)^{(2-q)/2}$ or, explicitly at

$$z_{\max} = \left(\frac{q}{2} \right)^{(2-q)/2} \cdot \frac{k}{\alpha q \sigma_0^{q-2}}. \tag{3.17}$$

To prevent the intensity maximum falling into the shadow region, in addition to $R > 2\sigma_0$, it is necessary to satisfy the inequality

$$R > \sigma_0 \sqrt{\frac{q}{2}}. \tag{3.18}$$

3.2.2 Complicated application of the stationary phase method

As we have seen above, the final expression of on-axis intensity (Eq. (3.14)) does not contain the dependence on $l(z)$ (turbulent medium), so we have applied the stationary phase method more flexibly. Namely, we replace the phases with quadratic expansions, replace the first powers of r and r' with stationary values r_0, and r'_0 respectively, but leave the real exponents in their original form. Then we get an expression for integral in Eq. (3.6) in the form:

$$
\begin{aligned}
T(z) \;\approx\; & \int_0^R \int_0^R \exp\left(-\frac{r^2 + r'2}{2\sigma_0^2}\right) \exp\left(-\frac{(r - r')^2}{l(z)^2}\right) \\
& \times \exp\left[i\left(\psi(r_0; z) + \frac{\partial^2 \psi(r_0; z)}{\partial r^2}\frac{(r - r_0)^2}{2}\right)\right] \\
& \times \exp\left[i\left(\psi(r'_0; z) + \frac{\partial^2 \psi(r'_0; z)}{\partial r'^2}\frac{(r' - r'_0)^2}{2}\right)\right] r_0 r'_0 \, dr \, dr',
\end{aligned}
\tag{3.19}
$$

where

$$
\psi(r_0; z) = \frac{k \, r_0^2 \, (q - 2)}{2qz} \quad \text{and} \quad \psi(r'_0; z) = -\frac{k \, r_0'^2 \, (q - 2)}{2qz}
\tag{3.20}
$$

Let us take into account that $r_0 = r'_0$ (see Eq. (3.11)), then $\psi(r_0; z) = -\psi(r'_0; z)$. In addition, from Eq. (3.12) we get $\frac{\partial^2 \psi(r_0; z)}{\partial r^2} = -\frac{\partial^2 \psi(r'_0; z)}{\partial r'^2}$. Then integral in Eq. (3.19) takes the following form:

$$
\begin{aligned}
T(z) \;\approx\; & r_0^2 \int_0^R \int_0^R \exp\left(-\frac{r^2 + r'^2}{2\sigma_0^2} - \frac{(r - r')^2}{l(z)^2}\right) \\
& \exp\left[\frac{i}{2}\frac{\partial^2 \psi(r_0; z)}{\partial r^2}\left((r - r_0)^2 - (r' - r_0)^2\right)\right] dr \, dr'
\end{aligned}
\tag{3.21}
$$

From Eq. (3.21) we can obtain the integral of the form:

$$
\iint_{-\infty}^{+\infty} \exp[-(Ax^2 + By^2 + Cxy + Dx + Ey)] \, dx \, dy
$$

$$
= \frac{\pi}{\sqrt{AB - C^2/4}} \exp\left[\frac{1}{4} \cdot \frac{AE^2 + BD^2 - CDE}{AB - C^2/4}\right]
\tag{3.22}
$$

3 Aberration laser beams with controlled autofocusing and self-healing

Expression in Eq. (3.22) is true if $AB > C^2/4$. In the case under consideration:

$$A = \frac{1}{2\,\sigma_0^2} + \frac{1}{l(z)^2} - \frac{i}{2}\frac{\partial^2 \psi(r_0;z)}{\partial r^2} \quad , B = \frac{1}{2\,\sigma_0^2} + \frac{1}{l(z)^2} + \frac{i}{2}\frac{\partial^2 \psi(r_0;z)}{\partial r^2},$$

$$C = -\frac{2}{l(z)^2} \quad , D = i\,r_0\,\frac{\partial^2 \psi(r_0;z)}{\partial r^2} \quad , E = -i\,r_0\,\frac{\partial^2 \psi(r_0;z)}{\partial r^2} \tag{3.23}$$

After simplification, integral (Eq. (3.21)) is solved and substituted to Eq. (3.6) to obtain a simplified form that is convenient for the analysis.

$$\langle I(0,z)\rangle = \left(\frac{k}{\alpha q z}\right)^{2/(q-2)} \frac{2\pi J_0^2(1)k^2\sigma_0^2}{z\cdot\sqrt{z^2\left(1 + \frac{4\sigma_0^2}{l(z)^2}\right) + k^2\sigma_0^4(q-2)^2}}$$

$$\exp\left(-\left(\frac{k}{\alpha q z}\right)^{2/(q-2)}\frac{1}{\sigma_0^2}\frac{k^2(q-2)^2\sigma_0^4}{z^2\left(1 + \frac{4\sigma_0^2}{l(z)^2}\right) + k^2(q-2)^2\sigma_0^4}\right) \tag{3.24}$$

Equation (3.24) shows the dependence of on-axis average intensity on the combination of various parameters, including input beam waist σ_0 and coherence length $l(z)$. If we omit the factors independent of z, then Eq. (3.24) can be re-written as

$$\langle I(0,z)\rangle \approx \frac{z^{q/(2-q)}}{\sqrt{\beta z^2 + \delta}}\exp\left(-\mu\frac{z^{2/(2-q)}}{\beta z^2 + \delta}\right), \tag{3.25}$$

where $\mu = \left(\frac{k\sigma_0^{2-q}}{\alpha q}\right)^{2/(q-2)}$, $\beta = 1 + \frac{4\sigma_0^2}{l(z)^2}$, and $\delta = k^2\sigma_0^4(q-2)^2$. From Eq. (3.25), one can obtain the position of the extremum, which is found from the equation:

$$\left[(2q-2)\beta z + q\delta z^{-1}\right](\beta z^2 + \delta) = \mu\left((2q-2)\beta z^{\frac{4-q}{2-q}} + 2\delta z^{\frac{q}{2-q}}\right). \tag{3.26}$$

It should be noted that expression (Eq. (3.16)) and more precise expression (Eq. (3.25)) are inapplicable for $q = 2$. Therefore, we consider separately the special case for $q = 2$. For $q = 2$, instead of Eq. (3.6), taking into account the value of the integral over the

angle, we obtain:

$$\langle I(0,z)\rangle|_{q=2} = \left(\frac{k}{z}\right)^2 J_0^2(1) \int_0^\infty \int_0^\infty \exp\left(-\frac{x^2+y^2}{2\sigma_0^2}\right) \exp\left(-\frac{(x-y)^2}{l(z)^2}\right)$$
$$\times \exp\left(\frac{ik}{2z}(x^2-y^2)\right) \exp[-i\alpha(x^2-y^2)]\, xy\, dx\, dy. \tag{3.27}$$

We simplify Eq. (3.27) using Eq. (3.22), choosing the maximum of the modulus of the integrand as the stationary point. After mathematical transformations, we get an explicit form:

$$\langle I(0,z)\rangle|_{q=2} = \left(\frac{k}{z}\right)^2 J_0^2(1)\, \sigma_0^2 \frac{\pi}{\sqrt{\frac{1}{4\sigma_0^4}+\frac{1}{l(z)^2\sigma_0^2}+(\alpha-\frac{k}{2z})^2}}. \tag{3.28}$$

The maximum will be at $\alpha = \frac{k}{2z}$, which corresponds to the lens focus position and coincides with Eq. (3.2) at $q=2$. Note that Eq. (3.28) is obtained by the stationary phase method, therefore, in principle, it is an approximate solution, for the coherent case $l(z)=\infty$, an exact solution can be obtained.

It is based on the equality

$$\int_0^\infty r\exp(-Ar^2)dr = \frac{1}{2A}. \tag{3.29}$$

In the coherent case, the integrand in Eq. (3.27) is separable and we obtain

$$\langle I(0,z)\rangle|_{q=2} = \left(\frac{k}{z}\right)^2 J_0^2(1)\frac{1}{4}\frac{1}{\frac{1}{4\sigma_0^4}+(\alpha-\frac{k}{2z})^2}. \tag{3.30}$$

The main difference between Eq. (3.30) and Eq. (3.28) is the absence of the root sign, which is especially pronounced far from the focus. In a partially coherent case, the calculation is more cumbersome, since the function must be made separable. Without giving details, we give the final result, which is similar to both expressions in Eqs. (3.28) and (3.30):

$$\langle I(0,z)\rangle|_{q=2} = \left(\frac{k}{z}\right)^2 J_0^2(1)\frac{1}{4}\frac{1}{\frac{1}{4\sigma_0^4}+\frac{1}{l(z)^2\sigma_0^2}+(\alpha-\frac{k}{2z})^2} \tag{3.31}$$

Using Eq. (3.31), it is possible to analytically obtain the autofocusing distance of ALB for

fixed values of the coherence length ($l(z)$=constant):

$$z_{\max} = \frac{k\alpha}{2\left(\alpha^2 + \frac{1}{4\sigma_0^4} + \frac{1}{l^2(z)\sigma_0^2}\right)} \tag{3.32}$$

As can be seen from Eq. (3.32), if $\left(\frac{1}{4\sigma_0^4} + \frac{1}{l^2(z)\sigma_0^2}\right) << \alpha^2$, then $z_{\max} = k/2\alpha$ which is equal to the lens focus position. This fact allows us to find the approximate position of the maximum for varying coherence length $l(z)$. We calculate first $l_0 = l(z = k/2\alpha)$. If $\left(\frac{1}{4\sigma_0^4} + \frac{1}{l_0^2\sigma_0^2}\right) << \alpha^2$, then the autofocusing distance can be approximately calculated as follows:

$$z_{\max} \approx \frac{k_0}{2\alpha}\left[1 - \frac{1}{\alpha^2}\left(\frac{1}{4\sigma_0^4} + \frac{1}{l_0^2\sigma_0^2}\right)\right] \tag{3.33}$$

Otherwise, the maximum can be determined from the graph of the function in Eq. (3.31), as shown in Fig. 3.1. Figure 3.1 shows the behaviour of on-axis intensity of ALB as
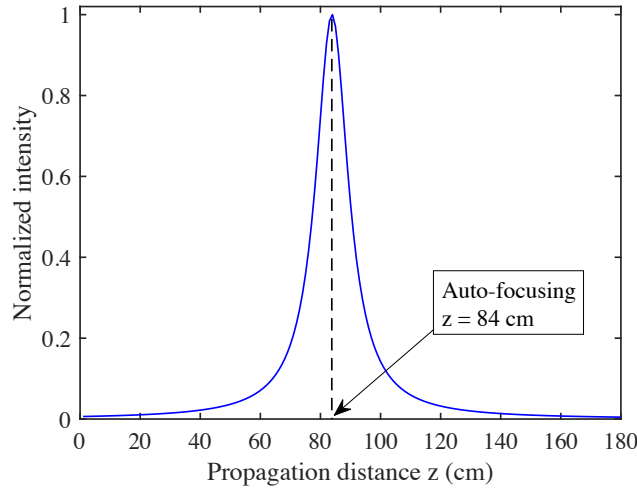
Figure 3.1: Variation of on-axis normalized intensity as a function of propagation distance z. Plot is obtained for the parameters: $\alpha = 3.5$ mm^{-2}, $q = 2$, $m = 4$, $\sigma_0 = 1.35$ mm, $\lambda = 1064$ nm, and $C_n^2 = 10^{-12}$ m$^{2/3}$. The peak value of on-axis intensity indicates the autofocusing position of ALB.

a function of propagation distance in a strong turbulent media. As evident, the plot consists of a peak at $z = 84$ cm, indicating the autofocusing position of ALB. However, in a free space, for the same ALB, the autofocusing distance is found to be $z = 84.36$ cm (calculated using Eq. (3.2)). It suggests that the autofocusing distance does not show

any considerable changes while propagating in a turbulent medium.

3.3 Results

For free space propagation, intensity distribution of a light field can be calculated (or simulated) by an extended Huygens-Fresnel integral. However, the propagation through an atmosphere needs the involvement of a random phase. For ideal considerations, the refractive index of air is taken as nearly unity, but in actual practice, random fluctuations of temperature and wind velocity affect the value of the refractive index in a random fashion, and induce a considerable effect on the spatial intensity and phase distributions of a light field, when propagated in the atmosphere. Similar effects also occur when light propagates through any disordered or diffusive media. For convenience, to examine the effect of atmospheric turbulence on the laser beam, turbulent media is prepared artificially by several methods, such as, aqueous suspension obtained from the mixing of distilled water with insoluble micro-powder [210], aerosol optical medium [205], heated Aluminum panel with high power resistors [211], artificial atmospheric and oceanic turbulence, soft biological tissues [208] (and ref. there in), turbulence chambers consisting of heating elements and fans to create distortions [212], glass plates etched with turbulence phase (turbulent plates), which can be rotated or translated to consider the effect of dynamic turbulence on the laser beam profile [213].

Further, turbulent medium in the laboratory is also realized by implementing random phase on Spatial Light Modulators (SLMs) and Digital Micromirror Devices (DMDs) [28]. These methods involve more flexibility, as turbulent strength as well as its phase distribution can be controlled and altered easily. To simulate the random phase screen that can behave like a turbulent media of desired strength, various methods are reported, namely, weighted superposition of Zernike polynomials [214], Monte-Carlo method [215] and subharmonic method [216]. Out of these methods, the Monte-Carlo method is considered to be simple and convenient. It generates a random phase screen by using Fourier transform of complex random matrix in spatial frequency domain, whose variance is directly

calculated from the von Karman power spectrum and mimics the atmospheric turbulence in the simulations [217, 218]. The phase screen based approach is further classified into two types: (i) single-phase screen method, and (ii) multiple-phase screen method. The method based on multiple phase screens involves the splitting of desired length (z) of the medium into small intervals Δz, and for each sub-part of the medium, a phase screen is prepared and placed at a distance of Δz [218, 219]. This method gives good results when the length of the medium is large enough, whereas, for smaller propagation distance in turbulent media, or the case when thickness of the medium is small as compared to the total propagation length of light beam, a single-phase screen is enough to mimic the turbulent media [28, 220]. In our study, the autofocusing distance is in the range of 1 m, so the single-phase screen approach is used. However, for the propagation of ALB through turbulent media, we have performed a comparison between the two approaches and obtained similar outcomes (see Appendix 3.8.1).

To analyze the propagation of ALB in a turbulent medium, we simulated a phase screen consisting of random phase fluctuations that represent a turbulent medium and imparted it on light field of ALB and propagated further, as shown schematically in Fig. 3.2. Figure 3.2 depicts the generation of ALB by illuminating DOE with an input Gaussian beam (laser output), as well as propagation in free space and turbulent media. The turbulence is imparted on the ALB by turbulent phase screen that consists of random fluctuations in the phase distribution.

To simulate the turbulent media, we employed the Monte-Carlo method that generates a random phase screen. The variance of random phase function is given by [28, 204]

$$\sigma_v^2(k_x, k_y) = 2\pi k^2 z \left(\frac{2\pi}{N\Delta x}\right)^2 \phi_n(k_x, k_y), \tag{3.34}$$

where Δx denotes grid spacing of $N \times N$ size matrix over which phase screen is generated, and k_x and k_y represent the spatial frequencies over the grid. z denotes distance over which turbulent phase screen is simulated. $\phi_n(k_x, k_y)$ represents a refractive index power
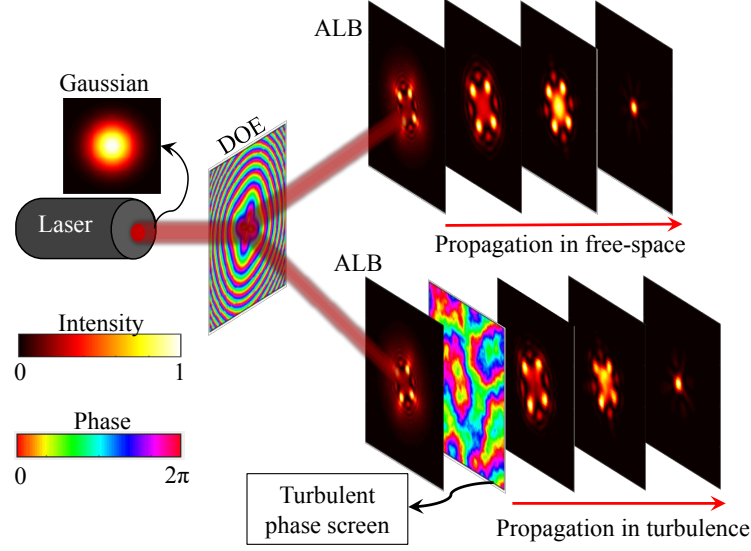
Figure 3.2: Schematic illustrating the formation of ALB by illuminating input light from a laser on DOE, and after that propagated in a free space as well as in a turbulent media. For the propagation in turbulent media, we imparted a random phase distribution on ALB and then propagated.

spectrum, which is given as [28, 204].

$$\phi_n(k_x, k_y) = 0.33\, C_n^2 \frac{\exp(-k_r^2/k_l^2)}{(k^2 + k_h^2)^{11/6}}, \qquad 0 \le k < \infty, \tag{3.35}$$

where $k_r^2 = k_x^2 + k_y^2$ is a radial vector in the spatial frequency domain. $k_l = 5.92/l_0$ and $k_h = 2\pi/L_0$. The l_0 and L_0 denote the size of small and large scale eddies. C_n^2 represents the strength of atmospheric turbulence. The values of C_n^2 ranges from 10^{-18} m$^{2/3}$ for weak turbulence up to 10^{-12} m$^{2/3}$ for strong turbulence conditions [28]. Now, a $N \times N$ size screen with random phase fluctuations can be generated as

$$\Phi(x, y) = \mathcal{F}^{-1}(rand(k_x, k_y) \times \sigma_v(k_x, k_y)), \tag{3.36}$$

where $\mathcal{F}^{-1}$ denotes the inverse Fourier transform, and a normal distribution with zero mean and variance one, is used to sample random entries of a complex matrix $rand(k_x, k_y)$. The simulated phase screens for two different propagation distances are shown in Fig. 3.3. Figure 3.3 clearly shows that although C_n^2 is fixed, but the randomness in the phase
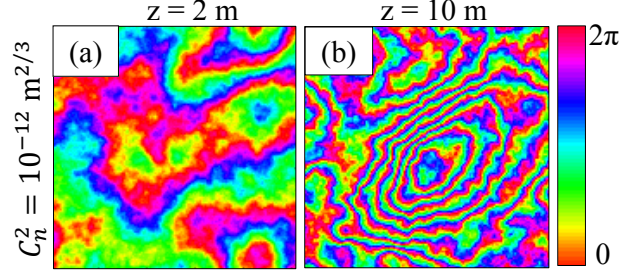
Figure 3.3: The random phase screen for (a) $z = 2$ m, and (b)$z = 10$ m, depicting turbulent medium with different randomness. The results are obtained for a fixed turbulence strength $C_n^2 = 10^{-12}$ m$^{2/3}$, $L_0 = 10$ m and $l_0 = 0.001$ m.

distribution can also be varied by changing the propagation distance z. Particularly, a longer propagation in a weak random medium is equivalent to a short propagation in a highly random medium.

To analyze the effect of turbulence on ALB, we have generated ALB with parameter values $\alpha = 3.5$ mm$^{-2}, q = 2, m = 4, \lambda = 1064$ nm, and input beam waist $\sigma_0 = 1.35$ mm (Fig. 3.2). After that, we impose random phase screens with different turbulence strengths on ALB, and then the resulting field is propagated, the results are shown in Fig.3.4. Note, the parameter values are chosen for the convenience of analytics and experiments. For example, $\alpha = 3.5$ mm^{-2} provides the autofocusing of ALB in the range of 1 m, suitable for experimental measurements. We have also verified numerical results for other values, but obtained similar findings except that the autofocusing distance will change to different values, as well as the lobe structure in ALB will also be different for different m. Figure 3.4(a) shows the intensity distribution of a generated ALB at $z = 10$ cm. Figures 3.4(b)-3.4(e) present the intensity distribution of ALB at various propagation distances in a free space. As evident the ALB autofocuses at a distance of $z = 85$ cm. Figures 3.4(f)-3.4(i) show the intensity distribution of ALB at various propagation distances in a weak turbulent medium with $C_n^2 = 10^{-14}$ m$^{2/3}$. The weak turbulence does not affect the ALB significantly, and it again autofocuses at $z = 85$ cm. Figures 3.4(j)-3.4(m) show the intensity distribution of ALB at intermediate turbulence strength $C_n^2 = 10^{-13}$ m$^{2/3}$, indicating that the spatial structure is distorted, however, ALB still autofocuses at the same distance $z = 85$ cm. Figures 3.4(n)-3.4(q) show the intensity
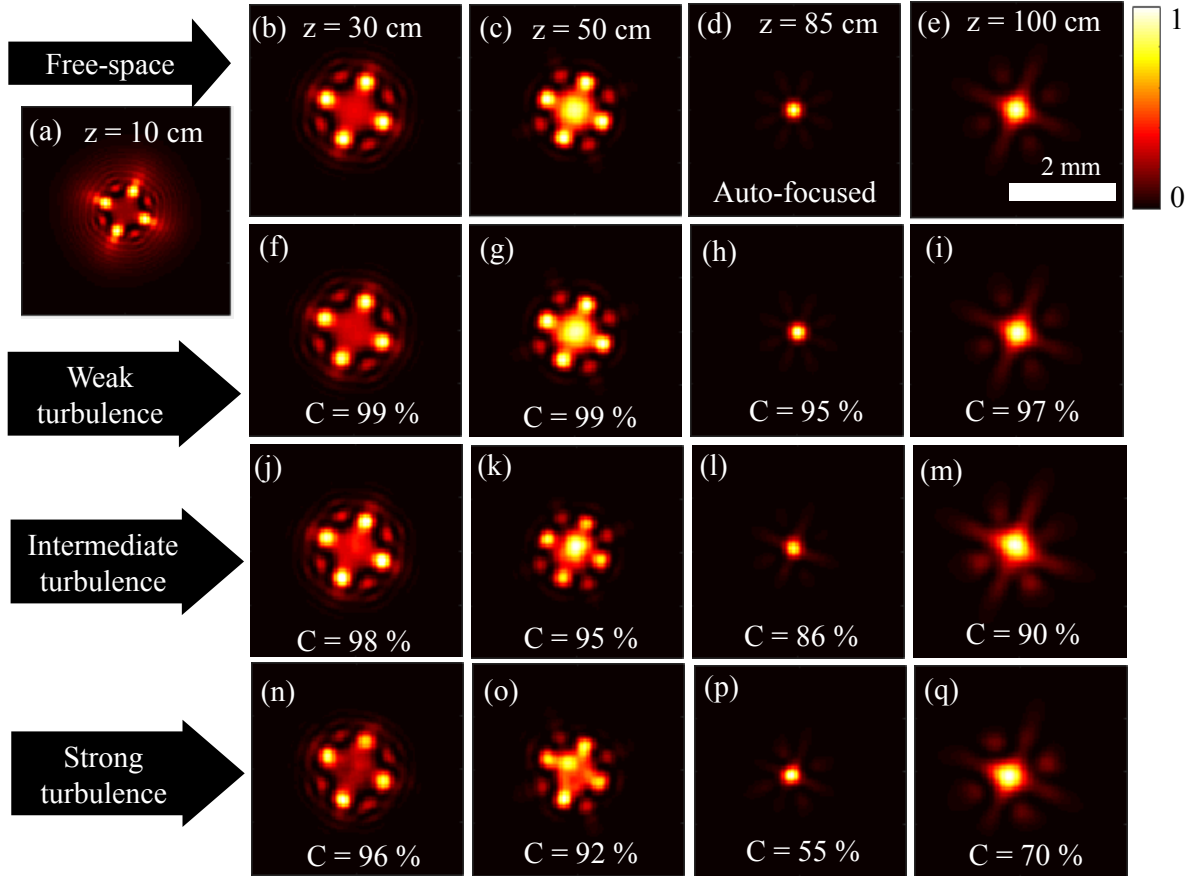
Figure 3.4: (a) Intensity distribution of ALB at $z = 10$ cm. The intensity distribution of ALB at various propagation distances in (b)-(e) free space, (f)-(i) weak turbulent medium with $C_n^2 = 10^{-14}$ m$^{2/3}$, (j)-(m) intermediate turbulent medium with $C_n^2 = 10^{-13}$ m$^{2/3}$, and (n)-(q) strong turbulent medium with $C_n^2 = 10^{-12}$ m$^{2/3}$. The results are simulated for the parameters: $\alpha = 3.5$ mm$^{-2}, q = 2, m = 4, \sigma_0 = 1.35$ mm, $\lambda = 1064$ nm, $L_0 = 10$ m, and $l_0 = 0.001$ m. For propagation in turbulent media with different strengths, the random phase screens are simulated for a propagation length of 2 m.

distribution of ALB at various propagation distances in a strong turbulent medium with $C_n^2 = 10^{-12}$ m$^{2/3}$. As evidenced, the spatial structure of ALB is significantly distorted during the propagation. However, the ALB shows autofocusing at the same distance $z = 85$ cm. From these results it is clear that, although the spatial structure of ALB is distorted due to randomness in turbulence, but autofocusing distance remains invariant, indicating the robustness of ALB.

We have quantified the effect of turbulence using an overlap integral, which is given by Eq. (1.26) [150]. The calculated values of overlap integral at various propagation distances in turbulent medium are written on the sub figures. As evident, the value of C decreases with an increase in randomness of turbulent medium (from weak to strong turbulence strength). Further, for a fixed value of C_n^2 (e.g., for strong turbulence) the value of C is $\sim 96\%$ at $z = 30$ cm (Fig. 3.4(n)) and it continues to decrease and becomes minimum ($C = 55\%$) at $z = 85$ cm (Fig. 3.4(p)), and afterward it again starts increasing. The decrease in C by increasing turbulence strength can be explained mainly by two reasons: i) beam wandering and ii) distortions in the spatial structure of beam. Beam wandering relates to the shifting of beam centre and beam trajectory due to insertion of random phase in the path of light, and later is the distortion in the spatial structure of light that happens due to distortion of the actual wavefront of ALB, as random phase adds a non-uniform path in various parts of ALB that ends up with an overall spatial distortion of the beam.

Figure 3.5 demonstrates the beam wandering effect as well as overlap integral as a function of propagation distance z. Figure 3.5(a) shows the intensity cross-section of ALB as a function of z in free space, indicating that ALB autofocuses at $z = 85$ cm. An arrow with a solid blue line marks the central position of the unshifted ALB. In Fig. 3.5(b), the intensity cross-section of ALB as a function of z in a strong turbulent medium clearly shows that the ALB still autofocuses at $z = 85$ cm, however, the center of ALB is shifted vertically, as shown by an arrow with a dashed green line. Figure 3.5(c) shows the overlap C as a function of propagation distance z in a strong turbulent medium. As evident, the overlap decreases with an increase in z, reaches a minimum value at
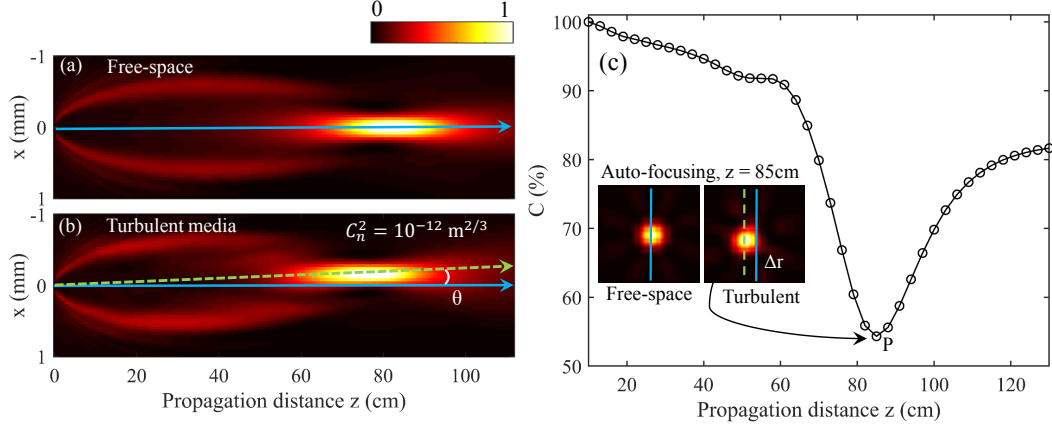
Figure 3.5: Intensity cross-section of ALB as a function of propagation distance in (a) free space, and (b) turbulent media. (c) The overlap integral as a function of propagation distance. The insets in (c) showing at autofocusing distance, a centered ALB in free space and wandered ALB in turbulent medium. The simulation parameters are kept the same as in Fig. 3.4. An arrow with blue solid line marks the central position of unshifted ALB, whereas, an arrow with a green dashed line marks the shifting of central position of ALB due to wandering effect in turbulence.

P, and after that, it again starts increasing. The point P where C becomes minimum corresponds to an autofocusing position of ALB. The lowest value of C at autofocusing distance can be understood by the fact that most of the energy of ALB is concentrated in a small region, and randomness in the turbulent medium leads to distortion in the spatial structure and beam wandering, which results in a large change in C. The observation of a dip with a minimum value of C can also be used to identify the autofocusing distance of ALB. Further, we also investigated the dependence of beam wandering on the turbulence strength of the turbulent media. We found that the beam wandering becomes more prominent for a stronger turbulent medium.

Figure 3.6, demonstrates the effects of beam wandering on the propagation of ALB in the turbulent media of different strengths. Beam wandering of ALB in turbulent media is analyzed by considering 40 realizations of random phase screens (for each turbulent strength) to obtain more reliable results. It is evident that for a fixed turbulence strength, beam wander increases as beam propagates through the turbulent medium. Further, beam wander becomes more prominent for stronger turbulence strength.
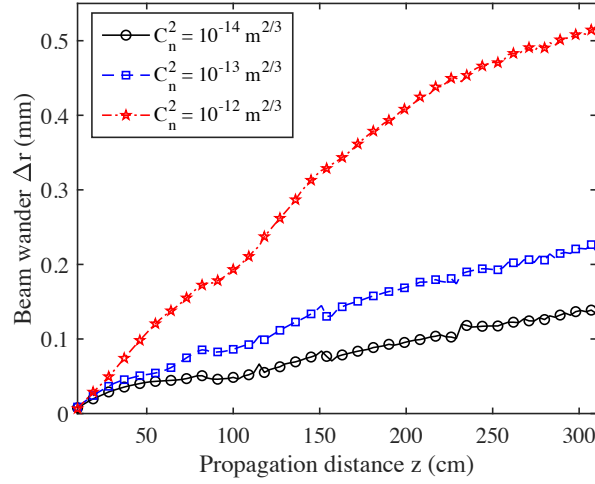
Figure 3.6: Beam wandering as a function of propagation distance z, when ALB is propagated in a turbulent medium with various turbulence strengths. Simulation parameters are $\alpha = 3.5$ mm^{-2}, $q = 2$, $m = 4$, $\sigma_0 = 1.35$ mm, $\lambda = 1064$ nm, $L_0 = 10$ m, and $l_0 = 0.001$ m. For propagation in turbulent media with different strengths, the random phase screens are simulated for a propagation length of 2 m.

Further, we have also quantified the findings presented in Fig. 3.4 for different turbulence strengths, the results are shown in Fig. 3.7. It is evident from Fig. 3.7 that for each turbulence strength the minimum of C falls exactly at the same distance, which denotes the same position of autofocusing of ALB. Note, the minimum value of C is found to be different for different turbulence strengths and can be understood by reasons explained in Fig. 3.5.

For the experimental verification of our simulation results, we have generated ALBs from SLM. A picture of the experimental setup is shown in Fig. 3.8. A linearly polarised CW laser of wavelength $\lambda = 1064$ nm is expanded with lenses L1 and L2 of focal lengths 5 cm and 10 cm respectively, and incident on SLM normally. The phase of the hologram for the generation of ALBs can be represented as [221]:

$$\psi = \psi((\alpha r^q + i \sin{(m\theta)}) + 2\pi N_x x + 2\pi N_y y) \tag{3.37}$$

Where $N_x = N_y = 100$ represents the grating frequencies along x and y directions. As per the requirements of the SLM, the phase of the hologram is divided into 256 gray levels
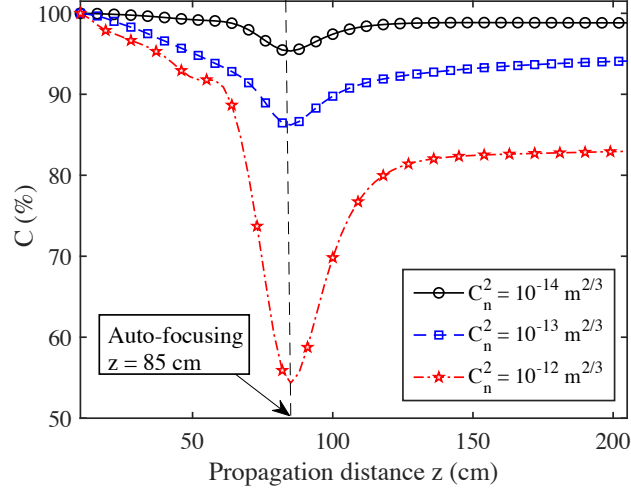
Figure 3.7: Overlap integral C as a function of propagation distance z, when ALB is propagated in a turbulent medium with different turbulence strengths. Solid black curve with circles: weak turbulence with $C_n^2 = 10^{-14}$ m$^{2/3}$; dashed blue curve with squares: intermediate turbulence with $C_n^2 = 10^{-13}$ m$^{2/3}$; red dot-dash curve with stars: strong turbulence with $C_n^2 = 10^{-12}$ m$^{2/3}$. Simulation parameters: $\alpha = 3.5$ mm^{-2}, $q = 2, m = 4, \sigma_0 = 1.35$ mm, $\lambda = 1064$ nm, $L_0 = 10$ m, and $l_0 = 0.001$ m. Each phase screen mimics the propagation of ALB in a turbulent medium of length 2 m.
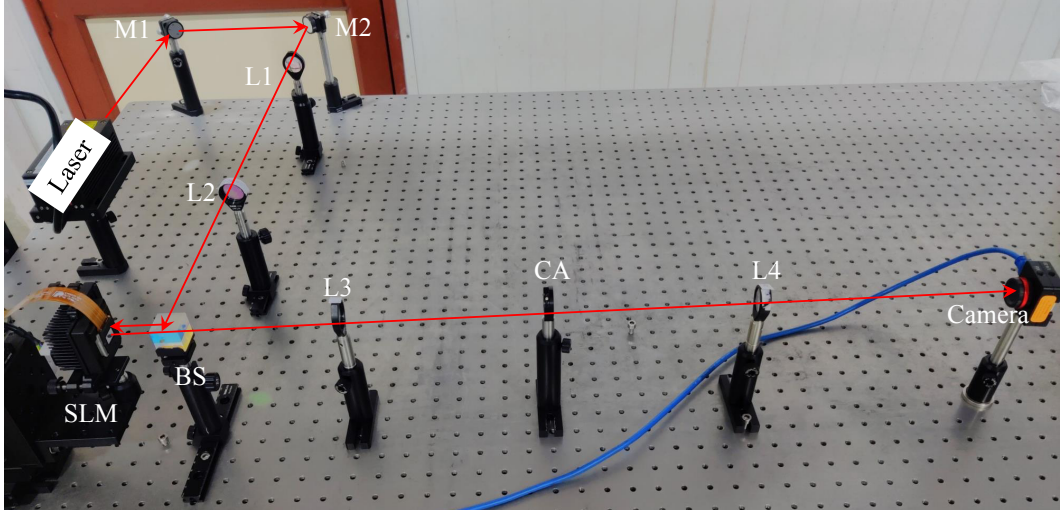
Figure 3.8: Experimental setup to generate ALBs. M1,M2: Mirrors; L1, L2, L3, L4: Plano convex lens with focal lengths 5 cm, 10 cm, 20 cm, and 20 cm respectively; BS: Beam splitter; SLM: Spatial light modulator; CA: Circular aperture.
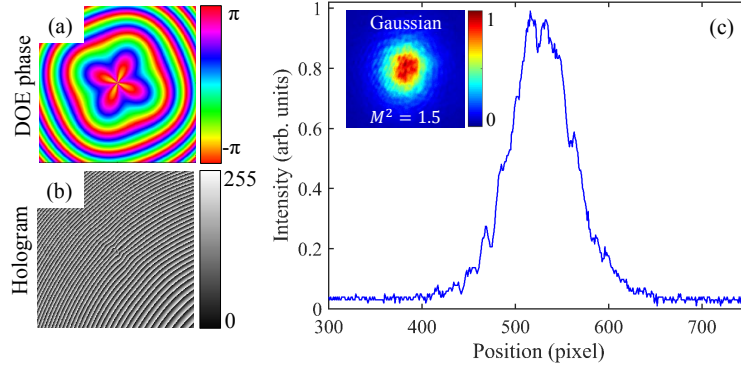
Figure 3.9: (a) Phase distribution of DOE for ALB. (b) Gray scale hologram to generate ALB. (c) Intensity cross-section of laser output (input beam). Inset shows the 2D intensity distribution of laser output with calculated value of $M^2 = 1.5$.

(Fig. 3.9(b)), which corresponds to DOE given in Fig. 3.9(a). This phase hologram is then encoded on a phase-only HOLOEYE SLM, with a resolution of 1920×1080 pixels and a pixel size of $8\,\mu$m. As the result of the blazed grating in the hologram, ALB can be filtered out by using a circular aperture of suitable size placed in the far-field of the telescope formed by lenses L3 and L4 of focal lengths 20 cm. To study the propagation of ALB in a turbulent medium, we have inserted an element carrying hot air in the path of ALB [212]. The hot air along the element consists of random fluctuations in temperature and affects the refractive index in a random fashion, which creates an optical turbulence effect. The temperature of hot element is stabilized at different values to produce the turbulence of various strengths. Note, Fig. 3.9(c) shows the output of laser, which is used for illuminating the SLM.

The propagation of ALB in free space as well as in turbulent medium with different strengths are shown in Fig. 3.10. Figures 3.10(a)-3.10(d) show the propagation of ALB in a free space, indicating that ALB is autofocused at a distance $z = 87$ cm. The results of propagation of ALB through turbulent medium (hot air) with different strengths (different temperatures) are shown in Figs. 3.10(e)-3.10(h), 3.10(i)-3.10(l) and 3.10(m)-3.10(p). As evident, upon increasing the temperature of hot air, the distortion in the spatial intensity distribution of ALB increases. However, at different temperatures, the ALB always autofocuses at the same distance $z = 87$ cm. This clearly indicates that
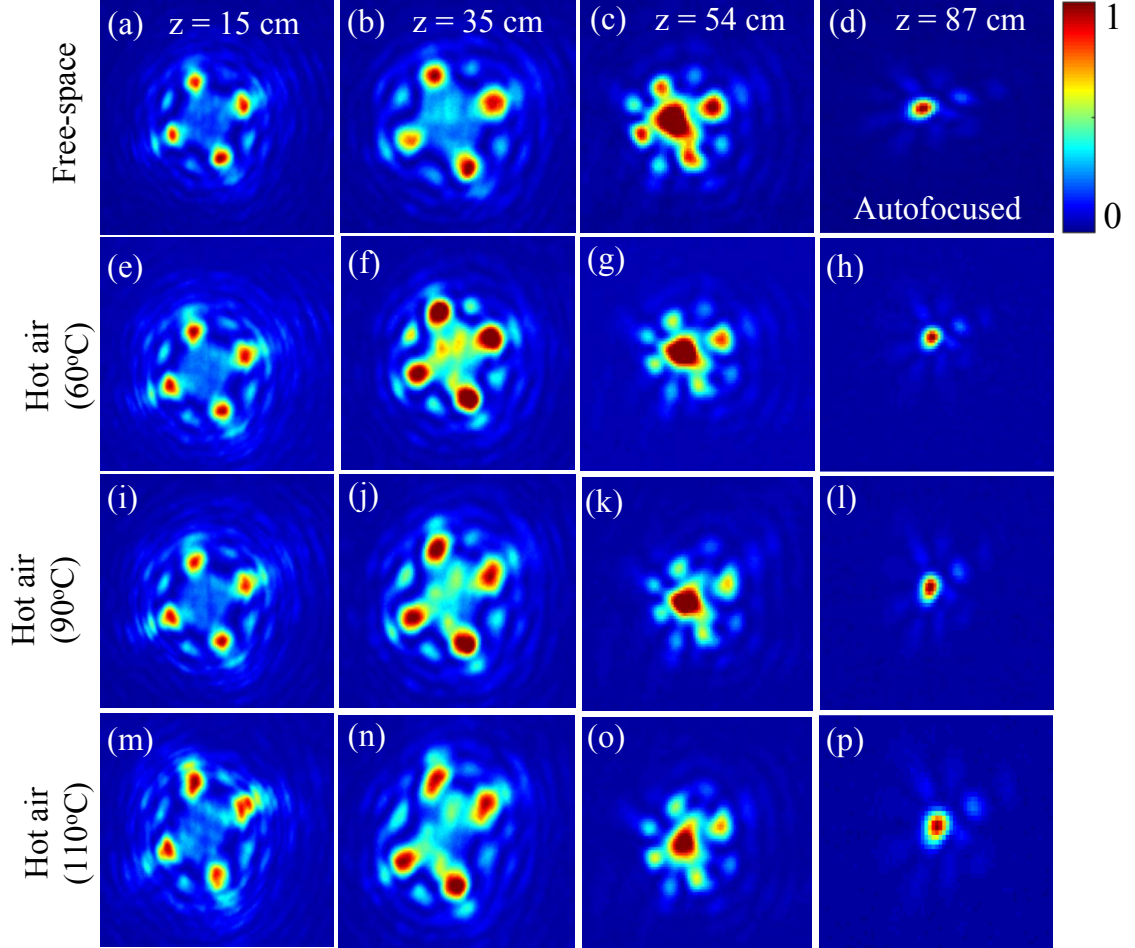
Figure 3.10: Experimental results. The intensity distribution of ALB at various propagation distances in (a)-(d) free space, (e)-(h) hot air with temperature $60\,^0$C (weak turbulence), (i)-(l) hot air with temperature $90\,^0$C (intermediate turbulence), and (m)-(p) hot air with temperature $110\,^0$C (strong turbulence). Experimental results are obtained for the parameters: $\alpha = 3.5$ mm^{-2}, $q = 2$, $m = 4$, $\sigma_0 = 1.35$ mm, $\lambda = 1064$ nm, and input beam diameter $= 3$ mm.

autofocusing distance of ALB remains invariant, which shows a good agreement with the numerical results. Note that there is a small mismatch between the values of autofocusing distance found in the experiment and simulations, which is anticipated due to the non-ideal experimental conditions. Unlike simulations, the input beam in the experiment is not a pure Gaussian (as $M^2 = 1.5$) as well as has different size, as shown in Fig. 3.9(c).

3.4 Spectral dependence of autofocusing of ALB in a turbulent medium

Spectral properties play a vital role in propagation of light, as spectral variations directly affect the focusing distance of ALB in free space [86]. It has been shown that the change
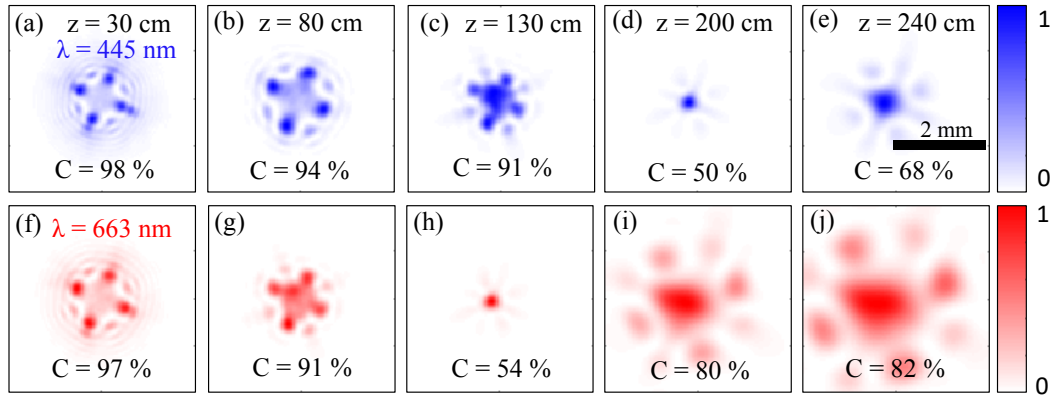
Figure 3.11: The intensity distribution of ALB at various propagation distances in a turbulent media for different wavelengths (a)-(e) $\lambda = 445$ nm, and (f)-(j) $\lambda = 663$ nm. Simulation parameters: $\alpha = 3.5$ mm^{-2}, $q = 2, m = 4, \sigma_0 = 1.35$ mm, $\lambda = 1064$ nm, $C_n^2 = 10^{-12}$ m$^{2/3}$, $L_0 = 10$ m, and $l_0 = 0.001$ m. Phase screen is prepared for propagation of ALB in the turbulent medium of length 2 m.

in the wavelength of ALB has no effect on the spatial intensity distribution, however, it affects the autofocusing distance (Eq. (3.2)). Here, we analyse the effect of turbulence on the autofocusing distance when the wavelength of ALB is varied. We impose a turbulent phase screen (as described above) simulated for wavelength $\lambda = 1064$ nm on ALB of different wavelengths, and then analysed its propagation. The results are shown in Fig. 3.11. Figures 3.11(a)-3.11(e) show the intensity distributions of ALB at various propaga-

tion distances in a turbulent media for a wavelength $\lambda = 445$ nm. As evident, the spatial intensity distribution of ALB is distorted due to turbulence, however, the ALB autofocuses at a distance ~ 200 cm. Figures 3.11(f)-3.11(j) show the intensity distribution of ALB in a turbulent media for a wavelength $\lambda = 663$ nm. The spatial distortion as well as autofocusing is again observed. However, the autofocusing distance is decreased by ~ 64 cm, and now ALB is focused at $z = 136$ cm. The values of C are obtained by calculating overlap integral (Eq. (1.26)) between ALBs in turbulent media and their respective ALBs in free space. A detailed plot for C as a function of propagation distance z is shown in Fig. 3.12. The variation in C can be described with the same reason as given above for Figs. 3.4 and 3.5. As evident, for each wavelength a dip with a minimum value of C is observed, indicating the value of z corresponding to an autofocusing distance of ALB. For
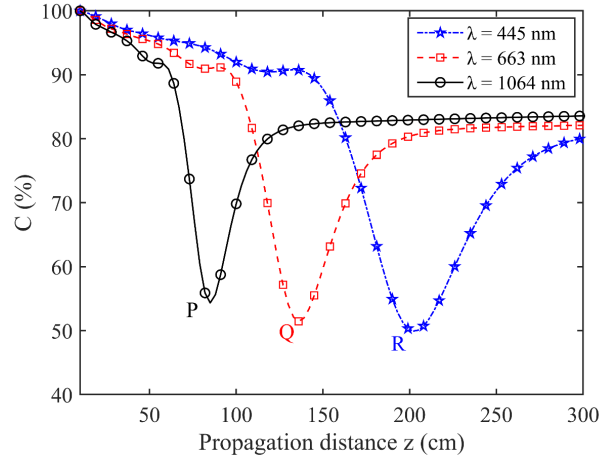
Figure 3.12: The overlap integral as a function of propagation distance for different wavelength $\lambda = 445$ nm (blue dot-dashed curve with stars), $\lambda = 663$ nm (red dashed curve with squares), $\lambda = 1064$ nm (black curve with circles). Points P, Q, and R indicate the autofocusing distances for the respective wavelengths.

the different wavelengths, the dip occurs at different values of z, indicating the spectral dependence of autofocusing distance. Specifically, the values of autofocusing distances are found to be 85 cm (for $\lambda = 1064$ nm), 136 cm (for $\lambda = 663$ nm), and 202 cm (for $\lambda = 445$ nm). The autofocusing distance decreases with the increase in wavelength. We have also calculated the autofocusing distances for propagation of ALBs in a free space using Eq. (3.2), and found the values of 84.36 cm (for $\lambda = 1064$ nm), 135.4 cm (for $\lambda = 663$ nm) and

201.7 cm (for $\lambda = 445$ nm). As evident, the simulated values of autofocusing distances are very close to the theoretical values, which indicates that the spectral dependence of autofocusing distance remains invariant in turbulent media.

3.5   Self-healing of ALBs in free space

We have investigated the self-healing of ALB in a free space. Specifically, we analyzed the effect of various types and amounts of truncation of ALBs on their self-healing abilities. For the quantification of self-healing, we calculate the overlap integral (Eq. (1.26)), which allows to identify the degree of similarity between the original and truncated beam [150]. The ALB is generated by illuminating DOE with an input Gaussian beam at $z = 0$ and then propagated up to a distance $z = 10$ cm so that ALB is well formed. The ALB is then truncated by an amplitude mask. The original and truncated beams are shown in Figs. 3.13(a) and 3.13(f), respectively. The truncation of main lobes leads to a decrease in the value of overlap integral to 58% (Fig. 3.13(f)). The truncated ALB is then propagated further to analyze the self-healing abilities (Figs. 3.13(f)-3.13(j)). For the comparison and quantification of overlap integral C, we have also propagated non-truncated ALB (ideal case), as shown in Figs. 3.13(a)-3.13(e).

   As evident, upon propagation of truncated ALB the energy from nearby areas moves into the truncated parts, and thereby it self-heals, as indicated by the complete recovery of the blocked main lobes (Figs. 3.13(g)-3.13(j)). However, as per the conservation of energy, the total energy contained in the beam will be smaller than the non-truncated beam, as a part of energy is removed by the truncation. The energy diffraction efficiency in the truncated beam is reduced to 68% with respect to the ideal ALB. The recovery of truncated lobes is also evidenced by the increased value of overlap integral. In addition to self-healing, the beam also retains the autofocusing property, as shown in Fig. 3.13(i). The ALB autofocuses at a distance $z = 85cm$, and also at this distance the beam completely self-heals, indicated by the maximum value of overlap integral $C = 99.53\%$. The autofocusing distance is found to be the same as in non-truncated case (Fig. 3.13(d)),
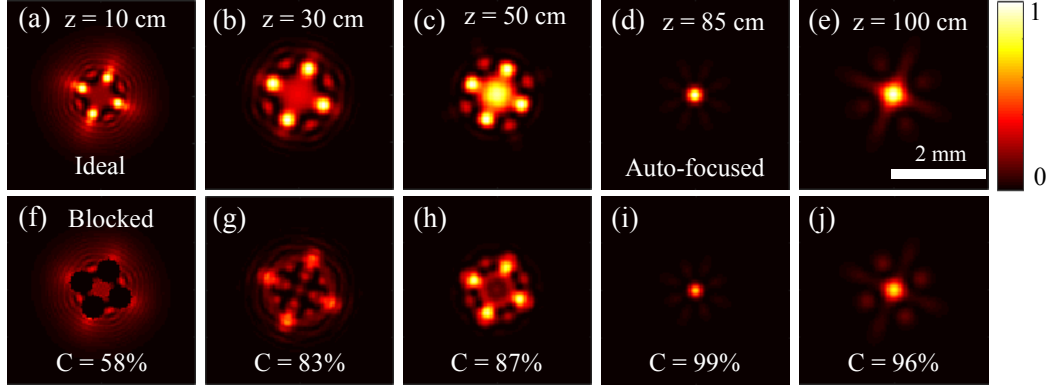
Figure 3.13: (a) The intensity distribution of ALB, showing a clear four lobes structure. (b)-(e) Intensity distribution of ideal ALB (non-truncated) at various propagation distances. (f) Intensity distribution of ALB with truncated lobes. (g)-(j) Intensity distribution of truncated ALB at various propagation distances. C denotes the calculated value of overlap integral with respect to the ideal case. The parameters for the ALB are $\alpha = 3.5 \text{ mm}^{-2}, q = 2, m = 4, \sigma_0 = 1.35$ mm, and $\lambda = 1064$ nm.

which also agrees with the theoretical value obtained from Eq. (3.2). Further, we have investigated how compound truncation with various percentages affects the self-healing abilities of ALB. The results are shown in Fig. 3.14. Figures 3.14(a)-3.14(e) show the propagation of a truncated beam, in which 20% of the beam area is blocked by an amplitude mask, in free space. As evident, the truncated ALB completely self-heals at the autofocusing distance $z = 85$ cm (Figs. 3.14(a)-3.14(e)), indicated by the maximum value of overlap C. The propagation of ALBs with 40% and 60% of truncations also shows that the maximum self-healing occurs at autofocusing distance $z = 85$ cm, which is evident from the maximum values of overlap C (Figs. 3.14(f)-3.14(j) and Figs. 3.14(k)-3.14(o)). From these results, it is clear that truncation of ALB does not affect the autofocusing distance as well as the self-healing distance. The self-healing can be understood by the fact that during the propagation of a truncated beam, the energy self-redistributes and flows towards the truncated parts, and slowly attains its original shape.

We have also calculated the overlap C as a function of propagation distance for various percentages of compound truncation, as shown in Fig. 3.15. It is found that the value of C increases with distance z, and reaches a maximum value, and after that, it again starts decreasing. The peak with highest C (marked by R in Fig. 3.15(a)) indicates a
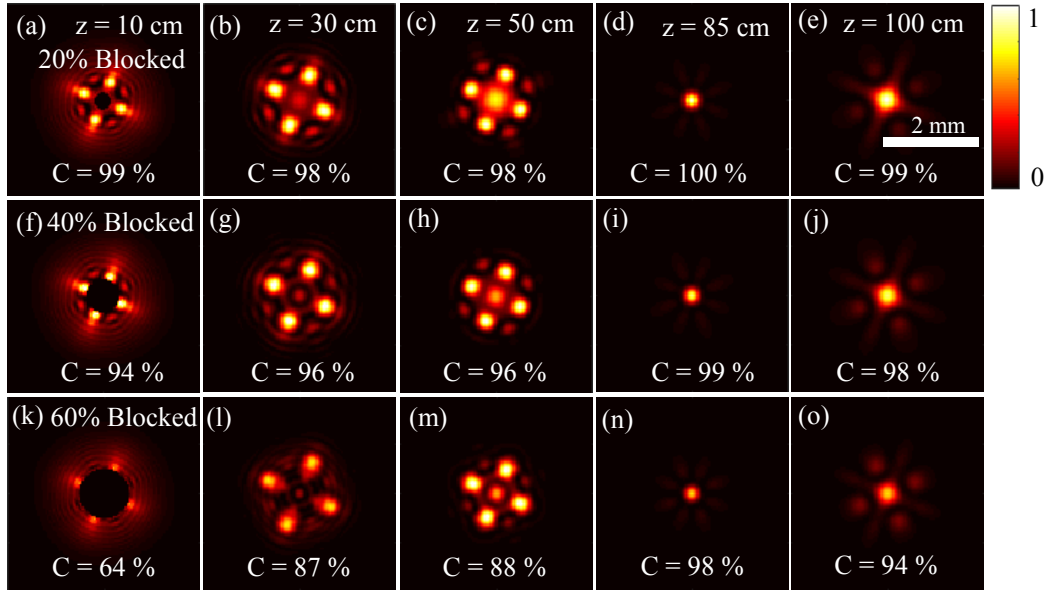
Figure 3.14: Self-healing of ALB when various percentages of beam are truncated. Intensity distribution at various propagation distances for the compound truncation of (a)-(e) 20%, (f)-(j) 40%, and (k)-(o) 60%. The corresponding values of overlap integral are written on them. The parameters for the ALB are $\alpha = 3.5$ mm$^{-2}, q = 2, m = 4, \sigma_0 = 1.35$ mm, and $\lambda = 1064$ nm.
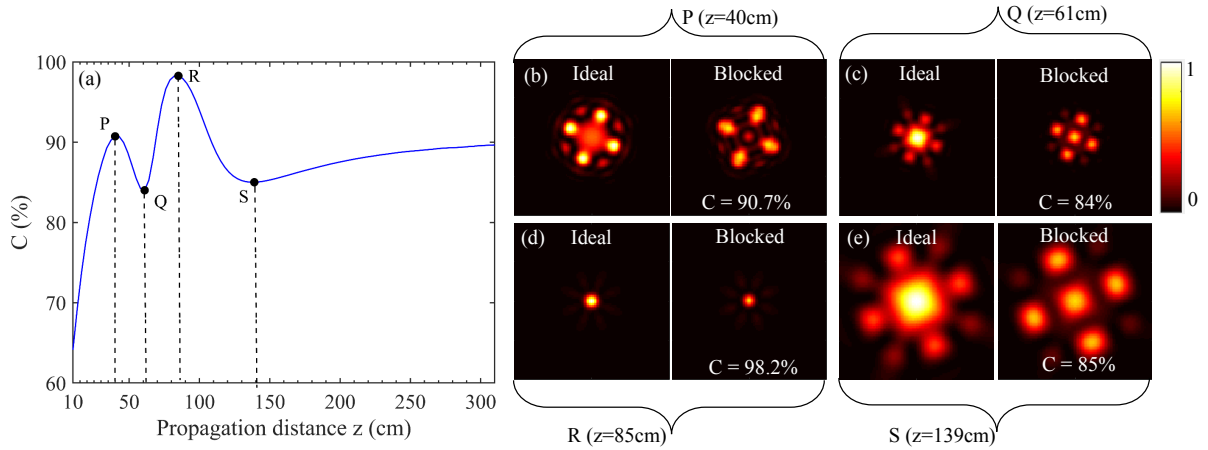
Figure 3.15: (a) The overlap integral as a function of propagation distance for 60 % of compound truncation. (b)-(e) The intensity distributions of truncated ALB together with the ideal non-truncated ALB, corresponding to points P, Q, R, and S. The parameters for the ALB are $\alpha = 3.5$ mm$^{-2}, q = 2, m = 4, \sigma_0 = 1.35$ mm, and $\lambda = 1064$ nm.

position at which truncated ALB recovers well, and shows maximum similarity with the ideal (original) beam at that propagation distance. Note that for the higher percentages of truncation, the value of C also becomes relatively smaller. The observation of another lower peak at P and minima at Q and S can be explained as follows. In free space, when a partially blocked ALB propagates, self-healing occurs due to the fact that different parts of the ALB interfere upon propagation, and redistribution of intensity takes place. Because of this, the spatial intensity distribution of ALB changes, which results a change in the values of overlap integral (marked by P, Q, and S in Fig. 3.15(a)). However, at the autofocusing distance, the ALB recovers maximally and a significant portion of intensity is tightly focused at the centre, and thus shows a high degree of similarity (high overlap integral value, marked by R) with an ideal ALB (unblocked ALB). After the autofocusing, upon further propagation the ALB defocuses and redistribution of intensity further takes place that results in the change of spatial intensity distribution of ALB, and thus the value of overlap integral again changes. Finally, when the spatial intensity distribution becomes stable, the overlap integral attains a constant value.

As evident, corresponding to points P, Q, R, and S (in Fig. 3.15 (a)), the Figs. 3.15 (b-e) show that the ideal and blocked beams have different spatial intensity distributions and therefore the value of C is different. After point S, the spatial intensity distribution of ALB changes slowly and tends to stabilise, and thus the value of C varies slowly and tends to approach a fixed value.

Furthermore, these beams (ALBs) show some other advantages such as, the self-healing distance being independent of the amount of truncation of ALB (as the self-healing reaches its maximum value for the same value of the propagation distance, i.e. autofocusing distance) which makes them different from the other beams exhibiting self-healing property.

Further, we have verified the autofocusing distance by analysing the intensity of ALB at the centre (on-axis), as it should increase to a maximum value at the autofocusing distance. Figure 3.16 shows cross-section of on-axis intensity of ALB as a function of propagation distance for various percentages of compound truncation. For the comparison, we have also included results for a non-truncated ALB. The on-axis intensities of

truncated beams are normalized with respect to the non-truncated beam (solid black curve). As evidenced, for all the cases of truncation the on-axis intensity becomes maximum (peak value) at $z = 85$ cm (which is the autofocusing distance of a non-truncated ALB, Fig. 3.13(d)), indicating that the truncation of ALB does not affect the autofocusing distance. The on-axis intensity at the autofocusing distance decreases with the increase of truncation, but the autofocusing properties remain invariant even after a large truncation of ALB (60%). These results clearly indicate that even if a major part of the
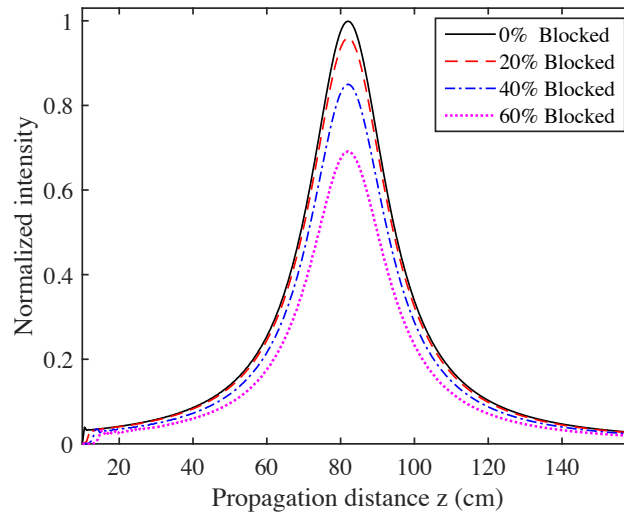
Figure 3.16: Cross-section of on-axis intensity of ALB as a function of propagation distance, for the various percentages of compound truncation.

beam is truncated, the ALBs do possess self-healing properties. Also, the truncation has no effect on the autofocusing distance of ALBs, indicating good robustness of ALBs.

To verify the simulation results of self-healing of ALB in free space, we have performed an experiment with the same parameter values. In the experiment, we have used a binary mask to truncate $\sim 25\%$ area of ALB (compound truncation) around center, which is kept at a distance of ~ 10 cm from the SLM. The truncated ALB is propagated further and intensity distribution is recorded at various propagation distances. The results are shown in Fig. 3.17. For the comparison, we have also recorded intensity distribution of an ideal ALB (non-truncated) at various propagation distances (Figs. 3.17(a)-3.17(e)). Figures 3.17(f)-3.17(j) show the intensity distribution of a truncated ALB at various prop-
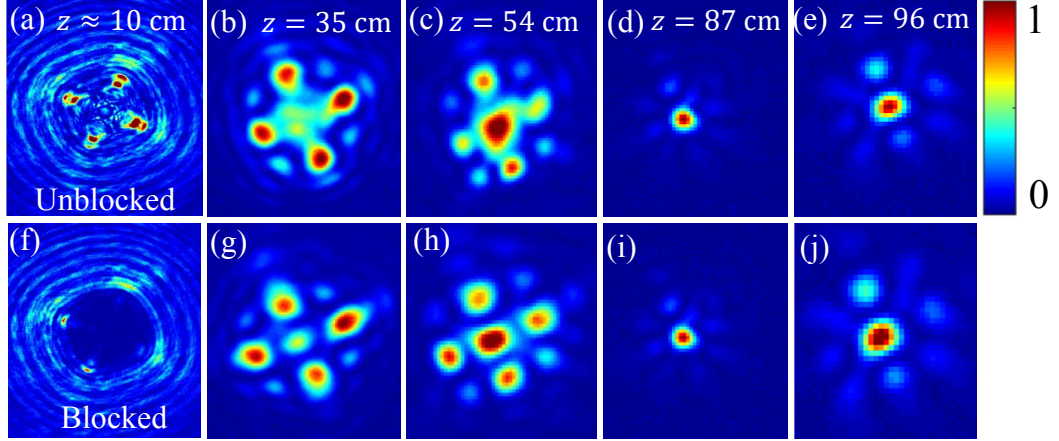
Figure 3.17: Experimental results of self-healing of ALB in free space, when $\sim 25\%$ area of ALB is truncated around the center. The parameters for the ALB are $\alpha = 3.5$ mm^{-2}, $q = 2$, $m = 4$, $\sigma_0 = 1.35$ mm, and $\lambda = 1064$ nm.

agation distances, which indicates that truncated ALB self-heals as well as autofocus. In both cases autofocusing is observed at the same distance $z = 87$ cm. The experimental results show good agreement with the simulations, which further confirms the self-healing abilities of ALB.

3.6 Self-healing in a turbulent media

We have also investigated the self-healing abilities of ALBs in a turbulent medium, the results are shown in Fig. 3.18. The ALB is considered with the same parameters as in Fig. 3.13 and then truncated differently by amplitude masks (Figs. 3.18(a) and 3.18(f)). Figures 3.18(b)-3.18(e) show the propagation in a strong turbulent medium with $C_n^2 = 10^{-12}$ m$^{2/3}$, when main lobes of the ALB are truncated. Whereas, Figs. 3.18(g)-3.18(j) show the propagation of a compound-truncated ALB in the same turbulent media. The C values in Figs. 3.18(a) and 3.18(f) show that the percentage of truncation is not the same in both cases. As evident, in both cases, the truncated parts of the ALBs recover upon propagation. However, as compared to Figs. 3.13 and 3.14, the spatial structure of ALB is distorted due to turbulent medium. The truncated ALBs show the autofocusing at a distance ~ 85 cm. As explained for the free space propagation in Figs. 3.13 and
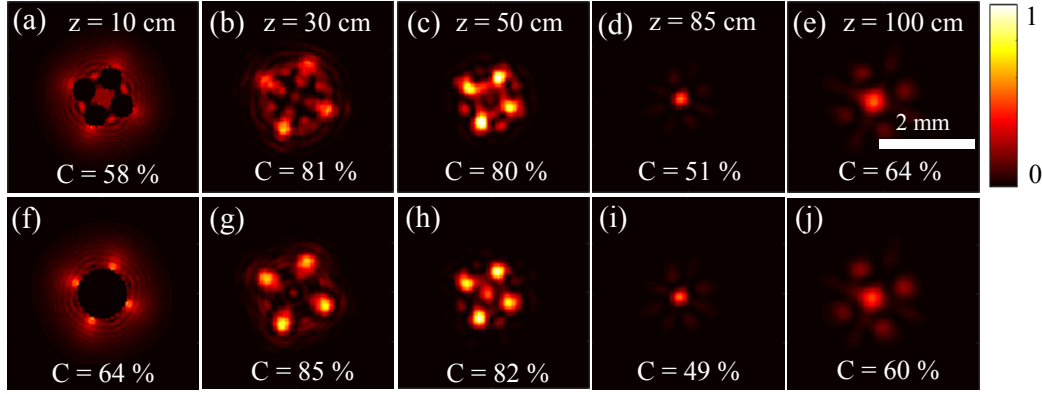
Figure 3.18:   The self-healing of ALBs in a turbulent media.   (a)-(e) Intensity distribution at various distances, when a lobe-truncated ALB is propagated in a turbulent media of strong turbulence strength. (f)-(j) Intensity distribution at various distances, when compound-truncated ALB is propagated in a turbulent media of the same strength. Simulation parameters: $\alpha = 3.5$ mm$^{-2}, q = 2, m = 4, \sigma_0 = 1.35$ mm, $\lambda = 1064$ nm, $C_n^2 = 10^{-12}$ m$^{2/3}$, $L_0 = 10$ m, and $l_0 = 0.001$ m.

3.14, the self-healing becomes maximum at autofocusing distance. In a turbulent medium, the maximum self-healing also occurs at the autofocusing distance. However, unlike the case in free space, a minimum value of overlap integral is observed at the autofocusing distance due to beam wandering effect, where a tightly focused energy beam is shifted from its original position, and distortion occurs in the spatial structure of ALB due to the presence of randomness in the phase. Further propagation after the autofocusing distance again leads to the defocusing of beam, and due to its large size, the beam exhibits more overlap with the non-truncated beam (at $z = 100$ cm), and hence an increased value of C is observed.

In a strong turbulent medium with $C_n^2 = 10^{-12}$ m$^{2/3}$, we have also analysed the self-healing of ALB with different percentages of compound truncation. The results are shown in Fig. 3.19. It is evidenced that ALB self-heals reasonably well for a compound truncation up to 60%. We have also checked for the increased compound truncation up to 80% (not shown here), and it is observed that ALB still can self-heal quite well.

Figure 3.19 shows the overlap C as a function of z for the various percentages of compound truncation of ALB. Again, a dip with a minimum value of C is observed at the same distance, corresponding to an autofocusing distance of non-truncated ALB (Fig.
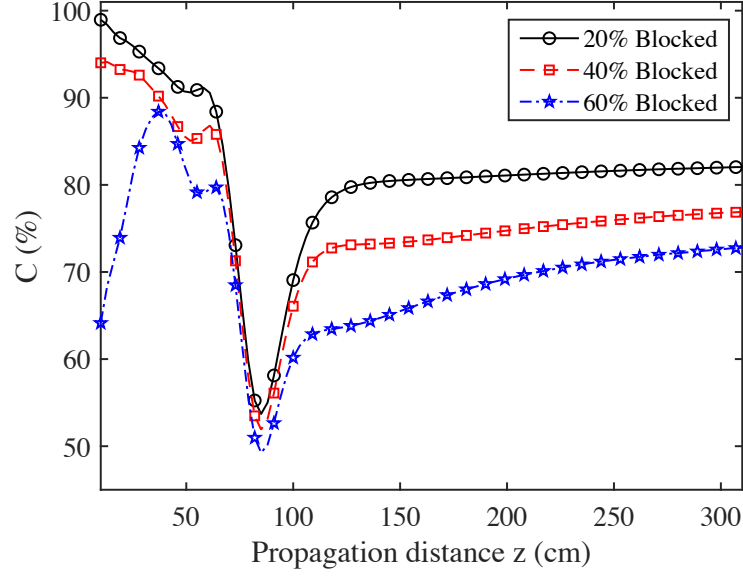
Figure 3.19: The variation of overlap C as a function of propagation distance for the various percentages of compound truncation.

3.13(d)). At this distance, the compound-truncated ALB exhibits a maximum self-healing.
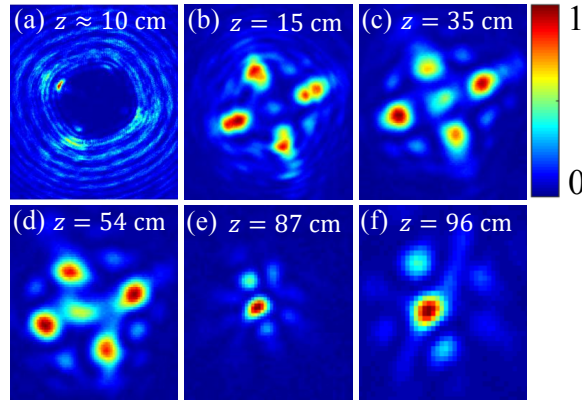
Figure 3.20: Experimental results. (a) Intensity distribution of truncated ALB. (b)-(f) Intensity distribution of truncated ALB at various propagation distances in a turbulent media (hot air at 110 ºC).

We have also recorded experimental results of self-healing of ALB in a turbulent medium. To do that we have truncated $\sim 25\%$ area of ALB from the center (Fig. 3.20(a)), and then propagated through hot air at temperature $110\,^0$C (Fig. 3.20(b)-3.20(f)). As evident, truncated ALB self-heals upon propagation as well as autofocuses at a distance of $z = 87$ cm, which shows a good qualitative agreement with numerical results (Fig. 3.18).

3 Aberration laser beams with controlled autofocusing and self-healing

We again observed the distortions in the spatial structure of ALB upon propagation, which is caused by the randomness in the turbulence.

3.7   Conclusions

In this Chapter, we have investigated outer-cavity based tailoring of light in the amplitude and phase degrees of freedom for generating ALBs containing multiple bright lobes and possessing exotic propagation properties, such as autofocusing and self-healing in both free space as well as in turbulent media [37]. The ALBs are generated from a DOE whose phase distribution consists of radial (r^q) and periodic angular dependence ($\sin m\phi$). The radial term in phase distribution provides the autofocusing properties, and autofocusing distance can be controlled from any small to large values by controlling the ALB parameters, such as λ, q, α, and input beam waist. Whereas, the presence of periodic angular dependence provides generation of diffraction pattern with m^{th}-order symmetry. Therefore, the intensity symmetrically distributes in various lobes depending on the m-values. We have investigated the effect of turbulence on the propagation (autofocusing) and self-healing properties of ALBs. First, we have analytically solved the extended Huygen-Fresnel integral for ALBs in turbulent media by using simple and complex stationary phase methods. Analytically, we have found that the autofocusing distance of an ALB does not change in the presence of turbulence. Further, we have verified our analytical findings in numerical simulations as well as in experiments. In numerical simulations, an ALB is propagated in turbulent media of different strengths (weak, intermediate, and strong) by means of random phase screens using Monte Carlo method, where turbulence strength is controlled by randomness in the phase distribution. Whereas, in experiments, turbulence is generated by hot air at different temperatures.

From numerical and experimental results we have found that the autofocusing of ALBs does not depend on the strength of turbulent medium, however, turbulence causes beam wander and distortions in the spatial intensity distribution of ALBs. To quantify the intensity distortions, an overlap integral is calculated. Further, overlap is found to be

minimum at autofocusing distance due to beam wandering and intensity distortions. We have also investigated the spectral dependence of autofocusing of ALBs in a turbulent medium and found that autofocusing distance does not depend on the turbulence, however, it decreases with an increase in wavelength.

Further, we have also investigated the self-healing of ALBs, both in free space as well as in turbulent media by propagating partially truncating ALBs. Owing to the redistribution of the intensity within the beam, ALBs show self-healing both in free space as well as in turbulent media. In particular, self-healing distance is found to be the same as autofocusing distance. It is also found that when a large portion of ALB ($\sim 60\%$) is truncated, the beam is still able to self-heal reasonably well. Further, for different percentages of truncation, the maximum self-healing always occurs at the auto-focusing distance, which remains invariant irrespective of amount of truncation and strength of turbulence. the self-healing distance remains the same. The ALBs are found to exhibit great robustness against truncation, which can be applied in various fields. The results presented in this Chapter are reported in Refs. [37, 39].

3.8 Appendix

3.8.1 Comparison between single-phase and multiple-phase screen methods
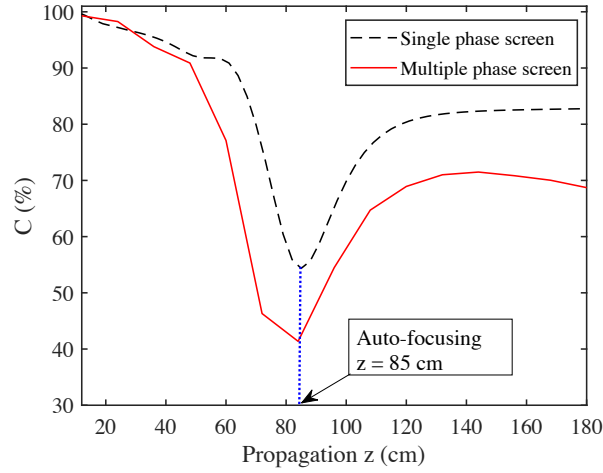
Figure 3.21: Comparison of results obtained from single phase screen method (black dashed curve) and multiple phase screen method (solid red curve). Simulation parameters: $\alpha = 3.5$, $q = 2$, and $C_n^2 = 10^{-12}\ m^{-2/3}$.

Here, we have compared the results obtained on the propagation of the ALB in turbulent media based on single-phase screen and multiple-phase screen methods. For the single-phase screen method, a turbulent phase screen is created for a propagation length of 1.8 m, representing a turbulent medium of length 1.8 m. The ALB is propagated through this turbulent medium, and overlap integral is calculated with respect to the free-space propagation, the results are shown in Fig. 3.21. For single-phase screen method (black dashed curve), a dip is observed at a distance $z = 85$ cm, which confirms the auto-focusing of ALB (also see Fig. 4.6). In the second method of multiple-phase screen, several phase screens are prepared corresponding to $\Delta z = 12$ cm and placed in the path of ALB at equal intervals. The obtained results are shown by a solid red curve in Fig. 3.21. Again, a dip is observed at the same auto-focusing distance ($z = 85$ cm) and provides similar information as was obtained from the single-phase screen method.

Chapter 4

Asymmetric aberration laser beams with controlled intensity distribution

4.1 Introduction

In previous Chapter 3, we have discussed the outer-cavity generation of ALBs, by tailoring amplitude and phase degrees of freedom of light. ALBs contain multiple bright lobes in a transverse plane and possess exotic propagation properties, such as controlled autofocusing and self-healing both in free space as well as in turbulent media [37]. In ALBs, the intensity is symmetrically distributed in all bright lobes and restricted to attain a precise control of intensity at arbitrary spatial locations. Further, ALBs always autofocus their intensity at on-axis center to create a high-energy density region, which can not be shifted to other spatial locations. These limitations on controlling intensity distribution of ALBs restrict their use for various applications. Therefore, in this Chapter, we present the generation of asymmetric aberration laser beams (aALBs) with controlled intensity distribution, based on an outer-cavity method using a diffractive optical element involving phase asymmetry.

Laser beams with controlled intensity distribution and containing high-energy densities are potentially crucial for improving light-matter interactions, thereby making laser

processing even more flexible, precise, and effective. For example, in material processing, the intensity distribution of a laser beam strongly influences the shape of heat-influenced zone [60]. Thus, by using controlled intensity distribution of laser beams, the processing quality and efficiency can be improved. More applications include metal or plastic welding, cladding, selective laser melting, hardening, brazing, and annealing.

It has been shown that asymmetry offers additional capabilities for controlling the laser intensity distribution [91]. Several types of asymmetric beams have been investigated, including Kummer laser beams with transverse complex shift, asymmetric Gaussian optical vortex, asymmetric Bessel modes, asymmetric Bessel-Gauss (BG) beams, asymmetric Laguerre-Gaussian (LG) beams, nonparaxial asymmetric Bessel beams, and paraxial asymmetric Bessel-Gaussian [91–95]. These beams have been exploited to form various types of optical tweezers that are used in many areas of physics. It has been shown that the rate of microparticle motion increases near linearly with increasing asymmetry of BG and LG beams [16, 222]. The LG beams with large asymmetry possess a crescent shape that rotates on propagation, which can be used for optical trapping and for controlling the motion of living cells without thermal damage [16, 223]. Such optical tweezers can be used to orient trapped objects and rotate during propagation. The asymmetric beams have also been used to generate a pair of entangled photons with broad orbital angular momentum using spontaneous parametric down-conversion [224].

Over the years, several other kinds of optical beams with distinct features have been theoretically proposed and realized experimentally. A few examples include Hermite-Gaussian beam [53], Airy beam [54], pin-like optical beam [55], abruptly auto-focused beam [50, 56], discrete vortex [43], and radial carpet beam [57]. In particular, ALBs have shown unique propagation properties and strong resilience against perturbations both in free space as well as in turbulent media [37], as detailed in Chapter 3. However, in ALBs, the autofocusing enables to obtain high-energy density focused spot, but spatially it always occurs at the centre of the beam, irrespective of parameters of ALB, as shown in Sec. 3.3 and in Refs. [37, 207, 225]. Further, the intensity in ALBs is symmetrically distributed in various bright lobes, and evolves symmetrically upon propagation, and

focuses tightly on a single spot at the autofocusing distance [37, 225]. It prevents us to precisely control the intensity distribution of ALB, thereby to form such high-energy density regions at desired spatial locations. Further, it also limits to control the shape of ALBs during the propagation. Although, ALBs possess several novel properties, but these limitations restrict their use for various applications as mentioned above. To overcome these limitations for enhancing the capabilities of ALBs for a wide range of applications, we have performed investigations to precisely control the intensity distribution of ALBs, and thereby to generate high-energy density regions at desired spatial locations.

In this Chapter, we have investigated asymmetric effects in the ALBs. Specifically, we have exploited asymmetry to precisely control the intensity distribution of ALBs to form asymmetric aberration laser beams (aALBs), and explored the mechanism of transfer of intensity inside the beam, and formation of the high-energy density regions at desired spatial locations. Further, the effect of asymmetry is also investigated on the autofocusing properties of aALBs. This study provides a more general framework for controlling the properties of aALBs, and making them potentially useful for a wide range of applications. A detailed analysis of asymmetric effects with quantification is presented. In Sec. 4.2, we have given an analytical description of asymmetric aberration laser beams (aALBs). In Sec. 4.3, we have described the experimental generation and numerical simulations of aALBs and compared their propagation properties with ideal ALB. In Sec. 4.4, we have described the role of different asymmetric parameters on the intensity distribution of aALBs. In Sec. 4.5, we present the results on spatial control of high-energy density regions in aALBs. Finally, in Sec. 4.7 concluding remarks are presented. The investigations presented in this Chapter are given in Refs. [38, 40].

4.2　Theoretical description

The expression of phase of ALB is given by [207, 225]

$$\xi(r, \phi) = \exp(-i\alpha r^q + i\sin(m\phi)) \quad r \leq R \tag{4.1}$$

such that

$$r \exp(i\phi) = x + iy, \quad r^2 = x^2 + y^2. \tag{4.2}$$

Here, q represents radial power, m is an integer, which controls the lobe structure in ALB, and α is a scale parameter, has a dimension of mm^{-q}, R is the radius of the diffractive optical element (DOE). The presence of periodic angular dependence in phase distribution provides generation of diffraction pattern with mth-order symmetry. The term $\exp(-i\alpha r^q)$ represents the transmission function of a generalized parabolic lens [226]. An optical element encoded with the above phase function is same as that of a zone plate with circular lines. The diffractive version of such a phase element is equivalent to a classical lens (quadratic phase dependence on radius) [227]. The circular Airy beams, which have an asymptotic phase dependence proportional to $r^{3/2}$, are regarded as autofocusing beams [50,228]. The beams with a dependence on r^q with $1 < q < 2$ have also been investigated [229]. The ALBs with a radial dependence r^q, where q takes any positive value ($q > 0$), including $q > 2$, the autofocusing has also been observed [207]. The ALBs possess greater flexibility in managing autofocusing properties as compared to circular Airy beams [207,227].

Further, to generate aALBs the phase asymmetry is introduced by complex coordinate shifting in Eq. (4.1) [91], we have

$$\xi = \exp(-i\alpha s^q + i\sin(m\theta)) = \exp\left(-i\alpha(s^2)^{q/2}\right)\exp(i\sin(m\theta)), \tag{4.3}$$

where,

$$s^2 = (x - x_o)^2 + (y - y_o)^2, \tag{4.4}$$

$$x_o = a + ib, \quad y_o = c + id, \quad a, b, c, d \in \mathbb{R}. \tag{4.5}$$

For the new polar coordinates p and θ:

$$p \exp(i\theta) = (x - x_o) + i(y - y_o) = (x - a + d) + i(y - c - b). \tag{4.6}$$

The angular coordinate θ is given by

$$p\,\cos(\theta) = (x - a + d),\ p\,\sin(\theta) = y - c - b, \tag{4.7}$$

$$\theta = \tan^{-1}\left(\frac{y - c - b}{x - a + d}\right). \tag{4.8}$$

The modified phase due to complex coordinate shifting can be calculated from Eq. (4.3). For simplification, we have taken $x - a = X$ and $y - c = Y$. Thus,

$$s^2 = (X^2 + Y^2 - b^2 - d^2) - i(2Xb + 2Yd), \tag{4.9}$$

$$= G\,\exp(i\gamma), \tag{4.10}$$

where,

$$G\,\cos(\gamma) = (X^2 + Y^2 - b^2 - d^2), \tag{4.11}$$

$$G\,\sin(\gamma) = -2(Xb + Yd). \tag{4.12}$$

Substituting s^2 into Eq. (4.3), we get

$$\begin{aligned}
\xi &= \exp(-i\alpha(G\exp(i\gamma))^{q/2})\exp(i\sin(m\theta)), \\
&= \exp\left(-i\alpha G^{q/2}\exp\left(i\frac{q\gamma}{2}\right)\exp(i\sin(m\theta)\right), \\
&= \exp(-i\alpha G^{q/2}(\cos(q\gamma/2) + i\sin(q\gamma/2)))\exp(i\sin(m\theta)), \\
&= \exp(-i\alpha G^{q/2}\cos(q\gamma/2) + i\sin(m\theta))\exp(\alpha G^{q/2}\sin(q\gamma/2))
\end{aligned} \tag{4.13}$$

The term $\exp(\alpha G^{q/2}\sin(q\gamma/2))$ is a real quantity and does not contribute to the phase, thus the phase expression is reduced as

$$\xi \approx \exp\left(-i\alpha\,G^{q/2}\cos\left(\frac{q\gamma}{2}\right) + i\sin(m\theta)\right), \tag{4.14}$$

As explained in Chapter 3, for the case of $q = 2$, ALB shows more prominent abrupt autofocusing, and it also provides more peculiarities, such as it becomes equivalent to a

4 Asymmetric aberration laser beams with controlled intensity distribution

simple lens and the mathematical analysis is significantly simplified [37, 225]. Therefore, in the present work, all the experimental results and most of the numerical simulations are presented for $q = 2$. Note, some of the numerical simulations are also presented for $q \neq 2$ (see Sec. 4.6). Now, for $q = 2$, Eq. 4.14 becomes:

$$
\begin{aligned}
\xi &= \exp(-i\alpha\, G\, \cos(\gamma) + i\sin(m\theta)), \\
&= \exp(-i\alpha\,((x-a)^2 + (y-c)^2 - b^2 - d^2) + i\sin(m\theta)).
\end{aligned}
\tag{4.15}
$$

The expression for θ and its dependence on parameters is given by Eq. (4.7). It can be readily noticed that the parameters a and c (real part of x_0 and y_0) are just shifting the origin in a real two-dimensional (2D) plane. From a practical point of view, it will just simulate the effect of a misaligned or off-axis input beam. By choosing $a = c = 0$, we impose the axis-to-axis alignment of an input beam with the DOE. This new modified phase for ALB can be expressed as

$$
\xi = \exp(-i\alpha\,(x^2 + y^2 - (b^2 + d^2)) + i\sin(m\theta)),
\tag{4.16}
$$

where,

$$
\theta = \tan^{-1}\left(\frac{y - b}{x - (-d)}\right).
\tag{4.17}
$$

It can be seen that for the part of chirped phase asymmetry parameters b and d are just rescaling the radius of concentric circles (origin $(0, 0)$). Whereas, in trigonometric term ($\exp(i\sin(m\theta))$, asymmetry shifts the origin to $(b, -d)$ locally. The asymmetry parameters b and d can be expressed in terms of angular parameters (w, β), which only relocates the origin for trigonometric phase without changing the functional form of chirped phase, as described below.

$$
d = -w\,cos(\beta), \quad b = w\,\sin(\beta).
\tag{4.18}
$$

Considering an input laser beam with fundamental transverse mode (Gaussian), the op-

tical field of an asymmetric ALB (aALB) can be written as

$$E(r, \theta) = \exp\left(\frac{-r^2}{2\sigma_0^2}\right) \exp\left(-i\alpha(r^2 - w^2) + i\sin(m\theta)\right). \tag{4.19}$$

The condition $0 < w^2 < 2\sigma_0^2$ makes sure that the asymmetric effects are well aligned with an input Gaussian beam. It should be noted that the symmetry of trigonometrically modulated phase is decided by parity of m [230]. As $\sin(m(\theta + \pi)) = \pm\sin(m\theta)$, the diametrically opposite points on phase distribution will be in and out of phase for even and odd parity, respectively. In earlier studies, it has been shown that the diffraction pattern of such a phase distribution consists of a number of bright spots depending upon the value of m [199]. In our work, we have considered the case of $m = 3$, however, similar findings can be obtained for other values of m. For $\sigma_0 = 1.45$ mm and $m = 3$, we find that the value of $w = 1$ mm introduces appreciable asymmetry into the phase of aALB. So, we have kept these parameters same throughout the work.
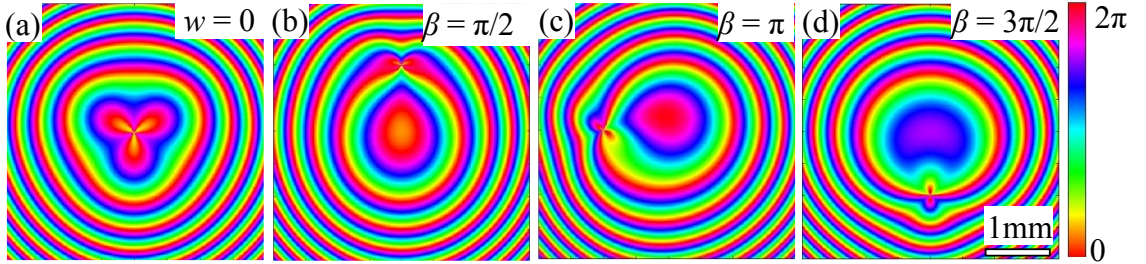
Figure 4.1: The phase distribution of DOE with (a) $w = 0$, $\beta = [0, 2\pi]$, (b) $w = 1$ mm, $\beta = \pi/2$, (c) $w = 1$ mm, $\beta = \pi$, (d) $w = 1$ mm, $\beta = 3\pi/2$. The other parameters are $m = 3$, $q = 2$, $\alpha = 5.9$ mm^{-2}.

The phase distributions of DOEs for generating the ideal and asymmetric ALBs are shown in Fig. 4.1. Figure 4.1(a) shows the DOE of an ideal ALB ($w = 0$). As substituting $w = 0$ in Eqs. (4.16)-(4.18), gives rise to Eq. (4.1) for an ideal ALB. Figures (4.1(b)-4.1(d)) show the DOEs of an asymmetric ALB (aALB) with different asymmetry parameters β. As evident, different values of β provide a different phase distribution of DOE and thereby provide an ability to control the propagation properties of aALBs.

4.3 Propagation of asymmetric ALBs

The schematic of experimental arrangement for the generation and characterization of aALBs is schematically shown in Fig. 4.2. We have generated aALBs by using the same experimental method used to generate ALBs in Chapter 3 (Fig. 3.8). A linearly polarized
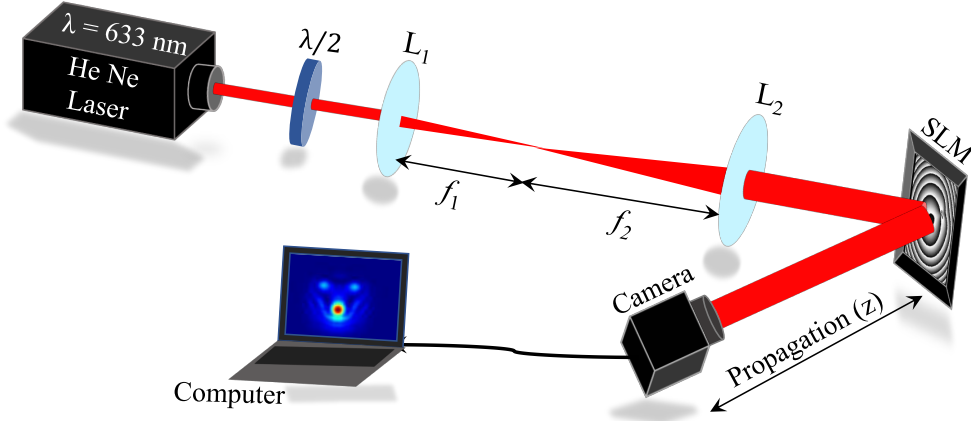
Figure 4.2: Experimental arrangement for generation and characterization of asymmetric ALB. L_1 and L_2: plano-convex lenses of focal length $f_1 = 5$ cm and $f_2 = 20$ cm, respectively. $\lambda/2$: half-wave plate, SLM: spatial light modulator.

light from a He-Ne laser ($\lambda = 632$ nm) incident on a half-wave ($\lambda/2$) plate to fix the polarization orientation in a specific direction. After that light is passed through a telescope made with lenses L_1 ($f_1 = 5$ cm) and L_2 ($f_2 = 20$ cm) to magnify its size in order to illuminate well the screen of a phase-only spatial light modulator (SLM). We impose a phase pattern (DOE) on the SLM, which modulates the phase of the incident light, and after propagating a certain distance aALB is formed. The intensity distribution of aALB at different propagation distances is recorded on a CCD camera.

Further, we have numerically simulated the propagation of an aALB using an extended Huygens-Fresnel integral as (Eq. (1.18))

$$
\begin{aligned}
E(\rho, \phi, z) &= -\frac{ik}{2\pi z}\exp(ikz)\exp\left(\frac{ik}{2z}\rho^2\right)\int\int E(r,\theta)\exp\left(\frac{ik}{2z}r^2\right) \\
&\times \exp\left(-\frac{ik}{z}\rho r\cos(\theta - \phi)\right)rdrd\theta,
\end{aligned}
\tag{4.20}
$$

where (r, θ) and (ρ, ϕ) represent coordinates of source and observation (output) planes, respectively, separated by a distance z. $k = 2\pi/\lambda$ represents the wave number of an optical field in free space.

The experimental and simulation results are shown in Fig. 4.3, presenting a comparison between the propagation of ideal ALB and aALB. The results are presented for parameter values of $m = 3$, $q = 2$, $\alpha = 5.9$ mm^{-2}. For aALB, the asymmetry parameters are taken as $w = 1$ mm and $\beta = \pi/2$. Figures. 4.3(a1)-4.3(e1) and Figs. 4.3(a2)-4.3(e2) show the
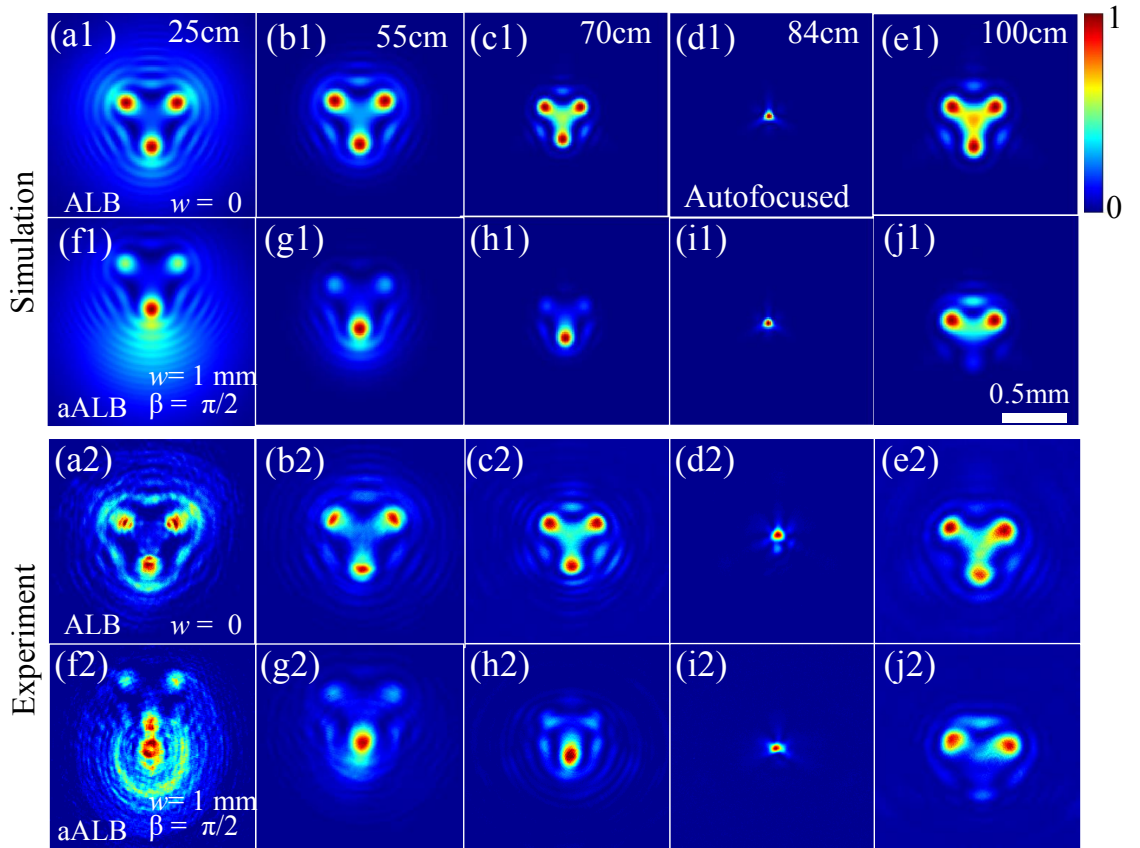
Figure 4.3: The intensity distributions of ideal ALB ($w = 0$) ((a1)-(e1), (a2)-(e2)) and aALB ($w = 1$ mm, $\beta = \pi/2$) ((f1)-(j1), (f2)-(j2)) at different propagation distances $z = 25$ cm, 55 cm, 70 cm, 84 cm, and 100 cm. The results are obtained for the following parameters: $\alpha = 5.9\,\text{mm}^{-2}$, $\sigma_0 = 1.45\,\text{mm}$, m = 3, q = 2 and $\lambda = 632$ nm.

simulation and experimental results of intensity distributions of an ideal ALB at different propagation distances, respectively. As evident, for $m = 3$ there are three bright lobes having equal intensity within them. During the propagation, the intensity from back-

ground moves inside the bright lobes, and evolution of intensity remains symmetrically as all three bright lobes are equally intense (Figs. 4.3(a1)-4.3(c1), Figs. 4.3(a2)-4.3(c2)). At a distance $z = 70$ cm, the bright lobe pattern is fully developed, as most of the intensity from all parts of the beam shifted equally into them. After further propagation, the bright lobe pattern starts shrinking by merging of bright lobes. At a distance $z = 84$ cm, all three bright lobes collapsed into a tightly focused single bright spot, called the autofocusing distance ($z = z_{af}$) (Figs. 4.3(d1) and 4.3(d2)). After autofocusing distance, the bright lobes again get separated and intensity distributes symmetrically and equally among them. Figures. 4.3(f1)-4.3(j1) and Figs. 4.3(f2)-4.3(j2) show the simulation and experimental results of intensity distributions of aALB at different propagation distances, respectively. As evident, by introducing asymmetry using complex coordinate shifting ($w = 1$ mm and $\beta = \pi/2$), the symmetry of equal intensity distribution in three bright lobes gets disturbed (Figs. 4.3(f1)-4.3(h1) and Figs. 4.3(f2)-4.3(h2)). More specifically, instead of three equal intensity bright lobes, the intensity in the bottom single bright lobe is larger than the top two bright lobes. Further, as aALB propagates there is a continuous transfer of intensity between the bright lobes. At $z = 70$ cm, the intensity in the upper two bright lobes reduced dramatically and enhanced significantly in the bottom bright lobe (Figs. 4.3(h1) and 4.3(h2)). It should be noticed that, for an ideal ALB, the lobes pattern develops around on-axis (beam axis) (Fig. 4.3(a1), 4.3(a2)). Whereas, for aALB, initially the lobes pattern develops around the point (w, β), and after that, it moves towards on-axis. At autofocusing distance $z = 84$ cm, again a tightly focused single bright spot centered on the beam axis is observed (Figs. 4.3(i1) and 4.3(i2)). After autofocusing distance, the intensity again redistributes such that it becomes larger in the upper two bright lobes as compared to the bottom bright lobe (Figs. 4.3(j1) and 4.3(j2)).

We have found that the autofocusing distance remains the same for both ideal ALB and aALB. However, for aALB, the asymmetry leads to a controlled variation of intensity distribution with the propagation distance, which can be used in guiding micro-particles longitudinally on a desired path. The asymmetry induced variation in the intensity distribution has also been observed with other beams such as LG, Bessel, Bessel-Gauss,

and Kummer laser beams [91–95]. For an ideal ALB, the relationship between the beam parameters and autofocusing distance is given as [225]

$$z_{af} \approx \frac{2\pi}{q\alpha\lambda(2\sigma_0/3)^{q-2}}.$$
$$(4.21)$$

By tuning the beam parameters, the autofocusing distance can be varied from small to large values.
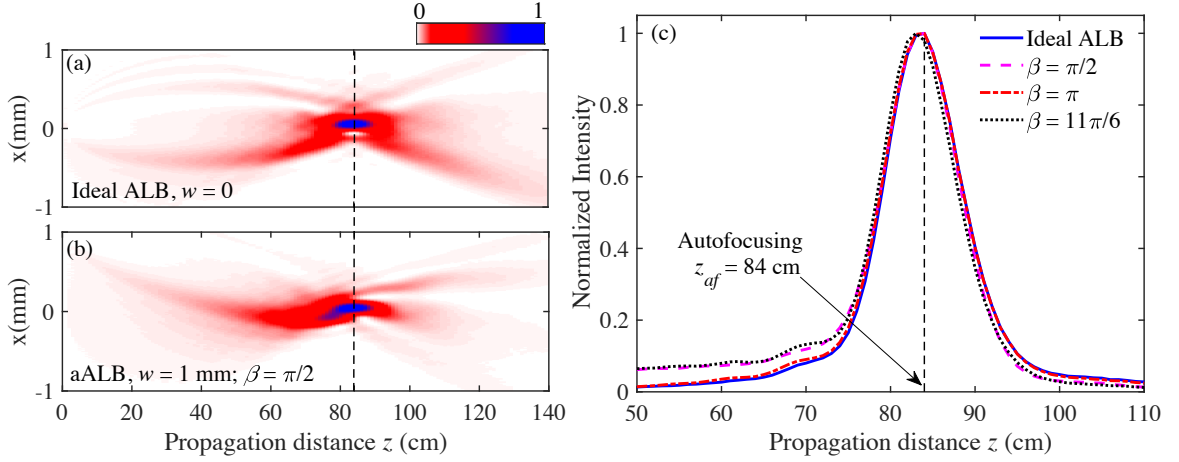
Figure 4.4: (a) Intensity distribution of an ideal ALB as a function of propagation distance. (b) The intensity distribution of an aALB (with $w = 1$ mm and $\beta = \pi/2$) as a function of propagation distance. (c) Longitudinal intensity cross-section is taken along the horizontal axis (at $x = 0$) (on-axis intensity) in (a) and (b), as a function of z. The blue solid curve: ideal ALB; dashed pink curve: aALB with $\beta = \pi/2$; dash-dotted red curve: aALB with $\beta = \pi$; dotted black curve: aALB with $\beta = 11\pi/6$. The parameters are taken as $w = 1$ mm, $\sigma_0 = 1.45$ mm, $\alpha = 5.9$ mm^{-2}, $m = 3$, $q = 2$ and $\lambda = 632$ nm. z_{af} denotes the autofocusing distance.

To check the dependence of autofocusing distance on asymmetry parameter β, we have propagated aALB with different β values and then analyzed on-axis intensity distribution. The results are shown in Fig. 4.4. Figures 4.4(a) and 4.4(b) show the propagation of an ideal ALB and aALB with $\beta = \pi/2$. As evidenced, the on-axis intensity peak is observed at $z = 84$ cm in both cases (marked by a vertical dashed-line), denotes the autofocusing distance. Figure 4.4(c) shows the longitudinal intensity cross-section taken along the horizontal axis ($x = 0$), indicating that on-axis intensity peak occurs at the same z value for ideal ALB and aALB with different β values, which shows that the autofocusing

distance remains invariant with respect to the asymmetry. Note, the 2D intensity plots for aALB with $\beta = \pi$ and $11\pi/6$ are not shown. The observed value of autofocusing distance agrees with the calculated value of $z_{af} = 84.25$ cm (Eq. (4.21)) for an ideal ALB. Similar to ideal ALB, the autofocusing distance of aALB can be controlled from small to large values by varying the beam parameters (q, α, λ, σ_0). Note, we have also verified the autofocusing properties for $q \neq 2$, and a similar trend is observed in the numerical results, except that the autofocusing distance will be different.

4.4   Intensity Distribution for different β
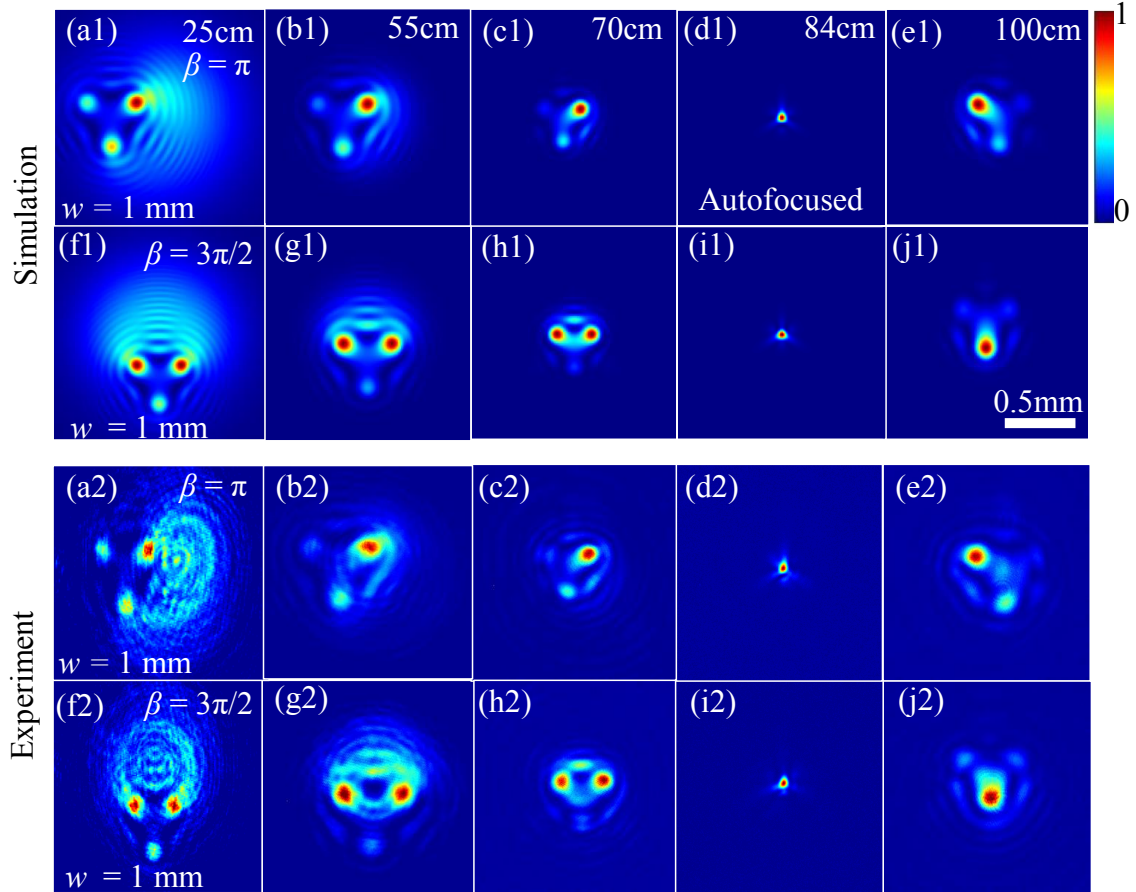
Figure 4.5: Intensity distribution of aALB at various propagation distances, for different values of β. ((a1) - (e1), (a2) - (e2)) $\beta = \pi/2$, and ((f1)-(j1), (f2) - (j2)) $\beta = 3\pi/2$. The results are obtained for the following parameters: $\alpha = 5.9\,\text{mm}^{-2}$, $\sigma_0 = 1.45\,\text{mm}$, $m = 3$, $q = 2$ and $\lambda = 632$ nm.

To generalize and gain a better understanding, we have further varied the phase asymmetry and analyzed its effect on the intensity distribution of aALBs. The results are shown in Fig. 4.5. Figures. 4.5(a1)-4.5(e1) and Figs. 4.5(a2)-4.5(e2) show the simulation and experimental results for an asymmetry parameter $\beta = \pi$, respectively. Figures 4.5(f1)-4.5(j1) and Figs. 4.5(f2)-4.5(j2) show the results for $\beta = 3\pi/2$. Note, for $\beta = \pi/2$, the results are shown in Fig. 4.3. As evident, the asymmetry leads to a significant change in the intensity distribution of aALB. For different values of β the intensity in the background as well as inside bright lobes migrates differently, thereby enabling a controlled intensity distribution of aALB. For example, for $\beta = \pi$ a greater portion of intensity can be transferred to a single bright lobe (Figs. 4.5(c1) and 4.5(c2)). Whereas, for $\beta = 3\pi/2$, the intensity transfers into two bright lobes (Figs. 4.5(h1) and 4.5(h2)). By a careful choice of β values, one can control the intensity distribution precisely. As mentioned above, for any asymmetry value, initially (for small z values) beam develops around the coordinates $(w,\ \beta)$, so spatial position of three bright lobes pattern (triangular pattern for $m = 3$) appears off-centered (Figs. 4.5(a1), 4.5(f1), 4.5(a2) and 4.5(f2)) from the on-axis. As the beam propagates for longer z values, in addition to migration of intensity into bright lobes, the spatial position of bright lobes pattern also moves towards the on-axis center. At autofocusing distance $z = 84$ cm, the intensity becomes tightly focused to a single bright spot (Figs. 4.5(d1), 4.5(i1), 4.5(d2) and 4.5(i2)). After the autofocusing distance (at $z = 100$ cm), the intensity distribution again changes depending on the value of β.

The off-centered position of the bright lobes pattern is quite evident at distance $z = 25$ cm (Figs. 4.5(a1), 4.5(f1), 4.5(a2) and 4.5(f2)) as well as for the small values of z. This can be attributed to the fact that the spatial position of indeterminate phase point [231] of trigonometric phase $(\exp(i\sin(3\theta)))$ is correlated with the asymmetry parameters $(w,\ \beta)$ (Eqs. (4.16)-(4.18)), as shown in Fig. 4.6. For an ideal ALB, the on-axis center of an input beam and indeterminate phase point coincide, and as a result of propagation, it leads to the formation of a three bright lobes pattern with triangular symmetry (Figs. 4.6(a)). However, for aALB (non-zero value of w), the indeterminate phase point does not coincide with the on-axis center of an input beam. Figures 4.6(b)-4.6(c) show the change in the
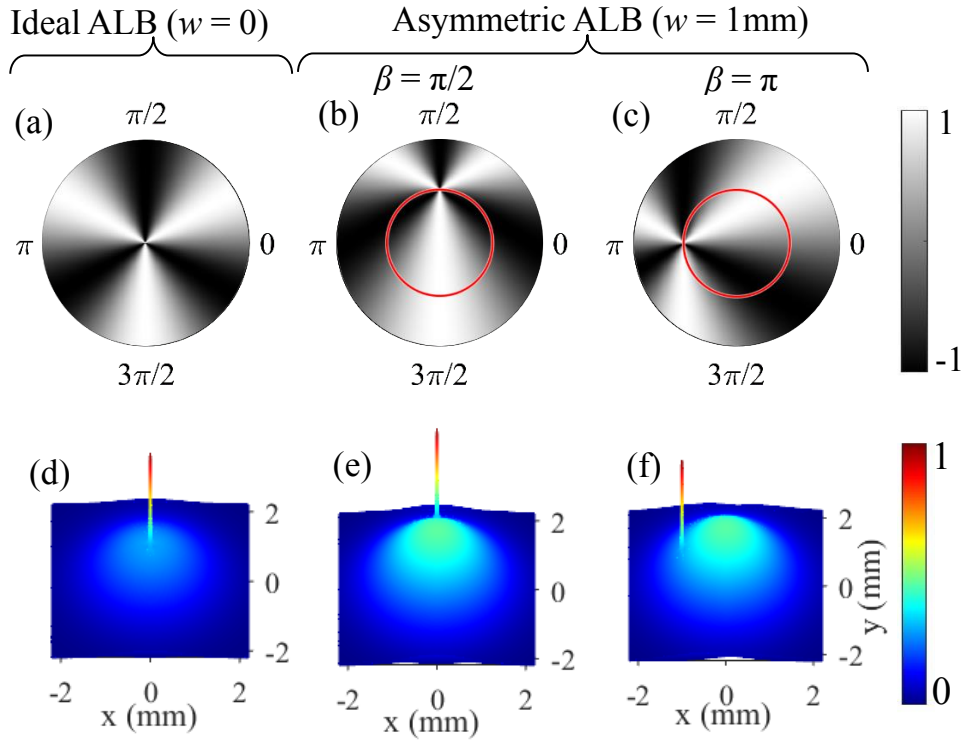
Figure 4.6: Trigonometric Phase ($\exp(i \sin(3\theta))$) for (a) $w = 0$ and $\beta = [0, 2\pi]$, (b) $w = 1$ mm, $\beta = \pi/2$, (c) $w = 1$ mm, $\beta = \pi$. A red circle of radius 1 mm with centre(0,0) is drawn to show the effect of asymmetry. (d)-(f) The intensity distribution of ideal ALB and aALB at $z = 0.027$ cm (near-field), corresponding to the phase distributions given in (a)-(c). The other simulation parameters are taken as $\alpha = 5.9$ mm^{-2}, $\sigma_0 = 1.45$ mm, $m = 3$, $q = 2$, and $\lambda = 632$ nm.

position of indeterminate phase point with the coordinates (w, β). A circle of radius 1 mm with center (0,0) is drawn to show the shifting of an indeterminate phase point from the center. This shift due to the asymmetry affects significantly the intensity distribution of aALB during the propagation. When both ideal ALB and aALB are propagated by a small distance $z = 0.027$ cm (near-field plane (close to DOE plane)), a peak with maximum intensity (say maximum intensity point (MIP)) on top of Gaussian distribution starts appearing at the precise location of indeterminate phase point (Figs. 4.6(d)-4.6(f)), which then helps to initially develop the bright lobes pattern in aALB, off-centered at coordinates (w, β). Upon propagation to large distances, this leads to an asymmetric intensity distribution, which can be precisely controlled by varying w and β, as shown in Figs. 4.3 and 4.5.

A detailed plot for varying the position of near-field MIP with asymmetry parameters (w, β) is shown in Fig. 4.7. The position of near-field MIP is extracted from aALB at
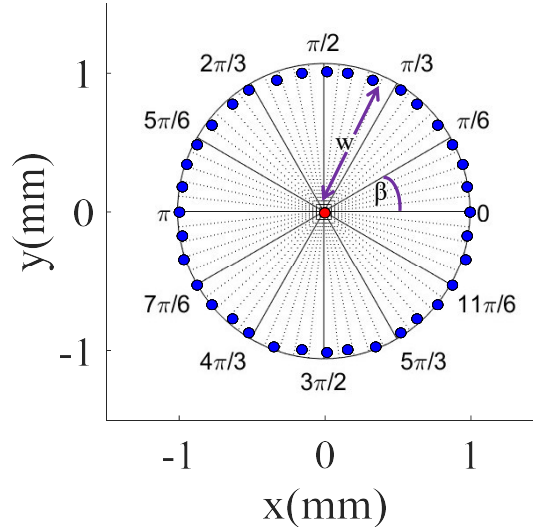
Figure 4.7: The positions of near-field MIP for different asymmetry parameters w and β. The position of near-field MIP is extracted from aALB at $z = 0.027$ cm. Red filled circle: MIP for an ideal ALB ($w = 0$); Blue filled circle: MIP for aALB ($w = 1$ mm).

$z = 0.027$ cm (Figs. 4.6(d)-4.6(f)). In Fig. 4.7, a red-filled circle in the center represents the location of a near-field MIP for ideal ALB (a special case of aALB for $w = 0$), and blue-filled circles denote the near-field MIPs for aALB ($w = 1$ mm).

We have also investigated the formation of MIP at $z = 0.027$ m, and its role in

developing high-intensity region around the coordinates (w, β) (shown in Fig. 4.8). As evident, due to asymmetry, a bright peak on the left of Gaussian distribution (MIP) starts to appear (Fig. 4.8(a)), which then initiates the development of bright lobes off-centered from the on-axis center (Figs. 4.8(b)-4.8(c)). With the propagation, the intensity keeps shifting from the background to bright lobes. Unlike ideal ALB, in aALB due to asymmetry, the intensity shifts inside the bright lobes asymmetrically. For a specific set of asymmetry parameters, it completely shifts in one of the bright lobes. Further, during the propagation over larger distances, the bright lobes shift toward the on-axis center, as shown in Figs. 4.8(d)-4.8(f).
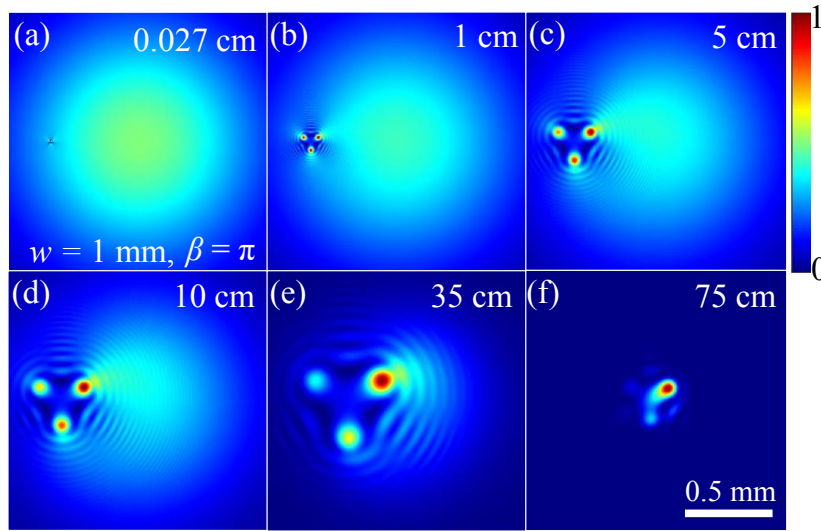
Figure 4.8: Intensity distribution of aALB for $\beta = \pi$ at various propagation distances z (a) 0.027 cm, (b) 1 cm, (c) 5 cm, (d) 10 cm, (e) 35 cm, (f) 75 cm. The other parameter values are $w = 1$ mm, $\alpha = 5.9$ mm^{-2}, $\sigma_0 = 1.45$ mm, $m = 3$, $q = 2$ and $\lambda = 632$ nm.

4.5   Spatial control of high-energy density regions

Autofocusing enables to obtain high power density focused spot, but spatially it always occurs at on-axis center of the beam, irrespective of parameters of ALB. In the ALB, the intensity symmetrically distributes in various lobes depending on m values, and evolves symmetrically, and focuses tightly on a single spot at the autofocusing distance. It prevents precise control of the spatial position of such high-energy density regions. However,

by introducing asymmetry, the high-energy density region can be formed by controlled transfer of intensity within the beam before and after the autofocusing distance and can be tuned to different desired spatial positions. Now, the question is for which set of asymmetry parameters such high-energy density lobes can be obtained at different desired spatial positions. So we have explored the correlation between the asymmetry parameters and the spatial position of bright lobes.

From Fig.4.4(c), it can be seen that a sharp rise of intensity due to autofocusing phenomenon occurs near the value of $z = 70$ cm. After this distance, the lobes in the pattern begin to merge and convert into a tightly focused bright spot at $z_{af} = 84$ cm. At the autofocusing distance, the peak power becomes maximum due to the merging of bright lobes, but it always appears at the on-axis center of the beam. Thus the spatial position of the tightly focused bright spot at autofocusing distance can not be changed. However, up to a distance of $z = 70$ cm, the high-intensity lobe continues to develop and remains well separated in a pattern. At $z = 70$ cm, most of the intensity becomes confined tightly within these bright lobes (lobes with high-energy density) (Figs. 4.3 and 4.5). At this distance, the spatial position of high-energy density lobe can be controlled by transferring intensity between the bright lobes using asymmetry parameter β. Note, a similar control can also be obtained at other distances after autofocusing, as these bright lobes are separated well and intensity is confined within them.

For different asymmetry parameters, the intensity distributions of aALB are given in Figs. 4.3 and 4.5. As evident, the spatial intensity distribution of aALB is different for different values of w and β. For the specific values of β, most of the intensity can be confined to any one of the bright lobes. For example, for $\beta = \pi/2$ and $w = 1$ mm, most of the intensity shifts and confines to a single bright lobe, which represents a high-energy density lobe (Figs. 4.3(h1) and 4.3(h2)). The spatial position of the high-energy density lobe can be varied by choosing other specific values of β, for which most of the intensity will transfer to the other bright lobe.

A controlled shift of intensity into any one of bright bright lobes can be explained by establishing a correlation between the autofocusing point ($z = z_{af}$) (Fig. 4.3(d1)), near-

field MIP (Fig. 4.7) and position of bright lobes in the pattern (Fig. 4.3(c1)). Particularly, a relative alignment among them decides the shifting of intensity in a certain direction, and accordingly high-energy density lobe forms at a specific spatial position. For two set of parameters ($w = 1$ mm, $\beta = 7\pi/6$) and ($w = 1$ mm, $\beta = 4\pi/3$), the results are shown in Fig. 4.9.
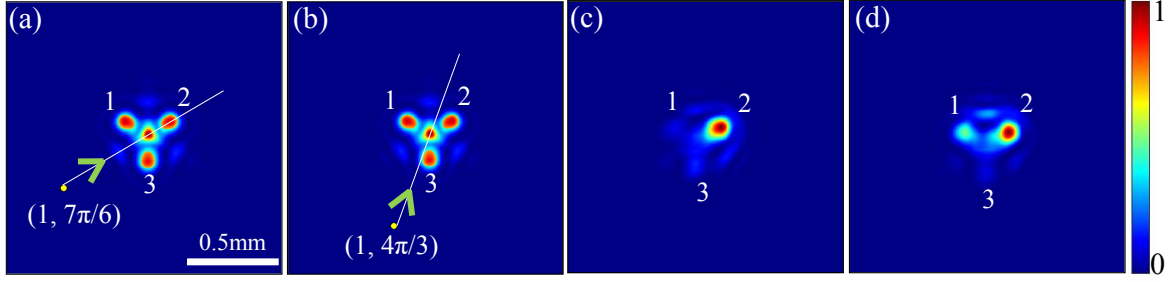
Figure 4.9: (a)-(b) The intensity distributions of ideal ALB at $z = 70$ cm (Fig. 4.3(c1)) and at autofocusing distance $z_{af} = 84$ cm (Fig. 4.3(d1)) are superimposed. The yellow dots in (a) and (b) mark the spatial position of near-field MIP (Fig. 4.7) for $w = 1$ mm and $\beta = 7\pi/6$ and $4\pi/3$, respectively. (c)-(d) The intensity distributions of aALB at $z = 70$ cm for $w = 1$ mm and $\beta = 7\pi/6$ and $4\pi/3$. Other parameters are taken as $m = 3$, $q = 2$, $\alpha = 5.9$ mm^{-2}, $\sigma_0 = 1.45$ mm and $\lambda = 632$ nm.

In Figs. 4.9(a)-4.9(b), the intensity distributions of ideal ALB at $z = 70$ cm (Fig. 4.3(c1)) and at autofocusing distance $z_{af} = 84$ cm (Fig. 4.3(d1)), are superimposed. The spatial position of MIPs (Fig. 4.7) for two set of asymmetry parameters ($w = 1$, $\beta = 7\pi/6$) and ($w = 1$, $\beta = 4\pi/3$) are represented by yellow dots in Figs. 4.9(a) and 4.9(b), respectively. A straight line connecting near-field MIP and center of the autofocused bright spot is drawn, where an arrow denotes the direction of flow of intensity in order to form high-energy density lobes. Figures 4.9(c)-4.9(d) show the intensity distributions of aALB at a distance of $z = 70$ cm for ($w = 1$ mm, $\beta = 7\pi/6$) and ($w = 1$ mm and $\beta = 4\pi/3$), respectively. The bright lobes in the pattern are marked as 1, 2, and 3. When near-field MIP, auto-focused central bright spot, and bright lobe in the pattern are aligned well in a straight line (shown by a solid line in Fig. 4.9(a)), the intensity flows towards that aligned bright lobe in the pattern and forms a high-power density lobe in that direction. For example, in Fig. 4.9(a) (for $w = 1$ mm and $\beta = 7\pi/6$), only bright lobe 2 is aligned perfectly, so most of the intensity shifts to only bright lobe 2, and forms a

high-energy density lobe (Fig. 4.9(c)). In this case, most of the intensity from bright lobes 1 and 2 transfers to bright lobe 2. When such alignment does not satisfy, for example, in Fig. 4.9(b) (for $w = 1$ mm and $\beta = 4\pi/3$), the shifting of most of the intensity in a single bright lobe does not occur, and a significant portion of intensity also remains in the other bright lobes, as shown in Fig. 4.9(d). In this case, the bright bright lobe 2 is closer to the alignment (marked by the solid line in Fig. 4.9(b)) as compared to the bright lobe 1, so it receives more intensity. As the arrow direction points from bottom to top, so intensity flows mostly in that direction. In this case, the intensity from bright lobe 3 transfers almost completely, and from bright lobe 1 transfers partially.

Note, for each bright lobe in the pattern this alignment can occur for two MIPs (diametrically opposite values in Fig. 4.7), where in one case high-energy density lobe is obtained before the autofocusing distance (at $z = 70$ cm), and for other after the autofocusing point ($z \approx 100$ cm). For example, it has been observed for $\beta = \pi/2$ (Fig. 4.3(h1)) and $\beta = 3\pi/2$ (Fig. 4.5(j1)). This can be attributed to the fact that there exists an on-axis symmetry around autofocusing distance (z_{af}) for both ideal ALB and aALB (Fig. 4.4(c)). More specifically, the spatial intensity distribution of ideal ALB at $z = 70$ cm (Fig. 4.3(c1)) and $z = 100$ cm (Fig. 4.3(e1)) are similar. However, for aALB, due to intensity migration the region of less intensity in aALB at $z = 70$ cm (Fig. 4.5(h1)) becomes a region of high intensity at $z = 100$ cm (Fig. 4.5(j1)).

In the considered examples of ALB and aALB, there are three bright lobes for $m = 3$, which are oriented at different angles. Thus, the high-energy density lobes can be created at three different spatial positions by choosing three specific values of β. For $m = 3$, three β values are $(\pi/2, 7\pi/6, 11\pi/6)$ (for distance $z = 70$ cm, before the autofocusing). However, to generate high-energy density lobes at more spatial positions, the value of m can be increased further ($m > 3$), and accordingly, there will be more values of β (shown later in Sec. 4.5.1). In general, for a given value of m, β can be found using the following empirical relation:

$$\text{Odd } m \quad \beta_n = \frac{\pi}{2m}(4n - 1) \quad n = 1, 2, ..m \tag{4.22}$$

$$\text{Even } m \quad \beta_n = \frac{\pi}{2m}(4n - 3) \quad n = 1, 2, ..m \tag{4.23}$$

Further, for the case of $m = 3$, we quantified the shift of intensity in bright lobes for three specific values of β. The results are shown in Fig. 4.10. Figures 4.10(a1) and 4.10(a2)
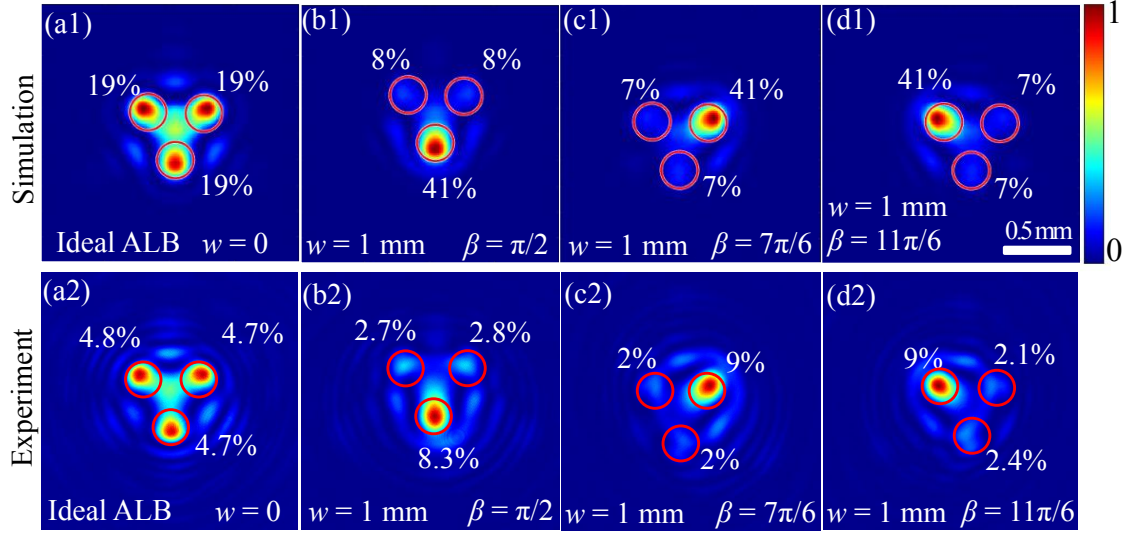
Figure 4.10: (a1)-(a2) The intensity distributions of ideal ALB at $z = 70$ cm. The intensity distributions of aALB at $z = 70$ cm for different values of β (b1)-(b2) $\pi/2$, (c1)-(c2) $7\pi/6$, and (d1)-(d2) $11\pi/6$. The other parameters: $w = 1$ mm, $\alpha = 5.9$ mm^{-2}, $\sigma_0 = 1.45$ mm, $m = 3$, $q = 2$ and $\lambda = 632$ nm.

show the simulated and experimental intensity distributions of ideal ALB at $z = 70$ cm, respectively, indicating the equal intensity in all three bright lobes. The percentage of intensity inside each lobe (marked by the red circle) is calculated by the method of diffraction efficiency [232]. The diffraction efficiency represents the amount of intensity inside the bright lobe (area marked by red circles) with respect to the total intensity of the beam. Note, in the experimental results the intensity inside the bright lobes is distributed equally, but their values are smaller than the numerical results. We attribute this difference due to the imperfections related to SLM, which causes a significant residual reflection. The SLM is anti-reflection (AR) coated at 1064 nm, however, the experimental results are obtained with He-Ne laser at 632 nm. Figures 4.10(b1)-4.10(d1) and 4.10(b2)-4.10(d2) show the simulation and experimental results of the intensity distribution of aALB at $z = 70$ cm for three different values of $\beta = \pi/2$, $7\pi/6$, and $11\pi/6$, respectively.

As evident, for these three specific values of β, most of the intensity is transferred to any of the bright lobes, spatially positioned at different locations. More specifically, for aALBs, the intensity is enhanced by a factor of > 2 in any one of these bright lobes (41%) as compared to ideal ALB (19%). Further, asymmetry shifts a major portion of intensity in one of the bright lobes (high-power density lobe), and the intensity between the high-power density lobe (41%) and other lobes ($\sim 7\%$) differs by a factor ~ 6, as shown in Figs. 4.10(b1)-4.10(d1). The experimental results show qualitatively the same behaviour, however, the difference factor is obtained between $3 - 4.5$ (Figs. 4.10(b2)-4.10(d2)).

4.5.1 Effect of m on the intensity distribution of aALB

We have also shown that by varying the aALB parameter m, it is possible to obtain a more flexible control of spatial intensity distribution. The number of bright lobes (having equal
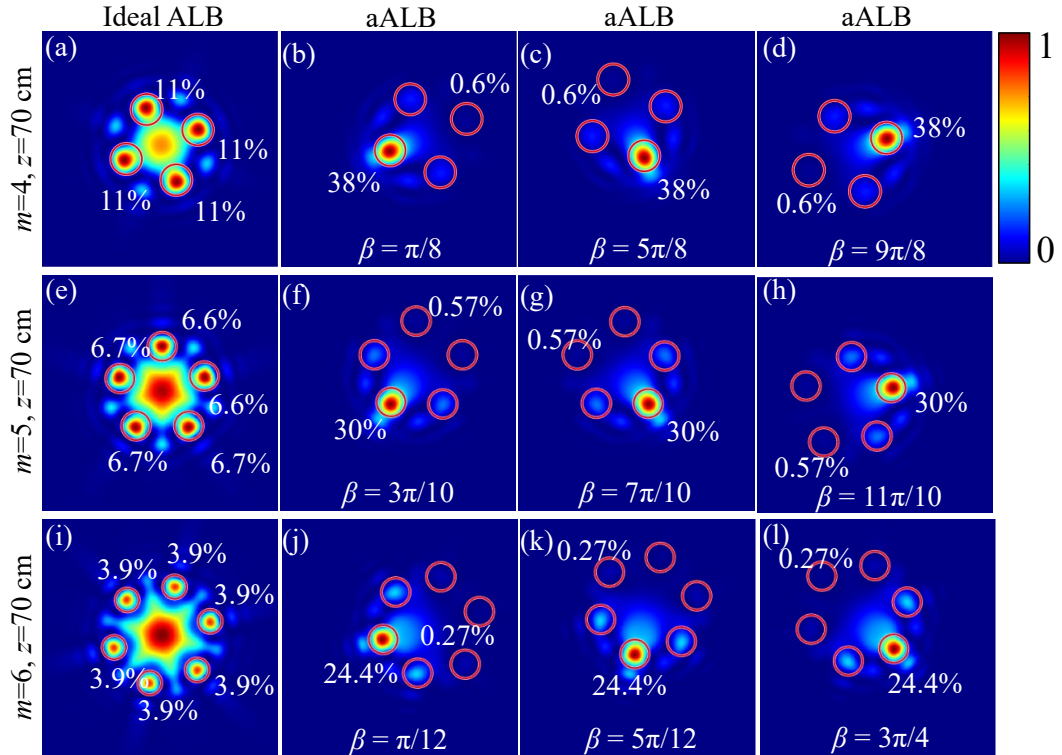
Figure 4.11: The intensity distributions of ideal ALB and aALBs with different β values for $m = 4$ (first row), $m = 5$ (second row), and $m = 6$ (third row). The propagation distance is taken to be $z = 70$ cm. The other parameter values are $\alpha = 5.9$ mm^{-2}, $\sigma_0 = 1.45$ mm, $q = 2$ and $\lambda = 632$ nm.

intensity) in ideal ALBs are determined by the value of m and thus enables the possibility to increase the number of spatial positions where high-energy density regions (most of the beam intensity transfer to a tightly focused lobe) can be formed using asymmetry. In Fig. 4.10, for $m = 3$, it was shown that the high-energy density regions can be created only at three different spatial positions. In general, the number of spatial positions carrying high-energy density lobes can be increased in proportional to m. To show it, we have simulated the results for different values of m, as shown in Fig. 4.11. The results consist of intensity distributions of ideal ALB and aALBs (with different β values) at $z = 70$ cm for various values of $m = 4$ (first row), $m = 5$ (second row) and $m = 6$ (third row). The percentage of intensity inside each bright lobe represents the diffraction efficiency. As evident, for ideal ALBs, the intensity in bright lobes is equally and symmetrically distributed. However, in aALBs, the intensity is asymmetrically distributed and can be migrated to a desired spatial location by controlling asymmetry parameter β. The specific values of β for which most of the intensity can be transferred to a single tightly focused bright lobe at different spatial positions can be determined by the empirical relations (Eq. (4.22) & Eq. (4.23)). As evident by changing the values of β, the spatial position of the high-energy density region can be precisely tuned. The number of spatial positions having high-energy density region are marked by the red circles, which shows that the number of these spatial positions are proportional to m. For other values of β, it is possible to migrate intensity at other spatial positions, but all the intensity will not be transferred to a single location to form a high-energy density region. For $m = 4$, with the specific values of β, the diffraction efficiency of high-energy density region can be enhanced by a factor of ~ 3.5 (11% in ideal ALB, 38% in aALB). This factor further increases with the value m, for example, for $m = 5$ and 6, it is found to be ~ 4.4 (Fig. 4.11(e)-4.11(h)) and ~ 6.2 (Fig. 4.11(i)-4.11(l)), respectively. Now, in aALBs with different m values, the intensity difference between the high-energy density and other lobes has significantly increased by several factors. Therefore, we have found that by varying the aALB parameter m, it is possible to obtain more flexible control of spatial intensity distribution. Specifically, it is found that the high-energy density bright lobe

can be generated at more spatial positions by increasing the parameter m.

4.6 Effect of non-quadratic phase distribution ($q \neq 2$)

For the generalization of our method, we have also investigated the controlled intensity distribution of aALBs having non-quadratic phase distribution ($q \neq 2$). We have considered two different cases of radial power $q = 1.5$ and $q = 2.5$. The intensity distribution of ideal ALBs with $q = 1.5$ and $q = 2.5$ are shown in Figs. 4.12(a) and 4.12(e), respectively. The different q values provide different phase distribution of ALBs, and thus their propagation properties become different. The autofocusing for ALBs with $q = 1.5$ and 2.5 is observed at $z = 117$ cm and 60 cm, respectively. These values of autofocusing distance show a small discrepancy with the calculated values of $z = 110$ cm and 68 cm from Eq. (4.21). This small discrepancy is due to the fact that the analytical expression (Eq. (4.21)) is obtained with a stationary phase method involving assumptions (described in Chapter 3).
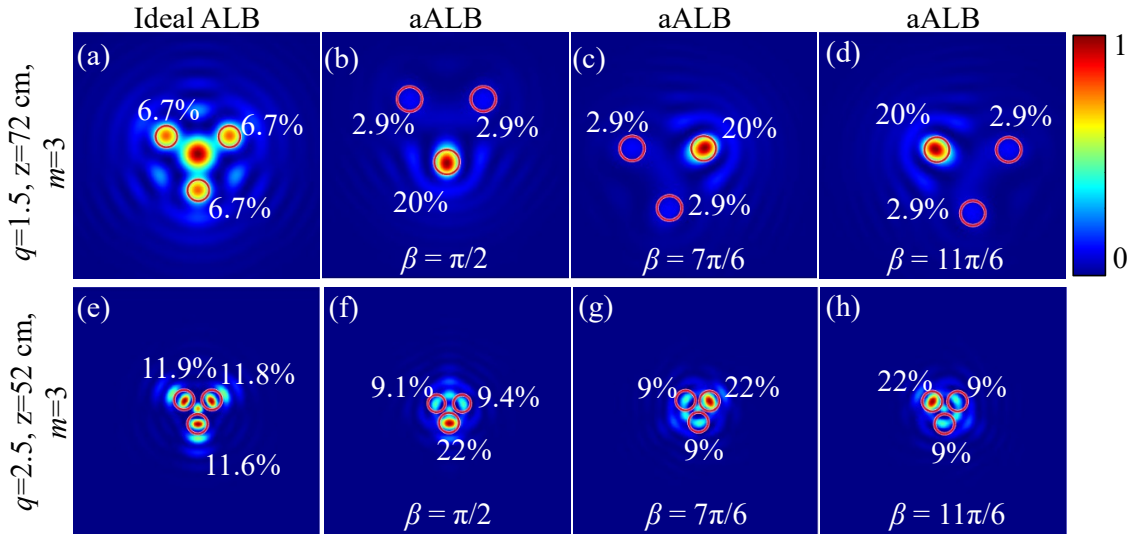
Figure 4.12: Intensity distributions of ideal ALB and aALBs with different β for (a-d) $q = 1.5$, and (e-f) $q = 2.5$. Note, due to different values of autofocusing distance, the propagation distance z is chosen differently for both cases of q. The other simulation parameters are taken as $m = 3$, $\alpha = 5.9 \text{ mm}^{-2}$, $\sigma_0 = 1.45 \text{ mm}$, and $\lambda = 632 \text{ nm}$.

Further, to show the effect of asymmetry for controlling spatial intensity distribution

(specifically to form high-energy density regions), we have chosen propagation distances $z = 72$ cm and 52 cm for $q = 1.5$ and 2.5, respectively. This is due to the fact that at these distances lobes are developed and separated well. For simplicity, we have kept the asymmetry parameter $w = 1$ mm and varied only β. To obtain high-energy density regions, the specific values of β are calculated from empirical relation (Eq. (4.22)). For $q = 1.5$, in an ideal ALB with $m = 3$, the intensity is symmetrically distributed in three lobes with a diffraction efficiency of 6.7% (Fig. 4.12(a)), and by introducing asymmetry β, the intensity migrates to form a high-energy density region with enhanced diffraction efficiency of 20% (Figs. 4.12(b)-4.12(d)). The spatial position of high-energy density region is changed by changing the specific values of β. The results for $q = 2.5$ are shown in Figs. 4.12(e)-4.12(h), indicating that high-energy density regions are obtained with enhanced diffraction efficiency of 22%. From the results, it is clear that our approach works well for aALBs with non-quadratic phase distribution.

Therefore, it is clear from these results, that we can generate high-energy density lobes with controlled spatial position by introducing the asymmetry as well as varying the beam parameters m and q.

4.7   Conclusions

In this Chapter, we have presented the generation of asymmetric aberration laser beams (aALBs) with controlled intensity distribution, based on an outer-cavity method using a diffractive optical element (DOE) involving phase asymmetry. In ALBs, the intensity is symmetrically distributed in all lobes, however, in aALBs, the asymmetry in phase distribution enables an additional control of intensity distribution by redistributing intensity within the beam, and forms the high-energy density regions at desired spatial locations. The asymmetry in phase distribution is introduced by shifting the coordinates in a complex plane. We have derived the mathematical formulations for general aALBs as well as the special cases of it. Specifically, we have exploited asymmetry to precisely control the intensity distribution of ALBs. In an ideal ALB, intensity is equally distributed in all

bright lobes. We have shown that, by the introduction of phase asymmetry, most of the intensity can be transferred to any one of the single lobes, and generate a high-energy density. Further, we have also investigated the mechanism of asymmetric control of intensity in aALBs. We have found that the asymmetry parameters control the position of indeterminate phase point of trigonometric phase term in aALB, which creates a controlled asymmetric intensity distribution in the near-field plane. As a result of propagation, it provides a controlled transfer of intensity within aALB. In general, for a given parameter m of aALB, the precise spatial location of high-energy density lobe can be controlled by asymmetry parameter β, and we have determined empirical relations between β and m. We have found that for the specific values of β and m, the intensity in the high-energy density lobe can be enhanced by several times the intensity in other lobes. For example, intensity in the high-energy density lobe can be enhanced by the factor of ~ 6.2 for $m = 6$ and $\beta = \pi/12$. Further, the effect of different beam parameters such as m and q is also investigated, which provides more flexibility in controlling the intensity distribution of aALBs.

Furthermore, unlike ideal ALBs, the aALBs possess more complex intensity and phase distributions, so we have investigated their propagation properties. We have found that similar to ideal ALBs, the aALBs also possess good autofocusing properties, which are not affected by the asymmetry parameters. The autofocusing distance of aALBs can be varied from small to large values by changing the beam parameters. The aALBs provides a more general framework for controlling intensity distribution, as for the specific values of asymmetry parameters ($w = 0$) aALB behaves as an ideal ALB. These aspects of aALBs make them potentially important for various applications of modern optics and photonics, such as forming various types of optical traps to guide and manipulate particles, material processing etc. The results presented in this Chapter are reported in Refs. [38, 40].

Chapter 5

Generating high-energy densities by sidelobe suppression in the far-field of phase-locked lasers

5.1 Introduction

In previous Chapter 4, we have presented the generation of asymmetric aberration laser beams (aALBs) with controlled intensity distribution, based on an outer-cavity method using a diffractive optical element involving the phase asymmetry. Owing to the phase asymmetry, in aALBs high-energy density lobes can be created at desired spatial locations within the beam. However, the total energy in the high-energy density lobe is limited by the output power of a laser. In general, the generation of high-energy density from a single laser is typically limited by several physical constraints, such as gain saturation, non-linear effects, optical facet damage, and damage threshold of gain medium [233, 234]. Further, strong pumping of the gain medium may excite undesired high-order transverse modes, which can degrade the quality of laser output ($M^2 >> 1$) [151, 235]. Also, the presence of higher-order transverse modes affects the propagation and focusing properties of a laser beam, which results in a significant decrease in the energy density of focused

spot in the far-field [151,235]. In this regard, phase-locking/coherent combining of several lasers can be employed, which increases the output power significantly while maintaining good output beam quality [236–239]. Various methods have been investigated for the phase-locking of lasers in different array geometries [136, 239–242]. However, different approaches suffer from different kinds of limitations, and based on their efficiency, the lasers in the arrays are phase-locked either in the in-phase or out-of-phase configurations. Unfortunately, in the far-field of these phase locked laser arrays, a significant percentage of the energy resides in undesired sidelobes (higher diffraction orders) and prevents from obtaining a high-energy density output beam [136, 243]. Therefore, in this Chapter, we present the generation of high-energy densities by suppression of higher-order sidelobes in the far-field of phase-locked lasers.

A high-energy density single lobe far-field can be obtained from a near-field consisting of uniform amplitude and uniform phase distributions [180]. For the in-phase locked lasers, the phase distribution becomes uniform, as all the lasers are locked with the same phase [239]. However, due to finite inter-laser separation, the amplitude of an optical field across the output becomes non-uniform [244, 245]. Due to such non-uniformities, the far-field intensity distribution of a laser array contains undesired sidelobes having a significant amount of energy [136, 243]. Thus, finding a method capable of redistributing the sidelobe energy to generate a high-energy zeroth-order lobe becomes a long-standing fundamental problem. Therefore, several efforts have been made to suppress the higher-order sidelobes to obtain a high-energy density zeroth-order lobe, for example, superposition of Bessel beams with opposite $k-$vectors [246, 247], arbitrary phasing based on active segmented mirrors [248], quantum cascade lasers with coupled ridged waveguides [249], diode laser arrays integrated with a phase shifter [250], conjugate and phase controlled Dammann grating [251, 252].

Furthermore, aperture filling approach has also been shown to successfully suppress the sidelobes in the far-field of coherent laser arrays and enables the generation of a tightly focused single-lobed far-field intensity distribution. In this method, a uniform near-field intensity distribution is generated by filling the intensity in the vacant space between

the lasers of a periodic array, based on the principle of conversion of amplitude non-uniformities to phase non-uniformities [244, 245]. However, in certain cases the reverse approach has also been shown, i.e., uniform near-field is obtained by the phase modification of central lobe of the far-field pattern [245]. A phase corrector is then employed to nullify the phase non-uniformities of near-field to obtain a high intensity central peak in the far-field. However, the method is limited due to two main assumptions: (i) Array fill factor should be greater than 25% and (ii) the array modes must consist of binary amplitudes. These two factors affect the efficiency of method [244, 245]. In particular, for reduced fill factors or nonbinary amplitude profiles, the efficiency can be considerably lower. An improved and generalized version of this approach has also been demonstrated, where phase of multiple orders in the Fourier plane is changed in order to produce a uniform function in the output plane, which ensures an improved efficiency [253]. Further, most of these aperture filling studies are performed with small system sizes and simple array geometries such as linear and two-dimensional square arrays. Further, the arrays are generated by illuminating an appropriately designed mask with an expanded, collimated beam from a highly coherent laser source [244, 245, 250, 252, 254, 255]. However, for real phase-locked laser arrays in various complex geometries such as square, triangular, Kagome, random, and 1D ring, the investigations are yet to be explored. Further, how the range of phase locking, effect of system size, and presence of topological defects in the phase-locked laser arrays could affect the efficiency of aperture filling method?

In this Chapter, we have extended the approach of aperture filling to real phase-locked laser arrays in various complex array geometries and investigated the effect of various system parameters on the efficiency of method for generating high-energy densities. In Sec. 5.2, we present a basic arrangement to generate phase-locked lasers in different array geometries. The method to suppress higher-order sidelobes is discussed and numerical results are presented, and show that aperture filling technique works well for different laser array geometries. In Sec. 5.3, we present a detailed robustness analysis of the method against the system size, range of phase locking, and presence of topological defects. In Sec. 5.4, the approach is demonstrated with an out-of-phase locked square laser array. In

Sec. 5.5, concluding remarks are presented. The results presented in this Chapter are reported in Refs. [41, 42].

5.2   Basic arrangement for phase locking laser arrays

The scheme for generation and phase-locking of lasers in various array geometries is depicted in Fig. 5.1. It is based on a modified degenerate cavity that comprised of two flat mirrors with reflectivities 99.5 % (back mirror) and 80 % (output coupler), solid-state gain medium, two plano-convex lenses (focal length = 40 cm), a spatial Fourier filter placed in the middle of two lenses (far-field (FF) plane) with Gaussian transmission function and a near-field (NF) mask adjacent to output coupler containing circular holes in desired geometry. In the NF mask, the area within the circular holes has a transmission value '1', and other outside areas have a transmission value '0'. Two lenses are arranged in a 4f telescope configuration that ensures perfect imaging inside the cavity such that every point $E(x, y)$ on the output coupler maps onto itself after every round-trip. This enables each hole on the mask to lase independently in a nearly Gaussian distribution (acts as an individual laser) [73, 75, 136], and accordingly it forms an array of lasers in the desired array geometry. The lasers in the array are coupled by a Gaussian apodizer in the far-field plane, which provides a positive coupling between the lasers and enables an in-phase locking of the lasers [239]. The range and strength of coupling can be controlled by the size of the Gaussian apodizer.

The Gaussian apodizer helps to eliminate the undesired phase distributions by introducing additional losses to them and, thereby, enables the lasers to find a correct phase distribution. Initially, all the lasers in the array have random phase distributions and, thus, are equally probable. During the several round-trip propagation of field inside the cavity, different phase distributions of lasers compete with each other for the same gain medium, and adding a Gaussian apodizer imposes different losses to the different phase distributions. As a result, only the phase distribution with minimum loss sustains, and others stop lasing inside the cavity. The minimum loss solution represents a steady-state
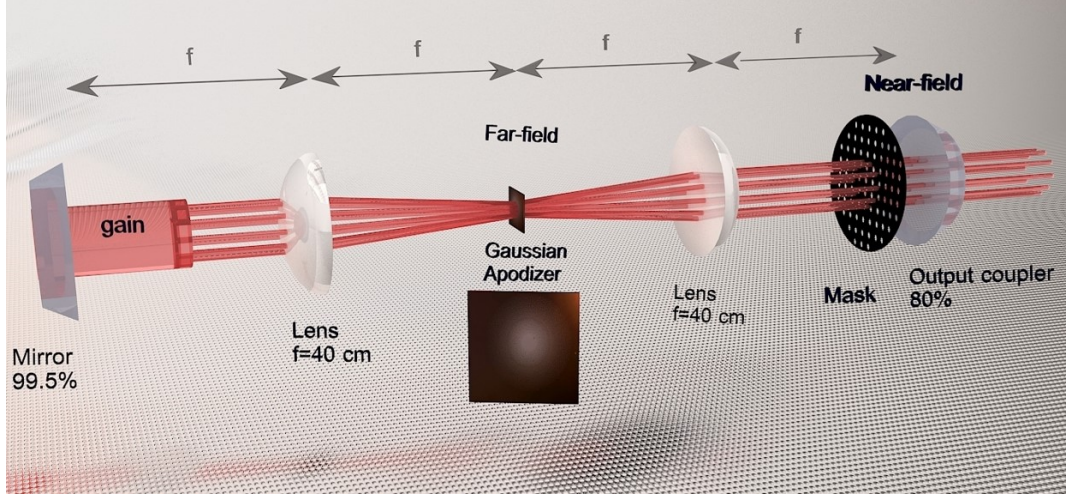
Figure 5.1: The schematic of a degenerate cavity for the generation and phase locking of lasers in different array geometries.

in-phase locked solution due to the positive nature of coupling between the lasers.

The scheme is simulated by using a modified Fox-Li iterative method, which has also been adopted earlier to reproduce the experimental findings of phase-locking of lasers in a degenerate cavity [136]. The method enables to simulate accurately the results of near-field and far-field intensity distributions of laser arrays, as well as corresponding phase distributions [37]. One round trip propagation of field inside the degenerate cavity is simulated by the following operations:

$$E_{m+1}(x,y) = M\left(\mathcal{F}^{-1}\left(T(k_x,k_y)\left(\mathcal{F}\left(g(x,y) \times E_m(x,y)\right)\right)\right)\right), \tag{5.1}$$

where $E_m(x,y)$ and $E_{m+1}(x,y)$ represent the field distributions of mth and $(m+1)^{th}$ round-trip at the output coupler. M represents the matrix corresponding to binary amplitude mask placed at the near-field plane. The transmission function of M is either 0 (where holes are absent) or 1 (where holes are present) arranged in a desired geometry. $T(k_x,k_y)$ denotes the transmission function of Gaussian apodizer, which can be written as

$$T(k_x,k_y) = \exp\left(-\frac{k_x^2 + k_y^2}{2\sigma_G^2}\right), \tag{5.2}$$

where σ_G represents the width of Gaussian aperture. $k_x = x/\lambda f$ and $k_y = y/\lambda f$ represent

5 *Generating high-energy densities by sidelobe suppression in the far-field of phase-locked lasers*

spatial frequencies in the Fourier domain, where f denotes the focal length of a Fourier transforming lens. $\mathcal{F}$ and $\mathcal{F}^{-1}$ denote the Fourier transform and inverse Fourier transform operations, respectively. g describes the gain saturation function and can be written as

$$g(x,y) = \frac{g_0}{1 + \frac{I(x,y)}{I_{sat}}}, \tag{5.3}$$

where $I(x,y) = E(x,y)^2$. I_{sat} is saturation intensity, and g_0 denotes the unsaturated gain.

One round-trip propagation of field inside the degenerate cavity is equivalent to one iteration in the simulation. For repetitive iterations in the simulation, the Eq. (5.1) is repeated several times. Our modified Fox-Li method needs around 200 iterations to reach the steady-state of in-phase locked laser array. The simulations are performed with the parameters as: $I_{sat} = 1000$, $g_0 = 8$, $\sigma_G = 0.5$ mm, and $\lambda = 1064$ nm. The simulated results of in-phase locked lasers in the square, triangular, Kagome, 1D ring, and random array geometries are shown in Fig. 5.2. Figures 5.2(a)-5.2(e) show the near-field intensity distributions of in-phase locked lasers in the square, triangular, Kagome, 1D ring, and random laser arrays, respectively. The lasers close to the boundaries in 2D arrays have less intensity, which is attributed to the Gaussian nature of transmission function of a far-field aperture. Note, for a large-size Gaussian apodizer, all the lasers become equally intense. The size (diameter) of each laser is considered 0.48 mm, and the separation between the two nearest neighbour lasers (centre to centre separation) is 0.72 mm. Figures 5.2(f) -5.2(j) show the phase distributions of in-phase-locked lasers in the square, triangular, Kagome, ring, and random arrays, respectively. Note, the black colour in the phase distribution plot represents the zero-intensity regions, where the phase is not defined, hence it is not included in the colormap of a well-defined phase. As evident, the phase is uniform throughout the array, indicating a long-range in-phase locking of lasers. Further, it confirms that the Gaussian coupling enables the in-phase locking of lasers irrespective of array geometry without changing the system parameters (fix diameter of Gaussian apodizer) [239]. Figures 5.2(k)-5.2(o) show the far-field intensity distribution of phase-locked lasers in the square, triangular, Kagome, ring, and random arrays, respectively. A

narrow sharp bright peak in the center again confirms a long-range in-phase locking of lasers. The corresponding phase distributions of far-fields are shown in Figs. 5.2(p)-5.2(t).
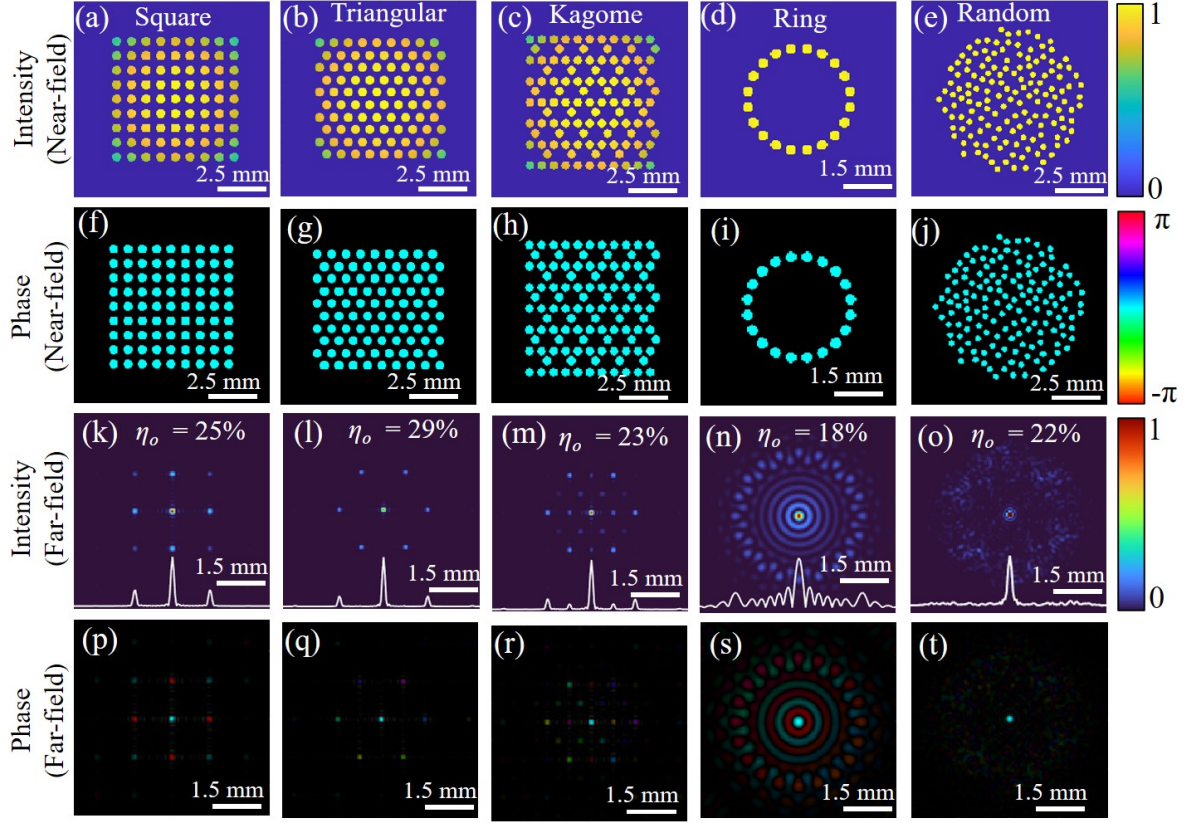
Figure 5.2: Results of in-phase locked lasers in various array geometries. (a-e) Near-field intensity distribution. (f-j) Phase distribution in a near-field plane. (k-o) Far-field intensity distribution. (p-t) Phase distribution in a far-field plane. Note, in the phase distribution plots, black colour represents the regions where phase is not defined due to zero intensity. η_o denotes the diffraction efficiency of zeroth-order central lobe (Eq. (1.31)).

In the far-field intensity distribution (Figs. 5.2(k)-5.2(o)), in addition to a central bright peak (zeroth-order) there are several higher orders (sidelobes) that consist of a significant amount of intensity. These undesired sidelobes reduce the available powers in the form a high-energy density beam. In other words, it causes a reduced diffraction efficiency of the zero-order lobe, as marked by η_o in Figs. 5.2(k)-5.2(o). Note, the diffraction efficiency is calculated using Eq. (1.31). The formation of sidelobes (higher orders) is anticipated by the discreteness and periodic arrangement of elements in the system, for

5 *Generating high-energy densities by sidelobe suppression in the far-field of phase-locked lasers*

example, finite inter laser separation that results in a non-uniform optical field of laser array across the near-field plane. To overcome these issues, several methods have been developed to suppress the sidelobes for the generation of a single-lobe far-field intensity distribution [244, 245, 250, 252, 254, 255]. However, the approaches still suffer several limitations, and improvements are still being made to reinforce the power in the zero-order lobe. We are using an aperture filling approach (called phase plate method) to transfer the intensity from the higher-order sidelobes to zeroth-order lobe, to improve its diffraction efficiency.
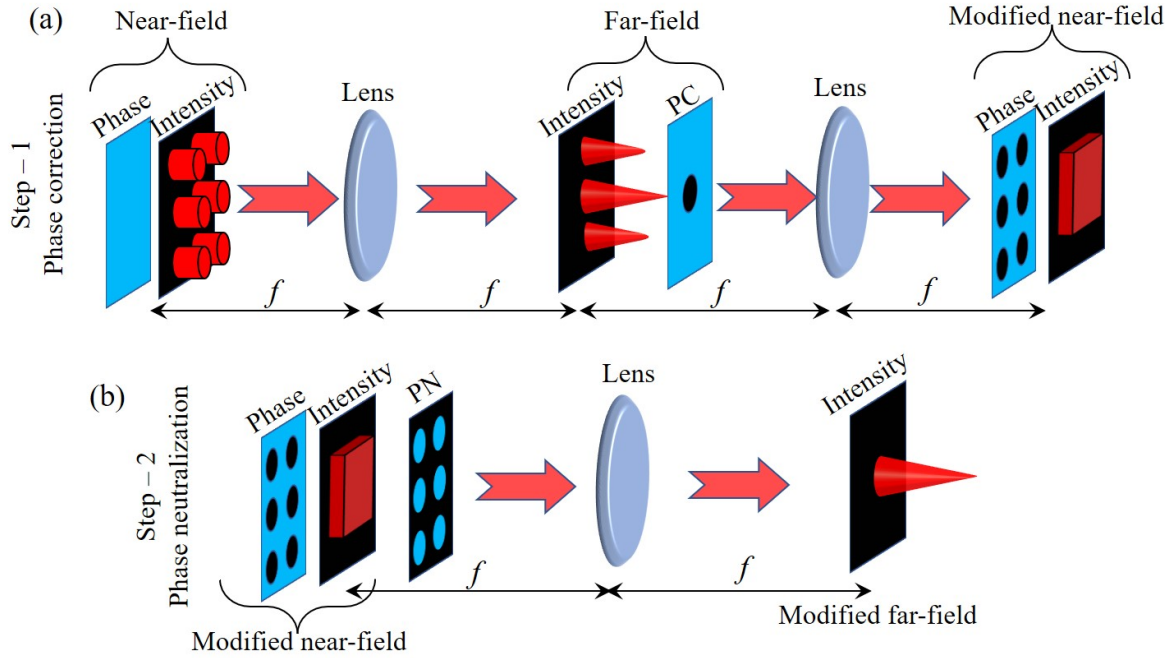
Figure 5.3: Illustration of method for suppressing higher-order sidelobes in the far-field of phase-locked laser array. (a) Step-I demonstrates the formation of uniform near-field amplitude of laser array. (b) The phase neutralization step to obtain uniform near-field amplitude with uniform phase distribution, which gives a tightly focused single high-intensity lobe in the far-field plane. PN and PC denote the phase neutralizer and phase corrector, respectively.

The approach is illustrated in Fig. 5.3, which is based on the principle of obtaining uniform near-field intensity distribution by the phase modification of far-field distribution. The phase distributions of zero and higher-orders in the far-field intensity distribution have a certain symmetry and relation between them, as shown in Figs. 5.2(p)-5.2(t). For

example, in a square laser array, the phase difference between the zero-order and first-order lobes is π (Fig. 5.2(p)). By changing the symmetry of phase (i.e., modifying the phase of lobes), it can create a nearly uniform amplitude in the near-field plane. A uniform amplitude with plane phase will have a single high-energy density lobe in the far-field intensity distribution. The method involves two steps, as illustrated in Fig. 5.3. In step -I (Fig. 5.3(a)), the initial in-phase locked laser array consists of uniform phase but non-uniform intensity (due to inter-laser separation) across the array, which upon Fourier transform gives lobe pattern (zero and higher-order lobes) in the far-field. The phase of zeroth-order lobe is modified by ϕ using a phase corrector (PC), and then inverse Fourier transform is performed to get the near-field of laser array. Due to the phase modification, light will redistribute to form a uniform near-field amplitude and binary phase distribution. In step-II (Fig. 5.3(b)), a phase neutralizer (PN) is imposed on the modified near-field (obtained from step-I), which converts a non-uniform phase distribution to the uniform phase distribution. This will result in a plane wave (uniform amplitude with uniform phase) and can be focused tightly to a single lobe in the far-field plane.

The success of the approach relies on how well the uniformity in the near-field amplitude and phase distribution of laser array is obtained, which strongly depends on the correction phase ϕ. To analyze the effect of ϕ, we impose the variation of ϕ in a range $[0-2\pi]$ on the zeroth-order lobe, and calculate the diffraction efficiency of it in the far-field intensity distribution (Eq. (1.31) and [232]). The results for various laser array geometries with maximum diffraction efficiency are presented in Fig. 5.4. Figures 5.4(a)-5.4(e) show the modified near-field intensity distribution of laser arrays after implementing the phase correction (step-I in Fig. 5.3(a)). It is evident that the phase correction (ϕ) leads to the redistribution of intensity to the regions where lasers were not present (inter-laser separation), and results in a nearly uniform amplitude/intensity. Note, the values of ϕ are chosen such that maximum diffraction efficiency is achieved. To quantify the uniformity of the modified near-field amplitude, we have calculated an overlap integral with respect to a uniform amplitude distribution (Eq. (1.26)) and [37]), which is found to be $87.68\%, 90.40\%, 86.21\%, 55.14\%$, and 95.8% for the square, triangular, Kagome,
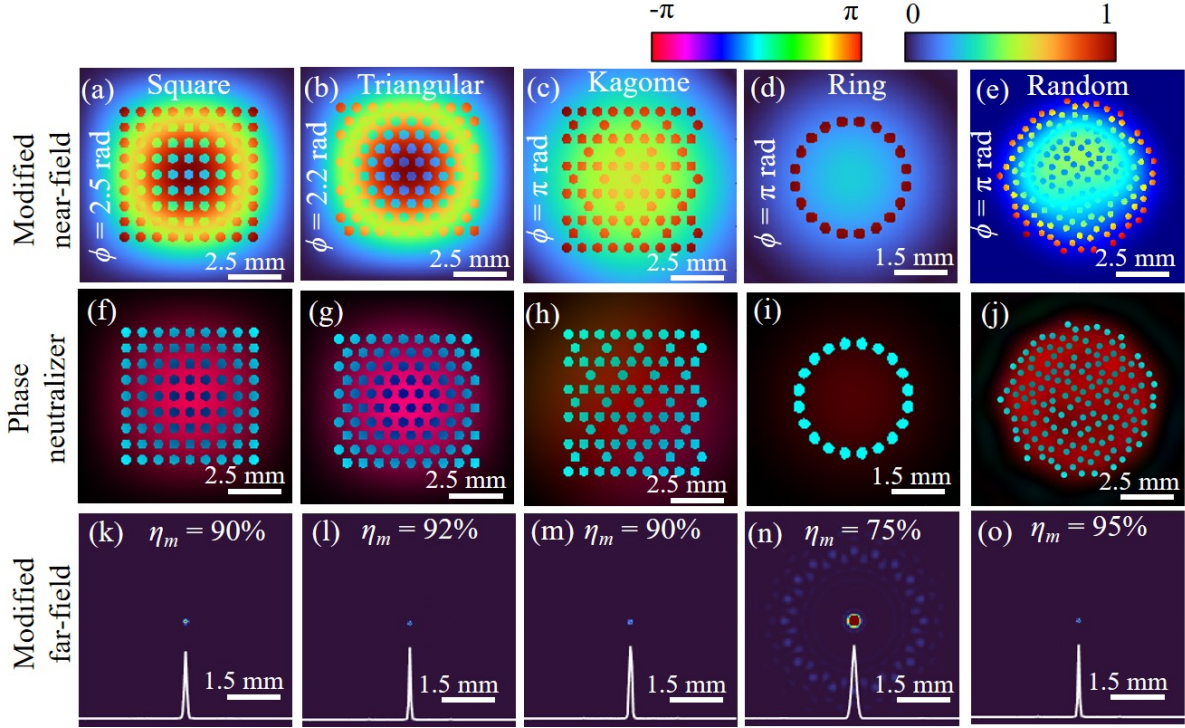
Figure 5.4: (a-d) Modified near-field of laser array after correcting the phase of zeroth-order lobe in the far-field. (e-h) The phase neutralizer for obtaining uniform phase distribution of modified near-field. (i-l) Modified far-field with suppressed higher-order side-lobes. η_m denotes the diffraction efficiency of the modified far-field. For the maximum diffraction efficiency, the results are obtained with $\phi = 2.5$ rad (square), 2.2 rad (triangular), and π rad (for Kagome and ring).

1D ring, and random array of lasers, respectively. After obtaining a nearly uniform amplitude distribution, the phase distribution is extracted and neutralized to produce an optical field that is similar to a plane wave (uniform amplitude and uniform phase distributions). Figures 5.4(f)-5.4(j) show the phase distribution of neutralizers that enable to obtain the uniform phase distribution of modified near-field of different laser arrays (step-II in Fig. 5.3(b)). As evident, the phase distribution of neutralizers is binary, which is easy to fabricate, and makes the method more simple, cost-effective, and advantageous. After performing steps I and II (Fig. 5.3), we obtain a modified far-field intensity distribution, where higher-orders are suppressed quite well and intensity is tightly focused in the form of a single zeroth-order lobe, as shown in Figs. 5.4(k)-5.4(o). The diffraction efficiency η_m is calculated for all laser arrays, which is found to be 90% for square array,

92% for triangular array, 90% for Kagome array, 75% for ring array, and 95% for random laser array. One of the reasons for observing $\eta_m < 100\%$ is due to the presence of a small non-uniformity in the modified near-field (Figs. 5.4(a)-5.4(e)) (as shown above by the calculated values of overlap integral). However, various other reasons have also been mentioned in earlier studies [244], which include i) smaller array fill factors, ii) binary mode profile of individual laser is an ideal approximation, iii) phase corrector is continuous for non-ideal systems, and iv) finite extent of the real laser array. Further, correcting the phase of multi-orders has also been shown to improve the diffraction efficiency [253].

To show an improvement in the diffraction efficiency quantitatively, we have compared the cross-sections of the original (Figs. 5.2(k)-5.2(o)) and modified (Figs. 5.4(k)-5.4(o)) far-field intensity distributions of various laser array geometries, as shown in Fig. 5.5. Note, the intensity cross-sections are normalized with respect to the intensity of the modified far-field. The diffraction efficiencies of zero-order lobe in original and modified far-field intensity distributions are denoted by η_o and η_m. As evident, in the original far-field intensity distribution, the intensity is distributed in zeroth-order and high-order sidelobes (shown by the dot-dashed blue curve), and the diffraction efficiency (η_o) of zeroth-order lobe is found to be 25% in a square array (Fig. 5.5(a)), 29% in a triangular array (Fig. 5.5(b)), 23% in a Kagome array (Fig. 5.5(c)), 18% in a ring array (Fig. 5.5(d)), and 22% in a random array (Fig. 5.5(e)). After applying our approach, in the modified far-field intensity distribution, the high-order sidelobes are suppressed quite well, and the diffraction efficiency of the zeroth-order lobe (η_m) is enhanced by the several factors $(3-4)$ (shown by solid red curve). Particularly, η_m is found to be 90% in square array (Fig. 5.5(a)), 92% in triangular array (Fig. 5.5(b)), 90% in Kagome array (Fig. 5.5(c)), 75% in ring array (Fig. 5.5(d)), and 95% in random laser array (Fig. 5.5(e)).

The above results are obtained for the fixed values of phase correction (ϕ) that correspond to a maximum diffraction efficiency. However, to understand the role of ϕ better for improving the diffraction efficiency, we have varied the value of ϕ in a complete range of $[0$ to $2\pi]$ and analyzed the diffraction efficiency of various laser arrays in different geometries. The results are shown in Fig. 5.6. It is evident that the diffraction efficiency (η_m)
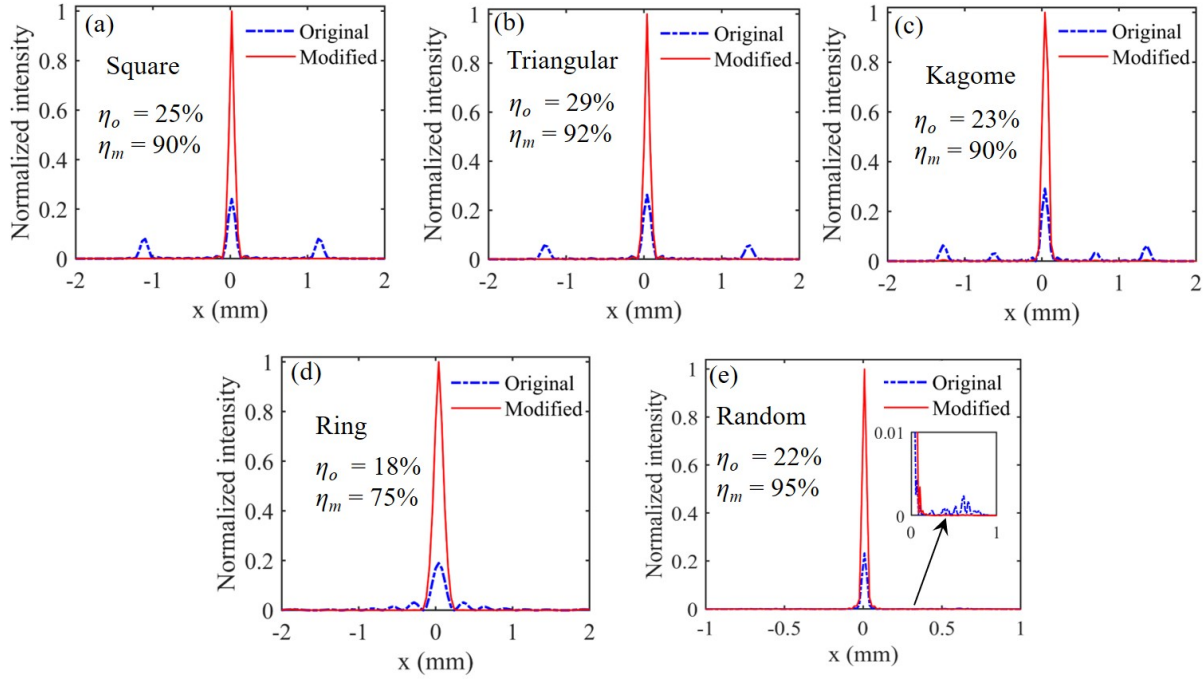
Figure 5.5: The cross sections of original (dash-dot blue curve) and modified (solid red curve) far-field intensity distributions of various arrays (a) square, (b) triangular, (c) Kagome, (d) 1D ring, and (e) random laser array. Note, the cross-sections are taken along the horizontal x-axis in Figs. 5.2(k)-5.2(o) (original far-field) and Figs. 5.4(k)-5.4(o) (modified far-field). The η_o and η_m are diffraction efficiencies of the central zero-order lobe in original and modified far-field intensity distributions.

of zeroth-order increases by increasing ϕ, and it attains a maximum value and remains the same for a certain range, and after that, it decreases. The curve is symmetric with respect to π for a range of $\phi \in [0, 2\pi]$. The range of ϕ for which maximum η_m occurs (say ϕ_m) varies with the laser array geometry, as shown in Fig. 5.5. The range of ϕ_m is found to be $1.88 - 4.4$ rad. for a square array, $1.73 - 4.55$ rad. for a triangular array, $2.04 - 4.24$ rad. for a ring array, and $2.2 - 4.15$ rad. for a random laser array. In a Kagome laser array, the maximum value of η_m occurs at $\phi_m = \pi$. Note, ϕ_m is calculated by taking η_m values within the 95% of maximum diffraction efficiency.

From above analysis, it is clearly evidenced that the approach works well for suppressing the higher-order sidelobes in 1D and 2D laser arrays. However, the redistribution of intensity from high-order to zeroth-order lobe depends on the parameters of array geometry, as evidenced by diffraction efficiency curves in Fig. 5.6. The approach clearly enables
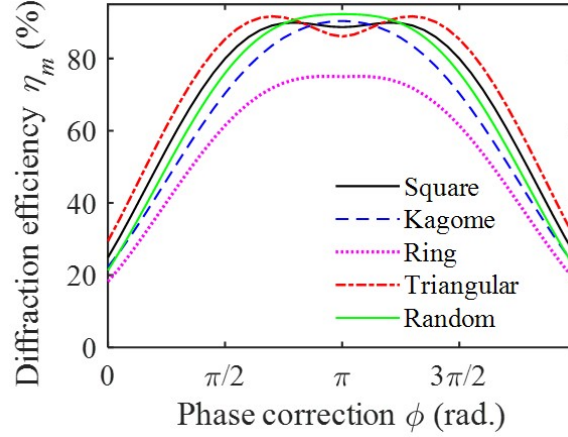
Figure 5.6: Variation of the diffraction efficiency η_m as a function of phase correction angle ϕ for various laser array geometries.

the efficient generation of high-energy density output laser beams.

5.3   Robustness Analysis

In Sec. 5.2, we have considered a long-range in-phase phase locking of lasers (all the lasers are fully phase-locked in all directions) in various array geometries, and no defects are present. However, achieving a long-range phase locking is a challenging task, as the presence of aberrations in a degenerate cavity can introduce detuning between the lasers, and critical value of coupling strength can be very high [256]. The phase locking of lasers in a 1D ring array is highly susceptible to topological defects [73, 75]. Thus, to check the reliability of our approach, we have carried out a detailed study by considering several factors such as effect of range of phase locking, effect of system size, and effect of topological defects.

5.3.1   Effect of range of phase-locking

It is possible that all the lasers in an array are not completely in-phase with each other in a real experimental situation. Due to this zeroth-order lobe in the far-field intensity distribution widens, and the suppression of higher-order sidelobes can be affected. To

study it, we have considered a square array of 81 lasers, where all the lasers are not perfectly in-phase with each other (short-range of phase-locking). Such a short range in-phase locking of lasers is obtained in a degenerate cavity (Fig. 5.1). The range of phase-locking can be controlled by varying the width (σ_G) of Gaussian apodizer [239]. Increasing the width of the Gaussian apodizer reduces the range of coupling between the lasers, and thus reduces the number of phase-locked lasers.
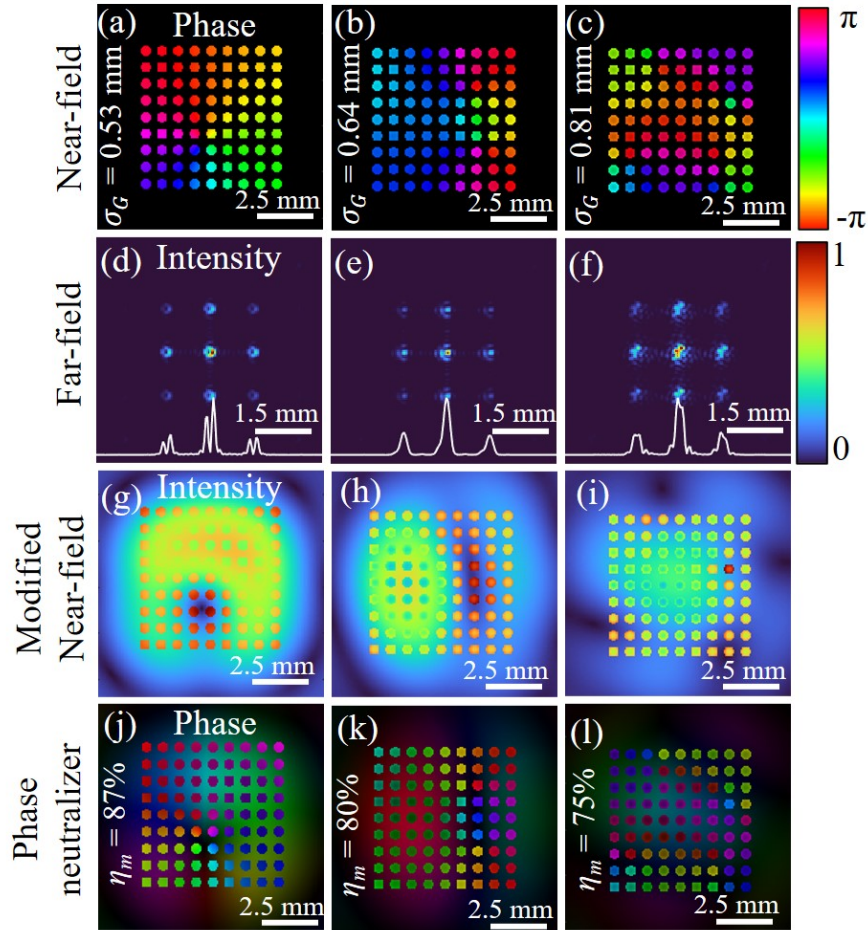
Figure 5.7: Effect of short-range phase-locking on the suppression of high-order sidelobes. (a)-(c) Phase distribution of lasers in the near-field plane. (d)-(f) Far-field intensity distribution. (g)-(i) Modified near-field intensity distribution. (j)-(l) Phase distribution of neutralizers. σ_G denotes the width of Gaussian apodizer. The value of phase correction is taken to be $\phi = 2.5$ rad, corresponding to a maximum diffraction efficiency (Fig. 5.4).

Figures 5.7(a)-5.7(c) show the phase distribution of lasers in a near-field plane for different widths of Gaussian apodizer, indicating a short-range in-phase locking as the

phase is not uniform throughout the array. The phase is uniform within small domains (as colour remains the same within each domain). The range of phase-locking decreases as the width of Gaussian apodizer increases. This is also evident by a decrease in the domain size and an increase in the number of domains. Figures 5.7(d)-5.7(f) show the far-field intensity distribution of lasers corresponding to Figs. 5.7(a)-5.7(c). A bright lobe in the center indicates in-phase locking of lasers, however, broadened lobes show a short-range of phase-locking. The increase in the width of lobes by increasing the width of Gaussian apodizer again confirms a decrease in range of phase-locking. Due to a short range of phase-locking, a significant portion of intensity also resides in the background (Fig. 5.7(f)). We have calculated the number of phase-locked lasers in x and y directions as $N_{x/y} = d/FWHM$, where d is the distance between zeroth-order lobe and first-order lobe in the far-field intensity distribution, and $FWHM$ is the full width at half-maximum of zeroth-order lobe [257]. The total number of phase-locked lasers in an array is given as $N = N_x \times N_y$. The number of phase locked lasers are found to be $N = 28$ (Fig. 5.7(a,d)), 15 (Fig. 5.7(b,e)) and 9 (Fig. 5.7(c,f)), corresponding to the Gaussian apodizer of widths $\sigma_G = 0.53$ mm, 0.64 mm, and 0.81 mm, respectively. Figures 5.7(g)-5.7(i) show the modified near-field intensities after the application of phase correction ($\phi = 2.5$ rad.). As evident, a decrease in the range of phase-locking leads to a decrease in the uniformity in a modified near-field intensity distribution. The reduced values of overlap integral are found to be 88.8% (Fig. 5.7(g)), 74.4% (Fig. 5.7(h)), and 68% (Fig. 5.7(i)), corresponding to $\sigma_G = 0.53$ mm, 0.64 mm, and 0.81 mm, respectively. Figures 5.7(j)-5.7(l) show the phase distribution of neutralizers, indicating that these consist of multi-phase structures (continuous phase), which is unlike the binary nature of a perfect long-range phase-locking of lasers (Fig. 5.4). The increase in non-uniformity affects the suppression of higher-order sidelobes in the far-field intensity distribution and thus affects the diffraction efficiency of zeroth-order lobe. We have found reduced diffraction efficiency of 87%, 80% and 75% for various short-range phase-locking of lasers obtained with $\sigma_G = 0.53$ mm 0.64 mm, and 0.81 mm, respectively. In particular, for the smallest phase-locking range, the diffraction efficiency has the lowest value (Fig. 5.7(l)). The range of phase-locking plays a crucial role in

5 *Generating high-energy densities by sidelobe suppression in the far-field of phase-locked lasers*

suppressing the higher-order sidelobes and obtaining a high-energy density laser output beam.

5.3.2   Effect of system size

High-energy density laser beam is desired for various applications, which can be generated by phase-locking more and more number of lasers. In principle, for the N number of perfectly phase-locked lasers, the intensity can be enhanced to $\sim N^2$ [233]. However, a significant portion of intensity still lies in the higher-order sidelobes. We have analyzed the effect of system size on the sidelobe suppression. To do that we have varied the number of lasers in a square array, and in-phase locked with a Gaussian apodizer of width $\sigma_G = 0.5$ mm, and after that calculated the diffraction efficiency of zeroth-order lobe in the modified far-field intensity distribution. The results are shown in Fig. 5.8. As evident, the diffraction efficiency remains approximately the same ($\approx 90\%$) upon variation of system size ($N = 16$ to 255 lasers).
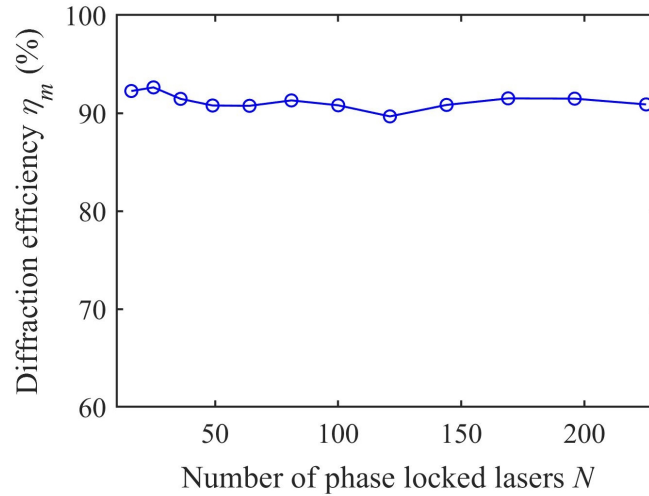
Figure 5.8: Variation of diffraction efficiency of zeroth-order lobe in a modified far-field intensity distribution, as a function of number of phase-locked lasers N. The parameters are taken as $\phi = 2.5$ rad. and $\sigma_G = 0.5$ mm.

It is evident that as long as the lasers in an array are perfectly phase-locked (long-range phase-locking), the diffraction efficiency remains almost the same (irrespective of the system size).

5.3.3 Effect of topological defects

Topological defects (vortex/anti-vortex) can occur during the phase-locking of laser arrays [73, 75, 136]. It has been observed that a 1D ring array geometry is highly susceptible to the occurrence of topological defects [73, 75]. Due to the phase singularity of topological defects, intensity remains zero at the center in the far-field intensity distribution. However, the intensity lies in multiple rings around the dark center. So, we have considered a ring array geometry to see the effect of topological defects on suppressing sidelobes and forming a high-energy density lobe in the center of far-field intensity distribution. We have phase-locked lasers (1D ring array) in a topological defect using the approach based on a degenerate cavity [37]. We have considered defects with various topological charges l, which determines the number of helices in the wavefront in one phase cycle. The results are shown in Fig. 5.9.
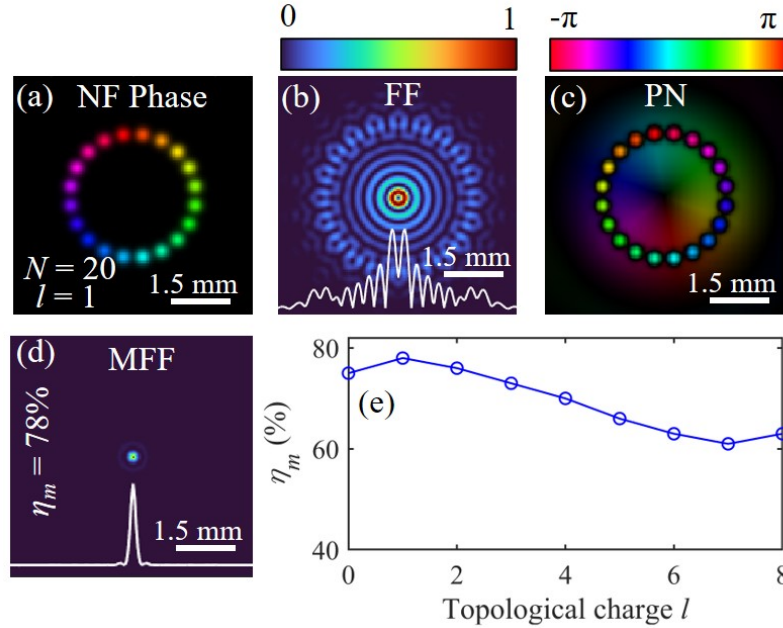
Figure 5.9: (a) The phase distribution of lasers in the near-field plane, where 20 lasers are phase-locked in a topological defect (vortex) with topological charge $l = 1$. (b) Far-field intensity distribution. (c) Phase distribution of neutralizer. (d) Modified far-field intensity distribution. (e) The diffraction efficiency of central lobe in the modified far-field intensity distribution as a function of topological charge l for $N = 20$ lasers.

Figure 5.9(a) shows the phase distribution of lasers in the near-field plane, where $N =$

20 lasers are phase-locked in a defect (vortex) with topological charge $l = 1$. As evident, the phase circulates from one site to the next, which confirms the vortex nature of output beam. The far-field intensity distribution of this topological defect is shown in Fig. 5.9, indicating almost zero intensity in the center, and all the intensity lies in multiple rings. To obtain modified near-field intensity, a phase correction of $\phi = \pi$ is applied to the innermost ring of the far-field distribution, and after that, a Fourier transform of the resultant field is performed. The modified near-field consists of an annular shape beam with same topological charge on the laser sites and an opposite topological charge in the background. To obtain the uniform phase distribution of modified near-field distribution, we neutralize the phase by a phase distribution given in Fig. 5.9(c). The modified near-field distribution with uniform phase results in a single lobe far-field (Fig. 5.9(d)), indicating that the intensity from multiple rings is successfully redistributed to form a high-energy density lobe in the center. The diffraction efficiency of this high-energy density lobe is found to be 78%. To see the effects of higher-order topological defects, we have varied l and calculated the diffraction efficiency, as shown in Fig. 5.9(e). As evident, the diffraction efficiency is found to be high for small values of l. A decrease in the diffraction efficiency for the large values of l can be attributed to the fact that size of dark region in the center becomes bigger and size of multiple rings also increases. It is clearly evidenced that even in the presence of topological defects, our approach is able to generate a high-energy density beam with a reasonably good diffraction efficiency.

5.4   High-energy densities from out-of-phase locked lasers

For the phase-locking of an array of lasers, the common passive techniques involve either Talbot diffraction or Fourier filtering. The method based on Talbot diffraction results in an efficient out-of-phase locking (usually at a half Talbot length) of lasers that can not be tightly focused. With the method based on spatial Fourier filtering, using an

aperture, the in-phase locking can be achieved. However, the efficiency of this method is low, specially, for small apertures, due to diffraction losses of the higher-orders, alignment sensitivity is relatively high, and the possible damage to the aperture due to strong intra-cavity fields. A recent approach based on combining the Talbot diffraction and Fourier filtering has been shown to obtain either in-phase locking or out-of-phase locking of large arrays with a good efficiency [136]. However, in both in-phase and out-of-phase locking a significant portion of intensity lies in higher-order sidelobes. So far, we have shown that by using the aperture filling approach, in the in-phase locked lasers, high diffraction efficiency of zeroth-order lobe can be obtained. However, a natural question arises whether the aperture filling approach can also be applied to the out-of-phase locked laser arrays, in order to obtain a high diffraction efficiency zeroth-order lobe in the far-field intensity distribution.

To check it, we have phase-locked the lasers in an out-of-phase configuration by using a simple approach of Fourier filtering with an aperture (a binary circular aperture). Placing a binary circular aperture in the far-field plane gives rise to a sinc coupling function in the near-field plane. The sinc function consists of both positive and negative values and thus enables phase-locking of lasers in an out-of-phase configuration [136]. We have phase-locked 121 lasers in an out-of-phase configuration in a square array with the help of a binary circular aperture of diameter 1.7 mm. The results are shown in Fig. 5.10. Figure 5.10(a) shows the phase distribution of lasers in a square array, indicating out-of-phase configuration throughout the array. The far-field intensity distribution consists of darkness in the center, and sharp first and higher-order lobes that again confirm a long-range out-of-phase locking of lasers (Fig. 5.10(b)). To obtain high-energy density lobe in the center, we have considered three different cases: i) phases of all the lobes (1 to 4 in Fig. 5.10(b)) are corrected by $\phi = \pi$, ii) phases of only lobes 1 and 2 are corrected by π, and iii) phase of only lobe 1 is corrected by π. Corresponding to these three cases, the phase distributions of neutralizers are shown in Figs. 5.10(c)-5.10(e). As evident, each case gives a different phase distribution of neutralizer. The modified far-field intensity distributions corresponding to these three different cases are shown in Figs. 5.10(f)-5.10(h).
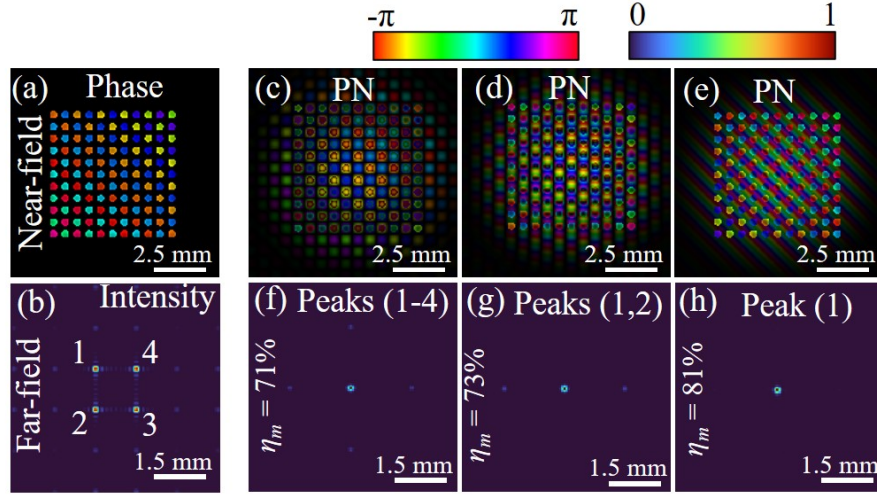
Figure 5.10: (a) The near-field phase distribution of lasers in a square array. (b) The far-field intensity distribution of out-of-phase locked lasers in a square array. The phase distribution of neutralizers, extracted from modified near-fields obtained by applying the phase correction $\phi = \pi$ to the first-order lobes (in the far-field) (c) 1 to 4, (d) 1 and 2, and (e) only 1. The modified far-field intensity distribution when phase correction is applied to (f) all lobes from 1 to 4,(g) only lobes 1 and 2, and (h) only lobe 1.

As evident, a majority of intensity is found to be tightly focused in the zeroth-order lobe with diffraction efficiency $\eta_m = 71\%$, 73%, and 81% corresponding to three different cases, respectively. It shows that our approach works reasonably well for the out-of-phase locked lasers.

5.5   Conclusions

In this Chapter, we have investigated the generation of high-energy densities by suppressing higher-order sidelobes in the far-field of phase-locked lasers. We have generated lasers in various 1D and 2D array geometries in a degenerate cavity and phase-locked them in the in-phase [out-of-phase] configuration with the far-field coupling using Gaussian apodizer [binary circular aperture]. Owing to the non-uniform amplitude and definite geometry, the far-field of phase-locked lasers consists of higher-order sidelobes. These higher-order sidelobes contain a significant amount of energy, which limits the use of an output beam for high-power applications. Further, the fraction of total energy residing in higher-order

sidelobes depends upon phase and geometry of laser arrays. To efficiently suppress higher-order sidelobes, the method involves two steps: (i) first step is the phase correction, where the phase of zeroth-order lobe in the far-field is changed by a certain angle, which results in a modified near-field, with nearly uniform-intensity distribution and non-uniform phase distribution, and (ii) second step includes the phase neutralization, where, in the modified near-field, the non-uniform phase distribution is neutralized to obtain a beam with a nearly uniform-intensity distribution and uniform-phase distribution. This beam yields a tightly focused high-energy density peak (zeroth-order lobe) in the far-field intensity distribution.

We have demonstrated our method for the phase-locked lasers in various 1D and 2D array geometries, such as square, triangular, Kagome, random, and 1D ring, based on a degenerate cavity. The results are quantified by calculating diffraction efficiency of the zeroth-order lobe. It is found that for long-range in-phase-locked laser arrays, the diffraction efficiency of zeroth-order lobe can be improved by several factors ($\sim 3 - 4$). The improved diffraction efficiencies are found to be in a range between $(90 - 95)\%$ (for 2D arrays) and $\sim 75\%$ (for 1D ring array). Further, for the long-range in-phase locking of lasers, the phase distribution of neutralizers is found to be binary in nature, which improves the simplicity of method.

Further, we have also analyzed the robustness of our method against various factors, such as system size, range of phase-locking, and presence of topological defects in a 1D ring array. It is found that a reduced phase-locking range decreases the diffraction efficiency of zeroth-order lobe. However, for a very short-range of phase-locking (only 9 lasers are phase-locked in an array of 81 lasers), the diffraction efficiency is found to be $\sim 75\%$, which is still significantly better than the efficiency of phase-locked laser array with higher-order sidelobes. The decrease in the diffraction efficiency can be attributed to the non-binary nature of phase distribution in neutralizers. We have found that the method works well for small to large system sizes, and diffraction efficiency approximately remains the same. In a 1D ring array, the high-energy density zeroth-order lobe can be generated with good diffraction efficiency even in the presence of topological defects.

---

5 *Generating high-energy densities by sidelobe suppression in the far-field of phase-locked lasers*

We have also applied our method for the out-of-phase locked square laser array, where the zeroth-order has no intensity. We have obtained a high-energy-density zeroth-order lobe with a high diffraction efficiency of 81%. Our results on producing high-energy density beams with suppressed higher-order sidelobes can be useful for various applications in different areas. The results presented in this Chapter are reported in Refs. [41, 42].

Chapter 6

Discrete optical vortex: Divergence and self-healing

6.1 Introduction

In previous chapters 2-5, we have discussed various types of spatially controlled structured light, with a particular emphasis on controlling intensity distributions as well as propagation properties. The optical vortex is also a well-known spatially structured light, which has attracted considerable interest in various fields, such as in optical communications, optical trapping and manipulation, microscopy, and material processing, etc [6, 11, 14, 258, 259]. Despite the remarkable progress on optical vortex, there still remains a vital issue that restricts the practical implementation and application of the optical vortex in the future, namely the limitation of power scaling capacity. In this Chapter, we present a novel and efficient intra-cavity method for the controlled generation of high-power discrete optical vortices by phase-locking a 1D ring array of lasers in a degenerate cavity. Further, a detailed investigation on the propagation properties such as divergence and self-healing are also performed.

An optical vortex is defined by a zero intensity point at the centre of beam with a screw-type dislocation in its phase distribution. Due to this screw-type dislocation in

the phase distribution, indefiniteness occurs at zero intensity spot, which is called phase-singularity point. Such beams possess an additional degree of freedom called orbital angular momentum (topological charge) that is different from the linear and spin angular momentum of field present due to its polarisation. There have been extensive studies on optical vortices such as Laguerre–Gaussian (LG) beam, Bessel-Gaussian (BG) beam, and Airy-vortex beam [77, 260, 261]. These are examples of continuous vortices that have continuous intensity and phase distribution over the contour. In addition to continuous vortices (exist on a uniform background), a new class of discrete optical vortices has been investigated both theoretically and experimentally in optics and atomic physics, such as in optical lattices of Bose-Einstein condensates (BECs) [262], 1D and 2D periodic photonic structures of light [74, 263–267], 1D ring network of coupled lasers [73, 75], 1D ring network of coupled parametric oscillators [268], and linear azimuthons in circular fiber arrays [269]. In such vortices, the core consists of zero intensity, and phase winds to provide localized circular energy flows between the sites. These consist of step-like phase functions over the discrete contour [74, 75, 270].

There are various methods for generating optical vortices, which include generation either directly at the source or externally. In several methods, a continuous optical vortex is generated from a single laser source, whose output power and beam quality are limited by the laser operation parameters. It is well-known that in high-power lasers, the presence of nonlinear effects, higher order modes, and thermal effects lead to the degradation of output beam quality. Further, the generation of optical vortices external to the laser source suffers more power loss due to optical transforming elements. However, for generating high-powers with ideal output beam quality, an alternate approach is to take several low-power laser beams (with fundamental Gaussian mode profile) and combine them coherently. In this regard, several methods based on coherent beam combining/phase locking of lasers have been proposed, where phases of all the laser beams are precisely controlled [271]. The idea of phase controlling ability has also been exploited to form high-power optical vortices in cyclic arrays of linear and nonlinear systems. For example, high-power vortices have been realized by coherent beam combination of a six-

element hexagonal fiber amplifier array [272], and by employing a concept of extracting cost functions at the non-focal-plane in a tiled aperture coherent beam combination system [273]. In a degenerate cavity configuration, 1D ring array of lasers with the nearest neighbour negative coupling has been shown to form a steady-state phase-locked solution that consists of topological charge, and behaves as a discrete optical vortex [73, 75]. Further, radial arrays of Gaussian beamlets with well-defined initial phase distributions have been shown to form an optical vortex [59, 270, 274]. The circular arrays of nonlinear waveguides and linear azimuthons in circular fiber arrays have also been shown to form discrete optical vortices [74, 269]. We present a novel and efficient method for controlled generation of discrete optical vortex of any arbitrary system size and topological charge.

Generally, the propagation of optical vortices is required for their use in applications, and in this context, several investigations have been performed. In 1D and 2D nonlinear systems (coupled nonlinear waveguides and optically induced photonic lattices), the formation of discrete optical vortex solitions as well as their propagation dynamics and stability have been extensively studied [74, 74, 263–267]. Further, the propagation of optical vortices, formed in 1D radial arrays (linear systems), has also been investigated [59, 269, 270, 272–274]. Particularly, it has been shown that the radial array of coherent Gaussian laser beams with specific initial phase distributions can be used to form an optical vortex after propagating a certain distance [59]. The effect of atmospheric turbulence on the propagation of these vortices has also been investigated, and it is shown that the turbulence can prohibit the formation of an optical vortex or it can lead to the disappearance of the formed optical vortex [274]. The propagation properties of phase-locked and non-phase-locked radial laser arrays have been investigated analytically based on calculations of irradiance distribution and M^2 factor [275]. Further, the propagation of well-known LG, BG, and Airy vortex beams have also been investigated in detail [14, 276, 277].

It is well-known that discrete systems behave differently than continuous systems. For example, in the context of vortex, a continuous system (e.g, LG, BG, and Airy vortex) can have a continuum of stable solutions (topological charge states), whereas, a discrete

system can have a finite number [74, 75, 269]. The discrete systems also provide the most general framework for studying networks of nonlinear coupled oscillators, and circulation of the power flow between occupied sites identifies the presence of a discrete optical vortex [75, 278–280]. In the continuous vortices, in addition to the power limitation, the size of vortex and divergence upon propagation depends strongly on the topological charge values [276], which limits the imposition of higher topological charge transfer over a long range because of the difficulty of detection due to limited size of detector. The question arises whether discrete optical vortices exhibit the same propagation properties or not. The self-healing in various types of continuous beams with and without topological charge has also been extensively investigated [57, 281–284]. However, for the discrete optical vortices, the question remains unexplored whether these exhibit similar self-healing properties or not.

The Chapter is organized as follows. In Sec. 6.2, we present the formation of discrete optical vortices by phase-locking 1D ring array of lasers in a degenerate cavity that involves spatial Fourier filtering with a specifically designed amplitude mask. This approach has enabled a controlled generation of discrete optical vortices with different topological charges. Further, in Sec. 6.3, we have discussed the propagation properties of generated discrete optical vortices, and have shown that for a fixed system size and distance between the lasers, the size of discrete optical vortex, as well as its divergence, do not depend on the topological charge, as opposed to the continuous optical vortices. In Sec. 6.4, a detailed analysis on the self-healing properties of discrete optical vortices is presented. The self-healing of optical vortex is quantified by an overlap integral (Eq. (1.26)) [150]. The conclusions of the chapter are given in Sec. 6.5. The investigations presented in this Chapter are given in Refs. [43–45].

6.2   Generation of a discrete optical vortex

A continuous optical vortex can be described as $E \propto r^{|l|} \exp(il\phi)$, where E is the field, r and ϕ are the polar coordinates [269, 276]. The integer quantity l is the topological charge

of the vortex that determines the number of helices in the wavefront, in a phase cycle of 0 to 2π. The intensity is continuous in a donut-shape around the center and consists of a non-zero phase circulation in multiplication of 2π.

A discrete optical vortex consists of a finite number of sites (lasers/beamlets/waveguides) in a cyclic array, where the intensity in the center is zero, and phase circulates from one site to the next in either clockwise (vortex) or anticlockwise (anti-vortex) direction [73–75, 269]. Unlike a continuous optical vortex, the discrete optical vortex consists of step-like behaviour of phase along the contour encompassing the phase singularity [269]. A discrete optical vortex is shown in Fig. 6.1, which is prepared by arranging 20 lasers in a ring array with a specific initial phase distribution in the vortex configuration. A discrete optical vortex has also been reported in Refs. [59, 269, 274].
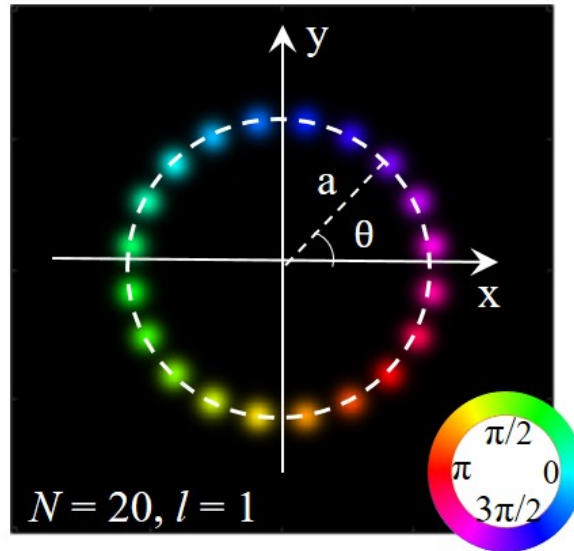
Figure 6.1: Illustration of a discrete optical vortex having topological charge $l = 1$, prepared by $N = 20$ lasers (with Gaussian TEM$_{00}$ mode profiles) arranged in a circular ring array. The other parameters are chosen as $a = 5.8$ mm, beam waist of each laser $\sigma_0 = 0.4$ mm, and distance between two neighbouring lasers $d = 1.8$ mm.

For a general case of N lasers, the electric field distribution of a discrete optical vortex can be written as (Eq. (1.1))

$$E(x, y; z = 0) = E_0 \sum_{j=1}^{N} e^{-\frac{(x-\alpha_j)^2 + (y-\beta_j)^2}{2\sigma_0^2}} e^{i\phi_j}, \tag{6.1}$$

where $(\alpha_j, \beta_j) = a(\cos\theta_j, \sin\theta_j)$, $a = d/\sqrt{1 - \cos(2\pi/N)}$, $\theta_j = \pi(2j - 1)/N$, and $\phi_j = 2\pi l(j - 1)/N$. d denotes the distance between the two nearest neighbour lasers. Each laser (j) has the same amplitude E_0, same beam waist σ_0, and different initial phase ϕ_j. Note, to form a discrete optical vortex the ring array must obey the periodic boundary conditions: $E_{j+N} = E_j$ [73]. The topological charge l of the discrete optical vortex is given by Eq. (1.2).

The discrete optical vortices have been formed by different methods, such as in optically induced photonic lattices [74, 263–267], nonlinear waveguides [74], circular fiber arrays [269], coherent beam combining technique [272, 273], coupled parametric oscillators [268], and phase-locked lasers [73, 75]. We present generation of discrete optical vortices by phase-locking of lasers in a degenerate cavity, involving spatial Fourier filtering in the far-field plane. In Refs. [73, 75], the discrete optical vortex has been formed by phase-locked lasers in a 1D ring array, where lasers were negatively coupled by diffractive coupling. It was found that with an odd number of lasers, a discrete optical vortex/anti-vortex with the lowest topological charge is the most probable solution. However, for an even number of lasers, the probability of finding discrete optical vortex/anti-vortex was negligible for $N \leq 10$, and increases monotonically for large N. The reported works mainly focused on the effect of optical vortices in phase-locking of lasers, and their links to Kibble-Zurek mechanism [73, 75], however, by this method a controlled generation of discrete optical vortex with specific l and arbitrary system size (N) was not possible. In this regard, we present a novel and efficient intra-cavity method to generate discrete optical vortex with precisely controlled topological charge l for a given system size N. The scheme as well as representative results are shown in Fig. 6.2.

The scheme is based on a similar degenerate cavity as described in Chapter 5, where a Gaussian apodizer in the far-field is replaced by a specifically designed amplitude mask (FF mask), whose transmission function is governed by the Fourier transform of desired discrete optical vortex beam. Note, a detailed description of degenerate cavity is already given in Sec. 5.2 of Chapter 5. The FF mask helps to eliminate the undesired phase distributions by introducing additional losses to them and thereby enables the lasers to
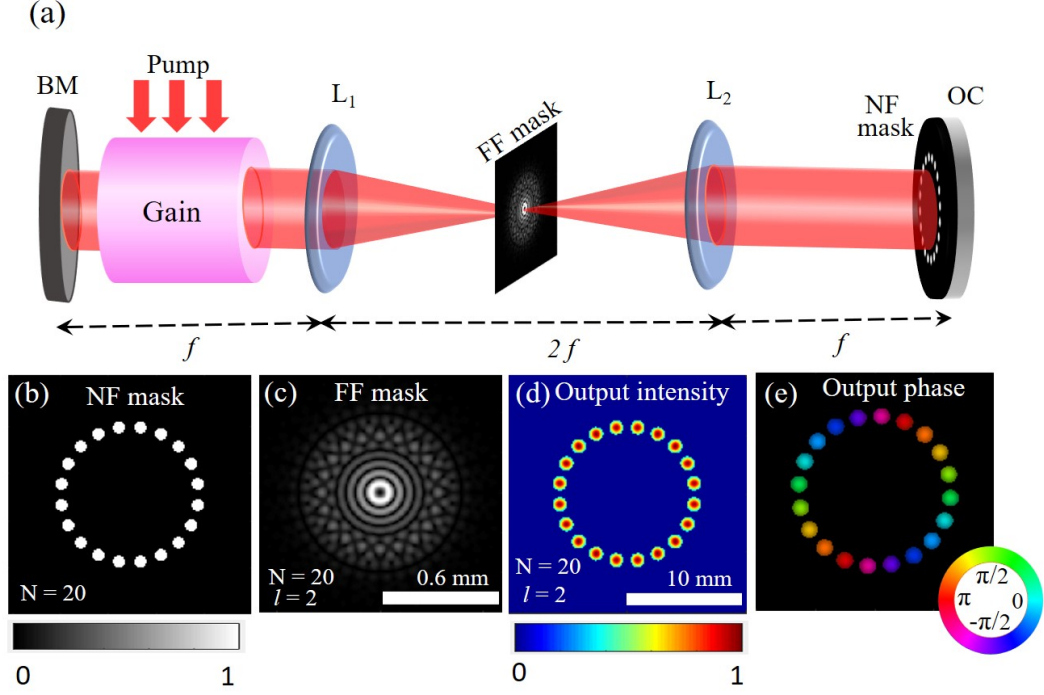
Figure 6.2: (a) Schematic of a degenerate laser cavity for generating a discrete optical vortex. (b) Near-field binary amplitude mask containing 20 circular holes in a ring geometry. (c) Far-field gray-scale mask. (d)-(e) Simulated near-field intensity and phase distributions of lasers in a ring array with topological charge $l = 2$.

find a correct phase distribution. In the beginning, all the lasers have random phase distributions, and thus are equally probable. As the process evolves (multi-round-trip propagation), different phase distributions of lasers compete with each other for the same gain medium, and upon introduction of an additional constraint FF mask, different phase distributions consist of different amounts of losses, and thus during the mode competition only the phase distribution with minimum loss sustains and others stop lasing. The minimum loss solution represents a phase-locked state of lasers, which is a desired discrete optical vortex. The spatial Fourier filtering (by FF mask) is a key parameter to find the correct and desired phase distribution of lasers. The role of additional constraints in the Fourier plane is also emphasized in phase retrieval problems solved by laser solver [139]. The obtained discrete optical vortex is a coherent steady-state solution.

We have simulated this scheme by using a modified Fox-Li iterative method, which is also adopted earlier to reproduce experimental findings of phase locking of lasers in a

degenerate cavity [136]. Corresponding to one-round trip propagation of field inside the degenerate cavity (Fig. 6.2), the simulation involves the following operations

$$E_{n+1}(x,y) = NF\left(\mathcal{F}^{-1}\left(FF\left(\mathcal{F}\left(g(x,y) \times E_n(x,y)\right)\right)\right)\right), \tag{6.2}$$

where E_n and E_{n+1} denote the field distributions of nth and $(n+1)^{th}$ round-trips at the near-field plane. One round trip propagation inside the degenerate cavity is equivalent to one iteration in the simulation. NF represents near-field binary amplitude mask and FF denotes the far-field gray-scale mask. $\mathcal{F}$ and $\mathcal{F}^{-1}$ indicate the Fourier transform and inverse Fourier transform operations, respectively. $g(x,y)$ denotes the saturated gain described as

$$g(x,y) = \frac{g_0}{1 + \frac{I(x,y)}{I_{sat}}}. \tag{6.3}$$

g_0 is the unsaturated gain, I_{sat} is saturation intensity and $I(x,y) = E^2(x,y)$ is the local intensity. In all our simulations, we have chosen $g_0 = 15$, $I_{\text{sat}} = 1000$, $a = 5.8$ mm, $d = 1.8$ mm, and $\sigma_0 = 0.4$ mm. Our simulations require around 100 iterations in order to converge to a desired steady-state discrete optical vortex. The representative results are shown in Figs. 6.2(b)-6.2(e). Figure 6.2(b) shows the binary near-field (NF) mask, where $N = 20$ holes of diameter 1.2 mm are arranged in a 1D ring geometry. Figure 6.2(c) shows the far-field (FF) mask, obtained by Fourier transform of a discrete optical vortex with $N = 20$ and $l = 2$. The steady-state solution of the laser output is shown in Figs. 6.2(d) and 6.2(e), indicating intensity and phase distributions of lasers. It is evident that phase-locking of lasers forms a discrete optical vortex, and phase circulation corresponds to a topological charge of $l = 2$. Note, each laser in the array consists of nearly a fundamental TEM$_{00}$ mode.

To demonstrate a controlled generation of discrete optical vortices, we have simulated the results for different N and l values, as shown in Figs. 6.3 and 6.4. Figure 6.3(a) shows a near-field binary amplitude mask for $N = 10$. Figures 6.3(b)-6.3(d) show the far-field
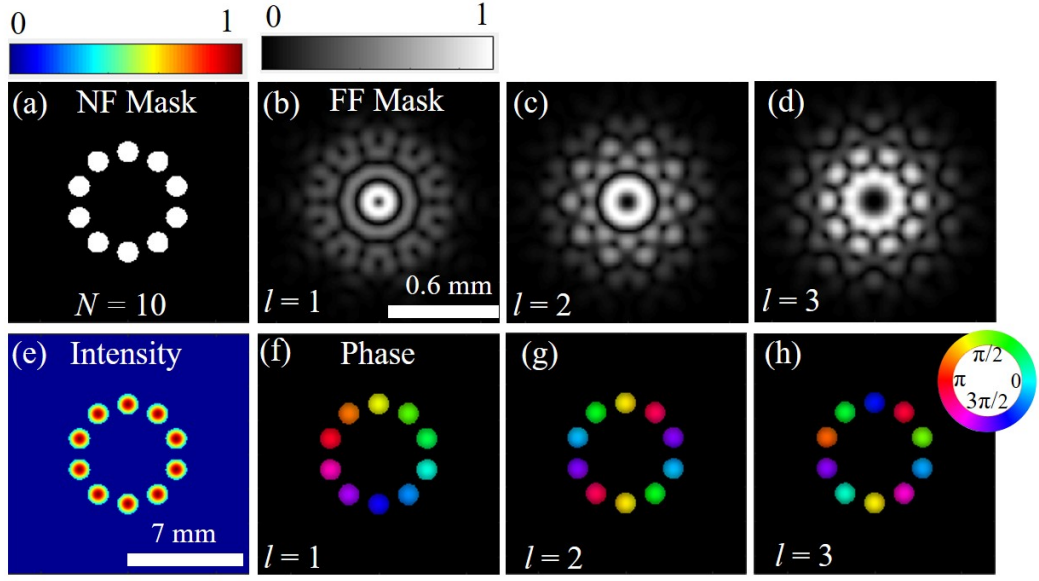
Figure 6.3: Simulated results of discrete optical vortices with various topological charges in a ring array of $N = 10$ lasers. (a) Near-field binary amplitude mask. (b)-(d) Far-field masks corresponding to $l = 1$, $l = 2$, and $l = 3$, respectively. (e) Near-field intensity distribution of phase-locked lasers in a discrete optical vortex, which remains the same for all l values. (f)-(h) Near-field phase distributions of phase-locked lasers in a discrete optical vortex with $l = 1$, $l = 2$, and $l = 3$, respectively.

masks, obtained by Fourier transform of discrete optical vortices with topological charges $l = 1$ (Fig. 6.3(b)), $l = 2$ (Fig. 6.3(c)), and $l = 3$ (Fig. 6.3(d)). As evident, for different l values, the far-field masks are different and thus enable a controlled generation of specific discrete optical vortex at the output. Figure 6.3(e) represents the near-field output intensity distribution of phase-locked lasers in a discrete optical vortex, which remains the same for all l values. Figures 6.3(f)-6.3(h) show the near-field phase distributions of phase-locked lasers in a discrete optical vortex with $l = 1$ (Fig. 6.3(f)), $l = 2$ (Fig. 6.3(g)), and $l = 3$ (Fig. 6.3(h)). As evident, by specifically designing a far-field mask, a discrete optical vortex with specific l can be generated efficiently. To show the generalization of our method, we have also generated discrete optical vortices for $N = 20$ and topological charges $l = 1$ and 3, the results are shown in Fig. 6.4. Note, for $l = 2$, the results are already shown in Fig. 6.2. It is clearly evidenced that a controlled generation of discrete optical vortex with specific N and l can be obtained by using a specifically designed
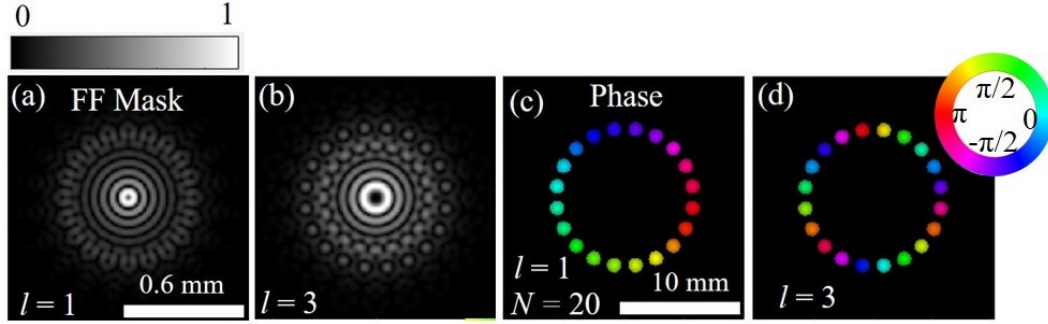
far-field mask.

Figure 6.4: Simulated results of discrete optical vortices with various topological charges in a ring array of $N = 20$ lasers. (a)-(b) Far-field mask corresponding to $l = 1$, and $l = 3$, respectively. (c)-(d) near-field phase distributions of phase-locked lasers in a discrete optical vortex with $l = 1$, and $l = 3$, respectively. Note, for $l = 2$ the results are shown in Fig. 6.2.

6.3 Propagation Properties

In various applications, an optical beam is required to travel in free space, through various optical components (having finite size aperture) and needs to be detected with a device that has finite active area. To maintain the efficiency of a system (complete beam should be reached and detected at the receiving end), the knowledge of beam divergence upon propagation is required. Recently, an analytical study on the divergence of a continuous vortex (LG beam) has been performed, and shown that LG beams with different topological charges exhibit different sizes, and consequently possess different divergence properties upon propagation [276].

The propagation of an optical beam in free space can be described by using an extended Huygens-Fresnel diffraction integral [148]:

$$E(x', y'; z) = \frac{-ik\, e^{ikz}}{2\pi z} \iint_{-\infty}^{\infty} E(x, y; z = 0) \exp\left(\frac{ik}{2z}\left[(x - x')^2 + (y - y')^2\right]\right) dx\, dy, \quad (6.4)$$

where k is a wave number, (x, y) and (x', y') are spatial coordinates of input and output plane separated by a distance z.

The LG modes with $p = 0$ (radial index) and $l > 0$, consist of single-ring-annular shapes with vortex phase distributions, and radius of maximum optical intensity can be given as [276]

$$r(I_{\max}^{\text{LG}}) = \sqrt{\frac{|l|}{2}}\sigma^{LG}(z). \tag{6.5}$$

where $\sigma^{LG}(z)$ is the beam waist. Equation (6.5) shows that the size of the LG beam is proportional to l, indicating that size grows with increasing l, and for high l it can be much larger than the beam waist.

However, for the discrete case, the size of a vortex does not depend on l, rather it depends on the number of lasers (N) in an array, as well as the distance between the nearest-neighbor lasers (d). To show it, we calculate the maximum intensity radius of a discrete optical vortex (Eq. (6.1)) at the waist plane $(z = 0)$. We first convert Eq. (6.1) in polar coordinates $(r$ and $\psi)$ using relations $x = r\cos\psi$ and $y = r\sin\psi$, and then find the derivative with respect to r as

$$\frac{\partial}{\partial r}\left(E_0 \sum_{j=1}^{N} \exp\left(\frac{r^2 + a^2 - 2ra\cos(\psi - \theta_j)}{2\sigma_0^2}\right) \exp\left(i\phi_j\right)\right) = 0. \tag{6.6}$$

The term $\exp\left(i\phi_j\right)$ describes the constant phase of each laser (j) that is independent of radial distance r. Therefore, for $\psi = \theta_j$, after simplifications we obtain

$$r(I_{max}^{Dis}) = a. \tag{6.7}$$

Equation (6.7) clearly shows that the size of a discrete optical vortex depends on parameter a, which is a function of N and d (Eq. (6.1)). Thus, for a fixed N, a discrete optical vortex with different l values exhibits the same size. Note, for a discrete system, there are finite number of topological charges $(|l| \leq N/2)$ [74], as opposed to a continuous system. Figure 6.5 shows a comparison between the continuous and discrete optical vortices, indicating that maximum intensity radius remains constant for various topological charges in

a discrete optical vortex. This property could be exploited to improve the efficiency of a system involving components with finite size apertures.
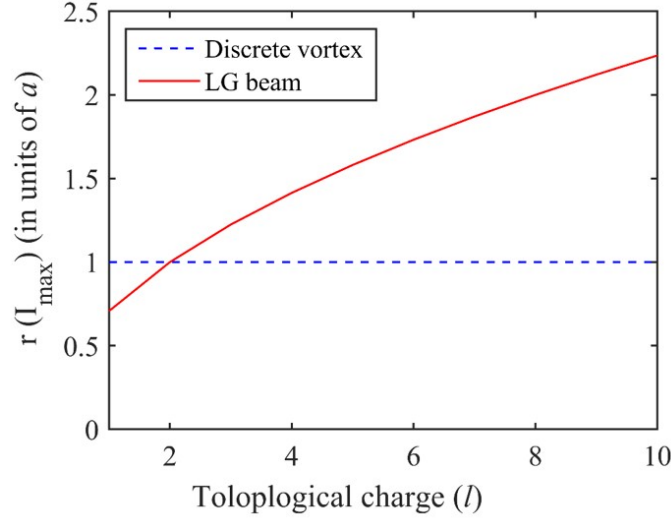
Figure 6.5: The maximum intensity radius as a function of topological charge (l). The radius increases with l for a continuous vortex (red-solid curve), whereas, it remains invariant for a discrete optical vortex (blue-dashed curve). Note, for the continuous vortex case, LG beams are considered with $p = 0$, $\sigma_0^{LG} = a$ and $l \neq 0$. For the discrete case, a ring array of $N = 20$ lasers is considered.

In a continuous vortex, for $l = 0$ the maximum intensity radius comes out to be zero (Eq. (6.6)), and fails to describe the size of a beam [276]. The size of a vortex can also be determined by calculating the root mean square radius or variance of laser intensity distribution. The root mean square radius can give accurate information on how the size of a beam grows with the propagation distance. In a discrete optical vortex, after a certain propagation distance, the intensity distribution consists of multiple rings, and then the size of a resulting beam can be accurately determined by calculating its variance. The root mean square radius can be described as [276]

$$r_{rms}^2 = \frac{\iint (x^2 + y^2)\, I\, dx\, dy}{\iint I\, dx\, dy}. \tag{6.8}$$

The root mean square radius for a continuous vortex (LG beam with radial index $p = 0$)

is given as [276]

$$r_{rms}(I^{LG}) = \sqrt{\frac{|l| + 1}{2}} \sigma^{LG}(z).$$ (6.9)

Equation (6.9) shows that it is also valid for a special case of $l = 0$. We have also determined the root mean square radius of a discrete optical vortex as a function of propagation distance ($z > 0$) and compared it with a continuous vortex. The intensity distribution of a discrete optical vortex at a propagation distance $z > 0$ can be given as [274]

$$
\begin{aligned}
I^{Dis}(x, y; z) &= \frac{E_0^2 \sigma_0^2}{\sigma(z)^2} \exp\left(-\frac{(x^2 + y^2 + a^2)}{\sigma(z)^2}\right) \sum_{p,q}^{N} \exp\left(i\phi_p - i\phi_q\right) \\
&\times \exp\left(\frac{x}{\sigma(z)^2}\left(a(\cos\theta_p + \cos\theta_q) - \frac{iza}{k\sigma_0^2}(\cos\theta_p - \cos\theta_q)\right)\right) \\
&\times \exp\left(\frac{y}{\sigma(z)^2}\left(a(\sin\theta_p + \sin\theta_q) - \frac{iza}{k\sigma_0^2}(\sin\theta_p - \sin\theta_q)\right)\right),
\end{aligned}
$$ (6.10)

where $\sigma(z) = \left[\sigma_0^2 + \frac{\lambda^2 z^2}{4\pi^2 \sigma_0^2}\right]^{1/2}$ is the beam waist at a distance z. To analyze the root mean square radius of a discrete optical vortex, we have used Eq. (6.10) in Eq. (6.8), and solved it numerically. The results of root mean square radius of discrete and continuous vortices with different l values are shown in Fig. 6.6. As evident, the size of a discrete optical vortex increases with propagation distance z, but it remains invariant for different l (Fig. 6.6(a)). Whereas, in a continuous vortex, the size varies with l (Fig. 6.6(b)).

It is well-known that divergence is an inherent property of light beams. The light beams with minimal divergence are required for various applications including long-range communications and high-rate data transfer. We have analyzed the divergence of a discrete optical vortex, and its dependence on l, and compared these properties with a continuous vortex. Mathematically, divergence $\alpha(z)$ can be written as:

$$\alpha(z) = \arctan\left(\frac{\partial r_{rms}}{\partial z}\right).$$ (6.11)
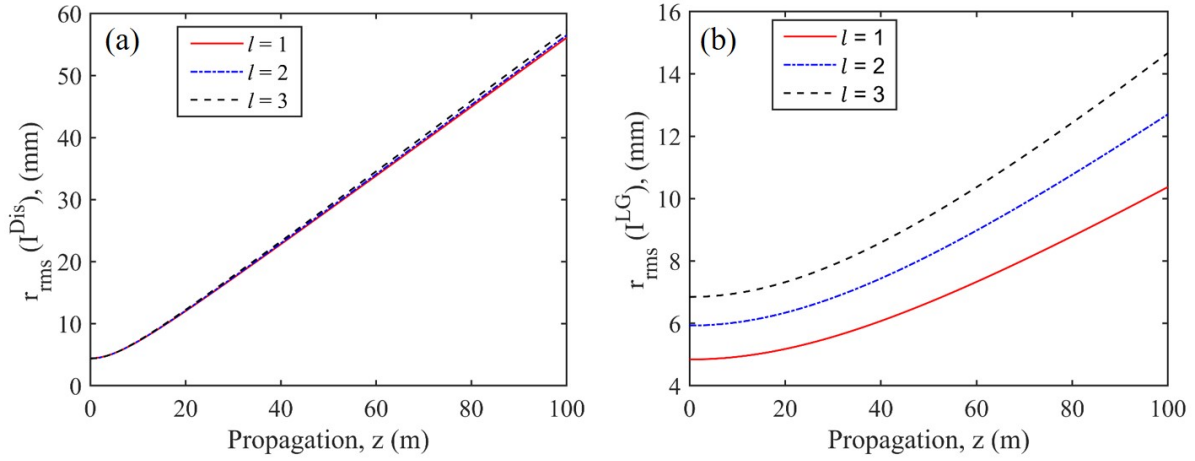
Figure 6.6: The root mean square radius as a function of propagation distance z, for (a) a discrete optical vortex with different l values, and (b) a continuous vortex with different l values. The continuous vortex is considered as an LG beam with $p = 0$ and $\sigma_0^{LG} = a$. A discrete optical vortex is considered with $N = 20$.

For a continuous vortex (LG beam with $p = 0$), the divergence is found to be dependent on l as [276]

$$\alpha^{LG}(z) = \sqrt{\frac{|l| + 1}{2}} \frac{2}{k\sigma_0^{LG}}, \tag{6.12}$$

where k is wave vector in free space. Equation (6.12) shows that divergence increases with the l. Particularly, a continuous vortex with high l exhibits large divergence. Using Eq. (6.11), we can find the divergence of a discrete optical vortex. The results for both continuous and discrete optical vortices for different values of l are presented in Fig. 6.7. As evident, the divergence of a discrete optical vortex remains almost invariant with l, as opposed to a continuous vortex.

6.4   Self-healing properties

Self-healing refers to the ability of an obstructed beam can regain its truncated parts by simply propagating a certain distance. It is an important property, which is associated
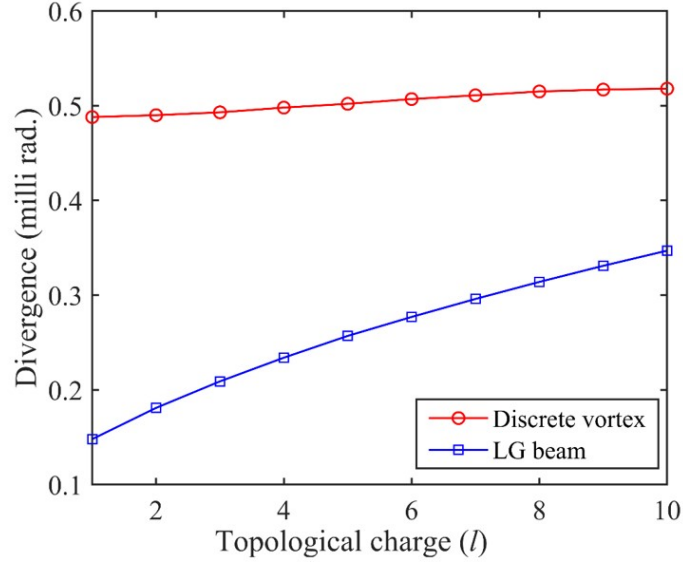
Figure 6.7: The divergence (α) as a function of topological charge l for a discrete optical vortex (red solid curve with circles) and a continuous vortex (blue dashed curve with squares). The discrete optical vortex is formed by $N = 20$ phase-locked lasers in a ring array, whereas, a continuous vortex is considered as an LG beam with $p = 0$ and $\sigma_0^{LG} = a$. α is calculated by propagating vortex up to a distance of $z = 100$ m.

with the robustness of a beam against perturbations, and is highly desired in applications. There have been several investigations to study the self-healing property of various kinds of beams including diffracting (Hermite-Gaussian (HG) and Laguerre-Gaussian (LG)) and non-diffracting (Bessel and Airy) beams [281, 283, 285, 286]. For a continuous vortex, self-healing has already been investigated in detail [281–283]. However, in a discrete optical vortex, self-healing has not yet been explored. As mentioned above, the size and divergence of a discrete optical vortex are found to exhibit different behaviour (Figs. 6.5, 6.6 and 6.7). A natural question arises whether a discrete optical vortex possesses similar or different self-healing effects than a continuous optical vortex. We have investigated self-healing of discrete optical vortex under different conditions, for example, truncation of a single laser as well as compound truncation at waist plane ($z = 0$) and truncation of multiple inner rings at propagation planes ($z > 0$). We have quantified the self-healing effects by calculating an overlap integral (Eq. (1.26)), which measures the resemblance between the self-healed and original beams.

To check the self-healing effects, first we have truncated a discrete optical vortex by truncating a laser at the waist plane $z = 0$ and then propagated it in a free space. The results of ideal and truncated discrete optical vortices are shown in Fig. 6.8. Figure 6.8(a) shows the intensity distribution of a discrete optical vortex with $N = 20$ and $l = 1$ at $z = 0$. The propagation shows alternations in the intensity distribution due to diffraction, and at a relatively large distance ($z \sim 15$ m) it acquires a multiple-ring intensity pattern (Figs. 6.8(b)-6.8(f)). Figure 6.8(g) shows a truncated discrete optical vortex, where one laser is removed from the array at $z = 0$. The propagation of this truncated vortex clearly shows that the removed part slowly reappears, and attains an almost similar multiple-ring pattern at a distance of $z = 15$ m, as shown in Figs. 6.8(h)-6.8(j). To understand the self-healing, we plotted the intensity cross-sections of truncated discrete optical vortex (blue-dashed curve) and compared with the intensity cross-sections of an ideal discrete optical vortex (green-solid curve) at various propagation distances, as shown in Figs. 6.8(m)-6.8(p). The intensity cross-sections are obtained along circles drawn in Figs. 6.8(a)-6.8(d) for an ideal discrete optical vortex and Figs. 6.8(g)-6.8(j) for a truncated discrete optical vortex. As evident, during the propagation, the intensity redistributes as a result of diffraction (Figs. 6.8(n) and 6.8(o)), and intensity from the nearest-neighbour lasers moves into the removed laser site, indicated by the decreased peak values of intensities (Fig. 6.8(p)). This results in the self-healing of a truncated discrete optical vortex.

Further, we have verified self-healing in the experiments. To do this, we have generated discrete optical vortices using a spatial light modulator (SLM), as shown in Fig. 6.9, based on our convenience and availability of equipment. The experimentally generated discrete optical vortices are completely identical to the ones simulated using degenerate laser cavity shown in Fig. 6.2. The phase hologram for SLM is prepared by complex amplitude modulation using a method described in Sec. 1.5.1. The SLM screen is illuminated normally with a Gaussian beam, expanded with lenses L$_1$ and L$_2$ of focal lengths $f_1 = 5$ cm and $f_2 = 30$ cm. The phase hologram on the SLM modulates amplitude and phase of an input Gaussian laser beam, and accordingly, the light from an input Gaussian laser

Figure 6.8: Simulated results of self-healing of a discrete optical vortex with $N = 20$ and $l = 1$. (a)-(f) Intensity distributions of an ideal discrete optical vortex at various propagation distances. (g)-(l) Intensity distributions of a truncated discrete optical vortex at various propagation distances. (m)-(p) The intensity cross-sections across the circles drawn in (a)-(d) and (g)-(j), for ideal and truncated discrete optical vortices, respectively.
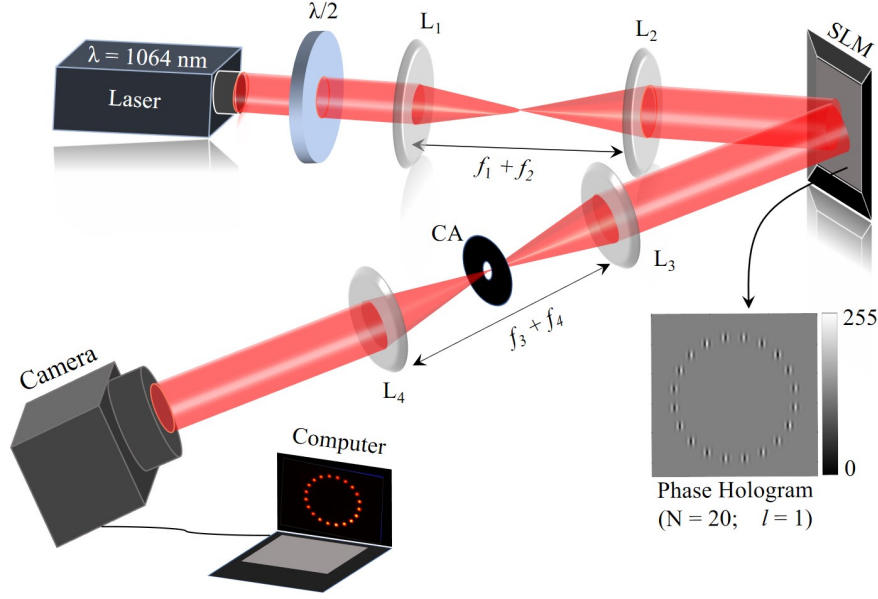
Figure 6.9: Schematic of experimental setup used to generate discrete optical vortices. $\lambda/2$: Half-wave plate; L_1, L_2, L_3, L_4: Plano-convex lens with focal lengths 5 cm, 30 cm, 20 cm and 20 cm. CA: Circular aperture; SLM: Spatial Light Modulator.

beam splits in the form of multiple lasers arranged on a 1D ring array with discrete phase distributions in a vortex configuration. After reflection from SLM, we obtain modulated light in several orders (see Sec. 1.5), which contains the desired discrete optical vortex. The desired discrete optical vortex in the first order is isolated with a spatial Fourier filter (CA) of suitable size, placed in the middle of a telescope made with lenses L_3 ($f_3 = 20$ cm) and L_4 ($f_4 = 20$ cm) (Fig. 6.9).
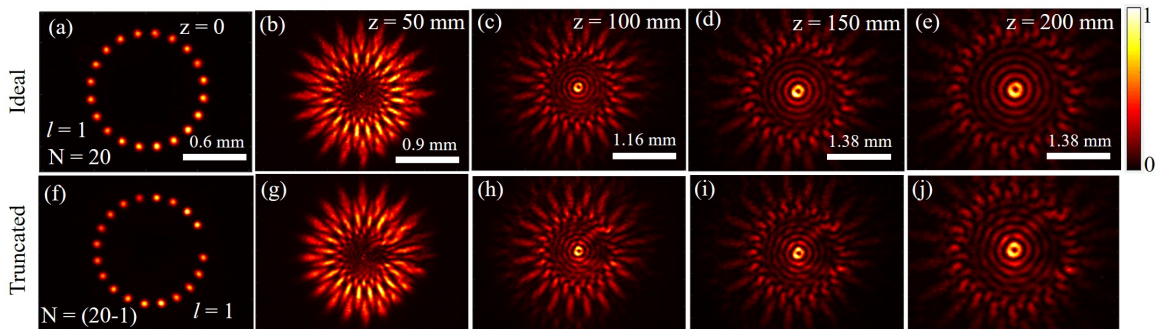
Figure 6.10: Experimental results of self-healing of a discrete optical vortex with $N = 20$ and $l = 1$. (a)-(e) Intensity distributions of an ideal discrete optical vortex at various propagation distances. (f)-(j) Intensity distributions of a truncated discrete optical vortex at various propagation distances.

Figure 6.10 shows the experimental results corresponding to the self-healing of discrete optical vortex for $N = 20$ and $l = 1$. In the experimental generation of discrete optical vortex, beam waist of each laser is chosen as 0.16 mm and centre-to-centre separation is 0.84 mm (Fig. 6.10(a)). Note, we have chosen different parameters in our experiments compared to the simulations, specially due to the limited dimensions of SLM and camera. Figures 6.10(a)-6.10(e) show the intensity distributions of ideal discrete optical vortex propagated to $z = 200$ mm. Figure 6.10(f) shows a truncated discrete optical vortex, where a laser is truncated from the array at $z = 0$. Figures 6.10(g)-6.10(j) show the self-healing of truncated discrete optical vortex, where the truncated part reappears during the propagation in free space, and at $z = 200$ mm, multiple ring type intensity distribution is observed. As evident, the experimental results show good agreement with the simulations.

Further, we have also investigated the propagation of truncated discrete optical vortices with topological charges $l = 2$ and 3, and have found similar effects of self-healing. At a propagation distance of ~ 15 m, we have observed that an innermost ring in intensity distribution consists of a lobe structure, which indicates the information of a topological charge of a discrete optical vortex. The results are shown in Fig. 6.11. Figures 6.11(a)-6.11(c) show the intensity distributions of discrete optical vortices with different l values, at a propagation distance of $z = 15$ m. As evident, the intensity distributions consist of multiple-ring structure, and for the different values of l an innermost ring consists of different number of intensity lobes (intensity maximas). This is clearly visible in the normalized intensity cross-sections of innermost rings (taken along dotted circles marked in Figs. 6.11(a)-6.11(c) for different l values, as shown in Fig. 6.11(d). It is evident that for different values of $l = 1$, 2 and 3, there are one (black-solid curve), two (red-dashed curve), and three (blue-dot-dashed curve) intensity lobes (maxima), respectively. The intensity lobes are found to be the same as l values, which precisely tell the information of topological charge carried by a discrete optical vortex. This suggests that by removing a single laser site, and propagation of this truncated discrete optical vortex enables to extract the information of topological charge carried by a discrete optical vortex. Our results on identification of topological charge of a discrete optical vortex show similarities
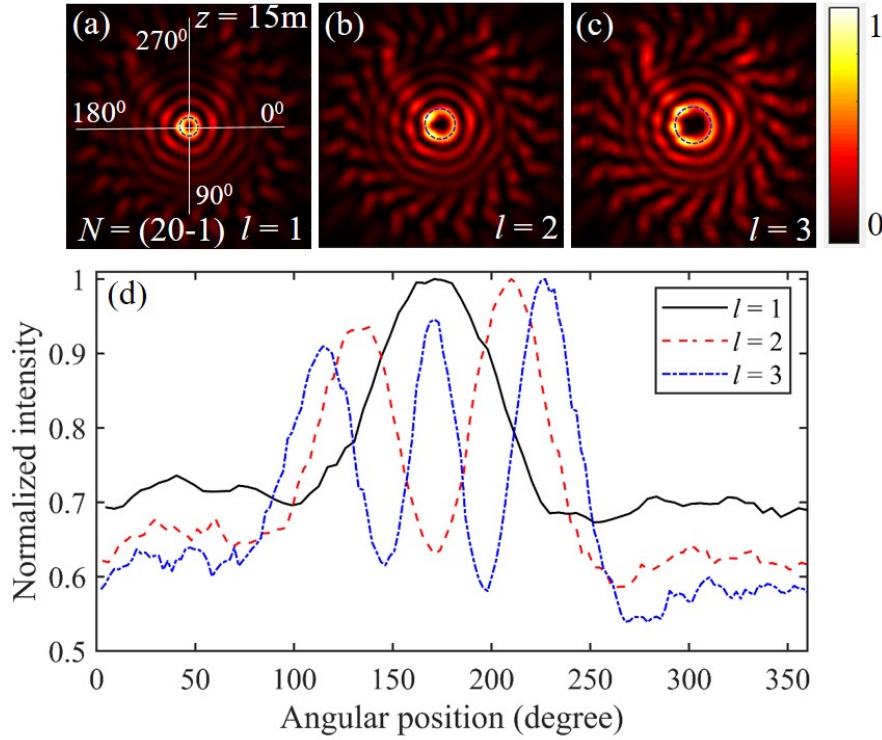
Figure 6.11: Simulated results. For a system size of $N = (20 - 1)$ lasers (one laser is truncated at $z = 0$), the intensity distributions of discrete optical vortices at a distance of $z = 15$ m, with different topological charges (a) $l = 1$, (b) $l = 2$, and (c) $l = 3$. (d) Intensity cross-sections of innermost rings, taken along dotted circles marked in (a), (b), and (c) for $l = 1$ (black-solid curve), $l = 2$ (red-dashed curve) and $l = 3$ (blue-dot-dashed curve).

with the findings of a similar method developed for a continuous vortex [287]. However, this method may not be suitable for higher-order topological charges, as the maximum intensity lobes will overlap, and will be difficult to distinguish for different l values.

We have also investigated the self-healing of a discrete optical vortex compound truncated at $z = 0$ plane. To do that we have considered a discrete optical vortex with $N = 20$ lasers and $l = 2$, and truncated partially each laser by the same amount using a binary amplitude mask, and after that propagated in a free space to check the self-healing. The results are shown in Fig. 6.12. Figure 6.12(a) shows the intensity distribution of a discrete optical vortex with $N = 20$ and $l = 2$ at $z = 0$. The propagation shows alternations in the intensity distribution due to diffraction, and at a relatively large distance ($z \sim 15$ m) it acquires a multiple-ring intensity pattern (Figs. 6.12(b)-6.12(f)). Figure 6.12(g) shows
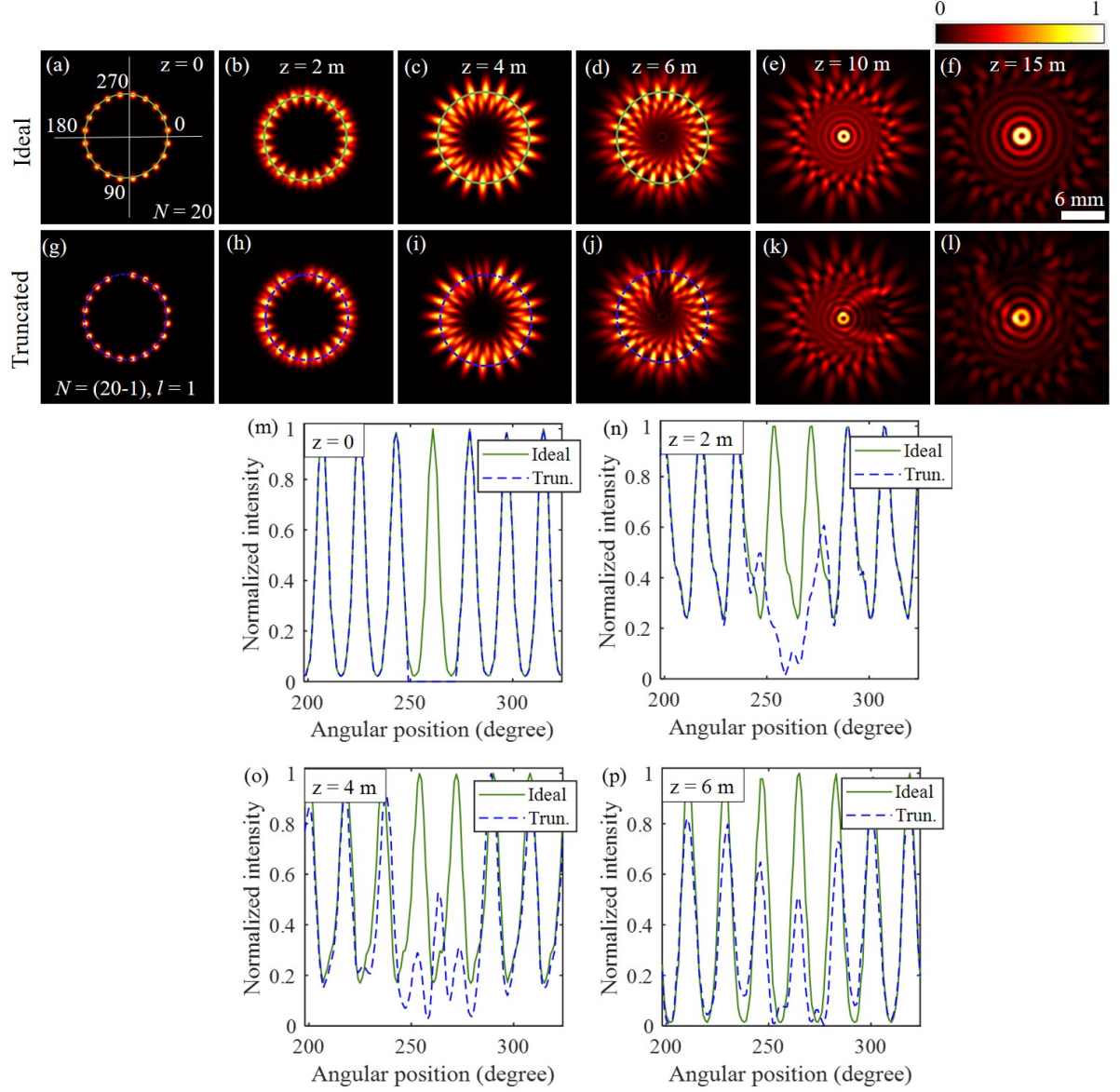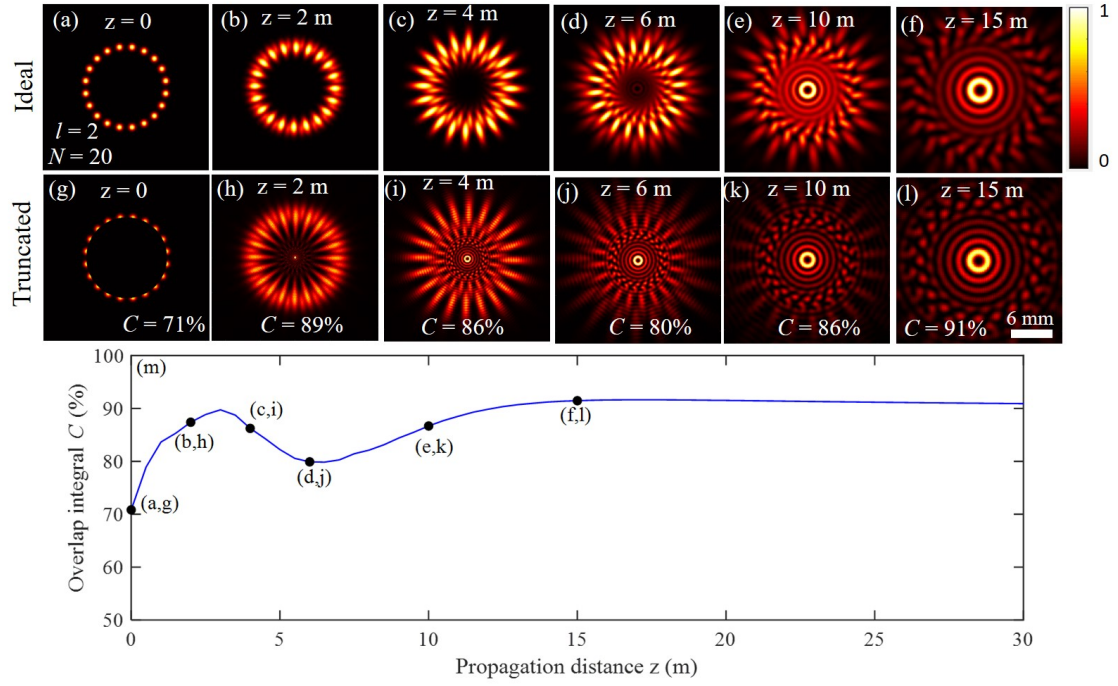
Figure 6.12: Simulation results of self-healing of a compound truncated discrete optical vortex with $N = 20$ and $l = 2$. (a)-(f) Intensity distributions of an ideal discrete optical vortex at various propagation distances. (g)-(l) Intensity distributions of a compound truncated discrete optical vortex at various propagation distances. (m) Overlap integral (Eq. (1.26)) as a function of propagation distance. Intensity distributions are normalized to a maximum value of 1.

a compound truncated discrete optical vortex, where all the lasers are partially truncated by an amplitude mask at $z = 0$ plane. The truncation removes $\sim 50\%$ of the intensity of an ideal discrete optical vortex (Fig. 6.12(a)), and leads to the reduction of an overlap integral value to $C = 71\%$ (Eq. (1.26)). The truncated discrete optical vortex is then propagated in free space, and its intensity distributions at different propagation distances are shown in Figs. 6.12(b)-6.12(f). As evident, the compound truncated discrete optical vortex regains its shape due to the redistribution of intensity and results in the formation of a stable multiple-ring pattern at $z = 15$ m (Fig. 6.12(f)), which shows a good similarity with an ideal discrete optical vortex at the same propagation distance (Fig. 6.12(f)). To quantify the self-healing effects, we have calculated an overlap integral C (Eq. (1.26)), as marked in Figs. 6.12(g)-6.12(l), and a detailed plot is shown in Fig. 6.12(m). As evident, the overlap C fluctuates for small values of z due to the redistribution of intensity that forms an unstable intensity distribution, and after that slowly approaches to a maximum value where intensity distribution becomes stable. After attaining a stable intensity distribution, the value of C remains approximately the same for further longer propagation distances. In a stable regime, a minimum propagation distance z at which a maximum value of C is obtained, called a self-healing distance, and at this distance, a truncated discrete optical vortex acquires a maximum similarity with an ideal discrete optical vortex (Figs. 6.12(f) and 6.12(l)). Specifically, in this case, we have found a self-healing distance of $z = 15$ m, where overlap approaches to $C = 91\%$.

The experimental results for the self-healing of compound truncated discrete optical vortex are shown in Fig. 6.13. Figures 6.13(a)-6.13(d) and Figs. 6.13(e)-6.13(h) show the intensity distributions of ideal and truncated discrete optical vortices at different propagation distances $z = 0$, 50 mm, 100 mm, and 150 mm, respectively. As evident, the compound truncated discrete optical vortex self-heals quite well, and the experimental results show good agreement with the simulations (Fig. 6.12).

Further, the maximum value of overlap integral is found to be $C = 91\%$ (less than 100%) (Fig. 6.12(l)), so to understand further insights, we have checked the cross-section of a truncated discrete optical vortex at different propagation distances. The results are
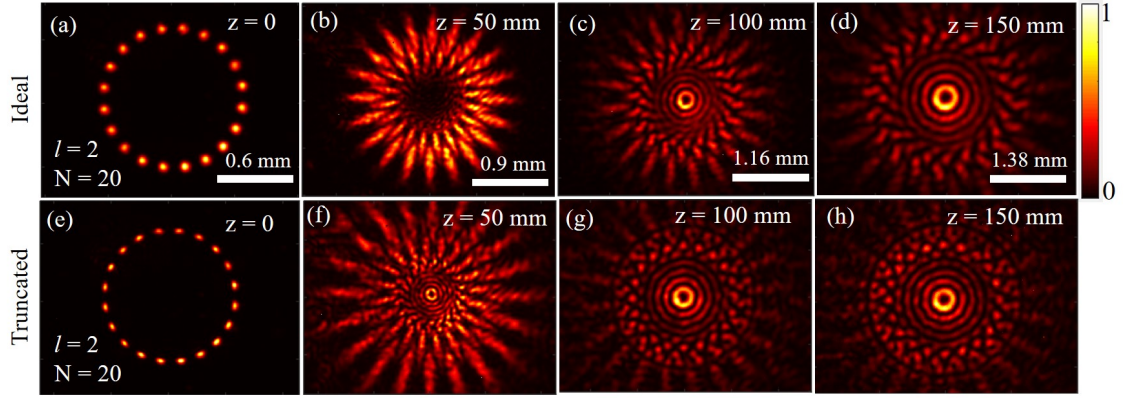
Figure 6.13: Experimental results. (a) Intensity distribution of an ideal discrete optical vortex of size $N = 20$ with $l = 2$ at $z = 0$, (b)-(d) Intensity distributions of an ideal discrete optical vortex at different propagation distances. (e) Intensity distribution of a compound truncated discrete optical vortex with size $N = 20$ and $l = 2$. (f)-(h) Intensity distributions of compound truncated discrete optical vortex at different propagation distances. Note, intensity distributions are normalized to a maximum value of 1.

shown in Fig. 6.14. Figures 6.14(a)-6.14(e) show the intensity cross-sections of ideal (solid-green curve) and compound truncated (blue-dashed curve) discrete optical vortices at propagation distances $z = 2$ m, 4 m, 6 m, 10 m, and 15 m, respectively. Note, the intensity cross-sections are taken along a horizontal line drawn through the center of Figs. 6.12(b)-6.12(f) (for ideal discrete optical vortex) and Figs. 6.12(h)-6.12(l) (for truncated discrete optical vortex). As evident, at $z = 2$ m, 4 m, and 6 m, the intensity cross-sections of ideal and truncated discrete optical vortices exhibit fewer similarities, which results in overlap values $C = 89\%$, 86% and 80%, respectively (Figs. 6.14(a)- 6.14(c)). At a propagation distance $z = 10$ m, the self-healing in a truncated discrete optical vortex leads to a better similarity, and an increased value of C is found to be 86% (Fig. 6.14(d)). Further propagation at $z = 15$ m, leads to an improved similarity with $C = 91\%$ (Fig. 6.14(e)), however, it has not reached to $\sim 100\%$. From Fig. 6.14(e), it is clear that peaks in the intensity cross-sections of ideal and truncated discrete optical vortices, match well close to the center, and away from the center matching degrades significantly. As most of the energy lies close to the central areas, so obtaining a good similarity in these areas can be considered as a good self-healing of a compound truncated discrete optical vortex.

Further, we have checked the self-healing of a discrete optical vortex when it is trun-
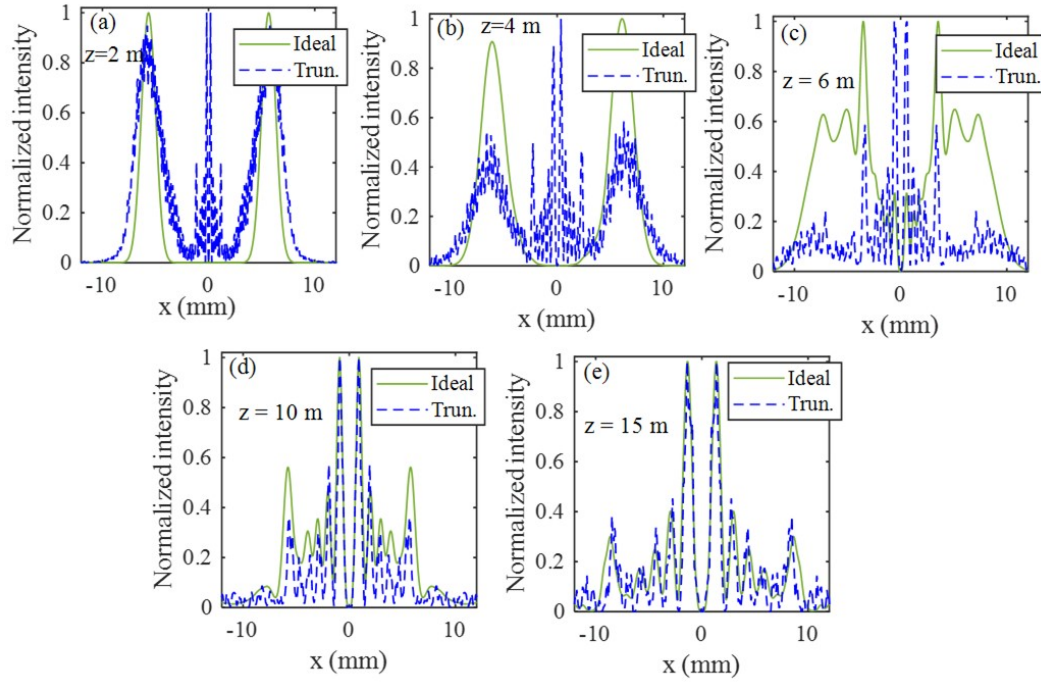
Figure 6.14: Simulated results. Normalized intensity cross-sections (along a horizontal line drawn through the center of a vortex) of ideal (solid-green curve) and compound truncated (blue-dashed curve) discrete optical vortices at various propagation distances (a) $z = 2$ m, (b) $z = 4$ m, (c) $z = 6$ m. (d) $z = 10$ m, and (e) $z = 15$ m. For the propagation distances $z = 2$ m, 4 m, 6 m, 10 m, and 15 m, the intensity distributions of ideal and compound truncated discrete optical vortices are given in Figs. 6.12(b)-6.12(f) and Figs. 6.12(h)-6.12(l).

cated in a propagation plane ($z > 0$). The results are shown in Fig. 6.15. Figures 6.15(a)-6.15(d) show the intensity distributions of ideal discrete optical vortices, with $N = 20$ lasers and different values of $l = 1$, 2, 3 and 4, at a propagation distance $z = 12$ m. The intensity distributions consist of multiple rings, and darkness in the center increases with increasing l. Figures 6.15(e)-6.15(h) show the truncated discrete optical vortices with different l values (corresponding to Figs.6.15(a)-6.15(d)), where the first innermost ring is truncated. Due to truncation, the overlap integral shows reduced values in a range $C = 85\% - 87\%$. The truncated discrete optical vortices are propagated to a distance such that maximum self-healing is obtained. Figures 6.15(i)-6.15(l) show the intensity distributions of ideal discrete optical vortices with different l values at $z = 40$ m. The propagation of truncated discrete optical vortices to the same distance are shown in

Figs. 6.15(m)-6.15(p). As evident, the truncated first innermost ring reappears and shows a good similarity with the ideal discrete optical vortices (Figs. 6.15(i)-6.15(l)). This is also evident by the increased values of C in a range of $96\% - 98\%$, indicating a good self-healing ability of discrete optical vortices.

Corresponding to the simulation results (Fig. 6.15), the experimental results are shown in Fig. 6.16. Note, the difference in propagation distances, which is due to the fact that the experimental results are obtained with different parameters of discrete optical vortex, as mentioned above. The experimental results show that the truncated discrete optical vortices having different l values self-heal very well. The experimental results also show a good agreement with the simulated results (Fig. 6.15).

For a detailed quantification of self-healing of truncated discrete optical vortices given in Figs. 6.15(e)-6.15(h), we have analyzed the overlap integral (Eq. (1.26)) as a function of propagation distance z, as shown in Fig. 6.17. Note, the propagation is shown for distances $z > 12$ m, since discrete optical vortex is truncated at $z = 12$ m. As evident, due to redistribution of intensity, the overlap decreases first and after that it increases to a maximum value, and becomes almost invariant for longer propagation distances. It is found that the self-healing distance varies with l, specifically, it increases with the increase in l. For smaller values of l, the truncated discrete optical vortex self-heals relatively faster.

Next, we have investigated the self-healing of a discrete optical vortex, truncated with different amounts at a propagated plane ($z = 12$ m). To do that we have propagated a discrete optical vortex with $N = 20$ and $l = 2$ to a distance of $z = 12$ m, and then truncated central part by various size amplitude masks. The truncated discrete optical vortex is propagated further ($z > 12$ m) to analyze the self-healing. The results are shown in Fig. 6.18. Figure 6.18(a) shows intensity distribution of an ideal discrete optical vortex of size $N = 20$ with $l = 2$ at a propagation distance of $z = 12$ m, which consists of multiple rings. Figures 6.18(b)-6.18(d) show the intensity distributions, where one, two, and three inner rings are truncated from an ideal discrete optical vortex given in Fig.6.18(a). The different amount of truncation leads to different values of C. In particular, for a large
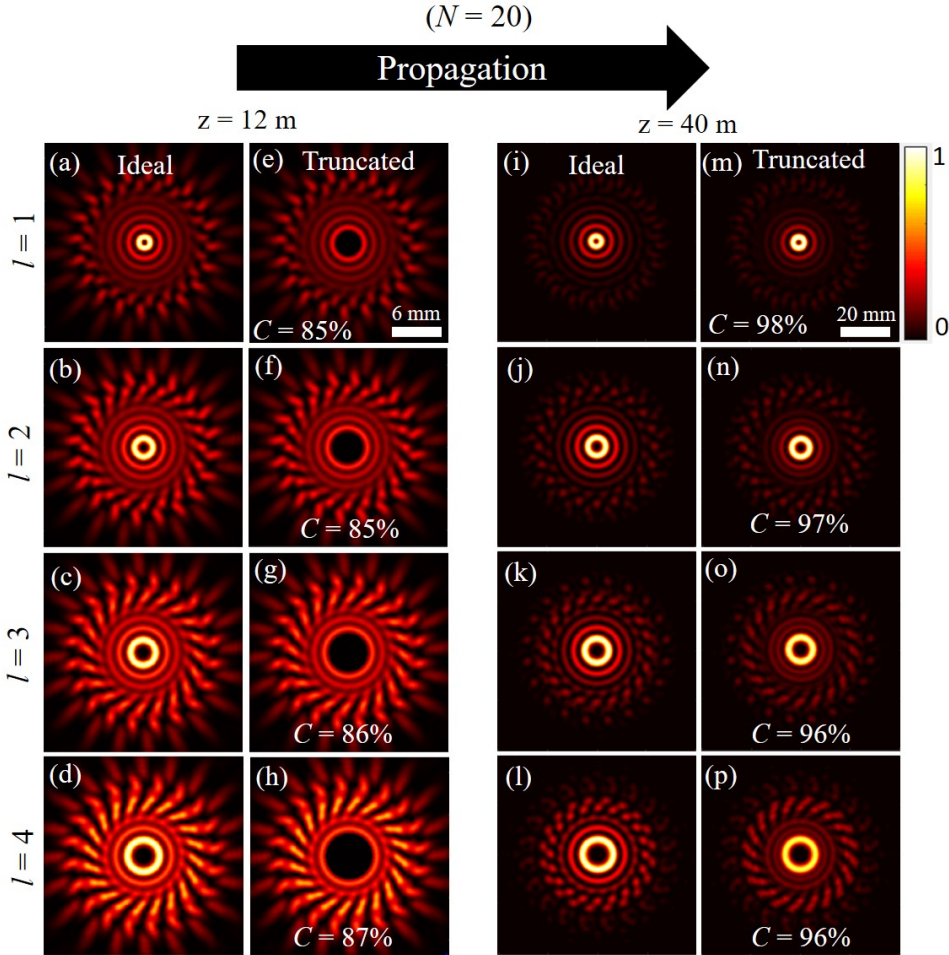
Figure 6.15: Simulated results of self-healing of a discrete optical vortex, when truncated at $z = 12$ m. (a)-(d) Intensity distributions of ideal discrete optical vortices, with $N = 20$ lasers and $l = 1$, 2, 3, and 4, at $z = 12$ m. (e)-(h) Intensity distributions of truncated discrete optical vortices at $z = 12$ m, which are obtained by truncating first innermost ring of discrete optical vortices given in (a)-(d). (i)-(l) Intensity distributions of ideal discrete optical vortices at a propagation distance of $z = 40$ m. (m)-(p) Intensity distributions of truncated discrete optical vortices at $z = 40$ m. C denotes the value of an overlap integral. Intensity distributions in the first, third, and fourth columns are normalized to a maximum value of 1. Intensity distributions in a second column are normalized by the corresponding distributions given in the first column.
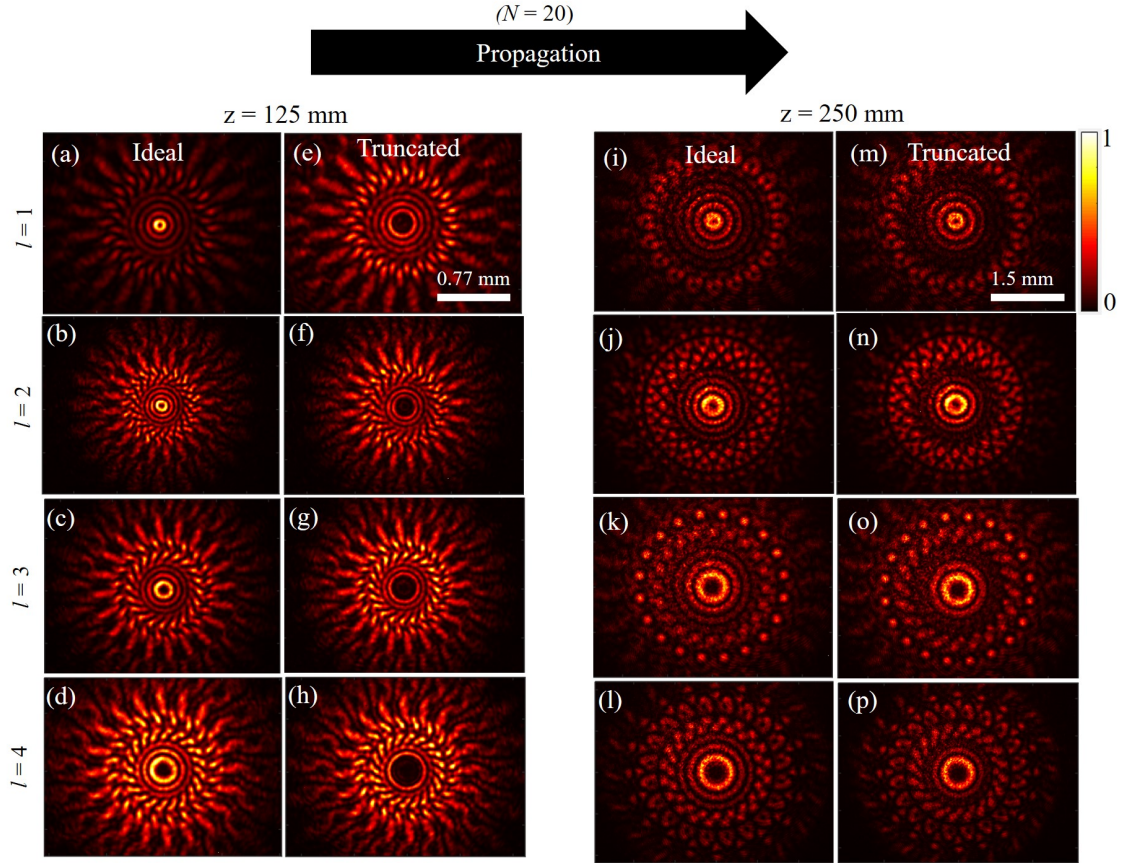
Figure 6.16: Experimental results of self-healing of a discrete optical vortex, when truncated at $z = 125$ mm. (a)-(d) Intensity distributions of ideal discrete optical vortices, with $N = 20$ lasers and $l = 1$, 2, 3, and 4, at $z = 125$ mm. (e)-(h) Intensity distributions of truncated discrete optical vortices at $z = 125$ mm, which are obtained by truncating first innermost ring of discrete optical vortices given in (a)-(d). (i)-(l) Intensity distributions of ideal discrete optical vortices at a propagation distance of $z = 250$ mm. (m)-(p) Intensity distributions of truncated discrete optical vortices at $z = 250$ mm.
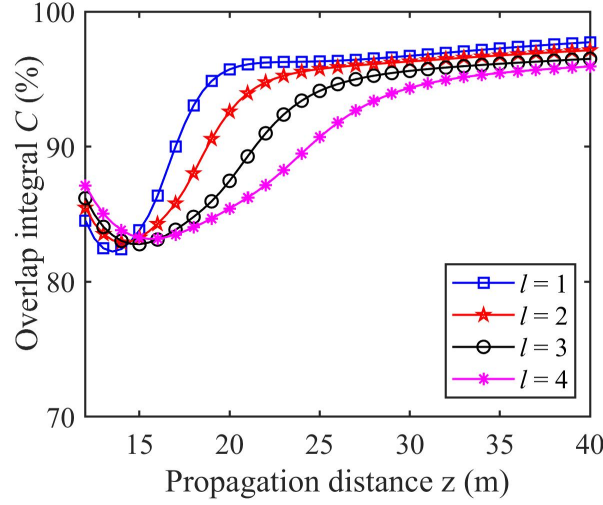
Figure 6.17: Simulated results. For the truncated discrete optical vortices of size $N = 20$ and different values of $l = 1, 2, 3,$ and 4, the overlap integral C as a function of propagation distance z. Note, the discrete optical vortex is truncated in a propagated plane at $z = 12$ m, by truncating first innermost ring as shown in Figs. 6.15(e)-6.15(h).

amount of truncation (Fig. 6.18(d)) the overlap C is reduced to 74%. The truncated discrete optical vortices (Figs. 6.18(b)-6.18(d)) are propagated to various distances to analyze the self-healing abilities, as shown in Figs. 6.18(e)-6.18(g). As evident, the self-healing distance (a point where C becomes maximum) is different for different amounts of truncation. In particular, truncation of one, two, and three inner rings, requires a distance of $z = 40$ m, 47 m, and 108 m, respectively, to self-heal the truncated discrete optical vortices to show maximum similarities with the ideal discrete optical vortices at the same propagation distances. In Fig. 6.18(h), we have analyzed an overlap integral as a function of propagation distance, for various amounts of truncation. As evident, for a fixed amount of truncation, the overlap varies with the propagation distance. In particular, it decreases initially, and after that increases to a maximum value and becomes constant for further longer propagation distances. Further, the distance required to increase the overlap to a maximum constant value also depends on the amount of truncation. Specifically, a discrete optical vortex with truncation of one inner ring requires less propagation distance as compared to truncation of two and three inner rings (Fig. 6.18(h)). It indicates that a discrete optical vortex with a large amount of truncation requires a longer distance for
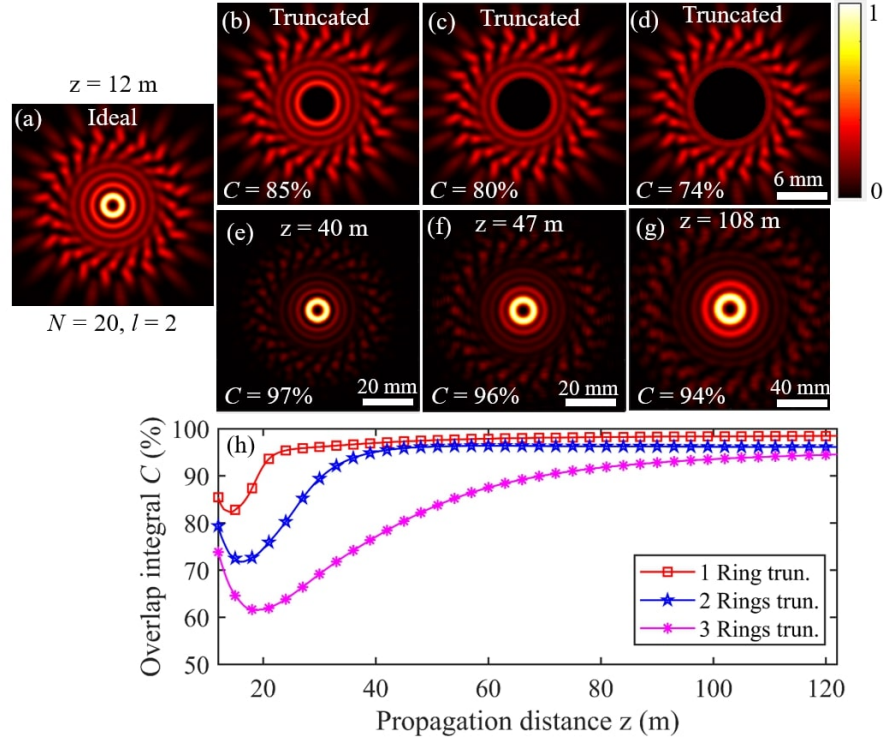
Figure 6.18: Simulated results of self-healing of a discrete optical vortex with various amounts of truncation. (a) Intensity distribution of an ideal discrete optical vortex of size $N = 20$ with $l = 2$ at a propagation distance $z = 12$ m. Intensity distribution of discrete optical vortex with truncation of (b) first inner ring, (c) two inner rings, and (d) three inner rings. (e)-(g) Intensity distributions of truncated discrete optical vortices, corresponding to Figs. 6.18(e)-6.18(d), at a propagation distance of $z = 40$ m, 47 m, and 108 m, respectively. (h) Overlap C as a function of propagation distance, for the truncated discrete optical vortices correspond to Figs. 6.18(e)-6.18(g). Note, (b)-(d) are normalized with respect to (a), and (e)-(g) are normalized to a maximum value of 1.

self-healing.

Corresponding to the simulated results (Fig. 6.18), the experimental results are shown in Fig. 6.19. As evident, the results show that the discrete optical vortex truncated with different amounts shows good self-healing ability, and the self-healing distance increases with an increase in the amount of truncation. The experimental results show good agreement with the simulated results.

Further, we have analyzed the self-healing of a truncated discrete optical vortex (Fig. 6.18(c)) by comparing its normalized intensity cross-section with an ideal discrete optical vortex at various propagation distances, as shown in Figs. 6.20(a)-6.20(f). Fig-
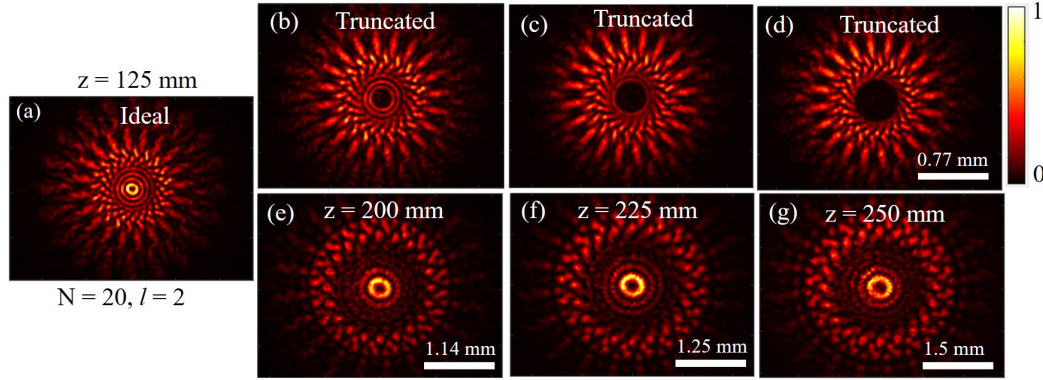
Figure 6.19: Experimental results of self-healing of a discrete optical vortex with different amounts of truncation in propagated plane. (a) Intensity distribution of an ideal discrete optical vortex of size $N = 20$ with $l = 2$ at a propagation distance $z = 125$ mm. Intensity distribution of discrete optical vortex with truncation of (b) first inner ring, (c) two inner rings, and (d) three inner rings. (e)-(g) Intensity distributions of truncated discrete optical vortices, corresponding to Figs. 6.18(b)-6.18(d), at a propagation distance of $z = 200$ mm, 225 mm, and 250 mm, respectively.

ure 6.20 shows the investigation of self-healing of discrete optical vortex in propagated plane ($z = 12$ m) when two inner rings are truncated by an amplitude mask. Figures 6.20(a)-6.20(f) show the intensity distributions of ideal discrete optical vortex beam for $N = 20$ and $l = 2$, at various propagation distances. Figures 6.20(g) shows the intensity distribution, where two innermost rings are truncated from the centre of discrete optical vortex shown in Fig. 6.20(a). As the truncated discrete optical vortex is propagated in free space, it regains its shape, which shows good self-healing (Figs. 6.20(h)-6.20(l)). To understand the self-healing and redistribution of the intensity within the beam, we have compared the intensity cross-sections of truncated and ideal beams (shown in Figs. 6.20(m)-6.20(r)). The intensity cross-sections are taken along a green-dashed horizontal line marked in the intensity distributions of ideal (Figs. 6.20(a)-6.20(f)) and blue-dashed horizontal line in truncated discrete optical vortex (Figs. 6.20(g)-6.20(l)). Figure 6.20(m) shows the intensity cross-sections of truncated (blue-dashed curve) and ideal (green-solid curve) discrete optical vortices at $z = 12$ m. For a truncated discrete optical vortex, the peaks corresponding to two inner-rings are missing, and due to which C is reduced to 80%. As the truncated discrete optical vortex propagates, as a result of redistribution of inten-
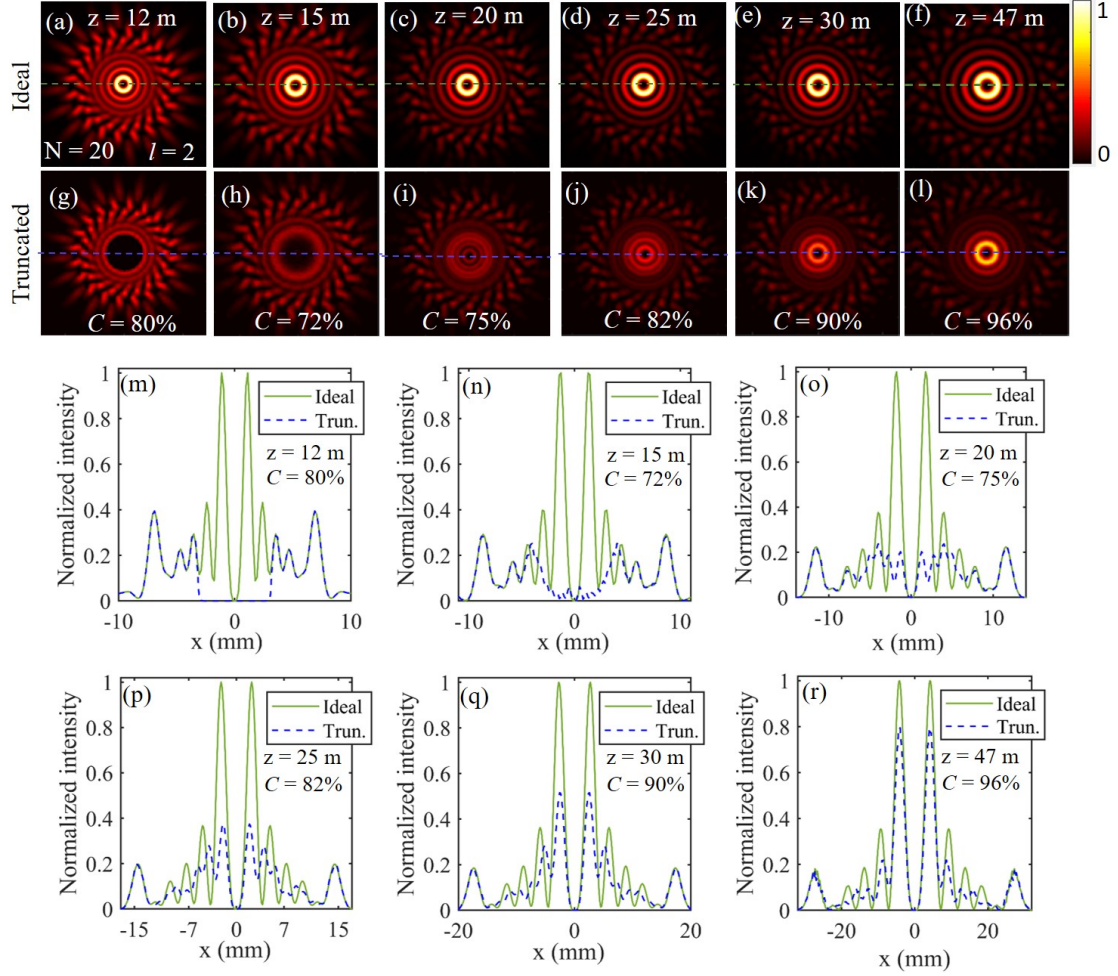
Figure 6.20: Simulated results. Intensity distributions of (a)-(f) ideal and (g)-(l) truncated (two inner rings are truncated) discrete optical vortex of system size $N = 20$ and $l = 2$ at various propagation distances $z = 12$ m, 15 m, 20 m, 25 m, 30 m, and 47 m. Intensity cross-sections of ideal discrete optical vortex (green-solid curve) and truncated discrete optical vortex (blue-dashed curve) and at various propagation distances (m) $z = 12$ m, (n) $z = 15$ m, (o) $z = 20$ m, (p) $z = 25$ m, (q) $z = 30$ m, and (r) $z = 47$ m. Intensity cross-sections are taken along a horizontal green-dashed line marked in (a)-(f) for ideal, and blue-dashed line marked on (g)-(l) for a truncated discrete optical vortex. Note, the intensities of self-healed truncated discrete optical vortices are normalized by the ideal discrete optical vortices at their respective propagation distances.

sity, the intensity moves into central truncated regions, which leads to the self-healing of truncated parts, as shown in Figs.6.20(n)-6.20(r). This is also evidenced by the increased values of C with z. The maximum value of C is found 96% at $z = 47$ m (Fig. 6.20(r)). Note, the overlap values at $z = 15$ m and 20 m (Figs. 6.20(n) and 6.20(o)) are found to be 72% and 75%, respectively, which are smaller than an initial value of $C = 80\%$ at $z = 12$ m (Fig. 6.20(m)). This is due to the fact that upon propagation of a truncated discrete optical vortex, the intensity from neighbouring rings redistributes to fill the truncated parts, which causes a distortion in the shape of neighbouring rings, and hence results in a reduction in the overlap values. As the truncated parts start reappearing, the overlap C starts increasing, and becomes 96% at $z = 47$ m (Fig. 6.20(r)), which is larger than an initial value of $C = 80\%$, as shown in Figs. 6.20(n)-6.20(r).

It has been shown that laser beams carrying helical phase distribution, exhibit rotation of their energy and momentum around the beam axis [288]. The rotational dynamics of transverse intensity pattern has been investigated in LG beams [289]. In a truncated vector vortex, the self-healing was shown to occur as a result of rotational dynamics in the transverse intensity [290]. We have also analyzed the rotation dynamics of intensity in a discrete optical vortex, as well as its effects on self-healing of a truncated discrete optical vortex. To do that we have considered a discrete optical vortex of size $N = 20$
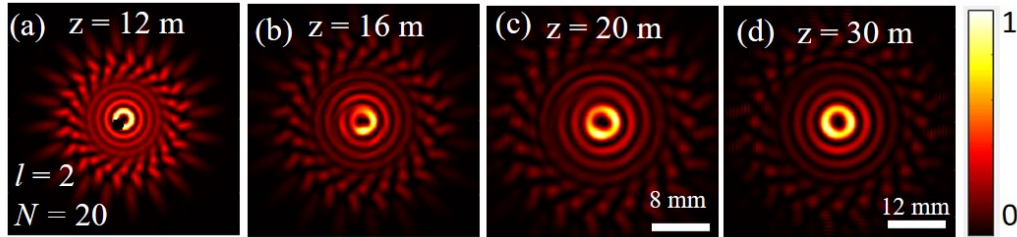
Figure 6.21: Simulated results. (a) Intensity distribution of a truncated discrete optical vortex of size $N = 20$ and $l = 2$ at a propagation distance $z = 12$ m. Intensity distributions of truncated discrete optical vortex propagated to various distances (b) $z = 16$ m, (c) $z = 20$ m, and (d) $z = 30$ m. The intensity distributions are normalized to a maximum value of 1.

and $l = 2$ (Figs. 6.2(d) and 6.2(e)) and propagated to a distance of $z = 12$ m so that it acquires multiple rings in the intensity distribution (Fig. 6.15(b)). After that, an inner-

most ring is partially truncated (Fig. 6.21(a)), and resulting beam is further propagated for longer distances (Figs. 6.21(b)-6.21(d)). As evident, upon propagation of truncated discrete optical vortex, the intensity shows rotation dynamics. As a result of rotation dynamics, the intensity moves into truncated parts, which results in the formation of a complete innermost ring, as shown in Fig. 6.21(d).

6.5   Conclusions

In conclusion, we have presented a novel and efficient intra-cavity method for the controlled generation of high-power discrete optical vortices by phase-locking a 1D ring array of lasers in a degenerate cavity that includes specific near-field and far-field masks. Despite the remarkable progress on conventional optical vortex, there still remains a vital issue that restricts the practical implementation and application of the optical vortex in the future, namely the limitation of power scaling capacity. However, the discrete optical vortices are realized by phase-locking of several lasers, thus having an improved power scaling capacity. Owing to the special geometry of a degenerate cavity, it enables an efficient formation of 1D ring array of lasers, where each laser consists of nearly fundamental Gaussian distribution, and is independent from each other. Initially, the lasers consist of random phase distribution and are equally probable. To force 1D ring array of lasers in a phase-locked steady state of desired optical vortex configuration, we employ a spatial Fourier filter (amplitude mask) at the Fourier plane inside the degenerate cavity, whose transmission function is engineered by the Fourier transform of desired discrete optical vortex. The spatial Fourier filtering mechanism helps to eliminate the undesired phase distributions by introducing additional losses to them, and, thereby, enables the lasers to find a correct phase distribution in the form of desired discrete optical vortex. With the specifically engineered spatial Fourier filters, we have demonstrated generation of discrete optical vortices with different system sizes and precisely controlled topological charges.

Further, it is well-known that discrete systems behave differently than continuous systems, so we have performed a detailed investigation on the propagation, such as divergence

and self-healing, of discrete optical vortices, and compared them with the conventional continuous optical vortices. We have found that for a given system size (number of lasers) and fixed distance between the neighbouring lasers, the size of a discrete optical vortex and its divergence does not depend on the topological charge, which is found to be different than the conventional continuous optical vortices (Laguerre-Gaussian/Bessel-Gaussian beams). Further, we have performed a detailed investigation of self-healing by partially truncating a discrete optical vortex in the waist plane ($z = 0$) and propagated plane ($z > 0$). In the waist plane, a discrete optical vortex is truncated in two ways: (a) single laser is truncated, and (b) compound truncation where all the lasers are equally partially truncated. To quantify the self-healing, we have calculated an overlap integral (Eq. 1.26) to analyze similarities between the self-healed and ideal discrete optical vortices. In both cases, when a partially truncated discrete optical vortex is propagated, as a result of intensity redistribution, the intensity from nearby regions propagates into truncated parts, and accordingly the beam self-heals. The results show that partially truncated discrete optical vortex can self-heal very well. The self-healing distance is also found to be dependent on the amount of truncation, particularly, it increases with an increase in the amount of truncation. Further, the simulation results of self-healing properties are verified experimentally, and we have found a good agreement between them.

These investigations have opened the door for new applications, where conventional continuous optical vortices pose limitations. The results reported in this chapter are given in Refs. [43–45]

Chapter 7

Method for characterization of topological charge of unknown discrete optical vortices

7.1 Introduction

In previous Chapter 6, we have presented a novel and efficient intra-cavity method for the controlled generation of high-power discrete optical vortices by phase-locking a 1D ring array of lasers in a degenerate cavity. The discrete optical vortices are particularly interesting for high-power applications, such as in long-distance optical communications, material processing, laser ablation, optical tweezers, etc. [6, 11, 258]. The applications of optical vortex are usually associated with its topological charge, thus accurate characterization (determination) of the value of topological charge (l) (magnitude and sign) is very important. Therefore, exploring simple and effective methods to accurately determine topological charge of an optical vortex has been a highly challenging issue, and continuous efforts are growing in this direction. Therefore in this Chapter, we present a new efficient method for accurate determination of magnitude and sign of topological charge of an unknown discrete optical vortex, which is formed by an array of lasers in a 1D ring

geometry.

Over the years, several methods have been investigated, which are broadly classified into two categories: first type is based on the interference approach, and the second type is based on the diffraction approach. The information of topological charge is manifested in the intensity distribution when an optical vortex beam either undergoes diffraction through slits/apertures [291, 292], or interfere with another beam (plane wave/vortex beam/spherical wave) [293, 294]. Therefore, from the diffraction pattern or interference pattern, the topological charge of optical vortex beam can be inferred. The interference approaches are mainly based on the Mach-Zehnder interferometer [293–295], Fizeau inteferometer [296], Sagnac interferometer [297], double-slit interferometer [298], multi-point interferometer [299], and Talbot interferometer [300]. Whereas, the diffraction approaches involve the annular aperture [301], triangular aperture [302], single-slit [291,292], multi-pinhole plate [303], gratings [304], and metasurfaces [305], etc. Further, some more methods for the detection of topological charges of optical vortex have also been proposed, which are based on conformal mappings [306], multiplane light conversion [307], mode converter [308], rotational Doppler effect [309], and two-dimensional materials [310]. The above methods rely on detecting the topological charges indirectly by analyzing the changes in the intensity distributions. However, some direct methods for determining topological charge of an optical vortex have also been investigated. These are based on directly measuring the phase distribution of a vortex, and the method includes phase-shifting digital hologram [311] and Shack-Hartmann wavefront sensors [312].

Many of these methods pose limitations in various forms, such as complexity in the setup, unable to precisely determine high-order topological charges (magnitude and sign), sensitive to aperture dimensions, and sensitive to aberrations in the system. Further, most of these methods infer the topological charge of a vortex by propagation and analysis of changes in its intensity distribution. These methods have been applied to the continuous systems (continuous vortices). However, it is well-known that discrete systems show different propagation behaviour, so a natural question arises that whether the above methods can be applied or not for identifying the topological charges of discrete optical

vortices.

Methods based on direct measurement of phase distribution of an optical vortex [311, 312] can be useful for determining small values of topological charge of discrete optical vortex, however, given the aberrations as well as very small differences in the phases of lasers for large topological charges, these may not be able to precisely determine the high-order topological charges of discrete optical vortices. Here, we present a new method for precisely determining the magnitude and sign of topological charges (from small to large values) of discrete optical vortices, based on measuring the interference patterns of 1D ring array of lasers. More specifically, we average the interference pattern of an unknown discrete optical vortex ($l \neq 0$) with the interference pattern of ring array with known topological charge, which gives rise to a variation in the fringe visibility as a function of laser number, and the number of dips observed in fringe visibility provides an accurate information of magnitude and sign of an unknown topological charge. Our method is also found to be robust against the phase disorder in a system.

The Chapter is organized as follows. In Sec. 7.2, we present the working principle of our method with the illustrative results. In Sec. 7.3, we have described the experimental generation of discrete optical vortex as well as measuring its interference pattern. In Sec. 7.4, we have presented the numerical and experimental results on accurate determination of topological charges of discrete optical vortices for different system sizes. Further, results on finding the sign of topological charge (positive/negative) are also presented. The robustness of our method is also verified against the phase disorder. Finally, in Sec. 7.5, we present the concluding remarks. The results reported in this Chapter are given in Ref [46].

7.2 Working principle

We consider the interference of two waves of intensities I_1 and I_2: one propagating in the z direction; the other propagating at an angle θ with respect to the z axis, in the $x - z$

plane. The fields of these interfering waves can be written as [313]

$$U_1 = \sqrt{I_1}\exp(-ikz)\exp(i\phi_1), \tag{7.1}$$

$$U_2 = \sqrt{I_2}\exp[-i(k\cos\theta z + k\sin\theta x)]\exp(i\phi_2), \tag{7.2}$$

where ϕ_1 and ϕ_2 are the phases of two waves. At the $z = 0$ plane, the resultant intensity after superposition of these two waves can be written as

$$I = |U_1 + U_2|^2 = I_1 + I_2 + 2\sqrt{I_1 I_2}\cos(k\sin\theta x - d\phi), \tag{7.3}$$

where $d\phi = \phi_2 - \phi_1$. For $I_1 = I_2 = I_0$, we get

$$I = 2I_0\left[1 + \cos\left(k\sin\theta x - d\phi\right)\right]. \tag{7.4}$$

The interference intensity distribution consists of straight fringes with maxima and minima positions vary with x, and the fringe spacing is $\beta = 2\pi/k_0\sin\theta = \lambda/\sin\theta$. The locations of minima and maxima can be determined from Eq. (7.4).

For maxima:
$$x_{\text{max}} = \frac{[2m\pi + d\phi]}{k\sin\theta}, \quad m = 0, \pm 1, \pm 2, \pm 3, ... \tag{7.5}$$

For minima:
$$x_{\text{min}} = \frac{[(2m+1)\pi + d\phi]}{k\sin\theta}, \quad m = 0, \pm 1, \pm 2, \pm 3, ... \tag{7.6}$$

The positions of maxima and minima in the interference fringe pattern depend on the value of relative phase shift $d\phi$. By changing it, these maxima and minima positions shift either on the left or right with respect to initial positions. To show this, we have considered two Gaussian beams with equal intensities $I_1 = I_2 = I_0$, tilt angle $\theta = 110^o$ and $d\phi = 0$ and $\pm\pi/2$. The interference expression for these cases can be written as:

(i) For $d\phi = 0$

$$I_{T1} = 2I_0\left[1 + \cos\left(0.94kx\right)\right]. \tag{7.7}$$

(ii) For $d\phi = -\pi/2$

$$I_{T2} = 2I_0 \left[1 + \cos\left(0.94kx + \pi/2\right)\right]. \tag{7.8}$$

(iii) For $d\phi = \pi/2$

$$I_{T3} = 2I_0 \left[1 + \cos\left(0.94kx - \pi/2\right)\right]. \tag{7.9}$$

The interference patterns obtained from Eqs. (7.7)-(7.9) are shown in Figs. 7.1(a)-7.1(c). As evident, for all three cases, interference patterns consist of straight fringes
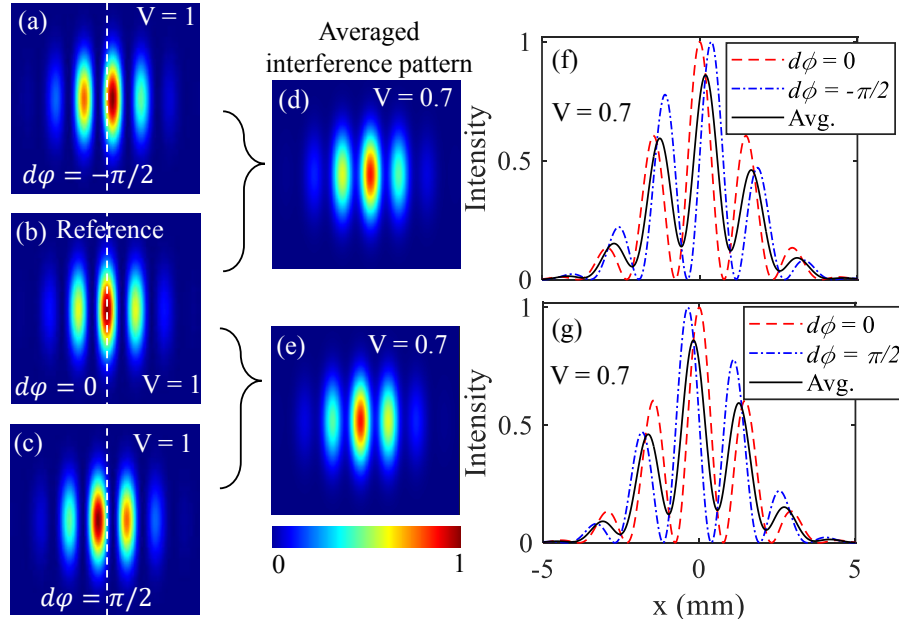
Figure 7.1: Interference pattern between the two waves having a relative phase shift of (a) $d\phi = -\pi/2$, (b) $d\phi = 0$, and (c) $d\phi = \pi/2$. The averaged interference pattern obtained with superposition of (d) $d\phi = 0$ and $-\pi/2$, and (e) $d\phi = 0$ and $\pi/2$. (f) The intensity cross-sections are taken along the horizontal axis in (a), (b), and (d). (g) The intensity cross-sections taken along the horizontal axis in (b), (c), and (e).

with maxima and minima at different positions. We consider the case of $d\phi = 0$ as the reference interference pattern. A vertical white dashed line marks the position of fringe with central maximum (Fig.7.1(b)). For $d\phi = -\pi/2$, the fringes in the interference pattern are shifted towards the right with respect to a reference white dashed line (Fig. 7.1(a)). Similarly, for $d\phi = \pi/2$, the fringes in the interference pattern are shifted towards the left with respect to a reference white dashed line (Fig. 7.1(c)). The interference pattern is quantified by the fringe visibility $V = (I_{\max} - I_{\min})/(I_{\max} + I_{\min})$ [313], where $I_{\max}$ and

$I_{\min}$ are the maximal and minimal values of time-averaged intensities in the interference pattern. In all three individual interference patterns (for $d\phi = 0, -\pi/2,$ and $\pi/2$) the fringe visibility is found to be $V = 1$ (Figs. 7.1(a)-7.1(c)).

Further, we have performed averaging of these interference patterns. The expression of averaged interference pattern can be written as following:

(i) For averaging the interference patterns corresponding to Figs. 7.1(a) and 7.1(b), we add Eqs.(7.7) and (7.8)

$$I_{\mathrm{Sum1}} = I_0 \left[2 + \cos\left(0.94kx\right) + \cos\left(0.94kx + \pi/2\right) \right]. \tag{7.10}$$

Note, due to averaging the factor 2 is dropped.

(ii) For averaging the interference patterns corresponding to Figs. 7.1(b) and 7.1(c), we add Eqs.(7.7) and (7.9)

$$I_{\mathrm{Sum2}} = I_0 \left[2 + \cos\left(0.94kx\right) + \cos\left(0.94kx - \pi/2\right) \right]. \tag{7.11}$$

The averaged interference patterns corresponding to Eqs. (7.10) and (7.11) are shown in Figs. 7.1(d) and 7.1(e), respectively. As evident, when two interference patterns with $d\phi = 0$ and $d\phi = \pm\pi/2$ (each with $V = 1$) are averaged, they produce a resultant interference pattern, where the fringe visibility is found to be reduced ($V = 0.7$) (Figs. 7.1(d) and 7.1(e)). This is more clearly shown in Figs. 7.1(f) and 7.1(g). Figure 7.1(f) shows the intensity cross-sections taken along the horizontal axis in Fig. 7.1(a) (blue dot-dashed curve), Fig. 7.1(b) (red dashed curve) and Fig. 7.1(d) (black solid curve). Similarly, Fig. 7.1(g) shows the intensity cross-sections taken along the horizontal axis in Fig. 7.1(b) (red dashed curve), Fig. 7.1(c) (blue dot-dashed curve) and Fig. 7.1(e) (black solid curve). It is clearly evidenced that the averaged intensity cross-section (black solid curve) results in a reduced value of the fringe visibility. Note, averaging the interference patterns corresponding to $d\phi = 0$ and $d\phi = \pm\pi$, results in the fringe visibility $V = 0$.

We utilize this principle of reduction in visibility by averaging the interference patterns,

for determining the magnitude and sign of topological charge of an unknown discrete optical vortex.

7.3 Experimental arrangement

A discrete optical vortex consists of a finite number of sites (lasers/beamlets/waveguides) in a 1D ring array, where intensity in the center is zero, and the phase circulates from one site to the next either in clockwise or anti-clockwise direction [73, 74, 269, 273, 314]. The field of a discrete optical vortex can be given as (Eq. (1.1))

$$E(x, y; z = 0) = E_0 \sum_{j=1}^{N} e^{-\frac{(x-\alpha_j)^2 + (y-\beta_j)^2}{2\sigma_o^2}} e^{i\phi_j}, \tag{7.12}$$

where $(\alpha_j, \beta_j) = a(\cos\theta_j, \sin\theta_j)$ represents the coordinates of each laser, $\theta_j = \pi(2j-1)/N$, $a = d/\sqrt{1 - \cos(2\pi/N)}$, and $\phi_j = 2\pi l(j-1)/N$. d denotes the center-to-center separation between two neighboring lasers. All lasers in a discrete optical vortex have the same amplitude E_0, beam waist σ_0, and different phase ϕ_j, satisfying the periodic boundary conditions: $E_{j+N} = E_j$. The topological charge l of a discrete optical vortex is given by Eq. (1.2). A continuous optical vortex is formed by a single laser source, so it suffers the limitation of the power scaling capacity. Whereas, the discrete optical vortex can be formed either by the coherent combining of several laser beams or by phase-locking of several lasers, thus overcomes the issue of power limitations.

In previous Chapter 6, we have shown the generation of discrete optical vortices with precisely controlled topological charges by phase-locking several lasers in a 1D ring array in a degenerate cavity. However, in this chapter, our main goal is to efficiently determine the topological charge (magnitude and sign) of a discrete optical vortex. To show the proof of concept of our method, we have generated a discrete optical vortex from a computer generated hologram using a spatial light modulator (SLM). The schematic of experimental setup as well as representative results are presented in Fig. 7.2. The picture of a real experimental setup is shown in Figure 7.3. We use a phase-only SLM with the screen
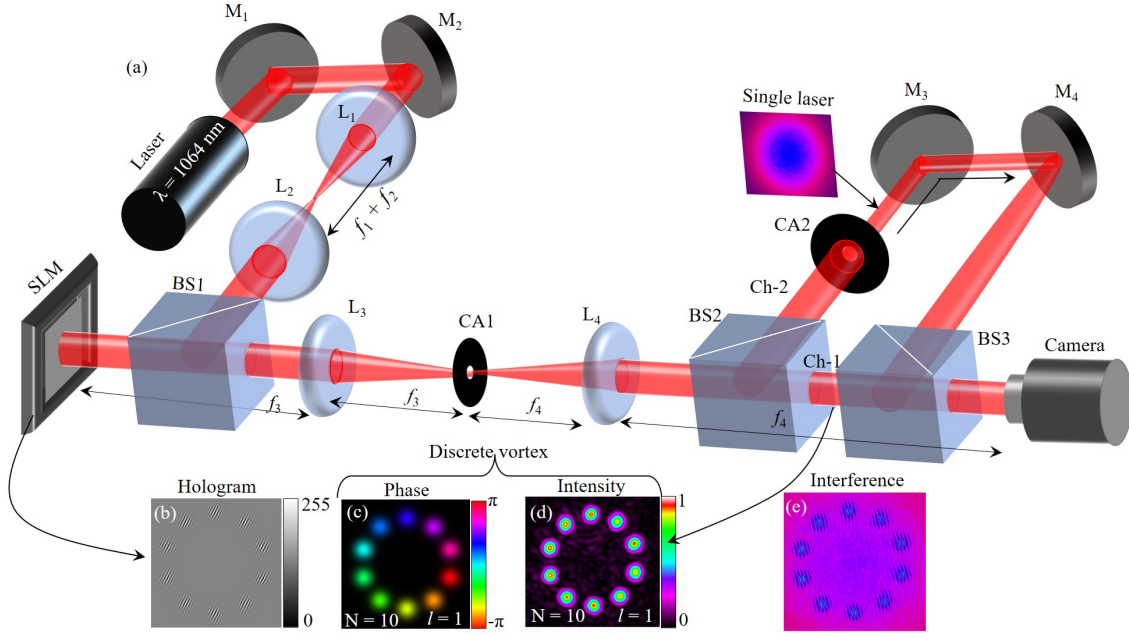
Figure 7.2: (a) Experimental arrangement for the generation of discrete optical vortex, and determining its topological charge (including magnitude and sign). SLM: Spatial light modulator; BS1, BS2, BS3: 50:50 Beam splitters; L_1, L_2, L_3 and L_4: Plano-convex lenses with focal lengths f_1, f_2, f_3 and f_4, respectively; M_1, M_2, M_3 and M_4: Mirrors, CA1, CA2: Circular apertures. (b) The phase hologram corresponding to a discrete optical vortex with $l = 1$. (c) The phase distribution of a discrete optical vortex with $l = 1$. (d) The intensity distribution of a discrete optical vortex with N= 10 lasers. (e) The interference pattern where a single selected reference laser interfered with itself and with all the other lasers.
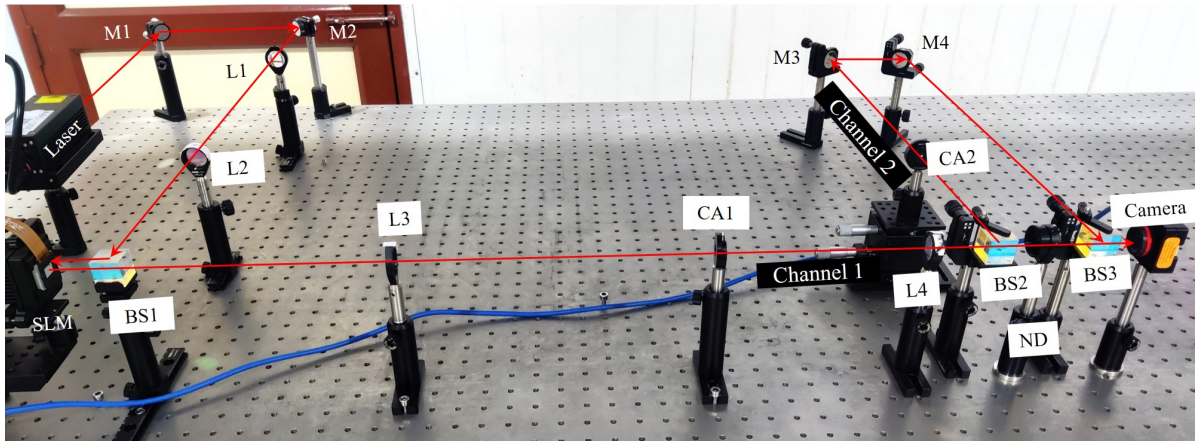
Figure 7.3: Picture of experimental setup for determining the topological charge (magnitude and sign) of a discrete optical vortex. SLM: Spatial light modulator; BS1, BS2, BS3: 50:50 Beam splitters; L_1, L_2, L_3 and L_4: Plano-convex lenses with focal lengths 5 cm, 30 cm, 30 cm and 20 cm, respectively; M_1, M_2, M_3 and M_4: Mirrors; CA1, CA2: Circular apertures; ND: Neutral density filter.

resolution 1920×1080 and pixel size 8 μm. A collimated linearly polarized laser beam with the fundamental Gaussian distribution, wavelength $\lambda = 1064$ nm, and beam waist radius 10 mm incidents normally on the SLM with a beam splitter (BS1). The size of an input Gaussian beam is chosen such that it illuminates whole screen of SLM. On the SLM screen a computer generated phase hologram corresponding to a discrete optical vortex is applied (Fig. 7.2(b)). The method for preparing the phase holograms is described in Sec. 1.5 of Chapter 1 (see also Appendix 7.6).

The phase hologram on the SLM modulates amplitude and phase of an input Gaussian laser beam, and accordingly the light from an input Gaussian laser beam splits in the form of multiple lasers arranged on a 1D ring array with discrete phase distributions in a vortex configuration. After reflection from SLM, we obtain modulated light in several orders (see Appendix 7.6), which contains the desired discrete optical vortex. The desired discrete optical vortex in the first order is isolated with a spatial Fourier filter CA1 placed in the middle of a telescope made with lenses L_3 ($f_3 = 30$ cm) and L_4 ($f_4 = 20$ cm) (Fig. 7.3). After spatial filtering, we obtain a clean discrete optical vortex at the focal plane of L_4. The phase distribution and intensity distribution of a generated discrete optical vortex are shown in Figs. 7.2(c) and 7.2(d), respectively. As evident, the discrete optical vortex consists of N=10 lasers (with TEM_{00} fundamental Gaussian mode profiles) in a 1D ring array (Fig. 7.2(d)), and the lasers possess discrete phase distribution (Fig. 7.2(c)) in a vortex configuration. This is identical to a discrete optical vortex obtained by phase-locking of lasers in a 1D ring array inside a degenerate cavity (Chapter 6).

To determine the magnitude and sign of topological charge of a discrete optical vortex, we measure the interference between the lasers using a Mach-Zhender interferometer, as shown in Figs. 7.2(a) and 7.3. The discrete optical vortex (Figs. 7.2(c) and 7.2(d)) splits into two channels (Ch-1 and Ch-2) at the beam splitter BS2. In one channel (Ch-1), the discrete optical vortex is imaged directly onto the camera. In the other channel (Ch-2), a single reference laser is selected with a circular aperture CA2, and then its light is expanded such that it fully overlaps and interferes with the light from all other lasers with a beam splitter BS3 on the camera (Figs. 7.2(a), Fig. 7.3). This enables that a

single selected reference laser interferes with itself and with all the other lasers. A small tilt (Eq. (7.2)) between two channels provides a few interference fringes for each laser (as shown in the interference pattern Fig. 7.2(e)) from which the fringe visibility is analyzed.

7.4 Results and discussions

To show that our method can efficiently determine the magnitude and sign of topological charge (from small to large values) of discrete optical vortex, we have performed several experiments considering different system size N. The experimental results are supported by the numerical simulations. First, we have demonstrated our approach for determining topological charges of discrete optical vortices, formed with a 1D ring array of N=10 lasers. The results for a discrete optical vortex with $l = 1$ are shown in Fig. 7.4.
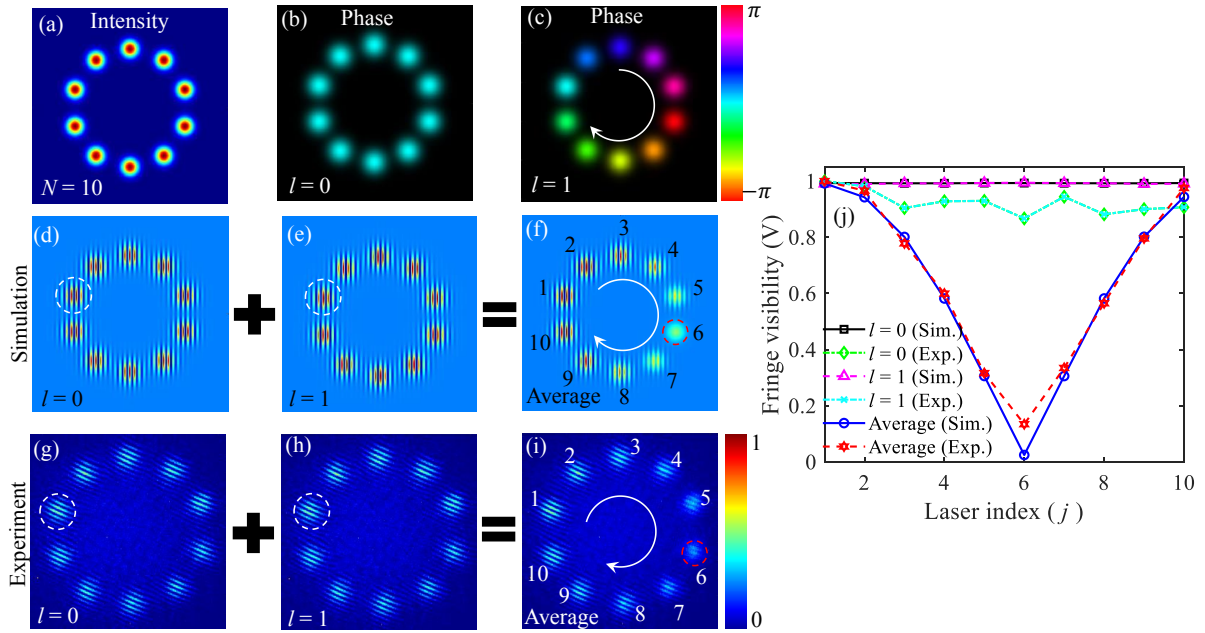
Figure 7.4: Results for a discrete optical vortex with $l = 1$. (a) The near-field intensity distribution of a discrete optical vortex formed by a 1D ring array of N=10 lasers. The near-field phase distribution with (b) $l = 0$, and (c) $l = 1$. Interference pattern when a single laser (reference laser denoted by a dashed circle) interferes with itself and with all the other lasers for (d),(g) $l = 0$, and (e),(h) $l = 1$. (f) The average of interference patterns of $l = 0$ (d) and $l = 1$ (e). (i) The average of interference patterns of $l = 0$ (g) and $l = 1$ (h). (j) The variation of fringe visibility as a function of laser index.

Figure 7.4(a) shows the intensity distribution of a discrete optical vortex, indicating that it consists of a 1D ring array of N=10 lasers with TEM_{00} fundamental Gaussian mode profiles, and each laser has the beam waist of 0.16 mm and separated with a distance of 0.84 mm (center-to-center). Figure 7.4(b) shows the phase distribution of 1D ring array of N=10 lasers with $l = 0$ (in-phase distribution), indicating that there is no net phase circulation around the center. Figure 7.4(c) shows the discrete phase distribution of 1D ring array of N=10 lasers with $l = 1$, indicating the phase circulation around the center (discrete optical vortex). Note, the intensity distribution of 1D ring array of lasers for both $l = 0$ and $l = 1$ is the same. Figures 7.4(d)-7.4(f) show the simulated results of individual interference patterns of 1D ring array of N=10 lasers with $l = 0$ and $l = 1$, and their averaged interference pattern, respectively. Figures 7.4(g)-7.4(i) show the experimental results of individual interference patterns of 1D ring array of N=10 lasers with $l = 0$ and $l = 1$, and their averaged interference pattern, respectively. The white dashed circles in Figs. 7.4(d), 7.4(e), 7.4(g) and 7.4(h) mark the location of a selected reference laser. The individual interference patterns of 1D ring array of N=10 lasers with $l = 0$ and $l = 1$ are obtained using a Mach-Zhender interferometer (Fig. 7.2(a)), where a selected reference laser interferes with itself and with all the other lasers. As evident, in the individual interference patterns corresponding to $l = 0$ and $l = 1$, the fringes are uniform at all the lasers and show no distinguishabilities between $l = 0$ and $l = 1$ (Figs. 7.4(d)& 7.4(e) and Figs. 7.4(g) & 7.4(h)). However, in the averaged interference pattern the fringes show variation at the lasers (Figs. 7.4(f) and 7.4(i)). Particularly, at the reference laser $j = 1$ the fringes appear with clear maxima and minima, and the fringes degrade monotonically for the lasers $j = 2 - 6$ and after that fringes again improve monotonically for the lasers $j = 6 - 10$.

We have analyzed the fringe visibility at all the lasers in these individual and averaged interference patterns (Figs. 7.5 and 7.6). The quantified simulated and experimental results are shown in Fig. 7.4(j), which shows the variation of fringe visibility as a function of laser index j ($j = 1$, 2, 3...10). As evident, for the individual interference patterns corresponding to $l = 0$ (solid black curve with squares (simulation) and dashed green curve

with diamonds (experiment)) and $l = 1$ (pink dashed curve with triangles (simulation) and cyan dashed curve with cross (experiment)), the fringe visibility does not show any variation and is found to be maximum V≈ 1 at all the lasers. Note, due to small intensity differences between the lasers, the experimental visibility is found to be a bit less than V$= 1$. However, in the averaged interference pattern the fringe visibility shows variation as a function of laser index j (shown by red dashed curve with stars (experiment) and blue solid curve with circles (simulation)). For example, the fringe visibility is found to be maximum (V$= 1$) at laser $j = 1$ and then it decreases monotonically until laser $j = 6$ (minimum V), and after that it again increases and becomes maximum again at laser $j = 10$.

These variations in the fringe visibility as a function of laser index can be understood by the working principle. The phase distribution of discrete optical vortex in a ring array of $N = 10$ lasers for a topological charge l is given as: $\phi_j = l.(j - 1).(2\pi/10)$, where $j = 1$, 2, 3... denote the laser number in the array. The interference patterns are obtained by using a Mach-Zhender interferometer (Fig. 7.2(a)), where a single selected reference laser interferes with itself and with all the other lasers in the array. The results of interference patterns are shown in Figs. 7.4(d)-7.4(f) (simulation) and Figs. 7.4(g)-7.4(i) (experiment). The analysis of fringe visibility at all lasers in the array is shown in Fig. 7.5 (simulation) and Fig. 7.6 (experiment).

The laser $j = 1$ is a selected reference laser, where light interferes with itself, and has initial phase difference $d\phi_{1,1} = 0$ (Eq. (7.4)) for both $l = 0$ and $l = 1$. The interference expressions at laser 1 in $l = 0$ and $l = 1$ can be written as follows. Using Eq. 7.4)

$$I_{T1} = I_{T2} = 2I_0 \left[1 + \cos\left(0.94kx\right)\right], \tag{7.13}$$

The expression of averaged interference pattern is given as

$$I_{Sum} = \frac{I_{T1} + I_{T2}}{2} = 2I_0 \left[1 + \cos\left(0.94kx\right)\right]. \tag{7.14}$$

As $d\phi_{1,1} = 0$ for both cases of $l = 0$ and $l = 1$, so maxima and minima in the fringe pattern (Eq. (7.13)) occur at the same locations (red dashed curve and blue dot-dashed curve in Figs. 7.5(a) and 7.6(a)). In both cases, the fringe visibility is found to be $V = 1$. The average of these two interference patterns gives no change in the fringe pattern (Eq. (7.14)), and the fringe visibility remains unchanged $V = 1$ (black solid curve in Figs. 7.5(a) and 7.6(a)). The interference fringes at laser 2 in $l = 0$ and $l = 1$ are obtained when the light
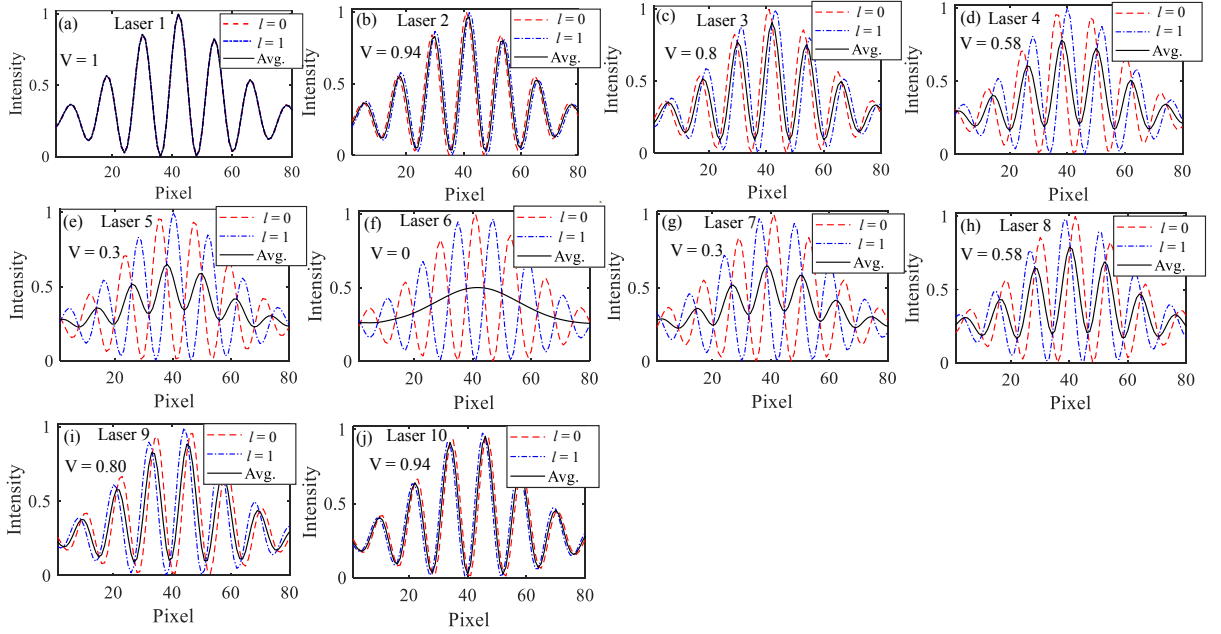
Figure 7.5: Simulated results. The intensity cross-section in the interference patterns of $l = 0$, $l = 1$ and averaged interference pattern $l = 0 + l = 1$ at (a) laser 1, (b) laser 2, (c) laser 3, (d) laser 4, (e) laser 5, (f) laser 6, (g) laser 7, (h) laser 8, (i) laser 9, and (j) laser 10. The red dashed curve denotes $l = 0$, blue dot-dashed curve denotes $l = 1$, and black solid curve denotes $l = 0 + l = 1$. Note, the intensity cross-sections in $l = 0$ and $l = 1$ are normalized to the maximum value of 1.

from a selected reference laser $j = 1$ interferes with the light from laser $j = 2$. In $l = 0$, the initial phase difference between the laser $j = 1$ and laser $j = 2$ is $d\phi_{1,2} = 0$, whereas, in $l = 1$ it is $d\phi_{1,2} = 2\pi/10$. The interference expressions I_{T1} (in $l = 0$) and I_{T2} (in $l = 1$) can be given as

$$I_{T1} = 2I_0\left[1 + \cos\left(0.94kx\right)\right], \tag{7.15}$$

$$I_{T2} = 2I_0\left[1 + \cos\left(0.94kx - 1.(2\pi/10)\right)\right]. \tag{7.16}$$

7 Method for characterization of topological charge of unknown discrete optical vortices
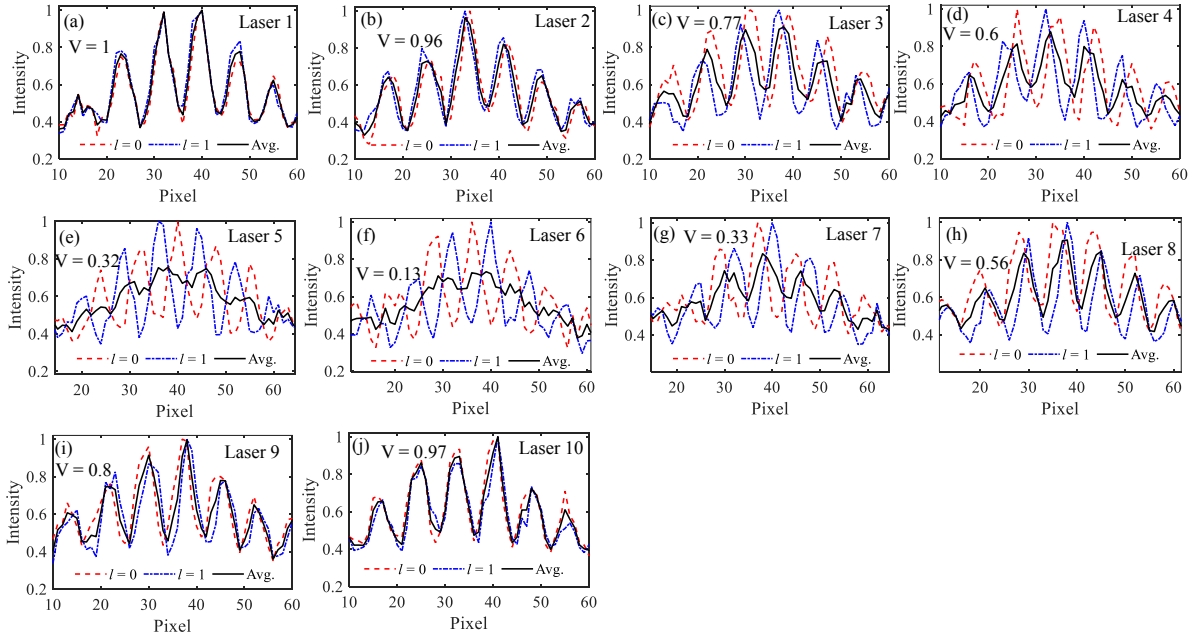
Figure 7.6: Experimental results with the details same as given in Fig. 7.5.

The averaged interference pattern is given as

$$I_{Sum} = I_0 \left[2 + \cos\left(0.94kx\right) + \cos\left(0.94kx - 1.(2\pi/10)\right) \right]. \tag{7.17}$$

The interference patterns (Eqs. (7.15) and (7.16)) consist of fringes with clear maxima and minima, which give rise to the fringe visibility of $V = 1$ (red dashed curve and blue dot-dashed curve in Figs. 7.5(b) and 7.6(b)). As evident, in these interference patterns, the fringes (maxima and minima) are shifted relative to each other, which occurs due to the different values of initial phase difference $d\phi_{1,2}$ in $l = 0$ and $l = 1$. When these interference patterns with shifted fringes are averaged, the resultant interference pattern (Eq. 7.17) consists of fringes with reduced fringe visibility $V = 0.94$ (black solid curve in Figs. 7.5(b) and 7.6(b)).

Similarly, the interference fringes at other lasers are obtained by interfering the light from a selected reference laser $j = 1$ and the light from other lasers $j > 2$. In general, in $l = 0$, the phase difference between the selected reference laser $j = 1$ and other lasers is given as $d\phi_{1,j\geq1} = 0$, whereas, in case of $l \neq 0$, it is given as $d\phi_{1,j\geq1} = l.(j-1).(2\pi/N)$,

where N denotes the number of lasers in a 1D ring array. Therefore, in case of $l = 0$ the interference fringes at lasers $j = 3, 4, ...10$ occur exactly at the same locations (red dashed curve in Figs. 7.5(c)-7.5(j) and Figs. 7.6(c)-7.6(j)). However, in case of $l = 1$ the interference fringes at $j = 3, 4, ...10$ occur at different locations due to different values of $d\phi_{1,j\geq3}$ (blue dot-dashed curve in Figs. 7.5(c)-7.5(j) and Figs. 7.6(c)-7.6(j)). Because of this when the interference patterns at the same lasers ($j = 3, 4, ...10$) for $l = 0$ and $l = 1$ are averaged, the resultant interference pattern consists of reduced visibility (black solid curve in Figs. 7.5(c)-7.5(j) and Figs. 7.6(c)-7.6(j)). For example, at lasers $j = 3 - 6$ the values of reduced fringe visibility are found to be 0.8 (Figs. 7.5(c) and 7.6(c)), 0.58 (Figs. 7.5(d) and 7.6(d)), 0.3 (Figs. 7.5(e) and 7.6(e)), and 0 (Figs. 7.5(f) and 7.6(f)), respectively. For the lasers $j = 7 - 10$, the values of fringe visibility are found to be 0.3 (Figs. 7.5(g) and 7.6(g)), 0.58 (Figs. 7.5(h) and 7.6(h)), 0.80 (Figs. 7.5(i) and 7.6(i)) and 0.94 (Figs. 7.5(j) and 7.6(j)), respectively. Note, a small discrepancy between simulated and experimental fringe visibility is anticipated by a small intensity difference between the lasers in the experiment. As evident, the fringe visibility decreases monotonically for lasers $j = 1 - 6$ and after that, it again increases from $j = 7 - 10$. The increase in the fringe visibility for $j = 7 - 10$ can be explained as follows. For laser $j = 7$, we have $d\phi_{1,7} = 1.6.(\frac{2\pi}{10})$, which can also be written as $\left[2\pi - (4.(\frac{2\pi}{10}))\right]$ or $-4.(\frac{2\pi}{10})$. This becomes equivalent to the phase difference between $j = 1$ and 5 with the negative sign i.e., $-d\phi_{1,5}$. Note, the positive and negative values of the same magnitude $d\phi$ produce the same shift of fringes in the interference pattern, as shown in Figs. 7.1(a) and 7.1(c). The phase difference $|d\phi_{1,7}| < |d\phi_{1,6}|$, and due to this the fringe visibility in the averaged interference at laser $j = 7$ is found to be higher than laser $j = 6$ (and same as for $j = 5$). Similarly, the increased values of V at laser $j = 8$, 9, and 10 can also be explained.

The variation in the fringe visibility as a function of laser index is characteristic to the topological charge of a discrete optical vortex, so it serves as the basis for an accurate determination of topological charge. In particular, the observation of number dips in the fringe visibility curve provides information of topological charge. For example, a single minimum denotes the value of $l = 1$.

---

7 Method for characterization of topological charge of unknown discrete optical vortices

Further, we have determined the large values of $l > 1$ in a discrete optical vortex formed with a 1D ring array of N=10 lasers. The results are shown in Fig. 7.7.
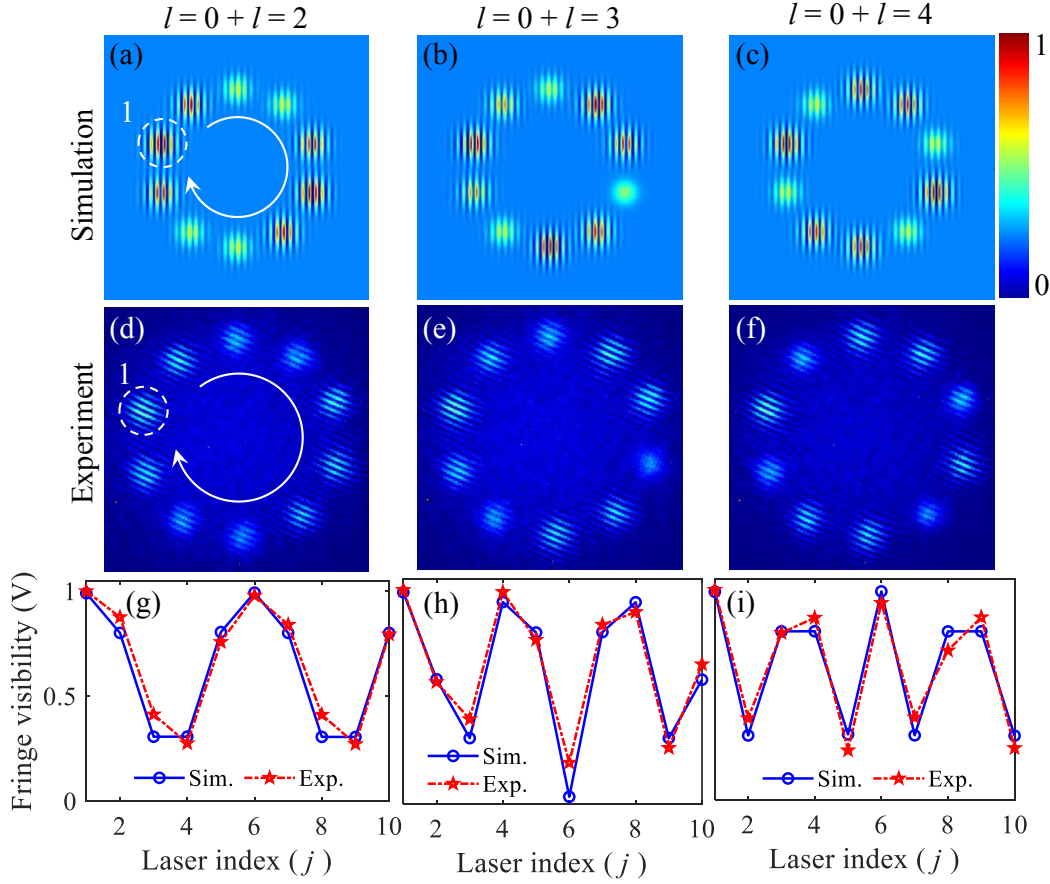
Figure 7.7: For a discrete optical vortex of system size N=10 lasers, the determination of $l = 2$, 3 and 4. The average of interference patterns of $l = 0$ and (a, d) $l = 2$, (b, e) $l = 3$, and (e, f) $l = 4$. (g-i) The Fringe visibility as a function of laser index, corresponding to (a, d), (b, e), and (e, f), respectively. Blue solid curve with circles represents the simulation, and Red dashed curve with stars represents the experiment. Dashed white circle on (a, d) marks the location of a selected reference laser $j = 1$.

Figures 7.7(a)-7.7(c) and 7.7(d)-7.7(f) show the simulated and experimental results obtained by averaging the interference patterns of $l = 2$, $l = 3$ and $l = 4$ with $l = 0$ ($l = 0$ + $l = 2$, $l = 0 + l = 3$, and $l = 0 + l = 4$), respectively. The white dashed circles in Figs. 7.7(a) and 7.7(d) mark the location of a selected reference laser $j = 1$. The location of reference laser remains the same in other averaged interference patterns (Figs. 7.7(b) & 7.7(c) and Figs. 7.7(e) & 7.7(f)). As evident, in the averaged interference patterns the

fringes at the lasers exhibit different behaviour. The analyzed fringe visibility as a function of laser index (j) corresponding to $l = 2$, 3 and 4 are presented in Figs. 7.7(g)-7.7(i), respectively, indicating different variations related to the values of topological charges. This is due to the fact that the phase distribution of discrete optical vortex depends on the value of l as $\phi_j = 2\pi l(j-1)/10$ ($j = 1$, 2, 3...10), and accordingly the fringes at the lasers are shifted by different amounts with respect to the fringes in $l = 0$. Thus, averaging of interference patterns of $l \neq 0$ and $l = 0$ results in a different variation in the fringe visibility with the laser index (explained above), and can be used to determine the value of l. For example, the averaging of $l = 0 + l = 2$ produces two dips in the fringe visibility curve, confirming the value of $l = 2$ (Fig. 7.7(g)). Similarly, the observation of three and four dips in the fringe visibility curve (Figs. 7.7(h) and 7.7(i)) confirms the value of $l = 3$ and 4, respectively. The simulation and experimental results show an excellent agreement.

Further, to show an accurate determination of higher-order topological charge of a discrete optical vortex, we have considered a 1D ring array of $N = 30$ lasers. Using the experimental arrangement shown in Fig. 7.2(a), we have generated discrete optical vortices with $l = 11$ to 14, and determined their values by averaging their interference patterns with $l = 0$. The results are shown in Fig. 7.8. Figures 7.8(a)-7.8(d) and 7.8(e)-7.8(h) show the simulated and experimental results obtained by averaging the interference patterns of $l = 11$, 12, 13 and 14 with $l = 0$ ($l = 0 + l = 11$, $l = 0 + l = 12$, $l = 0 + l = 13$ and $l = 0 + l = 14$), respectively. The white dashed circles in Figs. 7.8(a) and 7.8(e) mark the location of a selected reference laser $j = 1$. The location of reference laser remains the same in other averaged interference patterns. As evident, in the averaged interference patterns, corresponding to different topological charges, the fringes at the lasers exhibit different behaviour and enable accurate identification of corresponding topological charges of discrete optical vortices. The analyzed fringe visibility as a function of laser index (j) corresponding to $l = 11 - 14$ is shown in Figs. 7.8(i)-7.8(l), respectively. The phase distribution of discrete optical vortex with different topological charges, formed with a 1D ring array of $N = 30$ lasers can be given as $\phi_j = 2\pi l(j-1)/30$, where $j = 1$, 2, 3,...30. The
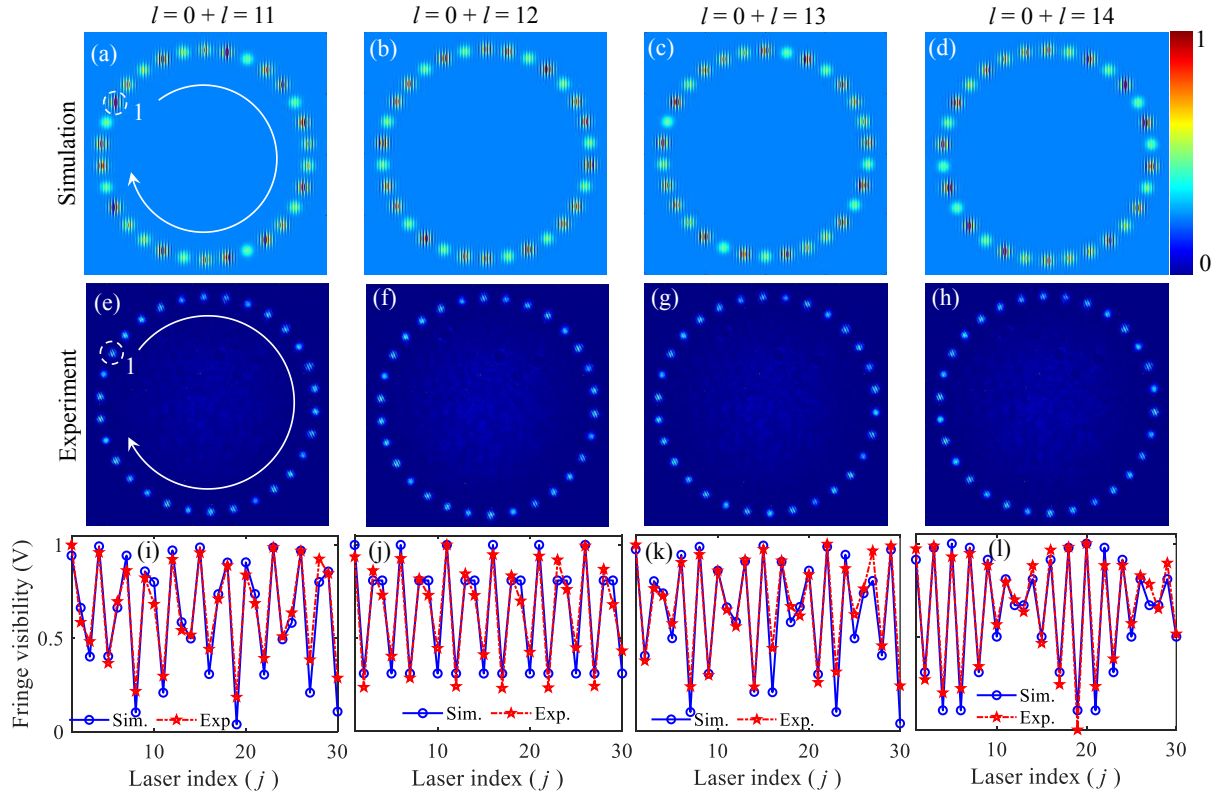
Figure 7.8: Determination of higher values of topological charge of a discrete optical vortex with a large system size N=30 lasers. The average of interference patterns of $l = 0$ and (a, e) $l = 11$, (b, f) $l = 12$, (c, g) $l = 13$, and (d, h) $l = 14$. (e-h)The Fringe visibility as a function of laser index, corresponding to (a, e), (b, f), and (c, g), respectively. Blue solid curve with circles represents the simulation, and red dashed curve with stars represents the experiment. Dashed white circle on (a, e) marks the location of a selected reference laser $j = 1$.

observed variation in the fringe visibility as a function of laser index (j) can be explained with the same reasons as explained above for discrete optical vortex with $N = 10$ lasers. It is clearly evidenced that the averaging of interference patterns $l = 0 + l = 11$, $l = 0 + l = 12$, $l = 0 + l = 13$, and $l = 0 + l = 14$ leads to distinct variations in the fringe visibility as a function of laser index, and produces different number of dips corresponding to different values of topological charges. For example, averaged interference pattern of $l = 0 + l = 11$ produces eleven dips, which confirms the value of $l = 11$ (Fig. 7.8(i)). Similarly, the observation of twelve, thirteen, and fourteen dips corresponding to $l = 0 + l = 12$, $l = 0 + l = 13$, and $l = 0 + l = 14$, confirms the values of $l = 12 - 14$, respectively. We

have observed an excellent agreement between the numerical and experimental results, which indicates an accurate determination of high-order topological charges of discrete optical vortices.

So far, we have successfully shown an accurate determination of magnitude of topological charge of a discrete optical vortex by averaging the interference patterns of $l \neq 0$ with $l = 0$. However, with this averaging the same results are obtained for both positive and negative values of topological charge, and can not distinguish the sign of $l \neq 0$. To determine the sign of topological charge of a discrete optical vortex, we average the interference pattern of an unknown discrete optical vortex having $l \neq 0$ with the interference pattern of a known discrete optical vortex having $l = 1$ (instead of $l = 0$ as earlier). To show it, we have considered discrete optical vortices with different topological charges in a 1D ring array of $N = 10$ lasers, as shown in Fig. 7.9.

Figures 7.9(a)-7.9(d) show the simulated averaged interference patterns of positive $l = 1, 2, 3$ and 4 with $l = 1$ ($l = 1 + l = 1$, $l = 1 + l = 2$, $l = 1 + l = 3$ and $l = 1 + l = 4$), respectively. Figures 7.9(e)-7.9(h) show the simulated averaged interference patterns of negative $l = -1, -2, -3$, and -4 with $l = 1$ ($l = 1 + l = -1$, $l = 1 + l = -2$, $l = 1 + l = -3$ and $= 1 + l = -4$, respectively. A white dashed circle in Fig. 7.9(a) represents the location of a selected reference laser $j = 1$, which also remains the same in all other interference patterns (Figs. 7.9(b)-7.9(h)). As evident, in the averaged interference patterns of positive and negative topological charges with $l = 1$, the fringes at the lasers appear differently, thus enabling to distinguish the sign of topological charge. These different interference patterns are again anticipated by the different phase distributions of discrete optical vortices having different topological charges. The analyzed fringe visibility as a function of laser index (j), corresponding to Figs. 7.9(a)-7.9(h), is shown in Figs. 7.9(i)-7.9(l). The red dashed curve with circles shows the visibility curve when interference patterns of positively charged $l = +1$ to $l + 4$ are averaged with $l = +1$, whereas, solid blue curve with squares denote the case when interference patterns of negatively charged $l = -1$ to $l - 4$ are averaged with $l = +1$. As evident, the variation of fringe visibility with laser index (j) for the positive and negative topological charges is found to be different, and
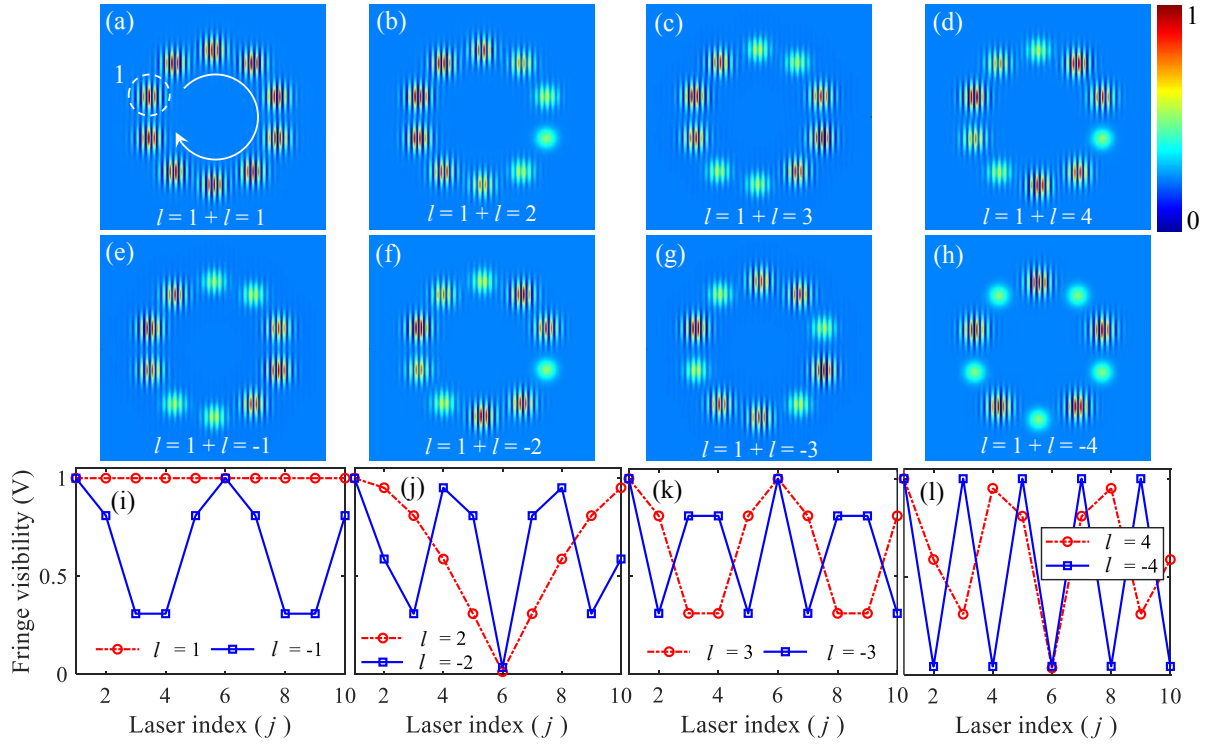
Figure 7.9: Simulation results for determining the sign of topological charge of a discrete optical vortex with $N = 10$ lasers. The averaging of interference patterns of $l = 1$ and (a) $l = 1$, (b) $l = 2$, (c) $l = 3$, and (d) $l = 4$. The averaging of interference patterns of $l = 1$ and (e) $l = -1$, (f) $l = -2$, (g) $l = -3$, and (h) $l = -4$. (i-l) The fringe visibility as a function of laser index, corresponding to (a,e), (b, f), (c, g), and (d, h), respectively. A dashed white circle in (a) marks the location of a selected reference laser $j = 1$.

thus enables to identify the sign of topological charge. In particular, for $l = +1$, the fringe visibility is found to be 1 for all the lasers (no variation), and no dip is observed (dashed red curve with circles in Fig. 7.9(i)). Whereas, for $l = -1$, the fringe visibility shows variation, and two dips are observed (solid blue curve with squares in Fig. 7.9(i)).

As discussed earlier in Figs. 7.4-7.8, when the interference patterns of positive and negative topological charges are averaged with the interference pattern of $l = 0$, the number of dips in the fringe visibility curve is found to be proportional to the magnitude of topological charge. For example, for $l = \pm 1$ only a single dip is observed in the fringe visibility curve (Fig. 7.4(j)). However, when the interference patterns of positive and negative topological charges are averaged with the interference pattern of $l = +1$, the number of dips in the fringe visibility curve decreases by one for the positive topological charges,

and increases by one for the negative topological charges. For example, in Fig. 7.9(i), no dip is observed for $l = +1$, and two dips are observed for $l = -1$. Similarly, for $l = +2, +3$, and $+4$, the number of dips are observed to be one, two, and three, respectively (red dashed curve with circles in Figs. 7.9(j)-7.9(l)). Whereas, for $l = -2, -3$, and -4, the number of dips are observed to be three, four, and five, respectively (solid blue curve with squares in Figs. 7.9(j)-7.9(l)). This clearly indicates that the observation of a decrease/increase in the number of dips in the fringe visibility curve provides accurate information of positive/negative sign of topological charge of a discrete optical vortex.

We have also verified these findings experimentally, the results are shown in Fig. 7.10. The experimental results show excellent agreement with the simulations. Thus, averaging the interference patterns of positive and negative topological charges with the interference pattern of $l = +1$ provides accurate information of the sign of topological charge of a discrete optical vortex. This approach can be used for identifying the sign of topological charge of any order.

Next, we have checked the robustness of our method against the phase disorder (for example, aberrations due to misalignment of optical components). We have generated phase disorder in a range [-π to π] through a random phase screen using Monte Carlo method, that behaves like a disorder media of desired length and having disorder strength C_n^2 [37]. We have considered a phase disorder with a strong strength $C_n^2 = 10^{-12}$. The simulated results are shown in Fig. 7.11. Figures 7.11(a)-7.11(d) show the ideal phase distribution of discrete optical vortices with $l = 1$ to 4 in a 1D ring array of $N = 10$ lasers. After multiplying the phase disorder, the distorted phase distributions of discrete optical vortices with $l = 1$ to 4 are shown in Figs. 7.11(e)-7.11(h). It is clearly evident that most of the lasers in the array consist of more than a single phase.

To show whether our method can still determine accurately the information of topological charge, we have measured the interference patterns of 1D ring array of lasers with $l = 1$ to 4 and $l = 0$ under the same phase disorder, using Fig. 7.2(a). The averaged interference patterns of $l = 1$ to 4 with $l = 0$ are shown in Fig. 7.11(i)-7.11(l). It is evident that in the averaged interference patterns of different topological charges, the
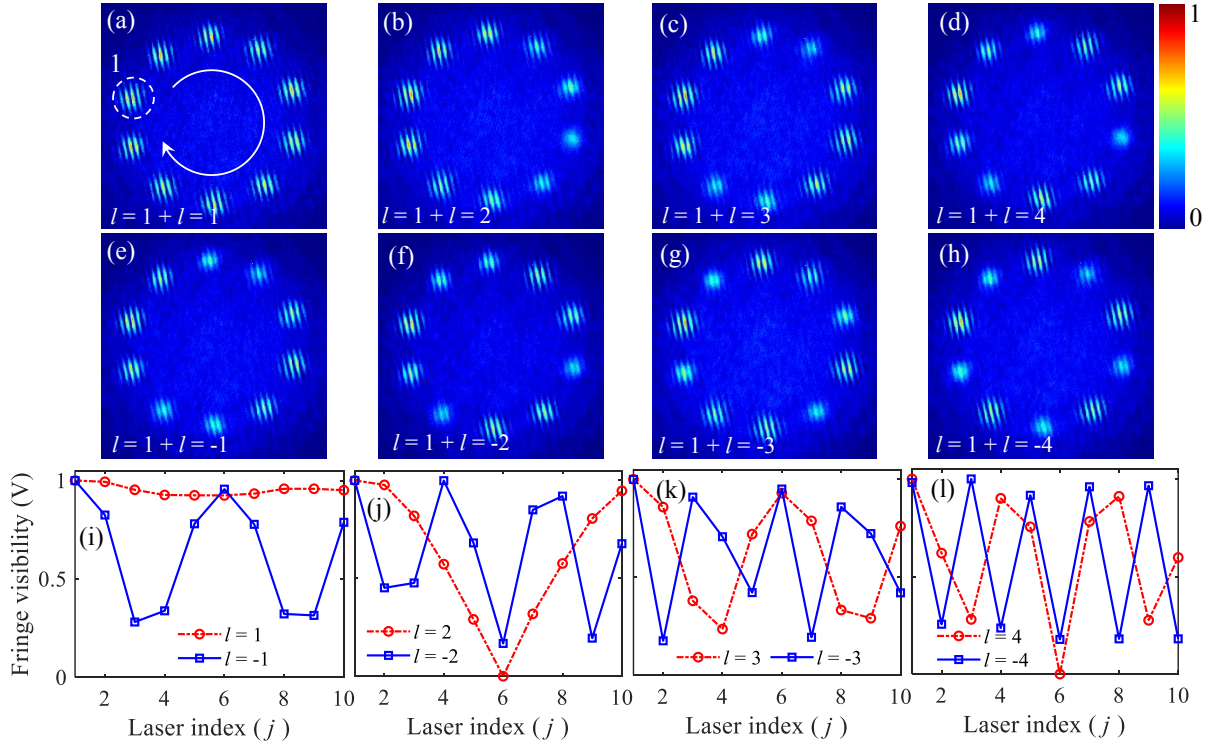
Figure 7.10: Experimental results for determining the sign of topological charge of a discrete optical vortex with $N = 10$ lasers. The averaging of interference patterns of $l = 1$ and (a) $l = 1$, (b) $l = 2$, (c) $l = 3$, and (d) $l = 4$. The averaging of interference patterns of $l = 1$ and (e) $l = -1$, (f) $l = -2$, (g) $l = -3$, and (h) $l = -4$. (i-l) The fringe visibility as a function of laser index, corresponding to (a,e), (b, f), (c, g), and (d, h), respectively. A dashed white circle in (a) marks the location of a selected reference laser $j = 1$.

fringes at the lasers are distributed differently with different fringe visibility. Further, the orientations of the fringes at the lasers are found to be different (unlike ideal discrete optical vortices in Figs. 7.2 and 7.4). This is anticipated by the multiple-phase structure in each laser. The analyzed fringe visibility as a function of laser index (j) for all $l = 1$ to 4 (blue solid curve with circle for $l = 1$, red dashed curve with squares for $l = 2$, black dot-dashed curve with star for $l = 3$ and pink dotted curve with triangles for $l = 4$), are shown in Fig. 7.11(m). As evident, for different values of topological charge, the variation in the fringe visibility consists of different number of dips. In particular, corresponding to $l = 1$ to 4, the number of dips in the fringe visibility are found to be one, two, three, and four, respectively, which clearly identifies the magnitude of topological charges.

We have also verified experimentally the effect of phase disorder on the determination
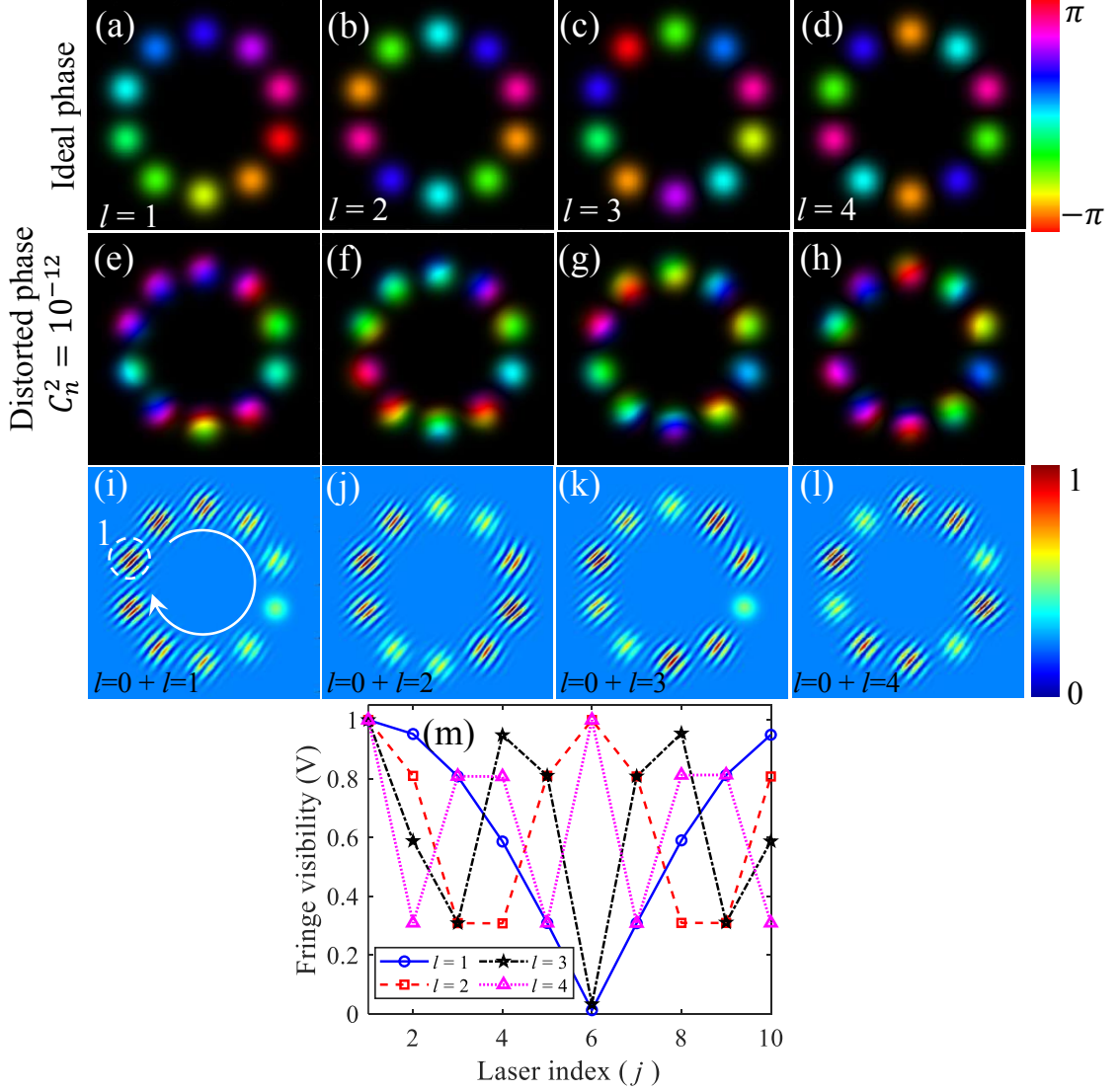
Figure 7.11: Simulation results showing the effect of phase disorder on the determination of topological charge of a discrete optical vortex with $N = 10$ lasers. The discrete optical vortex with topological charges $l = 1$ to 4 having (a-d) ideal phase distribution, and (e-h) disordered phase distribution. The average of interference patterns of $l = 0$ and (i) $l = 1$, (j) $l = 2$, (k) $l = 3$, and (l) $l = 4$. (m) The fringe visibility as a function of laser index corresponding to (i-l). A white dashed circle in (a) marks the location of a selected reference laser.
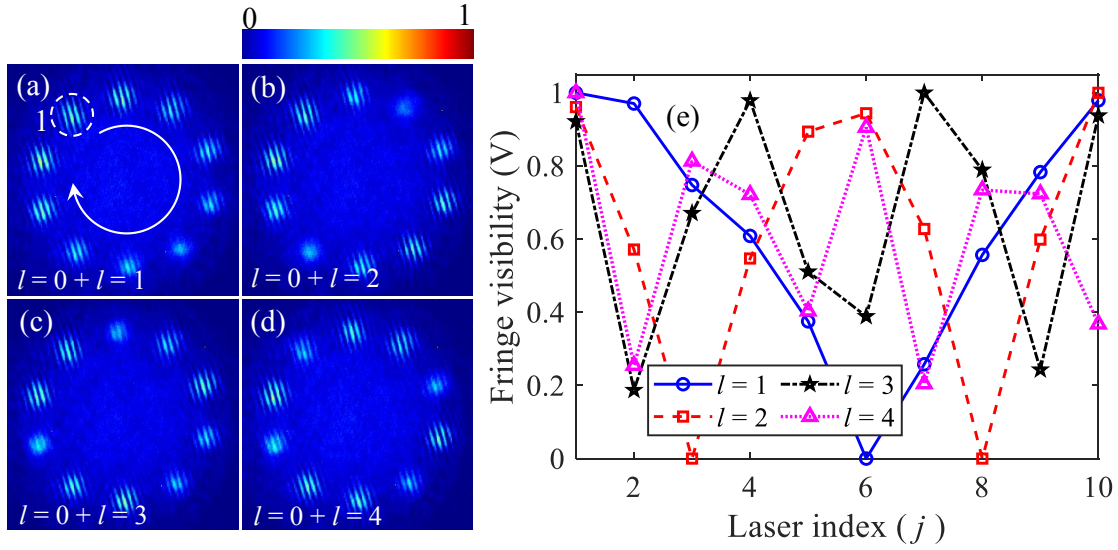
Figure 7.12: Experimental results showing the effect of phase disorder on the determination of topological charge of a discrete optical vortex with $N = 10$ lasers. The average of interference patterns of $l = 0$ and (a) $l = 1$, (b) $l = 2$, (c) $l = 3$, and (d) $l = 4$. (e) The fringe visibility as a function of laser index corresponding to (a-d). Note, the phase disorder is kept the same as in Fig. 7.11. A white dashed circle in (a) marks the location of a selected reference laser.

of topological charge. The results for different values of $l = 1$ to 4, under the same phase disorder strength $C_n^2 = 10^{-12}$ are presented in Fig. 7.12. Experimentally, the phase disorder on the discrete optical vortex is realized by imposing random phase on hologram along with the phase distribution of discrete optical vortex [37]. Figures 7.12(a)-7.12(d) show the averaged interference patterns of $l = 1$ to 4 with $l = 0$ ($l = 0 + l = 1$, $l = 0 + l = 2$, $l = 0 + l = 3$ and $l = 0 + l = 4$), respectively, indicating the different fringe distribution at the lasers in each case. Corresponding to Figs. 7.12(a)-7.12(d), the analyzed fringe visibility as a function of laser number (j) is shown in Fig. 7.12(e). As evidence, corresponding to different values of $l = 1$ to 4, the number of dips in the fringe visibility variation is found to be one (blue solid curve with circles), two (red dashed curve with squares), three (black dot-dashed curve with stars) and four (pink dotted curve with triangles), respectively. This clearly depicts that our approach is highly robust against the phase disorder, as it does not affect the accurate determination of magnitude of topological charge of a discrete optical vortex. Similarly, the sign of these disordered

topological charges can be determined by averaging their interference patterns with the interference pattern of disordered $l = 1$.

The numerical and experimental results show an excellent agreement and clearly depict that our method accurately determines the magnitude and sign of topological charge of a discrete optical vortex. The determination of topological charge is not affected by the imperfections such as the phase disorder caused by aberrations in the system. Further, the method can be used for determining any small to large values of topological charge.

7.5   Conclusions

In conclusion, we have presented a novel and efficient characterization method for the accurate determination of magnitude and sign of topological charge (l) of an unknown discrete optical vortex, formed by an array of lasers in a 1D ring geometry. Our method relies on measuring the interference pattern of a discrete optical vortex, which is obtained by interfering a single selected laser with itself and with all the other lasers in a 1D ring array, using a Mach-Zhender interferometer. The interference pattern is quantified by analyzing the fringe visibility at each laser in a 1D ring array. The discrete optical vortex with $l = 0$ and $l \neq 0$ have different phase distributions, thus producing interference patterns with shifted interference fringes. The averaging of these phase-shifted interference patterns gives rise to a variation in the fringe visibility as a function of laser number in the discrete optical vortex, thus enabling identification of l. The magnitude of l of a discrete optical vortex is found to be proportional to the number of dips observed in the fringe visibility curve.

Further, for an accurate determination of sign of unknown discrete optical vortex ($l \neq 0$), we have averaged its interference pattern with the interference pattern of a known discrete optical vortex with $l = +1$. The number of dips in the fringe visibility curve decreases by one for positive values of l and increases by one for negative values of l. We have also investigated the robustness of our method against the presence of phase disorder that may occur due to the presence of aberrations in a system. It is found that

the phase disorder does not affect an accurate measurement of topological charge of an unknown discrete optical vortex.

For the generalization of our method, we have demonstrated it for discrete optical vortices with topological charges from small to large values, and accurately measured their magnitude and sign. We have obtained an excellent agreement between the numerical and experiment results, indicating that our method is highly efficient and accurate. Our method can be useful in the applications of discrete optical vortices. The results reported in this Chapter are given in Ref [46].

7.6 Appendix

Computer generated phase hologram for a discrete optical vortex:

In order to generate discrete optical vortex with desired topological charge, the phase and amplitude of the incident Gaussian beam are modulated by phase-only holograms [155]. The complex electric field of discrete optical vortex can be expressed as

$$U(x,y) = A(x,y)\exp(i\phi(x,y)), \tag{7.18}$$

where the amplitude $A(x,y)$ and the phase $\phi(x,y)$ take values in the intervals [0,1] and $[-\pi,\pi]$. The aim is to encode the complex field $U(x,y)$ by means of a phase transmittance function (phase hologram) to incorporate amplitude variations as phase variations, that is, a function $h(x,y)$ must be given by

$$h(x,y) = \exp\left[i\psi\left(A,\phi\right)\right], \tag{7.19}$$

where $\psi(A,\phi)$ accounts both amplitude and phase variations. To find the desired form of phase function $\psi(A,\phi)$, a detailed description of the method is given in Sec. 1.5 of Chapter 1. The modulated field reflected from SLM consists of first and higher orders, thus to separate the first order, a blazed grating is added to the phase of hologram. The

resultant phase has the following form

$$\psi = \psi(A, \phi + 2\pi N_x x + 2\pi N_y y), \tag{7.20}$$

where N_x and N_y denote the grating frequencies along x and y directions, respectively. As per the requirement of SLM, the phase of hologram is divided into 256 levels. The spatial frequencies are chosen as $N_x = 120$ and $N_y = 60$. The holograms corresponding to $l = 0$ to 3 and system size N= 10 are shown in Fig. 7.13(a)-7.13(d), respectively. These holograms are used on the SLM to produce the desired phase distributions of lasers in 1D ring array with $l = 0$ to 3, as shown in Fig. 7.13(e)-7.13(h), respectively.
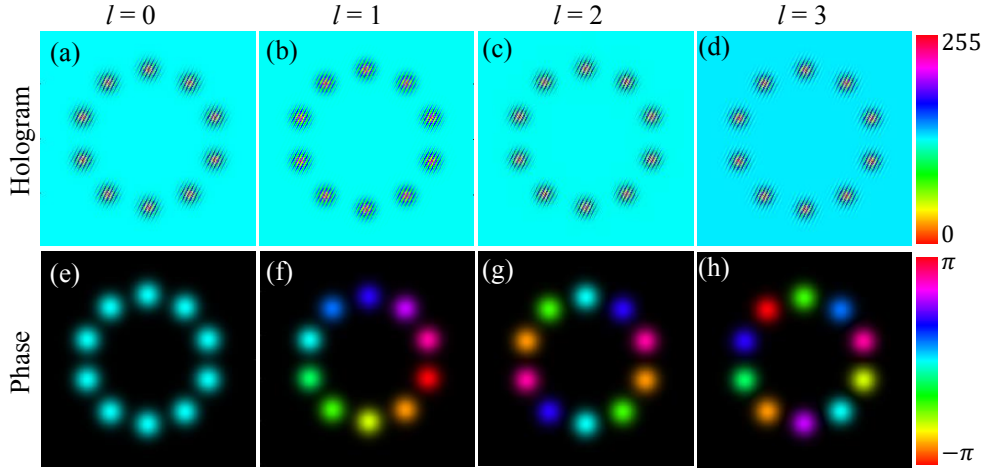
Figure 7.13: Phase holograms corresponding to (a) $l = 0$, (b) $l = 1$, (c) $l = 2$, and (d) $l = 3$. The phase distributions of lasers in 1D ring array corresponding to these holograms for (e) $l = 0$, (f) $l = 1$, (g) $l = 2$, and (h) $l = 3$.

A similar procedure is also used for generating discrete optical vortices with large system sizes and higher-order topological charges.

Chapter 8

Summary and Future Outlook

8.1 Summary

This thesis aims to shed new light on various aspects of spatially controlled structured light. Particularly, it proposes simple, cost-effective, and efficient methods for generation and characterization of novel spatially structured light with customized intensity and phase distributions as well as possessing exotic propagation properties. Further, our emphasis has also been to improve the quality, resolution, resilience against perturbations, and spectral range of spatially controlled structured light. The spatially controlled structured light and characterization methods have potential applications both in fundamental and applied fields.

Chapter 1 is an introduction to the thesis, where we have discussed structured light and its strong relevance in various fundamental and applied fields, where conventional Gaussian laser beams pose physical limitations. We have described various types of spatially controlled structured light and their exotic characteristics. We have discussed various intra-cavity and outer-cavity methods, including their challenges as well as evolution towards the development of improved simple, cost-effective, and efficient methods. Further, we have described the analytical and numerical methods for modelling the laser cavities, as well as propagation and quantification of spatially controlled structured light.

In **Chapter 2**, we have presented the tailoring of amplitude degree of freedom of light to generate uniform-intensity distribution with customized spatial shapes. Such structured light beams are non-trivial, as these are not the regular modes of a conventional laser system. We have generated these beams, based on an outer-cavity method, using diffractive optical elements (DOEs) whose phase distributions are obtained from an iterative phase retrieval algorithm that involves Fresnel propagation and spatial Fourier filtering. In particular, an input Gaussian beam from a laser illuminates the DOE, and after propagating a certain distance (working distance) transforms into a desired uniform-intensity output beam. The simple form of uniform-intensity beams have also been realized with other methods, however, many of these methods suffer various limitations, such as low-quality output, complex phase distribution of DOE, and strong dependence on initial conditions in algorithm. However, in our method, the spatial Fourier filtering enables to obtain a relatively simple design of DOE (smooth phase distribution) and produces a high-quality uniform-intensity output beam. The simple smooth phase distribution offers the possibility of easy manufacturing of DOEs. We have simulated different DOEs and demonstrated the generation of uniform-intensity beams with different spatial shapes, such as square, annular, rectangular, hollow square, and plus-sign. We have characterized the quality of shaped output beams by calculating root mean square error (RMSE) (Eq. (1.25)), and found that the shaped output beams consist of high-quality. The RMSE is found to be dependent on spatial shapes and increases with an increase in the complexity of shapes. The quality of shaped output beam also depends on the working distance (z) for which DOE is designed, in particular, for very small and large values of z, the phase distribution of DOE does not result in a high-quality conversion. The optimal working distance depends on several parameters, such as wavelength, input beam size, and output beam size.

Further, we have performed a detailed robustness analysis on the quality of generated shaped output beams against various imperfections in an input beam, for example, misalignment with respect to DOE, effect of asymmetry, speckle noise, presence of higher-order modes, and mismatch of beam sizes. We have found that for imperfections $< 10\%$,

the quality of shaped output beams remains reasonably good. In the case of speckle noise up to 18%, the quality of shaped output beam remains excellent. In this case, we have also shown that the quality of shaped output beam can be further improved using an additional external spatial Fourier filter of suitable transmission function. Further, structured light over a broad spectral range is desired in several applications. So, we have designed a DOE for a particular wavelength and illuminated it with an input beam of a broad spectral range. We have found that our method generates shaped output beam with excellent quality over a broad spectra range, however, the working distance z is found to be decreased with an increase in the wavelength. These uniform-intensity beams with customized spatial shapes have potential applications in various fields, such as material processing, lithography, interferometric gravity wave detectors, optical lattice atomic clocks, etc. [5, 159, 364].

In **Chapter 3**, we have presented the tailoring of light in the amplitude and phase degrees of freedom, for generating a special type of structured light (called aberration laser beams (ALBs)) containing multiple bright lobes and possessing exotic propagation properties, such as autofocusing and self-healing both in free space as well as in turbulent media. The ALBs are generated, based on an outer-cavity method, using a DOE whose phase distribution consists of radial (r^q) and periodic angular dependence ($\sin m\phi$). The presence of periodic angular dependence in the phase distribution provides generation of diffraction pattern with m^{th}-order symmetry. In particular, the intensity symmetrically distributes in various lobes depending on the m-values. The radial term provides the autofocusing features of ALBs. We have presented a detailed mathematical formulation for describing the propagation of ALBs in turbulent media by solving Huygen-Fresnel integral using stationary phase method. Numerically, the turbulent media is simulated by random phase screens using Monte Carlo method, where turbulence strength is controlled by randomness in the phase distribution. Experimentally, the turbulent media of different strengths is generated by hot air at different temperatures.

We have found that the presence of turbulence leads to distortions in the spatial intensity distribution of ALBs, as well as causes beam wandering. The effect of turbulence

on the propagation of ALBs is quantified by calculating an overlap integral with respect to ALB in free space. With an increase in the turbulence strength, the overlap integral is found to be decreased, indicating the spatial distortions in ALBs. The ALBs possess good autofocusing properties both in free space as well as in turbulent media, where on-axis peak intensity becomes maximum with tight focusing. In particular, the autofocusing properties of ALBs remain invariant irrespective of turbulence strength. The autofocusing distance can be controlled from any small to large values, by controlling the ALB parameters, such as λ, q, α, and input beam waist. Further, we have also investigated the spectral dependence of autofocusing of ALBs in turbulent medium, and found that the autofocusing distance does not depend on the turbulence, however, it decreases with an increase in wavelength.

Furthermore, we have performed a detailed investigation of self-healing of ALBs both in free space as well as in turbulent media with different turbulence strengths. To check the self-healing, we have truncated ALB with different amounts using different types of amplitude filters, and after that propagated. We have found that, both in free space and turbulent media, the truncated ALB self-heals by redistributing intensity within the beam. The ALBs self-heal reasonably well even for a large amount of truncation $\sim 60\%$. The maximum self-healing always occurs at the autofocusing distance, which remains invariant irrespective of the amount of truncation and strength of turbulence.

With these unique characteristics, we believe that our findings can be potentially exploited for a wide range of applications. For example, robustness against turbulence and obstructions makes them useful for optical communications in free space and turbulent atmosphere [55,189,190]. As the autofocusing forms a tightly focused spot with maximum power, and with the ability to control the autofocusing distance from small to large values, these beams are potentially useful for surgery and ablation applications [25]. These beams with good self-healing abilities in free space and turbulent media, may widely be used in imaging and investigation of biomedical materials and to examine small complex biological samples or tissues, trapping and guiding microparticles, and material processing [25, 56, 189].

In **Chapter 4**, we have presented the generation of asymmetric aberration laser beams (aALBs) with controlled intensity distribution, based on an outer-cavity method using a diffractive optical element involving the phase asymmetry. In ALBs, the intensity is symmetrically distributed in all the lobes, however, in aALBs the asymmetry in the phase distribution enables an additional control of intensity distribution by redistributing intensity within the beam and forms the high-energy density regions at desired spatial locations. The asymmetry in the phase distribution is introduced by shifting the coordinates in a complex plane, and we have derived the mathematical formulations for general aALBs as well as the special cases of it. We have shown that in an ideal ALB containing equal intensity bright lobes, by introducing asymmetry most of the intensity can be transferred to any one of the single lobes, and generates a high-energy density. Further, we have explored the mechanism of asymmetric control of intensity in aALBs and found that the asymmetry parameters control the position of indeterminate phase point of the trigonometric phase term in aALBs, which creates a controlled asymmetric intensity distribution in the near-field plane. As a result of propagation, it provides a controlled transfer of intensity within aALBs. In general, for a given parameter m of aALBs, a precise spatial location of high-energy density lobe can be controlled by the asymmetry parameter (β), and we have determined empirical relations between β and m. We have found that for the specific values of β and m, the intensity in high-energy density lobe can be enhanced by several times the intensity in other lobes. Further, the effect of different beam parameters, such as m and q are also investigated, which provides more flexibility in controlling the intensity distribution of aALBs.

Furthermore, unlike ideal ALBs, the aALBs possess more complex intensity and phase distributions, so we have investigated their propagation characteristics. We have found that similar to ideal ALBs, the aALBs also possess good autofocusing properties, which are not affected by the asymmetry. The autofocusing distance of aALBs can be varied from small to large values by changing the beam parameters. The aALBs provide a more general framework of controlling intensity distribution, as for the specific values of asymmetry parameters the aALB behaves as an ideal ALB. These aspects of aALBs mak-

ing them potentially important for various applications of modern optics and photonics, such as forming various types of optical traps to guide and manipulate particles, material processing, etc.

In **Chapter 5**, we have presented the generation of high-energy densities by suppressing higher-order sidelobes in the far-field of phase-locked lasers. We have generated lasers in various 1D and 2D array geometries in a degenerate cavity and phase-locked them in the in-phase [out-of-phase] configuration with the far-field coupling using Gaussian apodizer [binary circular aperture]. Owing to the non-uniform amplitude and definite geometry, the far-field of phase-locked lasers consists of higher-order sidelobes. These sidelobes contain a significant amount of energy, which limits the use of an output beam for high-power applications. To efficiently suppress such higher-order sidelobes, the method involves two steps: (i) The first step includes phase correction, where the phase of zeroth-order lobe in the far-field is changed by a certain angle, which results in a modified near-field with nearly uniform-intensity distribution and non-uniform phase distribution, and (ii) second step includes the phase neutralization, where, in the modified near-field, the non-uniform phase distribution is neutralized to obtain a beam with a nearly uniform-intensity distribution and uniform-phase distribution. This beam yields a tightly focused high-energy density peak (zeroth-order lobe) in the far-field intensity distribution.

We have demonstrated this method for the phase-locked lasers in various array geometries, such as square, triangular, Kagome, random, and 1D ring. The results are quantified by calculating the diffraction efficiency of the zeroth-order lobe. It is found that for the long-range in-phase locked laser arrays, the diffraction efficiency of zeroth-order lobe can be improved by several factors ($\sim 3 - 4$). The improved diffraction efficiencies are found to be in a range of $90\% - 95\%$ (for 2D arrays) and $\sim 75\%$ (for 1D ring array). Further, for a long-range in-phase locking of lasers, the phase distribution of neutralizers is found to be binary in nature, which improves the simplicity of the method.

Further, we have analyzed the robustness of our method against various factors, such as the range of phase-locking, system size, and presence of topological defects in a 1D ring array. We have found that the diffraction efficiency of the zeroth-order lobe decreases with

a decrease in the range of phase-locking. However, for a very short-range of phase-locking (for example, only 9 lasers are phase-locked in an array of 81 lasers), the diffraction efficiency is found to be $\sim 75\%$, which is still significantly better than the efficiency of phase-locked laser array with higher-order sidelobes. The decrease in the diffraction efficiency can be attributed to the non-binary nature of phase distribution in neutralizers. Further, we have found that the method works well for small to large system sizes, and diffraction efficiency remains almost the same. In a 1D ring array, the high-energy density zeroth-order lobe can be generated with good diffraction efficiency even in the presence of topological defects.

We have also investigated our method for an out-of-phase locked square laser array, where the zeroth-order has no intensity. We have obtained a high-energy-density zeroth-order lobe with a high diffraction efficiency of 81%. Our results on producing high-energy density beams with suppressed higher-order sidelobes can be useful for various applications in different areas.

In **Chapter 6**, we have presented a novel and efficient intra-cavity method for the generation of high-power discrete optical vortices with precisely controlled topological charges by phase-locking a 1D ring array of lasers in a degenerate cavity. Despite the remarkable progress on conventional optical vortex, there still remains a vital issue that restricts the practical implementation and application of the optical vortex in the future, namely, the limitation of power scaling capacity. However, the discrete optical vortices are realized by phase-locking of several lasers, thus having an improved power scaling capacity.

The special geometry of a degenerate cavity enables an efficient formation of a 1D ring array of lasers, where each laser consists of a nearly fundamental Gaussian distribution, and independent from each other. Initially, the lasers consist of random phase distribution and are equally probable. To force 1D ring array of lasers in a phase-locked steady state of desired optical vortex configuration, we employ a spatial Fourier filter (amplitude mask) at the Fourier plane inside the degenerate cavity, whose transmission function is engineered by the Fourier transform of a desired discrete optical vortex. The spatial Fourier filtering

mechanism helps to eliminate the undesired phase distributions by introducing additional losses to them, thereby, enabling the lasers to find a correct phase distribution in the form of a desired discrete optical vortex. With the specifically engineered spatial Fourier filters, we have demonstrated generation of discrete discrete optical vortices with different system sizes and precisely controlled topological charges.

It is well-known that discrete systems behave differently than continuous systems, so we have performed a detailed investigation on the propagation, such as divergence and self-healing, of discrete optical vortices, and compared them with the conventional continuous optical vortices. We have found that for a given system size (number of lasers) and fixed distance between the neighbouring lasers, the size of a discrete optical vortex and its divergence does not depend on the topological charge, which is found to be different than the conventional continuous optical vortices (Laguerre-Gaussian/Bessel-Gaussian beams). Further, we have performed a detailed investigation of self-healing by partially truncating a discrete optical vortex in the waist plane ($z = 0$) and propagated plane ($z > 0$). In the waist plane, a discrete optical vortex is truncated in two ways: (a) a single laser is truncated, and (b) compound truncation where all the lasers are equally partially truncated. To quantify the self-healing, we have calculated an overlap integral to analyze similarities between the self-healed and ideal discrete optical vortices. In both cases, when partially truncated discrete optical vortex propagated, as a result of intensity redistribution, the intensity from nearby regions propagates into truncated parts, and accordingly the beam self-heals. The results show that partially truncated discrete vortex can self-heal quite well. The self-healing distance is also found to be dependent on the amount of truncation, particularly, it increases with an increase in the amount of truncation. Further, the simulation results on self-healing properties are also verified experimentally, and we have found a good agreement between them.

These investigations have opened the door for new applications, where conventional continuous optical vortex pose limitations.

In **Chapter 7**, we have presented a novel and efficient characterization method for accurate determination of magnitude and sign of topological charge (l) of an unknown

discrete optical vortex, which is formed by an array of lasers in a 1D ring geometry. Since, the applications of optical vortex are associated with its topological charge, thus accurately determining the magnitude and sign of topological charge is very important. We have presented a simple analytical formulation of working principle of our method. It relies on measuring the interference pattern of a discrete optical vortex, which is obtained by interfering a single selected laser with itself and with all the other lasers in a 1D ring array, using a Mach-Zhender interferometer. The interference pattern is quantified by analyzing the fringe visibility at each laser in a 1D ring array. The discrete laser arrays with $l = 0$ and $l \neq 0$ have different phase distributions, thus producing interference patterns with shifted interference fringes. The averaging of these phase shifted interference patterns gives rise to a variation in the fringe visibility as a function of laser number in the discrete optical vortex, thus enabling the identification of l. The magnitude of l of a discrete optical vortex is found to be proportional to the number of dips observed in the fringe visibility curve.

Further, for an accurate determination of sign of an unknown discrete optical vortex ($l \neq 0$), we have averaged the interference pattern of it with the interference pattern of known discrete optical vortex with $l = +1$. The number of dips in the fringe visibility curve decreases by one for positive values of l, and increases by one for negative values of l. We have also investigated the robustness of our method against the presence of phase disorder that may occur due to aberrations in a system. It is found that the phase disorder does not affect an accurate determination of topological charge of an unknown discrete optical vortex.

We have demonstrated our method for discrete optical vortices with topological charges from small to large values and accurately determined their magnitude and sign. We have obtained an excellent agreement between the numerical and experiment results, indicating that our method is highly efficient. Our method can be useful in applications of discrete optical vortices.

8.2 Future outlook

The present work in this thesis discusses various outer-cavity and intra-cavity methods for generation and characterization of spatially structured light with customized intensity and phase distributions as well as possessing exotic propagation properties. However, the work can be further extended, and some prospective work in this direction may include, for example,

1. In the present thesis only coherent beam shaping is explored, however, an incoherent structured light is required for various applications. Therefore, new efficient methods can be developed for incoherent beam shaping.

2. We have explored the generation of discrete optical vortices with integer topological charges from phase-locked laser arrays in a degenerate cavity. However, optical vortices with fractional topological charges have also emerged as promising structured light that can be exploited for various technological applications. Therefore, the work can be extended to generate high-power discrete vortices with fractional topological charges.

3. Generation of arbitrarily shaped beams with uniform-intensity distribution directly from a degenerate cavity laser.

4. Demonstrations of controlled trapping and guiding the micro-particles based on asymmetric aberration laser beams with controlled intensity distribution.

5. Generation and characterization of vectorial structured light possessing robust propagation properties in a complex media.

6. Probing the phase transitions in soft matter (e.g., synchronization of vinegar eels) using structured light.

7. Generation of arbitrarily shaped output beams from the phase-locked lasers.

Structured light fields are increasingly finding applications in a wide variety of fields. They have shown potential where commonly used Gaussian beams have encountered physical limitations. The results presented in this thesis will contribute in developing novel, simple, cost-effective, and efficient structured light sources as well as characterization tools, with widespread potential applications. Our experimental and theoretical findings will open new possibilities in various fields, such as fundamental research, health, defense, industries, optical communications, optical computing, etc.

List of Publications

1. **Vasu Dev**, Andra N. K. Reddy, and Vishwa Pal, "Generation of uniform-intensity light beams with controllable spatial shapes," *Optics Communications* **475** 126226, (2020).

2. **Vasu Dev**, Andra N. K. Reddy, A.V. Ustinov, S.N. Khonina, and Vishwa Pal, "Auto-focusing and self-healing properties of aberration laser beams in a turbulent media," *Physical Review Applied* **16** 014061, (2021).

3. **Vasu Dev** and Vishwa Pal, "Divergence and self-healing of discrete vortex formed by phase-locked lasers," *Journal of Optical Society of America B* **38** 3683, (2021).

4. **Vasu Dev**, Andra N. K. Reddy, and Vishwa Pal, "Generating high-energy densities by sidelobe suppression in the far-field of phase-locked lasers," *Journal of Optical Society of America B* **39** 2254, (2022).

5. Sachleen Singh, **Vasu Dev**, and Vishwa Pal, "Generating asymmetric aberration laser beams with controlled intensity distribution," *Journal of Optics* **24** 125601, (2022).

6. **Vasu Dev** and Vishwa Pal, "Probing topological charge of discrete vortices," submitted to *Physical Review Applied* (2023).

7. **Vasu Dev** and Vishwa Pal, "Experimental investigation of propagation and self-healing of discrete vortex beams," to be submitted (2023).

8. Anita Kumari, **Vasu Dev** and Vishwa Pal, "Autofocusing and self-healing of partially blocked circular Airy derivative beams," submitted in *Optics and Laser Technology* (2023).

9. Andra Naresh K. Reddy, **Vasu Dev** and Vishwa Pal, "Effect of parabolic apodizer on improving the imaging of optical systems with aberrations," submitted to *Applied Physics B* (2023).

10. Anita Kumari, **Vasu Dev** and Vishwa Pal, "Propagation and self-healing of circular Airy derivative beams in turbulent media,"in preparation (2023).

Conference Proceedings:

1. **Vasu Dev**, Andra N. K. Reddy, and Vishwa Pal, "Design of diffractive optical elements for shaping the laser intensity distribution,"in K. Singh, A. K. Gupta, S. Khare, N. Dixit, K. Pant (eds) International Conference on Optics and Electro-Optics (ICOL-2019), Springer Proceedings in Physics, **258** pp. 89-91 (2021) Springer, Singapore.

2. **Vasu Dev**, Andra N. K. Reddy, A.V. Ustinov, S.N. Khonina, and Vishwa Pal, "Propagation invariant features of aberration laser beams in a turbulent media,"in Frontier in Optics and Laser Science (FiO LS 2021), Washington DC, USA, Technical Digest Series, paper JW7A.120 (2021) (Optica Publishing Group).

3. **Vasu Dev**, and Vishwa Pal, "High-power discrete vortex with phase locked lasers,"in 2022 International Conference Laser Optics (ICLO 2022), Saint Petersburg, Russian Federation, pp. 1-1 (2022) (IEEE Publisher).

4. Sachleen Singh **Vasu Dev**, and Vishwa Pal, "Autofocused asymmetric aberration laser beams,"in 2022 International Conference Laser Optics (ICLO 2022), Saint Petersburg, Russian Federation, pp. 1-1 (2022) (IEEE Publisher).

5. **Vasu Dev** and Vishwa Pal, "Enhanced output power-density by sidelobe suppression of phase-locked lasers,"in Frontiers in Optics + Laser Science (FiO LS 2022), Rochester, USA, Technical Digest Series, paper JTu4A.21 (2022) (Optica Publishing Group).

6. **Vasu Dev**, Andra Naresh K. Reddy and Vishwa Pal, "Aberration laser beams with controlled autofocusing, self-Healing and intensity distribution,"PHOTONICS 2023, Indian Institute of Science Bengaluru, India, July 5-8, 2023. To be appeared in Proceedings of the Springer-2023.

7. **Vasu Dev**, and Vishwa Pal, "High-power orbital angular momentum modes obtained by phase-locking lasers in a 1d ring array,"PHOTONICS-2023, Indian Institute of Science Bengaluru, India, July 5-8, 2023. To be appeared in Proceedings of the Springer-2023.

Conference Presentations:

1. Poster Presentation

   Vasu Dev and Vishwa Pal, "Generation of laser beams with uniform intensity and different spatial shapes,"Research conclave 2019, Indian Institute of Technology Ropar, Punjab, India. 14-15 May 2019.

2. Poster Presentation

   Vasu Dev and Vishwa Pal, "Generation of laser beams with uniform intensity and different spatial shapes,"4th-Physics Day, Department of Physics, Indian Institute of Technology Ropar, Punjab, India. 10 August 2019.

3. Poster Presentation [**Best poster award**]

   Vasu Dev and Vishwa Pal, "Tailoring laser beams with various spatial shapes and uniform intensity,"International symposium on photonics and plasmonics (ISPP-2019), Department of Physics, Central University Rajasthan, Ajmer, Rajasthan, India. 23-24 September 2019.

4. Poster Presentation

   Vasu Dev, Andra N. K. Reddy, and Vishwa Pal, "Design of diffractive optical element for shaping the laser intensity distribution,"International conference on optics and electro-optics (ICOL-2019), XLIII symposium by Optical Society of India, IRDE Dehradun, Uttrakhand, India. 19-22 October 2019.

5. Poster Presentation

   Vasu Dev, Andra Naresh K. Reddy, A.V. Ustinov, S.N. Khonina, and Vishwa

Pal,"Propagation invariant features of ALBs in a turbulent media,"Frontier in Optics + Laser Science (FiO LS 2021), Virtual event, USA. 31 October - 4 November 2021.

6. Poster Presentation

   Vasu Dev and Vishwa Pal, "Generation of discrete vortex with phase-locked lasers," Light-Matter Interactions in Low Dimensional and Topological Photonic Materials, Virtual event, Indian Institute of Science Bangalore, Banglore, India. 27 January – 1 February 2022.

7. Oral Presentation

   Vasu Dev and Vishwa Pal, "High-power discrete vortex with phase locked lasers," 20th International Conference Laser Optics (ICLO 2022), St. Petersburg, Russia. 20-24 June 2022.

8. Oral Presentation

   Sachleen Singh, **Vasu Dev** and Vishwa Pal, "Autofocused asymmetric aberration laser beams,"20th International Conference Laser Optics (ICLO 2022), St. Petersburg, Russia. 20-24 June 2022.

9. Poster Presentation [**Best poster award**]

   Vasu Dev, Andra Naresh K. Reddy, A.V. Ustinov, S.N. Khonina, and Vishwa Pal, "Propagation and Self-healing Properties of Auto-focused Aberration Laser Beams in Turbulent Media," 7th Student Conference on Optics and Photonics (SCOP 2022), Physical Research Laboratory, Ahmedabad, Gujrat, India. 28–30 September 2022.

10. Poster Presentation

    Vasu Dev and Vishwa Pal, "Enhanced output power-density by sidelobe suppression of phase-locked lasers,"Frontier in Optics + Laser Science (FiO LS 2022), USA. 17-20 October 2022.

11. Poster Presentation

    Vasu Dev and Vishwa Pal, "High power tightly focused output beam from phase-locked lasers,"DAE–BRNS National Laser Symposium (NLS–31), Indian Institute of Technology Kharagpur, West Bengal, India. 3-6 December 2022.

12. Poster Presentation

    Sachleen Singh, **Vasu Dev** and Vishwa Pal, "Generation of spatially controlled high-energy density regions with asymmetric aberration laser beams,"DAE–BRNS National Laser Symposium (NLS–31), Indian Institute of Technology Kharagpur, West Bengal, India. 3–6 December 2022.

13. Poster Presentation

    Vasu Dev and Vishwa Pal, "High power tightly focused output beam from phase-locked lasers,"Physics Day 2023, Department of Physics, Indian Institute of Technology Ropar, Punjab, India. 4 March 2023.

14. Accepted for Oral Presentation

    Vasu Dev, Andra Naresh K. Reddy and Vishwa Pal, "Aberration Laser Beams with Controlled Autofocusing, Self-Healing and Intensity Distribution,"Photonics 2023, Indian Institute of Science Bengaluru, Karnataka, India. 5-8 July 2023.

15. Accepted for Oral Presentation

    Vasu Dev and Vishwa Pal, "High-power orbital angular momentum modes obtained by phase-locking lasers in a 1d ring array,"Photonics 2023, Indian Institute of Science Bengaluru, Karnataka, India. 5-8 July 2023.

Invited Talks:

1. **Various aspects of controlled laser beam shaping**
   OPTICA Student Chapter IIT Roorkee, Department of Physics Indian Institute of Technology Roorkee, Roorkee, Uttarakhand, India, 13 April 2023.

References

[1] A. Forbes, M. Oliveira, and M. R. Dennis, "Structured light," *Nature Photonics*, vol. 15, pp. 253–262, 2021.

[2] A. Forbes, "Structured light from lasers," *Laser & Photonics Reviews*, vol. 13, no. 11, p. 1900140, 2019.

[3] L. Hargrove, R. L. Fork, and M. Pollack, "Locking of he–ne laser modes induced by synchronous intracavity modulation," *Applied Physics Letters*, vol. 5, no. 1, pp. 4–5, 1964.

[4] W. Kaiser and D. H. Auston, *Ultrashort laser pulses: generation and applications*. Springer, 1993.

[5] F. M. Dickey and T. E. Lizotte, *Laser beam shaping applications*, vol. 1. CRC Press, 2017.

[6] L. Allen, M. W. Beijersbergen, R. Spreeuw, and J. Woerdman, "Orbital angular momentum of light and the transformation of laguerre-gaussian laser modes," *Physical Review A*, vol. 45, no. 11, p. 8185, 1992.

[7] T. Bell, B. Li, and S. Zhang, "Structured light techniques and applications," *Wiley Encyclopedia of Electrical and Electronics Engineering*, pp. 1–24, 1999.

[8] A. E. Willner, H. Huang, Y. Yan, Y. Ren, N. Ahmed, G. Xie, C. Bao, L. Li, Y. Cao, Z. Zhao, *et al.*, "Optical communications using orbital angular momentum beams," *Advances in Optics and Photonics*, vol. 7, no. 1, pp. 66–106, 2015.

[9] Y. Yang, Y. Ren, M. Chen, Y. Arita, and C. Rosales-Guzmán, "Optical trapping with structured light: a review," *Advanced Photonics*, vol. 3, no. 3, p. 034001, 2021.

[10] P. Kner, B. B. Chhun, E. R. Griffis, L. Winoto, and M. G. Gustafsson, "Super-resolution video microscopy of live cells by structured illumination," *Nature Methods*, vol. 6, no. 5, pp. 339–342, 2009.

[11] M. Duocastella and C. B. Arnold, "Bessel and annular beams for materials processing," *Laser & Photonics Reviews*, vol. 6, no. 5, pp. 607–621, 2012.

[12] M.-J. Tsai and C.-C. Hung, "Development of a high-precision surface metrology system using structured light projection," *Measurement*, vol. 38, no. 3, pp. 236–247, 2005.

[13] X.-L. Wang, X.-D. Cai, Z.-E. Su, M.-C. Chen, D. Wu, L. Li, N.-L. Liu, C.-Y. Lu, and J.-W. Pan, "Quantum teleportation of multiple degrees of freedom of a single photon," *Nature*, vol. 518, no. 7540, pp. 516–519, 2015.

[14] H. Rubinsztein-Dunlop, A. Forbes, M. V. Berry, M. R. Dennis, D. L. Andrews, M. Mansuripur, C. Denz, C. Alpmann, P. Banzer, T. Bauer, E. Karimi, L. Marrucci, M. Padgett, M. Ritsch-Marte, N. M. Litchinitser, N. P. Bigelow, C. Rosales-Guzmán, A. Belmonte, J. P. Torres, T. W. Neely, M. Baker, R. Gordon, A. B. Stilgoe, J. Romero, A. G. White, R. Fickler, A. E. Willner, G. Xie, B. McMorran, and A. M. Weiner, "Roadmap on structured light," *Journal of Optics*, vol. 19, p. 013001, nov 2017.

[15] A. Forbes, "Structured light: tailored for purpose," *Optics and Photonics News*, vol. 31, no. 6, pp. 24–31, 2020.

[16] A. A. Kovalev, V. V. Kotlyar, and A. P. Porfirev, "Optical trapping and moving of microparticles by using asymmetrical laguerre–gaussian beams," *Optics Letters*, vol. 41, no. 11, pp. 2426–2429, 2016.

[17] A. A. Sirenko, P. Marsik, C. Bernhard, T. Stanislavchuk, V. Kiryukhin, and S.-W. Cheong, "Terahertz vortex beam as a spectroscopic probe of magnetic excitations," *Physical Review Letters*, vol. 122, no. 23, p. 237401, 2019.

[18] O. Emile and J. Emile, "Naked eye picometer resolution in a michelson interferometer using conjugated twisted beams," *Optics Letters*, vol. 42, no. 2, pp. 354–357, 2017.

[19] G. Verma and G. Yadav, "Compact picometer-scale interferometer using twisted light," *Optics Letters*, vol. 44, no. 14, pp. 3594–3597, 2019.

[20] G. Verma and K. P. Singh, "Universal long-range nanometric bending of water by light," *Physical Review Letters*, vol. 115, no. 14, p. 143902, 2015.

[21] A. Gatto, M. Tacca, F. Kéfélian, C. Buy, and M. Barsuglia, "Fabry-pérot-michelson interferometer using higher-order laguerre-gauss modes," *Physical Review D*, vol. 90, no. 12, p. 122011, 2014.

[22] S. S. Andrews and J. Tretton, "Physical principles of circular dichroism," *Journal of Chemical Education*, vol. 97, no. 12, pp. 4370–4376, 2020.

[23] C. Rosales-Guzmán, K. Volke-Sepulveda, and J. P. Torres, "Light with enhanced optical chirality," *Optics Letters*, vol. 37, no. 17, pp. 3486–3488, 2012.

[24] M. Pascucci, S. Ganesan, A. Tripathi, O. Katz, V. Emiliani, and M. Guillon, "Compressive three-dimensional super-resolution microscopy with speckle-saturated fluorescence excitation," *Nature Communications*, vol. 10, no. 1, p. 1327, 2019.

[25] D. G. Papazoglou, N. K. Efremidis, D. N. Christodoulides, and S. Tzortzakis, "Observation of abruptly autofocusing waves," *Optics Letters*, vol. 36, no. 10, pp. 1842–1844, 2011.

[26] S. Zhao, W. Zhang, L. Wang, W. Li, L. Gong, W. Cheng, H. Chen, and J. Gruska, "Propagation and self-healing properties of bessel-gaussian beam carrying orbital angular momentum in an underwater environment," *Scientific Reports*, vol. 9, no. 1, p. 2025, 2019.

[27] D. S. Simon, "Bessel beams, self-healing, and diffraction-free propagation," in *A Guided Tour of Light Beams (Second Edition): From lasers to optical knots*, IOP Publishing, 2020.

[28] M. A. Cox, N. Mphuthi, I. Nape, N. Mashaba, L. Cheng, and A. Forbes, "Structured light in turbulence," *IEEE Journal of Selected Topics in Quantum Electronics*, vol. 27, no. 2, pp. 1–21, 2020.

[29] Y. Shen, S. Pidishety, I. M. Nape, and A. Dudley, "Self-healing of structured light: a review," *Journal of Optics*, 2022.

[30] A. Curatolo, P. R. Munro, D. Lorenser, P. Sreekumar, C. C. Singe, B. F. Kennedy, and D. D. Sampson, "Quantifying the influence of bessel beams on image quality in optical coherence tomography," *Scientific Reports*, vol. 6, no. 1, p. 23483, 2016.

[31] A. Mathis, F. Courvoisier, L. Froehly, L. Furfaro, M. Jacquot, P.-A. Lacourt, and J. M. Dudley, "Micromachining along a curve: Femtosecond laser micromachining of curved profiles in diamond and silicon using accelerating beams," *Applied Physics Letters*, vol. 101, no. 7, p. 071110, 2012.

[32] V. Dev, A. N. K. Reddy, and V. Pal, "Generation of uniform-intensity light beams with controllable spatial shapes," *Optics Communications*, vol. 475, p. 126226, 2020.

[33] V. Dev, A. N. K. Reddy, and V. Pal, "Design of diffractive optical elements for shaping the laser intensity distribution," in *ICOL-2019: Proceedings of the International Conference on Optics and Electro-Optics, Dehradun, India*, pp. 89–91, Springer, 2021.

[34] E. Jane, G. Vidal, W. Dur, P. Zoller, and J. I. Cirac, "Simulation of quantum dynamics with quantum optical systems," *Quantum Inf. Comput.*, vol. 3, pp. 15–37, 2003.

[35] M. Takamoto, F.-L. Hong, R. Higashi, and H. Katori, "An optical lattice clock," *Nature*, vol. 435, no. 7040, pp. 321–324, 2005.

[36] W. Boutu, T. Auguste, O. Boyko, I. Sola, P. Balcou, L. Binazon, O. Gobert, H. Merdji, C. Valentin, E. Constant, *et al.*, "High-order-harmonic generation in gas with a flat-top laser beam," *Physical Review A*, vol. 84, no. 6, p. 063406, 2011.

[37] V. Dev, A. N. K. Reddy, A. V. Ustinov, S. N. Khonina, and V. Pal, "Autofocusing and self-healing properties of aberration laser beams in a turbulent media," *Physical Review Applied*, vol. 16, no. 1, p. 014061, 2021.

[38] S. Singh, V. Dev, and V. Pal, "Generating asymmetric aberration laser beams with controlled intensity distribution," *Journal of Optics*, vol. 24, no. 12, p. 125601, 2022.

[39] V. Dev, A. Reddy, A. V. Ustinov, S. Khonina, and V. Pal, "Propagation invariant features of aberration laser beams in a turbulent media," in *Laser Science*, pp. JW7A–120, Optical Society of America, 2021.

[40] S. Singh, V. Dev, and V. Pal, "Autofocused asymmetric aberration laser beams," in *2022 International Conference Laser Optics (ICLO)*, pp. 1–1, IEEE, 2022.

[41] V. Dev, A. N. K. Reddy, and V. Pal, "Generating high-energy densities by sidelobe suppression in the far-field of phase-locked lasers," *Journal of Optical Society of America B*, vol. 39, no. 8, pp. 2254–2263, 2022.

[42] V. Dev, A. Reddy, and V. Pal, "Enhanced output power-density by sidelobe suppression of phase-locked lasers," in *Laser Science*, pp. JTu4A–21, Optica Publishing Group, 2022.

[43] V. Dev and V. Pal, "Divergence and self-healing of a discrete vortex formed by phase-locked lasers," *Journal of Optical Society of America B*, vol. 38, no. 12, pp. 3683–3696, 2021.

[44] V. Dev and V. Pal, "Experimental investigation of propagation and self-healing of discrete vortex beams," *to be submitted*, 2023.

[45] V. Dev and V. Pal, "High-power discrete vortex with phase locked lasers," in *2022 International Conference Laser Optics (ICLO)*, pp. 1–1, IEEE, 2022.

[46] V. Dev and V. Pal, "Probing topological charge of discrete vortices," *arXiv preprint arXiv:2305.08410*, 2023.

[47] V. Pal, C. Tradonsky, R. Chriki, N. Kaplan, A. Brodsky, M. Attia, N. Davidson, and A. A. Friesem, "Generating flat-top beams with extended depth of focus," *Applied Optics*, vol. 57, no. 16, pp. 4583–4589, 2018.

[48] H. Kumar, H. Yao, T. Ei, N. Ashrafi, T. LaFave, S. Ashrafi, D. L. MacFarlane, and R. Henderson, "Physical phaseplate for the generation of a millimeter-wave hermite-gaussian beam," in *2016 IEEE Radio and Wireless Symposium (RWS)*, pp. 234–237, IEEE, 2016.

[49] M. A. Bandres and J. C. Gutiérrez-Vega, "Ince–gaussian beams," *Optics Letters*, vol. 29, no. 2, pp. 144–146, 2004.

[50] N. K. Efremidis, Z. Chen, M. Segev, and D. N. Christodoulides, "Airy beams and accelerating waves: an overview of recent advances," *Optica*, vol. 6, no. 5, pp. 686–701, 2019.

[51] D. McGloin and K. Dholakia, "Bessel beams: diffraction in a new light," *Contemporary Physics*, vol. 46, no. 1, pp. 15–28, 2005.

[52] P. Zhang, Y. Hu, T. Li, D. Cannan, X. Yin, R. Morandotti, Z. Chen, and X. Zhang, "Nonparaxial mathieu and weber accelerating beams," *Physical Review Letters*, vol. 109, no. 19, p. 193901, 2012.

[53] H. Kumar, H. Yao, T. Ei, N. Ashrafi, T. LaFave, S. Ashrafi, D. L. MacFarlane, and R. Henderson, "Physical phaseplate for the generation of a millimeter-wave hermite-gaussian beam," in *2016 IEEE Radio and Wireless Symposium (RWS)*, pp. 234–237, IEEE, 2016.

[54] J. Wen, L. Chen, B. Yu, J. B. Nieder, S. Zhuang, D. Zhang, and D. Lei, "All-dielectric synthetic-phase metasurfaces generating practical airy beams," *ACS nano*, vol. 15, no. 1, pp. 1030–1038, 2021.

[55] Z. Zhang, X. Liang, M. Goutsoulas, D. Li, X. Yang, S. Yin, J. Xu, D. N. Christodoulides, N. K. Efremidis, and Z. Chen, "Robust propagation of pin-like optical beam through atmospheric turbulence," *APL Photonics*, vol. 4, no. 7, p. 076103, 2019.

[56] P. Zhang, J. Prakash, Z. Zhang, M. S. Mills, N. K. Efremidis, D. N. Christodoulides, and Z. Chen, "Trapping and guiding microparticles with morphing autofocusing airy beams," *Optics Letters*, vol. 36, no. 15, pp. 2883–2885, 2011.

[57] S. Rasouli, A. M. Khazaei, and D. Hebri, "Radial carpet beams: a class of non-diffracting, accelerating, and self-healing beams," *Physical Review A*, vol. 97, no. 3, p. 033844, 2018.

[58] A. Porfirev and R. Skidanov, "Generation of an array of optical bottle beams using a superposition of bessel beams," *Applied Optics*, vol. 52, no. 25, pp. 6230–6238, 2013.

[59] L.-G. Wang, L.-Q. Wang, and S.-Y. Zhu, "Formation of optical vortices using coherent laser beam arrays," *Optics Communications*, vol. 282, no. 6, pp. 1088–1094, 2009.

[60] A. Völl, S. Vogt, R. Wester, J. Stollenwerk, and P. Loosen, "Application specific intensity distributions for laser materials processing: Tailoring the induced temperature profile," *Optics and Laser Technology*, vol. 108, pp. 583–591, 2018.

[61] E. Otte and C. Denz, "Optical trapping gets structure: Structured light for advanced optical manipulation," *Applied Physics Reviews*, vol. 7, no. 4, p. 041308, 2020.

[62] S. De Silvestri, P. Laporta, V. Magni, O. Svelto, and B. Majocchi, "Unstable laser resonators with super-gaussian mirrors," *Optics Letters*, vol. 13, no. 3, pp. 201–203, 1988.

[63] F. Gori, "Flattened gaussian beams," *Optics Communications*, vol. 107, no. 5-6, pp. 335–341, 1994.

[64] Y. Li, "New expressions for flat-topped light beams," *Optics communications*, vol. 206, no. 4-6, pp. 225–234, 2002.

[65] R. Borghi, "Elegant laguerregauss beams as a new tool for describing axisymmetric flattened gaussian beams," *Journal of Optical Society of America A*, vol. 18, no. 7, pp. 1627–1633, 2001.

[66] J. A. Hoffnagle and C. M. Jefferson, "Design and performance of a refractive optical system that converts a gaussian to a flattop beam," *Applied Optics*, vol. 39, no. 30, pp. 5488–5499, 2000.

[67] Y. Li, "Light beams with flat-topped profiles," *Optics Letters*, vol. 27, no. 12, pp. 1007–1009, 2002.

[68] Y. Baykal, "Intensity correlations of flat-topped beams in oceanic turbulence," *Journal of Modern Optics*, vol. 67, no. 9, pp. 799–804, 2020.

[69] H. Gerçekcioğlu, A. A. Abbas, and H. H. Göktaş, "Flat-topped gaussian laser beam scintillation in weakly turbulent marine atmospheric medium," *Optics Communications*, vol. 399, pp. 24–27, 2017.

[70] L. Allen and M. Padgett, "The orbital angular momentum of light: An introduction," *Twisted Photons: Applications of Light with Orbital Angular Momentum*, pp. 1–12, 2011.

[71] A. M. Yao and M. J. Padgett, "Orbital angular momentum: origins, behavior and applications," *Advances in Optics and Photonics*, vol. 3, no. 2, pp. 161–204, 2011.

[72] M. J. Padgett, F. M. Miatto, M. P. Lavery, A. Zeilinger, and R. W. Boyd, "Divergence of an orbital-angular-momentum-carrying beam upon propagation," *New Journal of Physics*, vol. 17, no. 2, p. 023011, 2015.

[73] V. Pal, C. Trandonsky, R. Chriki, G. Barach, A. A. Friesem, and N. Davidson, "Phase locking of even and odd number of lasers on a ring geometry: effects of topological-charge," *Opt. Express*, vol. 23, pp. 13041–13050, May 2015.

[74] A. S. Desyatnikov, M. R. Dennis, and A. Ferrando, "All-optical discrete vortex switch," *Phys. Rev. A*, vol. 83, p. 063822, Jun 2011.

[75] V. Pal, C. Tradonsky, R. Chriki, A. A. Friesem, and N. Davidson, "Observing dissipative topological defects with coupled lasers," *Phys. Rev. Lett.*, vol. 119, p. 013902, Jul 2017.

[76] B. E. Saleh and M. C. Teich, *Fundamentals of photonics.* john Wiley & sons, 2019.

[77] F. Gori, G. Guattari, and C. Padovani, "Bessel-gauss beams," *Optics Communications*, vol. 64, no. 6, pp. 491–495, 1987.

[78] G. A. Siviloglou and D. N. Christodoulides, "Accelerating finite energy airy beams," *Optics Letters*, vol. 32, no. 8, pp. 979–981, 2007.

[79] Y. Zhang, H. Zhong, M. R. Belić, and Y. Zhang, "Guided self-accelerating airy beams—a mini-review," *Applied Sciences*, vol. 7, no. 4, p. 341, 2017.

[80] M. Born and E. Wolf, *Principles of optics: electromagnetic theory of propagation, interference and diffraction of light.* Elsevier, 2013.

[81] T. Čižmár, M. Mazilu, and K. Dholakia, "In situ wavefront correction and its application to micromanipulation," *Nature Photonics*, vol. 4, no. 6, pp. 388–394, 2010.

[82] S. T. Thurman, "Phase-error correction in digital holography using single-shot data," *Journal of Optical Society of America A*, vol. 36, no. 12, pp. D47–D61, 2019.

[83] M. Jaffe, L. Palm, C. Baum, L. Taneja, and J. Simon, "Aberrated optical cavities," *Physical Review A*, vol. 104, p. 013524, 2021.

[84] O. Hernandez, M. Guillon, E. Papagiakoumou, and V. Emiliani, "Zero-order suppression for two-photon holographic excitation," *Optics Letters*, vol. 39, no. 20, pp. 5953–5956, 2014.

[85] S. Khonina, A. Ustinov, and E. Pelevina, "Analysis of wave aberration influence on reducing focal spot size in a high-aperture focusing system," *Journal of Optics*, vol. 13, no. 9, p. 095702, 2011.

[86] A. N. K. Reddy, S. N. Khonina, and V. Pal, "Generating autofocused aberration laser beams with different spectral performance," *Journal of Optics*, vol. 22, no. 4, p. 045606, 2020.

[87] J. Ni, C. Wang, C. Zhang, Y. Hu, L. Yang, Z. Lao, B. Xu, J. Li, D. Wu, and J. Chu, "Three-dimensional chiral microstructures fabricated by structured optical vortices in isotropic material," *Light: Science & Applications*, vol. 6, no. 7, pp. e17011–e17011, 2017.

[88] B. Hadad, S. Froim, H. Nagar, T. Admon, Y. Eliezer, Y. Roichman, and A. Bahabad, "Particle trapping and conveying using an optical archimedes' screw," *Optica*, vol. 5, no. 5, pp. 551–556, 2018.

[89] J. A. Rodrigo and T. Alieva, "Freestyle 3d laser traps: tools for studying light-driven particle dynamics and beyond," *Optica*, vol. 2, no. 9, pp. 812–815, 2015.

[90] A. Kuchmizhak, A. Porfirev, S. Syubaev, P. Danilov, A. Ionin, O. Vitrik, Y. N. Kulchin, S. Khonina, and S. Kudryashov, "Multi-beam pulsed-laser patterning of plasmonic films using broadband diffractive optical elements," *Optics Letters*, vol. 42, no. 14, pp. 2838–2841, 2017.

[91] A. Kovalev, V. Kotlyar, and A. Porfirev, "Asymmetric laguerre-gaussian beams," *Physical Review A*, vol. 93, no. 6, p. 063858, 2016.

[92] V. V. Kotlyar, A. A. Kovalev, and E. G. Abramochkin, "Kummer laser beams with a transverse complex shift," *Journal of Optics*, vol. 22, no. 1, p. 015606, 2019.

[93] V. V. Kotlyar, A. A. Kovalev, and A. P. Porfirev, "Asymmetric gaussian optical vortex," *Optics Letters*, vol. 42, no. 1, pp. 139–142, 2017.

[94] V. Kotlyar, A. Kovalev, and V. Soifer, "Asymmetric bessel modes," *Optics Letters*, vol. 39, no. 8, pp. 2395–2398, 2014.

[95] V. Kotlyar, A. Kovalev, R. Skidanov, and V. Soifer, "Asymmetric bessel–gauss beams," *Journal of Optical Society of America A*, vol. 31, no. 9, pp. 1977–1983, 2014.

[96] S. U. Alam, A. S. Rao, A. Ghosh, P. Vaity, and G. Samanta, "Nonlinear frequency doubling characteristics of asymmetric vortices of tunable, broad orbital angular momentum spectrum," *Applied Physics Letters*, vol. 112, no. 17, p. 171102, 2018.

[97] J. M. Auerbach and V. P. Karpenko, "Serrated-aperture apodizers for high-energy laser systems," *Applied Optics*, vol. 33, no. 15, pp. 3179–3183, 1994.

[98] C. Dorrer and J. D. Zuegel, "Design and analysis of binary beam shapers using error diffusion," *Journal of the Optical Society of America B*, vol. 24, no. 6, pp. 1268–1275, 2007.

[99] J. A. Hoffnagle and C. M. Jefferson, "Design and performance of a refractive optical system that converts a gaussian to a flattop beam," *Applied optics*, vol. 39, no. 30, pp. 5488–5499, 2000.

[100] J. A. Hoffnagle and C. M. Jefferson, "Beam shaping with a plano-aspheric lens pair," *Optical Engineering*, vol. 42, no. 11, pp. 3090–3099, 2003.

[101] C. Tradonsky, S. Mahler, G. Cai, V. Pal, R. Chriki, A. A. Friesem, and N. Davidson, "High-resolution digital spatial control of a highly multimode laser," *Optica*, vol. 8, no. 6, pp. 880–884, 2021.

[102] S. Ngcobo, I. Litvin, L. Burger, and A. Forbes, "A digital laser for on-demand laser modes," *Nature Communications*, vol. 4, no. 1, p. 2289, 2013.

[103] J. M. Auerbach and V. P. Karpenko, "Serrated-aperture apodizers for high-energy laser systems," *Applied Optics*, vol. 33, no. 15, pp. 3179–3183, 1994.

[104] C. Dorrer and J. D. Zuegel, "Design and analysis of binary beam shapers using error diffusion," *Journal of Optical Society of America B*, vol. 24, no. 6, pp. 1268–1275, 2007.

[105] H. Urey, "Spot size, depth-of-focus, and diffraction ring intensity formulas for truncated gaussian beams," *Applied Optics*, vol. 43, no. 3, pp. 620–625, 2004.

[106] A. Ruiz De la Cruz, A. Ferrer, J. Del Hoyo, J. Siegel, and J. Solis, "Modeling of astigmatic-elliptical beam shaping during fs-laser waveguide writing including beam truncation and diffraction effects," *Applied Physics A*, vol. 104, pp. 687–693, 2011.

[107] V. Oliker, "Optical design of freeform two-mirror beam-shaping systems," *Journal of Optical Society of America A*, vol. 24, no. 12, pp. 3741–3752, 2007.

[108] H. Kobayashi, K. Nonaka, and M. Kitano, "Helical mode conversion using conical reflector," *Optics Express*, vol. 20, no. 13, pp. 14064–14074, 2012.

[109] A. Forbes, A. du Plessis, and E. G. Rohwer, "Comparison of infrared laser beam shaping by diffractive and refractive methods," in *Laser Beam Shaping VI*, vol. 5876, pp. 138–149, SPIE, 2005.

[110] J. Xin, K. Dai, L. Zhong, Q. Na, and C. Gao, "Generation of optical vortices by using spiral phase plates made of polarization dependent devices," *Optics Letters*, vol. 39, no. 7, pp. 1984–1987, 2014.

[111] G. Liang and Q. Wang, "Controllable conversion between hermite gaussian and laguerre gaussian modes due to cross phase," *Optics Express*, vol. 27, no. 8, pp. 10684–10691, 2019.

[112] F. Cardano, E. Karimi, S. Slussarenko, L. Marrucci, C. de Lisio, and E. Santamato, "Polarization pattern of vector vortex beams generated by q-plates with different topological charges," *Applied Optics*, vol. 51, no. 10, pp. C1–C6, 2012.

[113] A. V. Carpentier, H. Michinel, J. R. Salgueiro, and D. Olivieri, "Making optical vortices with computer-generated holograms," *American Journal of Physics*, vol. 76, no. 10, pp. 916–921, 2008.

[114] C. C. Aleksoff, K. K. Ellis, and B. D. Neagle, "Holographic conversion of a gaussian beam to a near-field uniform beam," *Optical Engineering*, vol. 30, no. 5, pp. 537–543, 1991.

[115] M. Golub, I. Sisakyan, and V. Soifer, "Infra-red radiation focusators," *Optics and lasers in engineering*, vol. 15, no. 5, pp. 297–309, 1991.

[116] O. Bryngdahl, "Geometrical transformations in optics," *Journal of Optical society of America*, vol. 64, no. 8, pp. 1092–1099, 1974.

[117] S. Khonina, V. Kotlyar, R. Skidanov, and V. Soifer, "Levelling the focal spot intensity of the focused gaussian beam," *Journal of Modern Optics*, vol. 47, no. 5, pp. 883–904, 2000.

[118] R. W. Grechberg and W. O. Saxton, "A practical algorithm for the determination of the phase from image and diffraction plane pictures," *Optik*, vol. 35, pp. 237–246, 1972.

[119] D. Wang, B. Jin, Y. Wang, P. Jia, D. Cai, and Y. Gao, "Adaptive flattop beam shaping with a spatial light modulator controlled by the holographic tandem method," *IEEE Photonics Journal*, vol. 8, no. 1, pp. 1–7, 2016.

[120] G.-z. Yang, B.-z. Dong, B.-y. Gu, J.-y. Zhuang, and O. K. Ersoy, "Gerchberg–saxton and yang–gu algorithms for phase retrieval in a nonunitary transform system: a comparison," *Applied Optics*, vol. 33, no. 2, pp. 209–218, 1994.

[121] L. I. Voicu, W. A. Rabadi, and H. R. Myler, "Object support reconstruction from the support of its autocorrelation using multiresolution genetic algorithms," *Optical Engineering*, vol. 36, no. 10, pp. 2820–2827, 1997.

[122] S. Kirkpatrick, C. D. Gelatt Jr, and M. P. Vecchi, "Optimization by simulated annealing," *Science*, vol. 220, no. 4598, pp. 671–680, 1983.

[123] J. Liang, R. N. Kohn Jr, M. F. Becker, and D. J. Heinzen, "1.5% root-mean-square flat-intensity laser beam formed using a binary-amplitude spatial light modulator," *Applied Optics*, vol. 48, no. 10, pp. 1955–1962, 2009.

[124] B. Sephton, A. Dudley, and A. Forbes, "Revealing the radial modes in vortex beams," *Applied Optics*, vol. 55, no. 28, pp. 7830–7835, 2016.

[125] W. Rigrod, "Isolation of axi-symmetrical optical-resonator modes," *Applied Physics Letters*, vol. 2, no. 3, pp. 51–53, 1963.

[126] C. Pare and P.-A. Bélanger, "Custom laser resonators using graded-phase mirrors," *IEEE Journal of Quantum Electronics*, vol. 28, no. 1, pp. 355–362, 1992.

[127] J. R. Leger, D. Chen, and Z. Wang, "Diffractive optical element for mode shaping of a nd: Yag laser," *Optics Letters*, vol. 19, no. 2, pp. 108–110, 1994.

[128] U. D. Zeitner, F. Wyrowski, and H. Zellmer, "External design freedom for optimization of resonator originated beam shaping," *IEEE journal of quantum electronics*, vol. 36, no. 10, pp. 1105–1109, 2000.

[129] A. Kol'chenko, A. Nikitenko, and Y. K. Troitskiĭ, "Control of the structure of transverse laser modes by phase-shifting masks," *Soviet Journal of Quantum Electronics*, vol. 10, no. 8, p. 1013, 1980.

[130] R. Oron, Y. Danziger, N. Davidson, A. A. Friesem, and E. Hasman, "Laser mode discrimination with intra-cavity spiral phase elements," *Optics Communications*, vol. 169, no. 1-6, pp. 115–121, 1999.

[131] V. E. Sherstobitov and A. Y. Rodionov, "Laser resonators with helical optical elements," in *Laser Resonators III*, vol. 3930, pp. 62–73, SPIE, 2000.

[132] I. A. Litvin and A. Forbes, "Intra–cavity flat–top beam generation," *Optics Express*, vol. 17, no. 18, pp. 15891–15903, 2009.

[133] L. Burger, I. Litvin, S. Ngcobo, and A. Forbes, "Implementation of a spatial light modulator for intracavity beam shaping," *Journal of Optics*, vol. 17, no. 1, p. 015604, 2014.

[134] J. Arnaud, "Degenerate optical cavities," *Applied Optics*, vol. 8, no. 1, pp. 189–196, 1969.

[135] M. Nixon, B. Redding, A. Friesem, H. Cao, and N. Davidson, "Efficient method for controlling the spatial coherence of a laser," *Optics Letters*, vol. 38, no. 19, pp. 3858–3861, 2013.

[136] C. Tradonsky, V. Pal, R. Chriki, N. Davidson, and A. A. Friesem, "Talbot diffraction and fourier filtering for phase locking an array of lasers," *Applied Optics*, vol. 56, no. 1, pp. A126–A132, 2017.

[137] S. Mahler, C. Tradonsky, R. Chriki, A. A. Friesem, and N. Davidson, "Coupling of laser arrays with intracavity elements in the far-field," *OSA Continuum*, vol. 2, no. 6, pp. 2077–2084, 2019.

[138] N. Davidson, S. Mahler, A. Friesem, and A. Forbes, "Complex-light lasers," *Optics and Photonics News*, vol. 33, no. 5, pp. 26–33, 2022.

[139] C. Tradonsky, I. Gershenzon, V. Pal, R. Chriki, A. Friesem, O. Raz, and N. Davidson, "Rapid laser solver for the phase retrieval problem," *Science Advances*, vol. 5, no. 10, p. eaax4530, 2019.

[140] V. Pal, S. Mahler, C. Tradonsky, A. A. Friesem, and N. Davidson, "Rapid fair sampling of the x y spin hamiltonian with a laser simulator," *Physical Review Research*, vol. 2, no. 3, p. 033008, 2020.

[141] D. J. Watts and S. H. Strogatz, "Collective dynamics of 'small-world'networks," *Nature*, vol. 393, no. 6684, pp. 440–442, 1998.

[142] P. L. McMahon, A. Marandi, Y. Haribara, R. Hamerly, C. Langrock, S. Tamate, T. Inagaki, H. Takesue, S. Utsunomiya, K. Aihara, *et al.*, "A fully programmable 100-spin coherent ising machine with all-to-all connections," *Science*, vol. 354, no. 6312, pp. 614–617, 2016.

[143] N. Hodgson and H. Weber, *Optical resonators: fundamentals, advanced concepts, applications*, vol. 108. Springer Science & Business Media, 2005.

[144] A. G. Fox and T. Li, "Resonant modes in a maser interferometer," *Bell System Technical Journal*, vol. 40, no. 2, pp. 453–488, 1961.

[145] R. W. Gerchberg, "A practical algorithm for the determination of plane from image and diffraction pictures," *Optik*, vol. 35, no. 2, pp. 237–246, 1972.

[146] A. E. Siegman and H. Miller, "Unstable optical resonator loss calculations using the prony method," *Applied Optics*, vol. 9, no. 12, pp. 2729–2736, 1970.

[147] A. E. Siegman, *Lasers*. University science books, 1986.

[148] D. G. Voelz, *Computational fourier optics: a MATLAB tutorial*. SPIE press Bellingham, WA, 2011.

[149] D. Wang, B. Jin, Y. Wang, P. Jia, D. Cai, and Y. Gao, "Adaptive flattop beam shaping with a spatial light modulator controlled by the holographic tandem method," *IEEE Photonics Journal*, vol. 8, no. 1, pp. 1–7, 2016.

[150] R. Chriki, G. Barach, C. Tradosnky, S. Smartsev, V. Pal, A. A. Friesem, and N. Davidson, "Rapid and efficient formation of propagation invariant shaped laser beams," *Optics Express*, vol. 26, no. 4, pp. 4431–4439, 2018.

[151] A. E. Siegman, "How to (maybe) measure laser beam quality," in *Diode Pumped Solid State Lasers: Applications and Issues*, p. MQ1, Optica Publishing Group, 1998.

[152] J. Pinnell, V. Rodríguez-Fajardo, A. Forbes, S. Chabou, K. Mihoubi, and A. Bencheikh, "Revealing the modal content of obstructed beams," *Physical Review A*, vol. 102, no. 3, p. 033524, 2020.

[153] M. Nixon, M. Fridman, A. Friesem, and N. Davidson, "Enhanced coherence of weakly coupled lasers," *Optics letters*, vol. 36, no. 8, pp. 1320–1322, 2011.

[154] A. Dudley, R. Vasilyeu, V. Belyi, N. Khilo, P. Ropot, and A. Forbes, "Controlling the evolution of nondiffracting speckle by complex amplitude modulation on a phase-only spatial light modulator," *Optics Communications*, vol. 285, no. 1, pp. 5–12, 2012.

[155] V. Arrizón, U. Ruiz, R. Carrada, and L. A. González, "Pixelated phase computer holograms for the accurate encoding of scalar complex fields," *Journal of Optical Society of America A*, vol. 24, pp. 3500–3507, Nov 2007.

[156] T. W. Clark, R. F. Offer, S. Franke-Arnold, A. S. Arnold, and N. Radwell, "Comparison of beam generation techniques using a phase only spatial light modulator," *Optics Express*, vol. 24, no. 6, pp. 6249–6264, 2016.

[157] F. M. Dickey and S. C. Holswade, *Laser beam shaping - Theory and Techniques.* Marcel Dekker, 2000.

[158] J. Li, Z. Kuang, S. Edwardson, W. Perrie, D. Liu, and G. Dearden, "Imaging-based amplitude laser beam shaping for material processing by 2d reflectivity tuning of a spatial light modulator," *Applied Optics*, vol. 55, no. 5, pp. 1095–1100, 2016.

[159] T. Häfner, J. Strauß, C. Roider, J. Heberle, and M. Schmidt, "Tailored laser beam shaping for efficient and accurate microstructuring," *Applied Physics A*, vol. 124, pp. 1–9, 2018.

[160] M. G. Tarallo, J. Miller, J. Agresti, E. D'Ambrosio, R. DeSalvo, D. Forest, B. Lagrange, J. Mackowsky, C. Michel, J. Montorio, *et al.*, "Generation of a flat-top laser beam for gravitational wave detectors by means of a nonspherical fabry-perot resonator," *Applied Optics*, vol. 46, no. 26, pp. 6648–6654, 2007.

[161] M. Takamoto, F.-L. Hong, R. Higashi, and H. Katori, "An optical lattice clock," *Nature*, vol. 435, no. 7040, pp. 321–324, 2005.

[162] A. Turpin, Y. V. Loiko, T. K. Kalkandkiev, H. Tomizawa, and J. Mompart, "Supergaussian conical refraction beam," *Opt. Lett.*, vol. 39, pp. 4349–4352, Aug 2014.

[163] X. Tan, B.-Y. Gu, G.-Z. Yang, and B.-Z. Dong, "Diffractive phase elements for beam shaping: a new design method," *Appl. Opt.*, vol. 34, pp. 1314–1320, Mar 1995.

[164] A. J. Caley, M. J. Thomson, J. Liu, A. J. Waddie, and M. R. Taghizadeh, "Diffractive optical elements for high gain lasers with arbitrary output beam profiles," *Opt. Express*, vol. 15, pp. 10699–10704, Aug 2007.

[165] A. N. K. Reddy and V. Pal, "Robust design of diffractive optical elements for forming flat-top beams with extended depth of focus," *Appl. Phys. B*, vol. 125, p. 231, 2019.

[166] J. Liang, J. Rudolph N. Kohn, M. F. Becker, and D. J. Heinzen, "High-precision laser beam shaping using a binary-amplitude spatial light modulator," *Appl. Opt.*, vol. 49, pp. 1323–1330, Mar 2010.

[167] R. J. Beck, J. P. Parry, W. N. MacPherson, A. Waddie, N. J. Weston, J. D. Shephard, and D. P. Hand, "Application of cooled spatial light modulator for high power nanosecond laser micromachining," *Opt. Express*, vol. 18, pp. 17059–17065, Aug 2010.

[168] D. Liu, Y. Wang, Z. Zhai, Z. Fang, Q. Tao, W. Perrie, S. P. Edwarson, and G. Dearden, "Dynamic laser beam shaping for material processing using hybrid holograms," *Opt. Laser Technol.*, vol. 102, pp. 68 – 73, 2018.

[169] O. Korotkova, "Random sources for rectangular far fields," *Opt. Lett.*, vol. 39, pp. 64–67, Jan 2014.

[170] H. Lajunen and T. Saastamoinen, "Propagation characteristics of partially coherent beams with spatially varying correlations," *Opt. Lett.*, vol. 36, pp. 4104–4106, Oct 2011.

[171] S.-W. Bahk, E. Fess, B. E. Kruschwitz, and J. D. Zuegel, "A high-resolution, adaptive beam-shaping system for high-power lasers," *Opt. Express*, vol. 18, pp. 9151–9163, Apr 2010.

[172] C. Dorrer, "High-damage-threshold beam shaping using binary phase plates," *Opt. Lett.*, vol. 34, pp. 2330–2332, Aug 2009.

[173] S. N. Khonina, A. P. Porfirev, and A. V. Ustinov, "Diffraction patterns withmth order symmetry generated by sectional spiral phase plates," *J. Opt.*, vol. 17, p. 125607, oct 2015.

[174] A. Forbes, F. Dickey, M. DeGama, and A. du Plessis, "Wavelength tunable laser beam shaping," *Opt. Lett.*, vol. 37, pp. 49–51, Jan 2012.

[175] L. Romero and F. Dickey, "Lossless laser beam shaping," *Journal of the Optical Society of America A*, vol. 13, no. 4, pp. 751–760, 1996.

[176] F. M. Dickey and S. C. Holswade, "Gaussian laser beam profile shaping," *Opt. Eng.*, vol. 35, no. 11, pp. 3285–3295, 1996.

[177] J. Jiang, D. Sell, S. Hoyer, J. Hickey, J. Yang, and J. A. Fan, "Free-form diffractive metagrating design based on generative adversarial networks," *ACS Nano*, vol. 13, pp. 8872–8878, 2019.

[178] O. Hemmatyar, S. Abdollahramezani, Y. Kiarashinejad, M. Zandehshahvar, and A. Adibi, "Full color generation with fano-type resonant hfo2 nanopillars designed by a deep-learning approach," *Nanoscale*, vol. 11, pp. 21266–21274, 2019.

[179] R. Chriki, M. Nixon, V. Pal, C. Tradonsky, G. Barach, A. A. Friesem, and N. Davidson, "Manipulating the spatial coherence of a laser source," *Opt. Express*, vol. 23, pp. 12989–12997, May 2015.

[180] J. W. Goodman, *Introduction to Fourier Optics*. Roberts & Company, 2005.

[181] D. P. Kelly, "Numerical calculation of the fresnel transform," *J. Opt. Soc. Am. A*, vol. 31, pp. 755–764, Apr 2014.

[182] D. L. Shealy and J. A. Hoffnagle, "Laser beam shaping profiles and propagation," *Applied Optics*, vol. 45, no. 21, pp. 5118–5131, 2006.

[183] T. Hafner, J. Heberle, D. Holder, and M. Schmidt, "Speckle reduction techniques in holographic beam shaping for accurate and efficient picosecond laser structuring," *J. Laser Appl.*, vol. 29, no. 2, p. 022205, 2017.

[184] C. Hnatovsky, V. Shvedov, W. Krolikowski, and A. Rode, "Revealing local field structure of focused ultrashort pulses," *Phys. Rev. Lett.*, vol. 106, p. 123901, Mar 2011.

[185] J. Amako, K. Nagasaka, and N. Kazuhiro, "Chromatic-distortion compensation in splitting and focusing of femtosecond pulses by use of a pair of diffractive optical elements," *Opt. Lett.*, vol. 27, pp. 969–971, Jun 2002.

[186] A. S. Larkin, D. V. Pushkarev, S. A. Degtyarev, S. N. Khonina, and A. B. Savelev, "Generation of hermite gaussian modes of high-power femtosecond laser radiation using binary-phase diffractive optical elements," *Quantum Electron.*, vol. 46, pp. 733–737, aug 2016.

[187] S. Degtyarev, A. Porfirev, S. Khonina, and S. Karpeev, "Demonstration of vortical beams spectral stability formed in non-zero diffraction orders," *J. Phys.: Conference Series*, vol. 735, p. 012023, aug 2016.

[188] A. E. Siegman, "New developments in laser resonators," in *Optical Resonators* (D. A. Holmes, ed.), vol. 1224, pp. 2 – 14, International Society for Optics and Photonics, SPIE, 1990.

[189] D. Li, D. Bongiovanni, M. Goutsoulas, S. Xia, Z. Zhang, Y. Hu, D. Song, R. Morandotti, N. K. Efremidis, and Z. Chen, "Direct comparison of anti-diffracting optical pin beams and abruptly autofocusing beams," *OSA Continuum*, vol. 3, no. 6, pp. 1525–1535, 2020.

[190] X. Yan, L. Guo, M. Cheng, and J. Li, "Controlling abruptly autofocusing vortex beams to mitigate crosstalk and vortex splitting in free-space optical communication," *Optics Express*, vol. 26, no. 10, pp. 12605–12619, 2018.

[191] M. J. Booth, "Adaptive optical microscopy: the ongoing quest for a perfect image," *Light: Science & Applications*, vol. 3, no. 4, pp. e165–e165, 2014.

[192] A. N. K. Reddy, D. K. Sagar, and S. N. Khonina, "Asymmetric apodization for the comma aberrated point spread function," *Comput. Opt.*, vol. 41, no. 4, pp. 484–488, 2017.

[193] A. N. K. Reddy, M. Hashemi, and S. N. Khonina, "Apodization of two-dimensional pupils with aberrations," *Pramana*, vol. 90, no. 6, p. 77, 2018.

[194] R. Kant, "Superresolution and increased depth of focus: an inverse problem of vector diffraction," *J. Mod. Opt.*, vol. 47, no. 5, pp. 905–916, 2000.

[195] S. N. Khonina, A. V. Ustinov, and S. Chávez-Cerda, "Generalized parabolic nondiffracting beams of two orders," *Journal of Optical Society of America A*, vol. 35, no. 9, pp. 1511–1517, 2018.

[196] J. Serna, F. Encinas-Sanz, and G. Nemes, "Complete spatial characterization of a pulsed doughnut-type beam by use of spherical optics and a cylindrical lens," *Journal of Optical Society of America A*, vol. 18, no. 7, pp. 1726–1733, 2001.

[197] S. Khonina, V. Kotlyar, V. Soifer, K. Jefimovs, P. Pääkkönen, and J. Turunen, "Astigmatic bessel laser beams," *Journal of Modern optics*, vol. 51, no. 5, pp. 677–686, 2004.

[198] A. Dixit, S. K. Mishra, and A. K. Gupta, "Sensitivity of singular beams in the presence of zernike aberrations," *Opt. Lasers Eng.*, vol. 71, pp. 74–84, 2015.

[199] S. Topuzoski and L. Janicijevic, "Diffraction characteristics of optical elements designed as phase layers with cosine-profiled periodicity in the azimuthal direction," *Journal of Optical Society of America A*, vol. 28, no. 12, pp. 2465–2472, 2011.

[200] A. Lagendijk and B. A. Van Tiggelen, "Resonant multiple scattering of light," *Phys. Rep.*, vol. 270, no. 3, pp. 143–215, 1996.

[201] P. Sebbah, *Waves and imaging through complex media*. Springer Science & Business Media, 2001.

[202] T. Schwartz, S. Fishman, and M. Segev, "Localisation of light in disordered lattices," *Electron. Lett.*, vol. 44, no. 3, pp. 165–168, 2008.

[203] K. G. Makris, A. Brandstötter, P. Ambichl, Z. H. Musslimani, and S. Rotter, "Wave propagation through disordered media without backscattering and intensity variations," *Light Sci. Appl.*, vol. 6, no. 9, pp. e17035–e17035, 2017.

[204] L. C. Andrews and R. L. Phillips, "Laser beam propagation through random media," SPIE, 2005.

[205] A. P. Porfirev, M. S. Kirilenko, S. N. Khonina, R. V. Skidanov, and V. A. Soifer, "Study of propagation of vortex beams in aerosol optical medium," *Appl. Opt.*, vol. 56, no. 11, pp. E8–E15, 2017.

[206] W. Lu, X. Sun, H. Chen, S. Liu, and Z. Lin, "Abruptly autofocusing property and optical manipulation of circular airy beams," *Phys. Rev. A*, vol. 99, p. 013817, Jan 2019.

[207] S. N. Khonina, A. V. Ustinov, and A. P. Porfirev, "Aberration laser beams with autofocusing properties," *Applied Optics*, vol. 57, no. 6, pp. 1410–1416, 2018.

[208] V. A. Soifer, O. Korotkova, S. N. Khonina, and E. A. Shchepakina, "Vortex beams in turbulent media," *Comput. Opt.*, vol. 40, no. 5, pp. 605–623, 2016.

[209] M. Alavinejad, B. Ghafary, and F. Kashani, "Analysis of the propagation of flat-topped beam with various beam orders through turbulent atmosphere," *Opt. Lasers Eng.*, vol. 46, no. 1, pp. 1–5, 2008.

[210] S. Khonina, S. Karpeev, and V. Paranin, "A technique for simultaneous detection of individual vortex states of laguerre–gaussian beams transmitted through an aqueous suspension of microparticles," *Opt. Lasers Eng.*, vol. 105, pp. 68–74, 2018.

[211] S. M. Augustine and N. Chetty, "Experimental verification of the turbulent effects on laser beam propagation in space," *Atmósfera*, vol. 27, no. 4, pp. 385–401, 2014.

[212] H. Gamo and A. K. Majumdar, "Atmospheric turbulence chamber for optical transmission experiment: characterization by thermal method," *Appl. Opt.*, vol. 17, no. 23, pp. 3755–3762, 1978.

[213] T. A. Rhoadarmer and J. R. P. Angel, "Low-cost, broadband static phase plate for generating atmosphericlike turbulence," *Appl. Opt.*, vol. 40, no. 18, pp. 2946–2955, 2001.

[214] R. J. Noll, "Zernike polynomials and atmospheric turbulence," *J. Opt. Soc. Am. A*, vol. 66, no. 3, pp. 207–211, 1976.

[215] B. L. McGlamery, "Restoration of turbulence-degraded images," *J. Opt. Soc. Am. A*, vol. 57, no. 3, pp. 293–297, 1967.

[216] R. Lane, A. Glindemann, and J. Dainty, "Simulation of a kolmogorov phase screen," *Waves in Random Media*, vol. 2, pp. 209–224, 1992.

[217] J. Schmidt, "Numerical simulation of optical wave propagation with examples in matlab," SPIE, 2010.

[218] Y. Zhang, D. Ma, Z. Zhou, and X. Yuan, "Research on partially coherent flat-topped vortex hollow beam propagation in turbulent atmosphere," *Appl. Opt.*, vol. 56, no. 10, pp. 2922–2926, 2017.

[219] G. Gbur and R. K. Tyson, "Vortex beam propagation through atmospheric turbulence and topological charge conservation," *J. Opt. Soc. Am. A*, vol. 25, no. 1, pp. 225–230, 2008.

[220] L. Burger, I. A. Litvin, and A. Forbes, "Simulating atmospheric turbulence using a phase-only spatial light modulator," *South African Journal of Science*, vol. 104, no. 3-4, pp. 129–134, 2008.

[221] C. Rosales-Guzmán and A. Forbes, "How to shape light with spatial light modulators," Society of Photo-Optical Instrumentation Engineers (SPIE), 2017.

[222] V. Kotlyar, A. Kovalev, and A. Porfirev, "An optical tweezer in asymmetrical vortex bessel-gaussian beams," *Journal of Applied Physics*, vol. 120, no. 2, p. 023101, 2016.

[223] M. A. Rykov and R. V. Skidanov, "Modifying the laser beam intensity distribution for obtaining improved strength characteristics of anoptical trap," *Applied Optics*, vol. 53, pp. 156–164, Jan 2014.

[224] S. U. Alam, A. S. Rao, A. Ghosh, P. Vaity, and G. Samanta, "Nonlinear frequency doubling characteristics of asymmetric vortices of tunable, broad orbital angular momentum spectrum," *Applied Physics Letters*, vol. 112, no. 17, p. 171102, 2018.

[225] A. N. K. Reddy, S. N. Khonina, and V. Pal, "Generating autofocused aberration laser beams with different spectral performance," *Journal of Optics*, vol. 22, no. 4, p. 045606, 2020.

[226] A. V. Ustinov and S. N. Khonina, "Generalized lens: calculation of distribution on the optical axis," *Computer Optics*, vol. 37, no. 3, pp. 307–315, 2013.

[227] S. Khonina, A. Porfirev, and A. Ustinov, "Sudden autofocusing of superlinear chirp beams," *Journal of Optics*, vol. 20, no. 2, p. 025605, 2018.

[228] N. K. Efremidis and D. N. Christodoulides, "Abruptly autofocusing waves," *Optics Letters*, vol. 35, pp. 4045–4047, Dec 2010.

[229] I. Chremmos, N. K. Efremidis, and D. N. Christodoulides, "Pre-engineered abruptly autofocusing beams," *Optics Letters*, vol. 36, no. 10, pp. 1890–1892, 2011.

[230] S. N. Khonina and A. V. Ustinov, "Analyzing the symmetry properties of a distribution in the focal plane for a focusing element with periodic angle dependence of phase," *Advances in Optical Technologies*, vol. 2012, p. 918298, 2012.

[231] F. Hénault, A. Carlotti, and C. Vérinaud, "Analysis of nulling phase functions suitable to image plane coronagraphy," in *Advances in Optical and Mechanical Technologies for Telescopes and Instrumentation II*, vol. 9912, p. 99126K, International Society for Optics and Photonics, 2016.

[232] D. M. Miles, J. A. McCoy, R. L. McEntaffer, C. M. Eichfeld, G. Lavallee, M. Labella, W. Drawl, B. Liu, C. T. DeRoo, and T. Steiner, "Fabrication and diffraction efficiency of a large-format, replicated x-ray reflection grating," *The Astrophysical Journal*, vol. 869, no. 2, p. 95, 2018.

[233] A. E. Siegman, *Lasers*. University Science Books, 1986.

[234] O. Svelto, D. C. Hanna, *et al.*, *Principles of lasers*, vol. 1. Springer, 2010.

[235] A. E. Siegman, "Defining, measuring, and optimizing laser beam quality," *Laser Resonators and Coherent Optics: Modeling, Technology, and Applications*, vol. 1868, pp. 2–12, 1993.

[236] D. Sabourdy, V. Kermène, A. Desfarges-Berthelemot, L. Lefort, A. Barthélémy, P. Even, and D. Pureur, "Efficient coherent combining of widely tunable fiber lasers," *Optics Express*, vol. 11, no. 2, pp. 87–97, 2003.

[237] B. Liu, Y. Liu, and Y. Braiman, "Coherent addition of high power laser diode array with a v-shape external talbot cavity," *Optics Express*, vol. 16, no. 25, pp. 20935–20942, 2008.

[238] B. Shalaby, V. Kermène, D. Pagnoux, A. Desfarges-Berthelemot, A. Barthélémy, M. Abdou Ahmed, A. Voss, and T. Graf, "Quasi-gaussian beam from a multicore fibre laser by phase locking of supermodes," *Applied Physics B*, vol. 97, no. 3, pp. 599–605, 2009.

[239] A. N. K. Reddy, S. Mahler, A. Goldring, V. Pal, A. A. Friesem, and N. Davidson, "Phase locking of lasers with gaussian coupling," *Optics Express*, vol. 30, no. 2, pp. 1114–1129, 2022.

[240] J. Katz, S. Margalit, and A. Yariv, "Diffraction coupled phase-locked semiconductor laser array," *Applied Physics Letters*, vol. 42, no. 7, pp. 554–556, 1983.

[241] C. J. Corcoran and F. Durville, "Experimental demonstration of a phase-locked laser array using a self-fourier cavity," *Applied Physics Letters*, vol. 86, no. 20, p. 201118, 2005.

[242] S. Mahler, M. L. Goh, C. Tradonsky, A. A. Friesem, and N. Davidson, "Improved phase locking of laser arrays with nonlinear coupling," *Physical Review Letters*, vol. 124, no. 13, p. 133901, 2020.

[243] C. Tradonsky, M. Nixon, E. Ronen, V. Pal, R. Chriki, A. A. Friesem, and N. Davidson, "Conversion of out-of-phase to in-phase order in coupled laser arrays with second harmonics," *Photonics Research*, vol. 3, no. 3, pp. 77–81, 2015.

[244] J. R. Leger, G. J. Swanson, and M. Holz, "Efficient side lobe suppression of laser diode arrays," *Applied Physics Letters*, vol. 50, no. 16, pp. 1044–1046, 1987.

[245] G. J. Swanson, J. R. Leger, and M. Holz, "Aperture filling of phase-locked laser arrays," *Optics Letters*, vol. 12, no. 4, pp. 245–247, 1987.

[246] S. Mori, "Side lobe suppression of a bessel beam for high aspect ratio laser processing," *Precision Engineering*, vol. 39, pp. 79–85, 2015.

[247] G. Di Domenico, G. Ruocco, C. Colosi, E. DelRe, and G. Antonacci, "Cancellation of bessel beam side lobes for high-contrast light sheet microscopy," *Scientific Reports*, vol. 8, no. 1, pp. 1–7, 2018.

[248] Y. Zheng, X. Wang, L. Deng, F. Shen, and X. Li, "Arbitrary phasing technique for two-dimensional coherent laser array based on an active segmented mirror," *Applied Optics*, vol. 50, no. 15, pp. 2239–2245, 2011.

[249] Y. Zhao, J.-C. Zhang, C.-W. Liu, N. Zhuo, S.-Q. Zhai, L.-J. Wang, J.-Q. Liu, S.-M. Liu, F.-Q. Liu, and Z.-G. Wang, "Chirped coupled ridge waveguide quantum cascade laser arrays with stable single-lobe far-field patterns," *Photonics Research*, vol. 6, no. 8, pp. 821–824, 2018.

[250] S. Liu, M. Wang, P. Li, P. Zhang, and J. Zhao, "Abrupt polarization transition of vector autofocusing airy beams," *Optics Letters*, vol. 38, no. 14, pp. 2416–2418, 2013.

[251] A. Yan, L. Liu, E. Dai, J. Sun, and Y. Zhou, "Simultaneous beam combination and aperture filling of coherent laser arrays by conjugate dammann gratings," *Optics Letters*, vol. 35, no. 8, pp. 1251–1253, 2010.

[252] S. Li and Y. Lu, "Coherent beam combination using non-separable phase-controlled dammann grating," *Optics Communications*, vol. 407, pp. 321–326, 2018.

[253] M. Khajavikhan, A. Hoyer-Leitzel, and J. R. Leger, "Efficient conversion of light from sparse laser arrays into single-lobed far field using phase structures," *Optics Letters*, vol. 33, no. 20, pp. 2377–2379, 2008.

[254] A. Lapucci, F. Quercioli, and D. Jafrancesco, "Optimal phase filtering for high-power laser array far-field distribution," *Optics Letters*, vol. 18, no. 20, pp. 1694–1696, 1993.

[255] J. Abeles and R. Deri, "Suppression of sidelobes in the far-field radiation patterns of optical waveguide arrays," *Applied Physics Letters*, vol. 53, no. 15, pp. 1375–1377, 1988.

[256] L. Fabiny, P. Colet, R. Roy, and D. Lenstra, "Coherence and phase dynamics of spatially coupled solid-state lasers," *Phys. Rev. A*, vol. 47, pp. 4287–4296, May 1993.

[257] S. Mahler, A. A. Friesem, and N. Davidson, "Experimental demonstration of crowd synchrony and first-order transition with lasers," *Physical Review Research*, vol. 2, no. 4, p. 043220, 2020.

[258] J. Hamazaki, R. Morita, K. Chujo, Y. Kobayashi, S. Tanda, and T. Omatsu, "Optical-vortex laser ablation," *Optics Express*, vol. 18, no. 3, pp. 2144–2151, 2010.

[259] J. Fan, E. Parra, I. Alexeev, K. Kim, H. Milchberg, L. Y. Margolin, and L. Pyatnitskii, "Tubular plasma generation with a high-power hollow bessel beam," *Physical Review E*, vol. 62, no. 6, p. R7603, 2000.

[260] D. Shen and D. Zhao, "Measuring the topological charge of optical vortices with a twisting phase," *Optics Letters*, vol. 44, no. 9, pp. 2334–2337, 2019.

[261] J. Durnin, J. Miceli, and J. H. Eberly, "Comparison of bessel and gaussian beams," *Optics Letters*, vol. 13, no. 2, pp. 79–80, 1988.

[262] T. Cookson, K. Kalinin, H. Sigurdsson, J. D. Töpfer, S. Alyatkin, M. Silva, W. Langbein, N. G. Berloff, and P. G. Lagoudakis, "Geometric frustration in polygons of polariton condensates creating vortices of varying topological charge," *Nature Communications*, vol. 12, no. 1, pp. 1–11, 2021.

[263] D. N. Neshev, T. J. Alexander, E. A. Ostrovskaya, Y. S. Kivshar, H. Martin, I. Makasyuk, and Z. Chen, "Observation of discrete vortex solitons in optically induced photonic lattices," *Physical Review Letters*, vol. 92, no. 12, p. 123903, 2004.

[264] B. Malomed and P. Kevrekidis, "Discrete vortex solitons," *Physical Review E*, vol. 64, no. 2, p. 026601, 2001.

[265] J. W. Fleischer, G. Bartal, O. Cohen, O. Manela, M. Segev, J. Hudock, and D. N. Christodoulides, "Observation of vortex-ring "discrete" solitons in 2d photonic lattices," *Physical Review Letters*, vol. 92, no. 12, p. 123904, 2004.

[266] K. J. Law, P. Kevrekidis, T. J. Alexander, W. Królikowski, and Y. S. Kivshar, "Stable higher-charge discrete vortices in hexagonal optical lattices," *Physical Review A*, vol. 79, no. 2, p. 025801, 2009.

[267] M. S. Petrović, S. Prvanović, and D. M. Jović, "Soliton with different topological charges," *Physical Review A*, vol. 79, no. 2, p. 021803, 2009.

[268] S. Tamate, Y. Yamamoto, A. Marandi, P. McMahon, and S. Utsunomiya, "Simulating the classical xy model with a laser network," *arXiv preprint arXiv:1608.00358*, 2016.

[269] C. Alexeyev, A. Volyar, and M. Yavorsky, "Linear azimuthons in circular fiber arrays and optical angular momentum of discrete optical vortices," *Physical Review A*, vol. 80, no. 6, p. 063821, 2009.

[270] X. Chu, Q. Sun, J. Wang, P. Lü, W. Xie, and X. Xu, "Generating a bessel-gaussian beam for the application in optical engineering," *Scientific Reports*, vol. 5, no. 1, pp. 1–8, 2015.

[271] Y. Ma, X. Wang, J. Leng, H. Xiao, X. Dong, J. Zhu, W. Du, P. Zhou, X. Xu, L. Si, *et al.*, "Coherent beam combination of 1.08 kw fiber amplifier array using single frequency dithering technique," *Optics Letters*, vol. 36, no. 6, pp. 951–953, 2011.

[272] D. Zhi, T. Hou, P. Ma, Y. Ma, P. Zhou, R. Tao, X. Wang, and L. Si, "Comprehensive investigation on producing high-power orbital angular momentum beams by coherent combining technology," *High Power Laser Science and Engineering*, vol. 7, p. e33, 2019.

[273] T. Hou, Y. Zhang, Q. Chang, P. Ma, R. Su, J. Wu, Y. Ma, and P. Zhou, "High-power vortex beam generation enabled by a phased beam array fed at the nonfocal-plane," *Optics Express*, vol. 27, no. 4, pp. 4046–4059, 2019.

[274] L.-G. Wang and W.-W. Zheng, "The effect of atmospheric turbulence on the propagation properties of optical vortices formed by using coherent laser beam arrays," *Journal of Optics A: Pure and Applied Optics*, vol. 11, p. 065703, mar 2009.

[275] B. Lü and H. Ma, "Beam propagation properties of radial laser arrays," *Journal of Optical Society of America A*, vol. 17, no. 11, pp. 2005–2009, 2000.

[276] M. J. Padgett, F. M. Miatto, M. P. Lavery, A. Zeilinger, and R. W. Boyd, "Divergence of an orbital-angular-momentum-carrying beam upon propagation," *New Journal of Physics*, vol. 17, no. 2, p. 023011, 2015.

[277] S. Orlov, K. Regelskis, V. Smilgevičius, and A. Stabinis, "Propagation of bessel beams carrying optical vortices," *Optics Communications*, vol. 209, no. 1-3, pp. 155–165, 2002.

[278] S. Mahler, V. Pal, C. Tradonsky, R. Chriki, A. A. Friesem, and N. Davidson, "Dynamics of dissipative topological defects in coupled phase oscillators," *Journal of Physics B: Atomic, Molecular and Optical Physics*, vol. 52, no. 20, p. 205401, 2019.

[279] D. Christodoulides and R. Joseph, "Discrete self-focusing in nonlinear arrays of coupled waveguides," *Optics Letters*, vol. 13, no. 9, pp. 794–796, 1988.

[280] J. C. Eilbeck, P. Lomdahl, and A. C. Scott, "The discrete self-trapping equation," *Physica D: Nonlinear Phenomena*, vol. 16, no. 3, pp. 318–338, 1985.

[281] S. H. Tao and X. Yuan, "Self-reconstruction property of fractional bessel beams," *Journal of Optical Society of America A*, vol. 21, no. 7, pp. 1192–1197, 2004.

[282] X. Chu, "Analytical study on the self-healing property of bessel beam," *The European Physical Journal D*, vol. 66, no. 10, pp. 1–5, 2012.

[283] J. Broky, G. A. Siviloglou, A. Dogariu, and D. N. Christodoulides, "Self-healing properties of optical airy beams," *Optics Express*, vol. 16, no. 17, pp. 12880–12891, 2008.

[284] D. Hebri and S. Rasouli, "Combined half-integer bessel-like beams: a set of solutions of the wave equation," *Physical Review A*, vol. 98, no. 4, p. 043826, 2018.

[285] S. Chabou, A. Bencheikh, J. Pinnell, V. Rodríguez-Fajardo, and A. Forbes, "Do laguerre–gaussian beams recover their spatial properties after all obstacles?," *Applied Physics B*, vol. 126, no. 11, p. 190, 2020.

[286] D. Aguirre-Olivas, G. Mellado-Villaseñor, V. Arrizón, and S. Chávez-Cerda, "Self-healing of hermite-gauss and ince-gauss beams," in *Laser Beam Shaping XVI*, vol. 9581, p. 958105, International Society for Optics and Photonics, 2015.

[287] R. Chen, X. Zhang, Y. Zhou, H. Ming, A. Wang, and Q. Zhan, "Detecting the topological charge of optical vortex beams using a sectorial screen," *Applied Optics*, vol. 56, no. 16, pp. 4868–4872, 2017.

[288] M. Padgett, "Light's twist," *Proceedings of the Royal Society A: Mathematical, Physical and Engineering Sciences*, vol. 470, no. 2172, p. 20140633, 2014.

[289] A. Bekshaev and M. Soskin, "Rotational transformations and transverse energy flow in paraxial light beams: linear azimuthons," *Optics Letters*, vol. 31, no. 14, pp. 2199–2201, 2006.

[290] P. Srinivas, C. Perumangatt, N. Lal, R. Singh, and B. Srinivasan, "Investigation of propagation dynamics of truncated vector vortex beams," *Optics Letters*, vol. 43, no. 11, pp. 2579–2582, 2018.

[291] Q. S. Ferreira, A. J. Jesus-Silva, E. J. S. Fonseca, and J. M. Hickmann, "Fraunhofer diffraction of light with orbital angular momentum by a slit," *Opt. Lett.*, vol. 36, pp. 3106–3108, Aug 2011.

[292] J. P. C. Narag and N. Hermosa, "Probing higher orbital angular momentum of laguerre-gaussian beams via diffraction through a translated single slit," *Phys. Rev. Appl.*, vol. 11, p. 054025, May 2019.

[293] M. P. J. Lavery, A. Dudley, A. Forbes, J. Courtial, and M. J. Padgett, "Robust interferometer for the routing of light beams carrying orbital angular momentum," *New Journal of Physics*, vol. 13, p. 093014, sep 2011.

[294] P. Kumar, N. K. Nishchal, T. Omatsu, and A. S. Rao, "Self-referenced interferometry for single-shot detection of vector-vortex beams," *Sci. Rep.*, vol. 12, p. 17253, 2022.

[295] J. Ma, P. Li, Z. Zhou, and Y. Gu, "Characteristics of fork-shaped fringes formed by off-axis interference of two vortex beams," *Journal of Optical Society of America A*, vol. 38, pp. 115–123, Jan 2021.

[296] S. Cui, B. Xu, S. Luo, H. Xu, Z. Cai, Z. Luo, J. Pu, and S. Chávez-Cerda, "Determining topological charge based on an improved fizeau interferometer," *Optics Express*, vol. 27, pp. 12774–12779, Apr 2019.

[297] S. Slussarenko, V. D'Ambrosio, B. Piccirillo, L. Marrucci, and E. Santamato, "The polarizing sagnac interferometer: a tool for light orbital angular momentum sorting and spin-orbit photon processing," *Optics Express*, vol. 18, pp. 27205–27216, Dec 2010.

[298] H. I. Sztul and R. R. Alfano, "Double-slit interference with laguerre-gaussian beams," *Optics Letters*, vol. 31, pp. 999–1001, Apr 2006.

[299] Q. Zhao, M. Dong, Y. Bai, and Y. Yang, "Measuring high orbital angular momentum of vortex beams with an improved multipoint interferometer," *Photonics Research*, vol. 8, pp. 745–749, May 2020.

[300] P. Panthong, S. Srisuphaphon, S. Chiangga, and S. Deachapunya, "High-contrast optical vortex detection using the talbot effect," *Applied Optics*, vol. 57, pp. 1657–1661, Mar 2018.

[301] C.-S. Guo, L.-L. Lu, and H.-T. Wang, "Characterizing topological charge of optical vortices by using an annular aperture," *Optics Letters*, vol. 34, pp. 3686–3688, Dec 2009.

[302] L. E. E. de Araujo and M. E. Anderson, "Measuring vortex charge with a triangular aperture," *Optics Letters*, vol. 36, pp. 787–789, Mar 2011.

[303] C.-S. Guo, S.-J. Yue, and G.-X. Wei, "Measuring the orbital angular momentum of optical vortices using a multipinhole plate," *Applied Physics Letters*, vol. 94, no. 23, p. 231104, 2009.

[304] S. Zheng and J. Wang, "Measuring orbital angular momentum (oam) states of vortex beams with annular gratings," *Scientific Reports*, vol. 7, no. 1, p. 40781, 2017.

[305] Y. Guo, S. Zhang, M. Pu, Q. He, J. Jin, M. Xu, Y. Zhang, P. Gao, and X. Luo, "Spin-decoupled metasurface for simultaneous detection of spin and orbital angular momenta via momentum transformation," *Light: Science & Applications*, vol. 10, no. 1, p. 63, 2021.

[306] Y. Wen, I. Chremmos, Y. Chen, J. Zhu, Y. Zhang, and S. Yu, "Spiral transformation for high-resolution and efficient sorting of optical vortex modes," *Physical Review Letters*, vol. 120, p. 193904, May 2018.

[307] N. K. Fontaine, R. Ryf, H. Chen, D. T. Neilson, K. Kim, and J. Carpenter, "Laguerre-gaussian mode sorter," *Nature Communications*, vol. 10, no. 1, p. 1865, 2019.

[308] J. Zhou, W. Zhang, and L. Chen, "Experimental detection of high-order or fractional orbital angular momentum of light based on a robust mode converter," *Applied Physics Letters*, vol. 108, no. 11, p. 111108, 2016.

[309] H.-L. Zhou, D.-Z. Fu, J.-J. Dong, P. Zhang, D.-X. Chen, X.-L. Cai, F.-L. Li, and X.-L. Zhang, "Orbital angular momentum complex spectrum analyzer for vortex light based on the rotational doppler effect," *Light: Science & Applications*, vol. 6, no. 4, p. e16251, 2017.

[310] J. Zhurun, L. Wenjing, K. Sergiy, F. Xiaopeng, Z. Zhifeng, P. Anlian, F. Liang, D. Albert, and A. Ritesh, "Photocurrent detection of the orbital angular momentum of light," *Science*, vol. 368, no. 6492, p. 763, 2020.

[311] X. Hu, Z. Gezhi, O. Sasaki, Z. Chen, and J. Pu, "Topological charge measurement of vortex beams by phase-shifting digital hologram technology," *Applied Optics*, vol. 57, pp. 10300–10304, Dec 2018.

[312] M. Chen, F. S. Roux, and J. C. Olivier, "Detection of phase singularities with a shack-hartmann wavefront sensor," *Journal of Optical Society of America A*, vol. 24, pp. 1994–2002, Jul 2007.

[313] B. E. A. Saleh and M. C. Teich, *Fundamental of Photonics*. John Wiley & Sons, Hoboken, New Jersey, USA, second ed., 2007.

[314] R. Hamerly, K. Inaba, T. Inagaki, H. Takesue, Y. Yamamoto, and H. Mabuchi, "Topological defect formation in 1d and 2d spin chains realized by network of optical parametric oscillators," *International Journal of Modern Physics B*, vol. 30, no. 25, p. 1630014, 2016.

[315] J. Gourlay, S. Samus, P. McOwan, D. Vass, I. Underwood, and M. Worboys, "Real-time binary phase holograms on a reflective ferroelectric liquid-crystal spatial light modulator," *Applied Optics*, vol. 33, no. 35, pp. 8251–8254, 1994.

[316] J. A. Davis, K. O. Valadéz, and D. M. Cottrell, "Encoding amplitude and phase information onto a binary phase-only spatial light modulator," *Applied optics*, vol. 42, no. 11, 2003.

[317] D. Dantsker and S. Speiser, "Utilization of photoreversible optical nonlinearities in trans-cis photochromic molecules for spatial light modulation," *Applied Physics B*, vol. 58, pp. 97–104, 1994.

[318] H. M. Robert, K. Holanová, Ł. Bujak, M. Vala, V. Henrichs, Z. Lánský, and M. Piliarik, "Fast photothermal spatial light modulation for quantitative phase imaging at the nanoscale," *Nature Communications*, vol. 12, no. 1, p. 2921, 2021.

[319] F. M. Dickey, *Laser beam shaping: theory and techniques*. CRC press, 2018.

[320] J. C. Gutierrez-Vega, R. M. Rodriguez-Dagnino, M. D. I. Castillo, and S. Chavez-Cerda, "New class of nondiffracting beams: Mathieu beams," in *Optical Pulse and Beam Propagation III*, vol. 4271, pp. 73–80, SPIE, 2001.

[321] S. N. Khonina, A. V. Ustinov, and S. Chávez-Cerda, "Generalized parabolic non-diffracting beams of two orders," *Journal of the Optical Society of America A*, vol. 35, no. 9, pp. 1511–1517, 2018.

[322] J. Serna, F. Encinas-Sanz, and G. Nemes, "Complete spatial characterization of a pulsed doughnut-type beam by use of spherical optics and a cylindrical lens," *Journal of the Optical Society of America A*, vol. 18, no. 7, pp. 1726–1733, 2001.

[323] S. Khonina, V. Kotlyar, V. Soifer, K. Jefimovs, P. Pääkkönen, and J. Turunen, "Astigmatic bessel laser beams," *Journal of Modern Optics*, vol. 51, no. 5, pp. 677–686, 2004.

[324] M. A. Rykov and R. V. Skidanov, "Modifying the laser beam intensity distribution for obtaining improved strength characteristics of an optical trap," *Applied optics*, vol. 53, no. 2, pp. 156–164, 2014.

[325] V. V. Kotlyar, A. A. Kovalev, and A. G. Nalimov, *Topological charge of optical vortices*. CRC Press, 2022.

[326] J. R. Leger, D. Chen, and K. Dai, "High modal discrimination in a nd: Yag laser resonator with internal phase gratings," *Optics Letters*, vol. 19, no. 23, pp. 1976–1978, 1994.

[327] C. He, Y. Shen, and A. Forbes, "Towards higher-dimensional structured light," *Light: Science & Applications*, vol. 11, no. 1, p. 205, 2022.

[328] T. Mairnan, "Stimulated optical radiation in ruby," *Nature*, vol. 4736, pp. 493–494, 1960.

[329] A. L. Schawlow and C. H. Townes, "Infrared and optical masers," *Physical Review*, vol. 112, no. 6, p. 1940, 1958.

[330] M. G. Gustafsson, "Surpassing the lateral resolution limit by a factor of two using structured illumination microscopy," *Journal of microscopy*, vol. 198, no. 2, pp. 82–87, 2000.

[331] C. Rosales-Guzmán, N. Hermosa, A. Belmonte, and J. P. Torres, "Experimental detection of transverse particle movement with structured light," *Scientific Reports*, vol. 3, no. 1, p. 2815, 2013.

[332] N. Hermosa, C. Rosales-Guzmán, S. Pereira, and J. Torres, "Nanostep height measurement via spatial mode projection," *Optics Letters*, vol. 39, no. 2, pp. 299–302, 2014.

[333] D. G. Grier, "A revolution in optical manipulation," *Nature*, vol. 424, no. 6950, pp. 810–816, 2003.

[334] N. K. Langford, R. B. Dalton, M. D. Harvey, J. L. O'Brien, G. J. Pryde, A. Gilchrist, S. D. Bartlett, and A. G. White, "Measuring entangled qutrits and their use for quantum bit commitment," *Physical Review Letters*, vol. 93, no. 5, p. 053601, 2004.

[335] W. T. Buono and A. Forbes, "Nonlinear optics with structured light," *Opto-Electronic Advances*, vol. 5, no. 6, pp. 210174–1, 2022.

[336] G. Steinmeyer, "A review of ultrafast optics and optoelectronics," *Journal of Optics A: Pure and Applied Optics*, vol. 5, no. 1, p. R1, 2002.

[337] J. Berthelot, S. S. Aćimović, M. L. Juan, M. P. Kreuzer, J. Renger, and R. Quidant, "Three-dimensional manipulation with scanning near-field optical nanotweezers," *Nature Nanotechnology*, vol. 9, no. 4, pp. 295–299, 2014.

[338] A. Belmonte, C. Rosales-Guzmán, and J. P. Torres, "Measurement of flow vorticity with helical beams of light," *Optica*, vol. 2, no. 11, pp. 1002–1005, 2015.

[339] H. He, N. Heckenberg, and H. Rubinsztein-Dunlop, "Optical particle trapping with higher-order doughnut beams produced using high efficiency computer generated holograms," *Journal of Modern Optics*, vol. 42, no. 1, pp. 217–223, 1995.

[340] V. Loriot, G. Gitzinger, and N. Forget, "Self-referenced characterization of femtosecond laser pulses by chirp scan," *Optics Express*, vol. 21, no. 21, pp. 24879–24893, 2013.

[341] M. Malinauskas, A. Žukauskas, S. Hasegawa, Y. Hayasaki, V. Mizeikis, R. Buividas, and S. Juodkazis, "Ultrafast laser processing of materials: from science to industry," *Light: Science & Applications*, vol. 5, no. 8, pp. e16133–e16133, 2016.

[342] M. Trippenbach, T. Scott, and Y. Band, "Near-field and far-field propagation of beams and pulses in dispersive media," *Optics Letters*, vol. 22, no. 9, pp. 579–581, 1997.

[343] S. L. Shapiro and D. H. Auston, *Ultrashort light pulses: picosecond techniques and applications*. Springer, 1977.

[344] H. Li, X. Gong, H. Ni, P. Lu, X. Luo, J. Wen, Y. Yang, X. Qian, Z. Sun, and J. Wu, "Light-induced ultrafast molecular dynamics: From photochemistry to optochemistry," *The Journal of Physical Chemistry Letters*, vol. 13, no. 25, pp. 5881–5893, 2022.

[345] L. Jiang, A.-D. Wang, B. Li, T.-H. Cui, and Y.-F. Lu, "Electrons dynamics control by shaping femtosecond laser pulses in micro/nanofabrication: modeling, method, measurement and application," *Light: Science & Applications*, vol. 7, no. 2, pp. 17134–17134, 2018.

[346] C. Yin, S. Zhang, Y. Dong, Q. Ye, and Q. Li, "Molecular-dynamics study of multipulsed ultrafast laser interaction with copper," *Advances in Production Engineering & Management*, vol. 16, no. 4, pp. 457–472, 2021.

[347] A. M. Weiner, J. P. Heritage, and J. A. Salehi, "Encoding and decoding of femtosecond pulses," *Optics Letters*, vol. 13, no. 4, pp. 300–302, 1988.

[348] O. Wada, "Femtosecond all-optical devices for ultrafast communication and signal processing," *New Journal of Physics*, vol. 6, no. 1, p. 183, 2004.

[349] K. Singh, N. Tabebordbar, A. Forbes, and A. Dudley, "Digital stokes polarimetry and its application to structured light: tutorial," *Journal of the Optical Society of America A*, vol. 37, no. 11, pp. C33–C44, 2020.

[350] K. Sugioka and Y. Cheng, "Ultrafast lasers—reliable tools for advanced materials processing," *Light: Science & Applications*, vol. 3, no. 4, pp. e149–e149, 2014.

[351] S. Sogomonian, S. Klewitz, and S. Herminghaus, "Self-reconstruction of a bessel beam in a nonlinear medium," *Optics Communications*, vol. 139, no. 4-6, pp. 313–319, 1997.

[352] S. Li and J. Wang, "Adaptive free-space optical communications through turbulence using self-healing bessel beams," *Scientific Reports*, vol. 7, no. 1, p. 43233, 2017.

[353] F. O. Fahrbach and A. Rohrbach, "Propagation stability of self-reconstructing bessel beams enables contrast-enhanced imaging in thick media," *Nature Communications*, vol. 3, no. 1, p. 632, 2012.

[354] J. Arlt, V. Garcés-Chávez, W. Sibbett, and K. Dholakia, "Optical micromanipulation using a bessel light beam," *Optics Communications*, vol. 197, no. 4-6, pp. 239–245, 2001.

[355] I. Nape, E. Otte, A. Vallés, C. Rosales-Guzmán, F. Cardano, C. Denz, and A. Forbes, "Self-healing high-dimensional quantum key distribution using hybrid spin-orbit bessel states," *Optics Express*, vol. 26, no. 21, pp. 26946–26960, 2018.

[356] J. Park, S. Hong, Y. S. Lee, H. Lee, S. Kim, K. Dholakia, and K. Oh, "Optical manipulation of a dielectric particle along polygonal closed-loop geometries within a single water droplet," *Scientific Reports*, vol. 11, no. 1, p. 12690, 2021.

[357] F. Courvoisier, P.-A. Lacourt, M. Jacquot, M. Bhuyan, L. Furfaro, and J. Dudley, "Surface nanoprocessing with nondiffracting femtosecond bessel beams," *Optics Letters*, vol. 34, no. 20, pp. 3163–3165, 2009.

[358] J.-y. Lu, X.-L. Xu, H. Zou, and J. F. Greenleaf, "Application of bessel beam for doppler velocity estimation," *IEEE transactions on ultrasonics, ferroelectrics, and frequency control*, vol. 42, no. 4, pp. 649–662, 1995.

[359] P. Senthilkumaran, *Singularities in Physics and Engineering*. 2053-2563, IOP Publishing, 2018.

[360] J. Zhang, M. Yu, Z. Li, Y. Liu, Q. Zhang, R. Jiang, and S. Sun, "The effect of laser energy density on the microstructure, residual stress and phase composition of h13 steel treated by laser surface melting," *Journal of Alloys and Compounds*, vol. 856, p. 158168, 2021.

[361] J. Wang, B. Gu, Y. Xu, and H. Wang, "Enhanced sensitivity of z-scan technique by use of flat-topped beam," *Applied Physics B*, vol. 95, pp. 773–778, 2009.

[362] Y. Deng, X. Ji, H. Yu, X. Li, H. Wang, and L. Chen, "Uniform irradiation generated by beam self-focusing in the inhomogeneous atmosphere," *Optics Express*, vol. 27, no. 10, pp. 14585–14593, 2019.

[363] Z. Hu, D. Jiang, X. Liu, B. Zhu, Q. Zeng, and K. Qin, "Performance research on flat-topped beam-based small satellites free space optical communication," *Optics Communications*, vol. 487, p. 126802, 2021.

[364] M. G. Tarallo, J. Miller, J. Agresti, E. D'Ambrosio, R. DeSalvo, D. Forest, B. Lagrange, J. Mackowsky, C. Michel, J. Montorio, *et al.*, "Generation of a flat-top laser beam for gravitational wave detectors by means of a nonspherical fabry-perot resonator," *Applied Optics*, vol. 46, no. 26, pp. 6648–6654, 2007.

[365] Y. Zheng, W. Tan, D. Han, K. Ren, Y. Wang, F. Zhao, and J. Si, "Propagation of high-power optical flat-topped beams in strongly nonlinear media," *Results in Physics*, vol. 31, p. 105016, 2021.

[366] A. Parent, M. Morin, and P. Lavigne, "Propagation of super-gaussian field distributions," *Optical and Quantum Electronics*, vol. 24, pp. S1071–S1079, 1992.

[367] K. Guo, J. Xie, G. Chen, Y. Wu, Y. Liang, S. Hong, F. Ye, J. Zhang, and D. Deng, "Abruptly autofocusing properties of the chirped circular airy gaussian vortex beams," *Optics Communications*, vol. 477, p. 126369, 2020.

[368] M. A. Bandres, "Elegant ince–gaussian beams," *Optics Letters*, vol. 29, no. 15, pp. 1724–1726, 2004.

[369] Y. Zhang, X. Liu, M. R. Belić, W. Zhong, F. Wen, and Y. Zhang, "Anharmonic propagation of two-dimensional beams carrying orbital angular momentum in a harmonic potential," *Optics Letters*, vol. 40, no. 16, pp. 3786–3789, 2015.

[370] T. Pearcey, "The structure of an electromagnetic field in the neighbourhood of a cusp of a caustic (from philosophical magazine 1946)," *Spie Milestone Series Ms*, vol. 89, pp. 432–432, 1993.

[371] I. Chremmos, P. Zhang, J. Prakash, N. K. Efremidis, D. N. Christodoulides, and Z. Chen, "Fourier-space generation of abruptly autofocusing beams and optical bottle beams," *Optics Letters*, vol. 36, no. 18, pp. 3675–3677, 2011.

[372] T.-C. Poon and T. Kim, *Engineering optics with Matlab®*. World Scientific, 2006.

[373] C. Sun, D. Deng, X. Yang, and G. Wang, "Propagation dynamics of autofocusing circle pearcey gaussian vortex beams in a harmonic potential," *Optics Express*, vol. 28, no. 1, pp. 325–333, 2020.

[374] L. Gong, Q. Zhao, H. Zhang, X.-Y. Hu, K. Huang, J.-M. Yang, and Y.-M. Li, "Optical orbital-angular-momentum-multiplexed data transmission under high scattering," *Light: Science & Applications*, vol. 8, no. 1, p. 27, 2019.

[375] W. Shao, S. Huang, X. Liu, and M. Chen, "Free-space optical communication with perfect optical vortex beams multiplexing," *Optics Communications*, vol. 427, pp. 545–550, 2018.

[376] H. Laabs, "Propagation of hermite-gaussian-beams beyond the paraxial approximation," *Optics Communications*, vol. 147, no. 1-3, pp. 1–4, 1998.

[377] S. Saghafi, C. Sheppard, and J. Piper, "Characterising elegant and standard hermite–gaussian beam modes," *Optics Communications*, vol. 191, no. 3-6, pp. 173–179, 2001.

[378] B. Lü and H. Ma, "A comparative study of elegant and standard hermite–gaussian beams," *Optics Communications*, vol. 174, no. 1-4, pp. 99–104, 2000.

[379] X. Ji, X. Chen, and B. Lü, "Spreading and directionality of partially coherent hermite-gaussian beams propagating through atmospheric turbulence," *Journal of Optical Society of America A*, vol. 25, no. 1, pp. 21–28, 2008.

[380] L. Novotny, E. J. Sánchez, and X. S. Xie, "Near-field optical imaging using metal tips illuminated by higher-order hermite–gaussian beams," *Ultramicroscopy*, vol. 71, no. 1-4, pp. 21–29, 1998.

[381] J. C. Gutiérrez-Vega and M. A. Bandres, "Ince–gaussian beams in a quadratic-index medium," *Journal of Optical Society of America A*, vol. 22, no. 2, pp. 306–309, 2005.

[382] D. Deng and Q. Guo, "Ince-gaussian solitons in strongly nonlocal nonlinear media," *Optics Letters*, vol. 32, no. 21, pp. 3206–3208, 2007.

[383] H. T. Eyyuboğlu, "Propagation analysis of ince–gaussian beams in turbulent atmosphere," *Applied Optics*, vol. 53, no. 11, pp. 2290–2296, 2014.

[384] U. Andrade, A. Garcia, and M. Rocha, "Bessel beam optical tweezers for manipulating superparamagnetic beads," *Applied Optics*, vol. 60, no. 12, pp. 3422–3429, 2021.

[385] J. Amako, D. Sawaki, and E. Fujii, "Microstructuring transparent materials by use of nondiffracting ultrashort pulse beams generated by diffractive optics," *Journal of Optical Society of America B*, vol. 20, no. 12, pp. 2562–2568, 2003.

[386] K.-S. Lee and J. P. Rolland, "Bessel beam spectral-domain high-resolution optical coherence tomography with micro-optic axicon providing extended focusing range," *Optics Letters*, vol. 33, no. 15, pp. 1696–1698, 2008.

[387] S. Khonina, S. Karpeev, and V. Paranin, "Birefringence detection of a gradient-index lens based on astigmatic transformation of a bessel beam," *Optik*, vol. 164, pp. 679–685, 2018.

[388] C. Rickenstorff, J. García-García, A. Sampayo-Martínez, A. S. Ostrovksy, and V. Arrizón, "Generation of the "perfect" vortex for optical trapping," in *Frontiers in Optics*, pp. JW3A–34, Optica Publishing Group, 2013.

[389] G. Siviloglou, J. Broky, A. Dogariu, and D. Christodoulides, "Observation of accelerating airy beams," *Physical Review Letters*, vol. 99, no. 21, p. 213901, 2007.

[390] G. Siviloglou, J. Broky, A. Dogariu, and D. Christodoulides, "Ballistic dynamics of airy beams," *Optics Letters*, vol. 33, no. 3, pp. 207–209, 2008.

[391] P. Polynkin, M. Kolesik, J. V. Moloney, G. A. Siviloglou, and D. N. Christodoulides, "Curved plasma channel generation using ultraintense airy beams," *Science*, vol. 324, no. 5924, pp. 229–232, 2009.

[392] S. Jia, J. C. Vaughan, and X. Zhuang, "Isotropic three-dimensional super-resolution imaging with a self-bending point spread function," *Nature Photonics*, vol. 8, no. 4, pp. 302–306, 2014.

[393] J. Baumgartl, M. Mazilu, and K. Dholakia, "Optically mediated particle clearing using airy wavepackets," *Nature Photonics*, vol. 2, no. 11, pp. 675–678, 2008.

[394] X. Zang, W. Dan, Y. Zhou, H. Lv, F. Wang, Y. Cai, and G. Zhou, "Abruptly autofocusing of generalized circular airy derivative beams," *Optics Express*, vol. 30, no. 3, pp. 3804–3819, 2022.

[395] P. Senthilkumaran, "Singularities in physics and engineering," *IOP Publishing*, vol. 10, pp. 978–0, 2018.

[396] R. Vinu, Z. Chen, J. Pu, Y. Otani, and R. K. Singh, "Speckle-field digital polarization holographic microscopy," *Optics Letters*, vol. 44, no. 23, pp. 5711–5714, 2019.

[397] L. Nikolova and P. S. Ramanujam, *Polarization holography*. Cambridge University Press, 2009.

[398] X. Chen, D. Deng, J. Zhuang, X. Peng, D. Li, L. Zhang, F. Zhao, X. Yang, H. Liu, and G. Wang, "Focusing properties of circle pearcey beams," *Optics Letters*, vol. 43, no. 15, pp. 3626–3629, 2018.

[399] M. Wollenhaupt, A. Assion, and T. Baumert, "Femtosecond laser pulses: linear properties, manipulation, generation and measurement," *Springer Handbook of Lasers and Optics*, p. 937, 2007.

[400] V. Dev and V. Pal, "Probing topological charge of discrete vortices," *arXiv:2305.08410*, 2023.

[401] J. Kreuzer, *Laser light redistribution in illuminating optical signal processing systems*. Massachusetts Institute of Technology Press, 1965.

[402] P. W. Malyak, "Two-mirror unobscured optical system for reshaping the irradiance distribution of a laser system," *Appl. Opt.*, vol. 31, pp. 4377–4383, 1992.

[403] P. W. Scott and W. H. Southwell, "Reflective optics for irradiance redistribution of laser beams: design," *Appl. Opt.*, vol. 20, pp. 1606–1610, 1981.

[404] H. Aagedal, M. Schmid, S. Egner, J. Muller-Quade, J. Beth, and F. Wyrowski, "Analytical beam shaping with application to laser-diode arrays," *J. Opt. Soc. Am. A*, vol. 14, pp. 1549–1553, 1997.

[405] B. Hao and J. R. Legger, "Polarization beam shaping," *Appl. Opt.*, vol. 46, pp. 8211–8217, 2007.

[406] B. Hao, J. Burch, and J. Leger, "Smallest flattop focus by polarization engineering," *Appl. Opt.*, vol. 47, pp. 2931–2940, Jun 2008.

[407] R. Sundar, K. Ranganathan, and S. M. Oak, "Generation of flattened gaussian beam profiles in a nd:yag laser with a gaussian mirror resonator," *Appl. Opt.*, vol. 47, pp. 147–152, Jan 2008.

[408] A. Parent, M. Morin, and P. Lavigne, "Propagation of super-gaussian field distributions," *Opt. Quant. Electron.*, vol. 24, pp. S1071–S1079, Sep 1992.

[409] Z. Mei and O. Korotkova, "Random sources generating ring-shaped beams," *Opt. Lett.*, vol. 38, pp. 91–93, Jan 2013.

[410] S. Sahin and O. Korotkova, "Light sources generating far fields with tunable flat profiles," *Opt. Lett.*, vol. 37, pp. 2970–2972, Jul 2012.

[411] H. Ma, H. Zhao, P. Zhou, X. Wang, Y. Ma, X. Xu, and Z. Liu, "Adaptive conversion of multimode beam to near-diffraction-limited flattop beam based on dual-phase-only liquid-crystal spatial light modulators," *Opt. Express*, vol. 18, pp. 27723–27730, Dec 2010.

[412] N. Davidson, A. A. Friesem, and E. Hasman, "Holographic axilens: high resolution and long focal depth," *Opt. Lett.*, vol. 16, pp. 523–525, Apr 1991.

[413] S. Khonina, V. Kotlyar, and V. Soifer, "Calculation of the focusators into a longitudinal line-segment and study of a focal area," *J. Mod. Opt.*, vol. 40, no. 5, pp. 761–769, 1993.

[414] V. V. Kotlyar, S. N. Khonina, and V. A. Soifer, "Iterative calculation of diffractive optical elements focusing into a three-dimensional domain and onto the surface of the body of rotation," *J. Mod. Opt.*, vol. 43, no. 7, pp. 1509–1524, 1996.

[415] Y. Zhao, Q. Zhan, Y. Zhang, and Y.-P. Li, "Creation of a three-dimensional optical chain for controllable particle delivery," *Opt. Lett.*, vol. 30, pp. 848–850, Apr 2005.

[416] A. Forouzmand and H. Mosallaei, "All-dielectric c-shaped nanoantennas for light manipulation: Tailoring both magnetic and electric resonances to the desire," *Adv. Opt. Mater.*, vol. 5, no. 14, p. 1700147, 2017.

[417] S. Abdollahramezani, A. Chizari, A. E. Dorche, M. V. Jamali, and J. A. Salehi, "Dielectric metasurfaces solve differential and integro-differential equations," *Opt. Lett.*, vol. 42, pp. 1197–1200, Apr 2017.

[418] A. M. Shaltout, V. M. Shalaev, and M. L. Brongersma, "Spatiotemporal light control with active metasurfaces," *Science*, vol. 364, no. 6441, 2019.

[419] A. Kovalev, V. Kotlyar, and A. Porfirev, "Auto-focusing accelerating hypergeometric laser beams," *Journal of Optics*, vol. 18, no. 2, p. 025610, 2016.

[420] J. D. Ring, J. Lindberg, A. Mourka, M. Mazilu, K. Dholakia, and M. R. Dennis, "Auto-focusing and self-healing of pearcey beams," *Opt. Express*, vol. 20, no. 17, pp. 18955–18966, 2012.

[421] J. A. Davis, D. M. Cottrell, and D. Sand, "Abruptly autofocusing vortex beams," *Opt. Express*, vol. 20, no. 12, pp. 13302–13310, 2012.

[422] V. P. Lukin, P. A. Konyaev, and V. A. Sennikov, "Beam spreading of vortex beams propagating in turbulent atmosphere," *Appl. Opt.*, vol. 51, no. 10, pp. C84–C87, 2012.

[423] I. P. Lukin, "Mean intensity of vortex bessel beams propagating in turbulent atmosphere," *Appl. Opt.*, vol. 53, no. 15, pp. 3287–3293, 2014.

[424] X. Chu, "Evolution of an airy beam in turbulence," *Opt. Lett.*, vol. 36, no. 14, pp. 2701–2703, 2011.

[425] R. Dasgupta, S. Ahlawat, R. S. Verma, and P. K. Gupta, "Optical orientation and rotation of trapped red blood cells with laguerre-gaussian mode," *Optics Express*, vol. 19, no. 8, pp. 7680–7688, 2011.

[426] D. Zhang, J. Liu, J. Yao, Z. Zhang, B. Chen, Z. Lin, J. Cao, and X. Wang, "Enhanced sub-terahertz microscopy based on broadband airy beam," *Advanced Materials Technologies*, p. 2100985, 2021.

[427] D. Kim and J. Kim, "High-power tem 00 and laguerre–gaussian mode generation in double resonator configuration," *Applied Physics B*, vol. 121, no. 3, pp. 401–405, 2015.

[428] C. H. Acevedo, R. Wu, J. K. Miller, E. G. Johnson, and A. Dogariu, "Colloidal density control with bessel–gauss beams," *Scientific Reports*, vol. 11, no. 1, p. 12284, 2021.

[429] R. W. Bowman, A. J. Wright, and M. J. Padgett, "An slm-based shack–hartmann wavefront sensor for aberration correction in optical tweezers," *Journal of Optics*, vol. 12, no. 12, p. 124004, 2010.

[430] M. J. Booth, M. A. Neil, R. Juškaitis, and T. Wilson, "Adaptive aberration correction in a confocal microscope," *Proceedings of the National Academy of Sciences*, vol. 99, no. 9, pp. 5788–5792, 2002.

[431] G. D. Love, "Wave-front correction and production of zernike modes with a liquid-crystal spatial light modulator," *Applied Optics*, vol. 36, no. 7, pp. 1517–1524, 1997.

[432] J. Dudutis, R. Stonys, G. Račiukaitis, and P. Gečys, "Aberration-controlled bessel beam processing of glass," *Optics Express*, vol. 26, no. 3, pp. 3627–3637, 2018.

[433] E. Vera and P. Meza, "Snapshot compressive imaging using aberrations," *Optics Express*, vol. 26, no. 2, pp. 1206–1218, 2018.

[434] J. Zhuang, L. Zhang, and D. Deng, "Tight-focusing properties of linearly polarized circular airy gaussian vortex beam," *Optics Letters*, vol. 45, no. 2, pp. 296–299, 2020.

[435] Y. Jiang, W. Yu, X. Zhu, and P. Jiang, "Propagation characteristics of partially coherent circular airy beams," *Optics Express*, vol. 26, no. 18, pp. 23084–23092, 2018.

[436] G. A. Deschamps, "Gaussian beam as a bundle of complex rays," *Electronics Letters*, vol. 7, no. 23, pp. 684–685, 1971.

[437] E. Zauderer, "Complex argument hermite–gaussian and laguerre–gaussian beams," *Journal of Optical Society of America A*, vol. 3, no. 4, pp. 465–469, 1986.

[438] A. Ashkin, "Acceleration and trapping of particles by radiation pressure," *Physical Review Letters*, vol. 24, no. 4, p. 156, 1970.

[439] K. C. Neuman and S. M. Block, "Optical trapping," *Review of Scientific Instruments*, vol. 75, no. 9, pp. 2787–2809, 2004.

[440] M. Manousidaki, D. G. Papazoglou, M. Farsari, and S. Tzortzakis, "Abruptly autofocusing beams enable advanced multiscale photo-polymerization," *Optica*, vol. 3, no. 5, pp. 525–530, 2016.

[441] G. Vizsnyiczai, L. Kelemen, and P. Ormos, "Holographic multi-focus 3d two-photon polymerization with real-time calculated holograms," *Optics Express*, vol. 22, no. 20, pp. 24217–24223, 2014.

[442] V. V. Apollonov, *High-Power Optics*. Springer, 2016.

[443] F. Bachmann, P. Loosen, and R. Poprawe, *High power diode lasers: technology and applications*, vol. 128. Springer, 2007.

[444] M. N. Zervas and C. A. Codemard, "High power fiber lasers: a review," *IEEE Journal of Selected Topics in Quantum Electronics*, vol. 20, no. 5, pp. 219–241, 2014.

[445] V. Rogalin, E. Ashkinazi, A. Popovich, V. Ral'chenko, V. Konov, S. Aranchii, M. Ruzin, and M. Rogozhin, "Behavior of the water-cooled polycrystalline diamond plate at extreme densities of laser radiation," *Physics of Wave Phenomena*, vol. 26, no. 2, pp. 75–84, 2018.

[446] R. Li, Y. Jin, Z. Li, and K. Qi, "A comparative study of high-power diode laser and co2 laser surface hardening of aisi 1045 steel," *Journal of Materials Engineering and Performance*, vol. 23, no. 9, pp. 3085–3091, 2014.

[447] M. S. Andreeva, N. V. Artyushkin, M. I. Krymskii, A. I. Laptev, N. I. Polushin, V. E. Rogalin, and M. V. Rogozhin, "Effect of co2-laser power density on the absorption coefficient of polycrystalline cvd diamonds," *Quantum Electronics*, vol. 50, no. 12, p. 1140, 2020.

[448] B. Li, Z. Liu, S. Guo, L. Chen, J. Li, and H. Ma, "Preparation and properties of laser cladding cu-w alloy coating on pure copper electrical contacts," in *Advances in Materials Science and Engineering*, pp. 212–218, CRC Press, 2021.

[449] P. Willmott and J. Huber, "Pulsed laser vaporization and deposition," *Reviews of Modern Physics*, vol. 72, no. 1, p. 315, 2000.

[450] P. Cheo, A. Liu, and G. King, "A high-brightness laser beam from a phase-locked multicore Yb-doped fiber laser array," *IEEE Photonics Technology Letters*, vol. 13, no. 5, pp. 439–441, 2001.

[451] E. Bochove, P. Cheo, and G. King, "Self-organization in a multicore fiber laser array," *Optics Letters*, vol. 28, no. 14, pp. 1200–1202, 2003.

[452] C. Corcoran and R. Rediker, "Operation of five individual diode lasers as a coherent ensemble by fiber coupling into an external cavity," *Applied Physics Letters*, vol. 59, no. 7, pp. 759–761, 1991.

[453] V. Pal, S. Mahler, C. Tradonsky, A. A. Friesem, and N. Davidson, "Rapid fair sampling of the XY spin hamiltonian with a laser simulator," *Physical Review Research*, vol. 2, no. 3, p. 033008, 2020.

[454] M. Fridman, V. Eckhouse, N. Davidson, and A. A. Friesem, "Effect of quantum noise on coupled laser oscillators," *Physical Review A*, vol. 77, no. 6, p. 061803, 2008.

[455] X. Zhou, H. Qu, A. Qi, Z. Chen, X. Xing, X. Wang, Y. Wang, and W. Zheng, "Sidelobe suppression of laser diode arrays by on-chip phase and amplitude manipulation," in *High-Power Lasers and Applications IX*, vol. 10811, pp. 67–72, SPIE, 2018.

[456] F. Xiao, L. Kong, and J. Chen, "Beam-steering efficiency optimization method based on a rapid-search algorithm for liquid crystal optical phased array," *Applied Optics*, vol. 56, no. 16, pp. 4585–4590, 2017.

[457] F. Zhang, D. Zhang, and S. Pan, "Fast and wide-range optical beam steering with ultralow side lobes by applying an optimized multi-circular optical phased array," *Applied Optics*, vol. 57, no. 18, pp. 4977–4984, 2018.

[458] D. Zhang, F. Zhang, and S. Pan, "Grating-lobe-suppressed optical phased array with optimized element distribution," *Optics Communications*, vol. 419, pp. 47–52, 2018.

[459] Y. Arita, M. Mazilu, and K. Dholakia, "Laser-induced rotation and cooling of a trapped microgyroscope in vacuum," *Nature Communications*, vol. 4, no. 1, pp. 1–7, 2013.

[460] X. Wang, Z. Nie, Y. Liang, J. Wang, T. Li, and B. Jia, "Recent advances on optical vortex generation," *Nanophotonics*, vol. 7, no. 9, pp. 1533–1556, 2018.

[461] T. Omatsu, K. Miyamoto, and A. J. Lee, "Wavelength-versatile optical vortex lasers," *Journal of Optics*, vol. 19, no. 12, p. 123002, 2017.

[462] A. Forbes, "Controlling light's helicity at the source: orbital angular momentum states from lasers," *Philosophical Transactions of the Royal Society A: Mathematical, Physical and Engineering Sciences*, vol. 375, no. 2087, p. 20150436, 2017.

[463] M. Beijersbergen, R. Coerwinkel, M. Kristensen, and J. Woerdman, "Helical-wavefront laser beams produced with a spiral phaseplate," *Optics Communications*, vol. 112, no. 5-6, pp. 321–327, 1994.

[464] E. Abramochkin and V. Volostnikov, "Beam transformations and nontransformed beams," *Optics Communications*, vol. 83, no. 1-2, pp. 123–135, 1991.

[465] M. W. Beijersbergen, L. Allen, H. Van der Veen, and J. Woerdman, "Astigmatic laser mode converters and transfer of orbital angular momentum," *Optics Communications*, vol. 96, no. 1-3, pp. 123–132, 1993.

[466] C. Rosales-Guzmán, N. Bhebhe, and A. Forbes, "Simultaneous generation of multiple vector beams on a single slm," *Optics Express*, vol. 25, no. 21, pp. 25697–25706, 2017.

[467] S. Yu, L. Li, and N. Kou, "Generation, reception and separation of mixed-state orbital angular momentum vortex beams using metasurfaces," *Optical Materials Express*, vol. 7, no. 9, pp. 3312–3321, 2017.

[468] N. Heckenberg, R. McDuff, C. Smith, and A. White, "Generation of optical phase singularities by computer-generated holograms," *Optics Letters*, vol. 17, no. 3, pp. 221–223, 1992.

[469] P. Coullet, L. Gil, and F. Rocca, "Optical vortices," *Optics Communications*, vol. 73, no. 5, pp. 403–408, 1989.

[470] F. T. Arecchi, G. Giacomelli, P. L. Ramazza, and S. Residori, "Vortices and defect statistics in two-dimensional optical chaos," *Phys. Rev. Lett.*, vol. 67, pp. 3749–3752, Dec 1991.

[471] P. Genevet, S. Barland, M. Giudici, and J. R. Tredicce, "Bistable and addressable localized vortices in semiconductor lasers," *Phys. Rev. Lett.*, vol. 104, p. 223902, Jun 2010.

[472] L. Corman, L. Chomaz, T. Bienaimé, R. Desbuquois, C. Weitenberg, S. Nascimbene, J. Dalibard, and J. Beugnon, "Quench-induced supercurrents in an annular bose gas," *Physical Review Letters*, vol. 113, no. 13, p. 135302, 2014.

[473] W. H. Zurek, "Cosmological experiments in superfluid helium?," *Nature*, vol. 317, no. 6037, pp. 505–508, 1985.

[474] M. Dong, C. Zhao, Y. Cai, and Y. Yang, "Partially coherent vortex beams: Fundamentals and applications," *Sci. China-Phys. Mech. Astron.*, vol. 64, no. 2, p. 224201, 2021.

[475] M. Anguiano-Morales, A. Martínez, M. D. Iturbe-Castillo, S. Chávez-Cerda, and N. Alcalá-Ochoa, "Self-healing property of a caustic optical beam," *Applied Optics*, vol. 46, no. 34, pp. 8284–8290, 2007.

[476] V. Arrizón, D. Aguirre-Olivas, G. Mellado-Villaseñor, and S. Chávez-Cerda, "Self-healing in scaled propagation invariant beams," *arXiv preprint arXiv:1503.03125*, 2015.

[477] G. Milione, A. Dudley, T. A. Nguyen, O. Chakraborty, E. Karimi, A. Forbes, and R. R. Alfano, "Measuring the self-healing of the spatially inhomogeneous states of polarization of vector bessel beams," *Journal of Optics*, vol. 17, no. 3, p. 035617, 2015.

[478] F. O. Fahrbach, P. Simon, and A. Rohrbach, "Microscopy with self-reconstructing beams," *Nature Photonics*, vol. 4, no. 11, pp. 780–785, 2010.

[479] V. Garcés-Chávez, D. McGloin, H. Melville, W. Sibbett, and K. Dholakia, "Simultaneous micromanipulation in multiple planes using a self-reconstructing light beam," *Nature*, vol. 419, no. 6903, pp. 145–147, 2002.

[480] M. McLaren, T. Mhlanga, M. J. Padgett, F. S. Roux, and A. Forbes, "Self-healing of quantum entanglement after an obstruction," *Nature Communications*, vol. 5, no. 1, pp. 1–8, 2014.

[481] P. Vaity, J. Banerji, and R. Singh, "Measuring the topological charge of an optical vortex by using a tilted convex lens," *Physics Letters A*, vol. 377, no. 15, pp. 1154–1156, 2013.

[482] A. Dogariu and S. Amarande, "Propagation of partially coherent beams:turbulence-induced degradation," *Opt. Lett.*, vol. 28, pp. 10–12, Jan 2003.

[483] Z. Lecz, I. V. Konoplev, A. Seryi, and A. Andreev, "Gigagauss solenoidal magnetic field inside bubbles excited in under-dense plasma," *Sci. Rep.*, vol. 6, no. 1, p. 36139, 2016.

[484] A. Denoeud, L. Chopineau, A. Leblanc, and F. Quéré, "Interaction of ultraintense laser vortices with plasma mirrors," *Phys. Rev. Lett.*, vol. 118, p. 033902, Jan 2017.

[485] G. C. G. Berkhout and M. W. Beijersbergen, "Method for probing the orbital angular momentum of optical vortices in electromagnetic waves from astronomical objects," *Phys. Rev. Lett.*, vol. 101, p. 100801, Sep 2008.

[486] M. P. J. Lavery, F. C. Speirits, S. M. Barnett, and M. J. Padgett, "Detection of a spinning object using light's orbital angular momentum," *Science*, vol. 341, pp. 537–540, 2013.

[487] Y. Shen, X. Wang, Z. Xie, C. Min, X. Fu, Q. Liu, M. Gong, and X. Yuan, "Optical vortices 30 years on: Oam manipulation from topological charge to multiple singularities," *Light Sci. Appl.*, vol. 8, p. 90, 2019.

[488] C. Liu, J. Liu, L. Niu, X. Wei, K. Wang, and Z. Yang, "Terahertz circular airy vortex beams," *Sci. Rep.*, vol. 7, p. 3891, 2017.

[489] J. W. Fleischer, G. Bartal, O. Cohen, O. Manela, M. Segev, J. Hudock, and D. N. Christodoulides, "Observation of vortex-ring "discrete" solitons in 2d photonic lattices," *Phys. Rev. Lett.*, vol. 92, p. 123904, Mar 2004.

[490] K. Zhu, G. Zhou, X. Li, X. Zheng, and H. Tang, "Propagation of bessel-gaussian beams with optical vortices in turbulent atmosphere," *Opt. Express*, vol. 16, pp. 21315–21320, Dec 2008.

[491] C. Maurer, A. Jesacher, S. Bernet, and M. Ritsch-Marte, "What spatial light modulators can do for optical microscopy," *Laser & Photonics Reviews*, vol. 5, no. 1, pp. 81–101, 2011.

[492] A. Vaziri, J.-W. Pan, T. Jennewein, G. Weihs, and A. Zeilinger, "Concentration of higher dimensional entanglement: Qutrits of photon orbital angular momentum," *Phys. Rev. Lett.*, vol. 91, p. 227902, Nov 2003.

[493] Q.-F. Chen, B.-S. Shi, Y.-S. Zhang, and G.-C. Guo, "Entanglement of the orbital angular momentum states of the photon pairs generated in a hot atomic ensemble," *Phys. Rev. A*, vol. 78, p. 053810, Nov 2008.

[494] J. Ng, Z. Lin, and C. T. Chan, "Theory of optical trapping by an optical vortex beam," *Phys. Rev. Lett.*, vol. 104, p. 103601, Mar 2010.

[495] M. Padgett and R. Bowman, "Tweezers with a twist," *Nat. Photon.*, vol. 5, pp. 343–348, 2011.

[496] G. Tkachenko and E. Brasselet, "Helicity-dependent three-dimensional optical trapping of chiral microparticles," *Nat. Commun.*, vol. 5, p. 4491, 2014.

[497] J. Schliemann and F. G. Mertens, "Vortices in quantum spin systems," *Eur. Phys. J. B*, vol. 9, pp. 237–243, 1999.

[498] S. W. Hell and J. Wichmann, "Breaking the diffraction resolution limit by stimulated emission: stimulated-emission-depletion fluorescence microscopy," *Opt. Lett.*, vol. 19, pp. 780–782, Jun 1994.

[499] G. Xie, H. Song, Z. Zhao, G. Milione, Y. Ren, C. Liu, R. Zhang, C. Bao, L. Li, Z. Wang, K. Pang, D. Starodubov, B. Lynn, M. Tur, and A. E. Willner, "Using a complex optical orbital-angular-momentum spectrum to measure object parameters," *Opt. Lett.*, vol. 42, pp. 4482–4485, Nov 2017.

[500] J. Wang, J.-Y. Yang, I. M. Fazal, N. Ahmed, Y. Yan, H. Huang, Y. Ren, Y. Yue, S. Dolinar, M. Tur, and A. E. Willner, "Terabit free-space data transmission employing orbital angular momentum multiplexing," *Nat. Photon.*, vol. 6, pp. 488–496, 2012.

[501] N. Bozinovic, Y. Yue, Y. Ren, M. Tur, P. Kristensen, H. Huang, A. E. Willner, and S. Ramachandran, "Terabit-scale orbital angular momen- tum mode division multiplexing in fibers," *Science*, vol. 340, pp. 1545–1548, 2013.